DEVELOPMENT OF A NOVEL ULTRA-WIDEBAND ANTENNA AND PROTOTYPE SCANNER FOR DETECTION AND LOCATION OF VOIDS IN WOOD

by

Kim V. Dotto, P.Eng.

B.Sc. The University of British Columbia, 1979
B.A.Sc. The University of British Columbia, 1982
M.A.Sc. The University of British Columbia, 1995

A THESIS SUBMITTED IN PARTIAL FULFILMENT OF
THE REQUIREMENTS FOR THE DEGREE OF

DOCTOR OF PHILOSOPHY

in

THE FACULTY OF GRADUATE STUDIES

ELECTRICAL AND COMPUTER ENGINEERING

THE UNIVERSITY OF BRITISH COLUMBIA

March 22, 2005

Abstract

The design of a prototype ultra-wideband scanner for the detection of voids in wooden models is presented along with the design of a novel Ultra-Wideband Antenna.

The design and performance of a new type of antipodal tapered slot antenna are described. The three-dimensional structure of the antenna is given as well as the experimental results for gain, radiation pattern, cross polarization, VSWR and Return Loss (S_{11}). The new Fleur-de-Lis (FDL) antenna shows a 10 dB bandwidth greater than 20 GHz with an S_{11} Return Loss curve that is flatter than those for current antipodal tapered slot antenna designs. The effects of varying physical parameters are also investigated, giving some insight into the antenna's wideband operation.

The FDL antenna is used as the basis for an ultra-wideband RF scanning system, which is used to measure ultra-wideband transmission (S_{21}) response profiles. These transmission response profiles show that it is possible to determine the size of a cylindrical object of metal or dielectric material with a set of readings taken over an ultra-wideband frequency range for a single transmission line of sight. It is also shown that, with a simple pattern-matching algorithm, it is possible to detect and locate the position of an air-filled void in a "cylindrical" wooden model with readings taken over an ultra-wideband frequency range for a single transmission line of sight.

Table of Contents

List of Tables

List of Figures

List of Abbreviations

BW	-	bandwidth
dB	-	Decibels
DUT	-	Device Under Test
FDL	-	Fleur-de-Lis
FEKO	-	**FE**ldberechnung bei **K**örpern mit beliebiger **O**berfläche
GHz	-	Gigahertz
GPIB	-	General Purpose Interface Bus
GPS	-	Global Positioning Satellite
MHz	-	Megahertz
MoM	-	Method of Moments
PCB	-	Printed Circuit Board
PO	-	Physical Optics
LTSA	-	Linear Tapered Slot Antenna
TSA	-	Tapered Slot Antenna
UTD	-	Uniform Theory of Diffraction
UWB	-	Ultra Wideband
VSWR	-	Voltage Standing Wave Ratio

Acknowledgements

I would like to thank my supervisor Dr. M.J. Yedlin for his support, encouragement, enthusiasm and advice during this thesis project. I would also like to thank my wife Patricia for her support and patience, and my children Alex and Laura for their view on the world to help keep everything in perspective.

I would also like to acknowledge Dr. David Michelson and Kim Lam for their help during my thesis project.

Chapter 1

1.0 Introduction

Each year telephone companies, power distribution companies and government departments install or replace a large number of telephone/power poles. The vast majority of these poles are made of wood and have a finite service life. In 1999 BC Hydro estimated that it replaces 4000 wooden poles per year [1]. Replacing these poles is very expensive and the longer a pole can be left in service, the lower the operating costs for the utility or government. As well, there is an environmental cost associated with replacing these poles as trees must be cut to produce the replacement poles and the retired poles must be disposed of.

The length of service of a telephone pole is determined mostly by how well it withstands the elements of nature. Rain, ice and snow, temperature, sun and insects all contribute to the eventual breakdown of the pole by introducing cracks and voids that weaken the pole structurally. These voids also allow bacteria and fungi to enter the pole, causing rot, which further weakens the pole. If the structural integrity of a pole deteriorates excessively, the pole will eventually break under stress, most likely during a period of high storm activity. The results of such a catastrophic failure are power and communication outages, which can sometimes last for days.

In addition to pole management and replacement, the management, cutting and harvesting of forests requires knowledge of the internal condition of the trees to be harvested. The presence or absence of cracks, insect damage or rot can determine if a tree is suitable for harvesting or should be left to promote good reforestation practices [2].

Chapter 1 - Introduction

Currently, the most common method for determining the condition of these items is visual inspection of the outside of the object or coring of the tree, log or pole. Visual inspection means looking at the surface condition of the object and assuming that the degradation of the structural integrity on the inside of the object is proportional to the visual damage on the outside. Coring involves boring a hole in the tree or log with an instrument known as an increment borer and removing a cross-section of material. It is hoped that an examination of the cross-section of material removed from a single sample will determined the condition of the entire object [3-7].

Neither visual inspection nor core sampling can adequately determine the profile for the entire object. Internal damage to a tree or pole is often done by burrowing insects that leave only small visual traces of their presence on the outside of the tree. Coring can detect internal damage if a core that contains damaged material is removed, but to do a profile of a tall tree or pole would require many core samples, which is both time-consuming and expensive. In addition, coring is a destructive testing method. Once the core sample has been removed, a hole remains, which opens the tree or log to more internal damage from insects and weather. For processing logs into lumber, coring is not an acceptable test mechanism as it introduces holes into the finished product, which would lessen the strength and value of the lumber. Clearly what is needed is a non-invasive and non-destructive method for determining the interior condition of these objects.

1.1 Wood Properties and Composition

Wood is not a homogeneous material. Different types of wood are made from different materials and have differing properties such as density and chemical composition. While chemical composition changes with density, density is related to the way the wood was grown, rather than the chemical composition itself. Wood that grows faster is less dense than slower

growing wood, and knots that are denser than trunk wood are formed by growing branches. Non-destructive testing based on density changes has been performed and will be discussed later.

The chemical makeup of the wood depends upon the species of wood and the growth pattern of the tree. Once a tree has been cut, its chemical composition can be ascertained by standard chemical methods. This does not, however, help for non-destructive testing. One feature that depends upon chemical composition, however, and that can be examined non-destructively, is the wood's dielectric property. It has been shown that several factors such as frequency, temperature, moisture content, density, electric field and grain direction all have an effect on the dielectric behaviour of wood [8].

1.2 Dielectric Properties of Wood

The dielectric properties of wood are normally characterized by two parameters: the real part of the relative dielectric constant (ε') and the dielectric loss tangent ($tg\delta$). The relative dielectric constant tells us by how much the capacity of a capacitor with the insulating material between its conducting surfaces is greater than that of the same capacitor in which the vacuum is dielectric. In principle, the dielectric constant is a measure of how much electric potential energy is stored in the material when it is placed in a given electric field [9]. The dielectric loss tangent is numerically equal to the ratio between the active current and the reactive current in a material [10]. The dielectric loss factor ($\varepsilon' \cdot tg\delta$) is also used to characterize the dielectric properties of wood. The values of ε' and $tg\delta$ are dimensionless.

The total dielectric effect of samples are determined by the bulk dielectric properties of the various materials that make up that piece and, in general, ε' can depend on frequency in with significant changes in the microwave region due to different types of polarizations [11].

Chapter 1 - Introduction

Wood (wood cell walls) is a composite material that is made up mostly of the 3 following compounds: cellulose, hemicellulose and lignin. Cellulose and hemicellulose are polysaccharides, which make up 70% -75% of the wood. Lignin is a mixture of polymers based on phenyl propane units and accounts for between 18% - 30%. The remainder is made up of ash and other substances that are soluble in either ether or water. In addition, the dielectric properties of the sample will depend upon the amount of water in the wood sample.

Cellulose, hemicellulose and lignin are polar polymers. These substances are considered to have high molecular weights and have a number of polar groups. As such, they are subject to dipole-radical polarization. This kind of polarization is caused by the movement of the polar group with respect to the main body of the molecule. The polarizability of each of the materials depends on a number of factors: the type of polar group (-OH, $-CH_2OH$, etc), the molecule to which the group is attached, and the surrounding environment (presence of other polar groups, including water). The amount of polarization, energy loss and the relaxation or response frequency will change depending on the combination of materials that make up the sample under consideration.

Water is present in any sample of wood. The amount present and its form are determined by the conditions under which the tree was grown and how the wood has been treated since harvesting. Water is present in 3 forms in wood: free, bound and ice. Free water is water found inside the cell cavities. Bound water is water bound in the cell walls themselves. Ice forms when the temperature drops below 0°C . As the temperature drops free water first forms into ice. As the temperature drops further, to between -50°C and -80°C, the bound water freezes. It appears that below -80°C most of the freezing has occurred and a small portion of the water (~5%) remains unconverted to ice. Under the influence of an external electric field both dry and moist wood are considered polar dielectrics.

1.2.1 Polarization, Relaxation Times and Transmitted Spectrum

One of the important properties of wood is its polarization capabilities. With no applied external field, the net sum of charges in a sample adds up to zero, and there is no charge displacement in the sample. Under the influence of an external electric field, the materials that make up a sample of wood undergo a realignment, and the sample acquires a net dipole moment. The sample acquires a total moment P, which is the sum of all individual dipole moments.

Wood is a linear dielectric material [10] up to the point at which an applied electric field causes the wood to break down. For our application, we will be using small applied field strengths well below this limit. Wood is a material for which the dielectric polarization depends linearly on the strength of the applied field E. $\vec{P}$ is then given by

$$\vec{P} = \chi \varepsilon_0 \vec{E} \qquad (1.1)$$

where

$\vec{P}$ and $\vec{E}$ are both vector quantities

χ = electric susceptibility

ε_0 = permittivity of free space= 8.854×10^{-12} F/m.

Since the electric susceptibility can also be written as

$$\chi = (\varepsilon' - 1) \qquad (1.2)$$

this gives

$$\vec{P} = (\varepsilon' - 1)\varepsilon_0 \vec{E}. \qquad (1.3)$$

1.2.2 Polarization Components

The total polarization of a sample of wood can be broken down into a sum of five kinds of polarization that take place in moist wood:

$$P = P_e + P_a + P_d + P_v + P_z \tag{1.4}$$

where

P_e = electronic polarization

P_a = ionic (atomic) polarization

P_d = dipole (orientation) polarization

P_v = interfacial (structural) polarization

P_z = electrolytic polarization.

Electronic polarization arises from the shift of the electrons in orbit around the nucleus and occurs in a very short time (10^{-14} to 10^{-16} seconds) after the application of the electric field. It does not depend on the temperature and is outside of the range of RF frequencies.

Ionic polarization is due to the elastic displacement of atoms in a molecule as well as the displacement of charged ions in molecules with ionic bonds. In this case the polarization occurs because the applied electric field causes the different charge centres in the molecules to move relative to each other and their normal equilibrium locations. This polarization increases with a rise in temperature. As the molecules heat up, the increased thermal energy causes an increase in distance between ions, which tends to weaken the interaction between them. The time to produce this kind of polarization in response to an applied field is about 10^{-12} to 10^{-13} seconds.

Chapter 1 - Introduction

Dipole polarization is caused by the rotation of dipolar molecules in alignment with an applied electric field. Dipole polarization depends upon temperature because the thermal motion of the molecules tends to randomize the alignment of the molecules. Dipole polarization is present in water as well as in other polar molecules that make up wood. One other type of dipole polarization is *dipole-radical polarization.* Cellulose, hemicellulose and lignin possess polar groups such as -OH or $-CH_2OH$, which will realign in the presence of an electric field relative to the rest of the molecule. Both types of dipole polarization will also show a gradual increase or decrease with the application or removal of an electric field. The realignment of the molecules or radical groups within a molecule are not instantaneous. Forces and interactions between molecules will slow the alignment process. After the molecules have aligned, random thermal motion will cause the alignment to gradually disappear in the absence of the applied field. This effect is called dielectric relaxation. The value of the polarization diminishes in accordance with the exponential law [10]:

$$P_d(t) = P_d(0) \exp(-t/t_0) \qquad (1.5)$$

where

$P_d(0)$ = the polarization level at the time the field is removed

t_0 = dipole polarization relaxation time

t = current time

The relaxation time is the period of time taken for the polarization level to decrease by a factor of $e = 2.72$ times relative to its initial value. Usually t_0 is in the range of 10^{-6} to 10^{-12} seconds and for this reason manifests itself at frequencies below 10^{12} Hz. The value of t_0 increases with a decrease in temperature due to the reduction of thermal motion. Dipole

polarization also causes a dissipation of electric energy, which is transformed into thermal energy. The energy used to align the molecules is released as thermal energy through the physical interaction with other molecules.

In nonuniform (heterogeneous) materials, interfacial polarization can take place. Moist wood is composed of substances in the solid, liquid and gaseous phases. The cell walls absorb moisture to form bound water (water that is less free to move). Inside the cell walls, in the interfibril channels and cell wall channels, and inside the cell itself, there is both air and water vapour. If the quantity of moisture exceeds the fibre saturation point, there is free water as well. Under normal conditions the cell wall material and the free ions in the wall and the cell cavities will align themselves due to different contact potentials. Under the influence of an external electric field, these alignments will be distorted by the electric field. After the imposition of the electric field, the realignment will gradually take place and the polarization will increase. This increase in polarization is also bound by a relaxation time and the time constant for this kind of relaxation is between 10^{-3} and 10^{-8} seconds [10].

Electrolytic polarization can occur since moist wood is made up of a number of chemical substances and usually has a residual electrochemical or electrolytic polarization due to the displacement of dissociated ions. When an external field is applied, there will be an increase in the dissociation of the chemical components and a corresponding increase in the electrolytic polarization. The increase in this type of polarization is much slower and is between 10^{-4} and 10^{2} seconds.

Under the influence of an electric field, all of the different types of polarization will take place. The effect of each of the types of polarization will depend on the chemical composition

of the wood, the amount of free and bound water, the size of the cellular structures and the frequency of the applied external field. The variety of polarizations in wood will lead to a varying response to an applied electric field at different frequencies [12]. The responses of these dielectric materials will also be different than those of the voids in an object which possesses no dielectric or polarizable materials This is the key property that should allow voids in the wooden models to be located by an examination of the spectral response to a range of radio frequency signals.

1.3 Current Non-Destructive Testing Methods

While there are currently many different types of non-destructive testing methods being evaluated by the wood industry, many are not suitable for field application and others suffer from limitations in their ability to detect certain types of defects. The most important requirements for non-destructive testing are: 1) the ability to make measurements to determine if a tree or log is suitable; 2) the ability to scan the entire sample or at least the critical areas; 3) the ability to produce fast results in the field in real time [13].

All non-destructive testing methods rely on the different material properties between clear wood and wood with defects. Current methods include CT Scan using X-rays [14-17], Impulse Radar [14], Radio Frequency Moisture Scanning [18] as well as sound wave transmission [19], NMR relaxometry [20], thermography [21], Visible Light Spectral Analysis [22] and polarimetry [23].

The CT X-ray method functions reasonably well on logs in industrial settings such as sawmills but can not be taken into the field due to the nature of the equipment. Additionally, CT scans have problems detecting the differences between areas of knots, voids and higher density

wood in materials with high moisture content [14]. Also, the high cost of CT equipment and operation, which is about 100 times more expensive than other methods [14], and the time required to produce a standard tomographic image [24] means that CT imaging is unsuitable for most industrial environments.

Sound wave technology uses travel times based on differing wood densities to provide information about the internal state of a log. Although the equipment is relatively inexpensive, the test is far from non-destructive. To perform the required measurements, two transducers must be placed on opposite sides of the log or tree. This requires removing the bark from the tree or driving pins into the tree before testing begins [19]. This opens the tree to insect and environmental damage along the 2mm- to 20mm-wide gaps opened in the bark and wood. Additionally, since the process requires good mechanical contact, it is difficult to automate this process. Even once good mechanical contact is made, the results can be inconclusive. For very knotty trees, transmission times are highly variable, and the relationship between transmission time and defect position is not clear. Although large voids and severely degraded material can be detected, it is difficult to identify the type of defect or determine if multiple defects are present [14]. Additionally, due to the high noise and vibration environment of mills, noise interference is significant.

Thermography and NMR techniques are based on the bulk properties of the wood being examined and can be used to detect large differences in the wood being tested. However, the measurements are not sensitive enough to localize defects nor to detect small changes [20, 21]. These methods are also subject to errors introduced by ambient conditions such as local temperature and humidity.

Impulse radar in the microwave range has also been used for non-destructive testing of wood. Due to their relatively long wavelengths, microwaves can penetrate deeply into the materials. Microwaves are reflected or diffracted from any boundaries between materials of differing properties. Because clear wood, wood with no defects, provides relatively insignificant boundaries, abrupt changes caused by defects will generate more noticeable changes. Current use of impulse radar is limited to a small range of frequencies in the GHz range. The impulse radar is scanned along the length of the log, rather than a cross-section, and this produces a series of wavy lines on a chart, called a pulse-echo chart, that depend upon the internal features of the log. A log with few defects produces a chart that is "relatively smooth"; one with severe degradation produces a chart that is "very wavy." It has been found that the pulse-echo charts do not generate a repeatable set of numerical values that can be used in an automated process, nor do they provide a detailed or easily interpreted image [14].

1.4 Theoretical Model

It is possible to create a theoretical model of a log or tree section by dividing up a large cylinder into the sum of an arbitrary number of smaller dielectric cylinders [25]. This model is constructed from a number of regular cylinders of dielectric material. To simulate a void or defect in the model log, one or more of the smaller cylinders can be removed from the model. If the model is then subjected to an EM plane wave, the resulting field at any point in space can then be calculated. If this is repeated over a number of frequencies, a graph of the response at a chosen point in space *vs.* frequency can be created.

Figure 1.1 shows the resulting spectral curves generated by a theoretical model that has had a number of single elements removed from the model at different times [26]. Although the curves shown in Figure 1.1 have similar profiles that overlap at some frequencies, there are

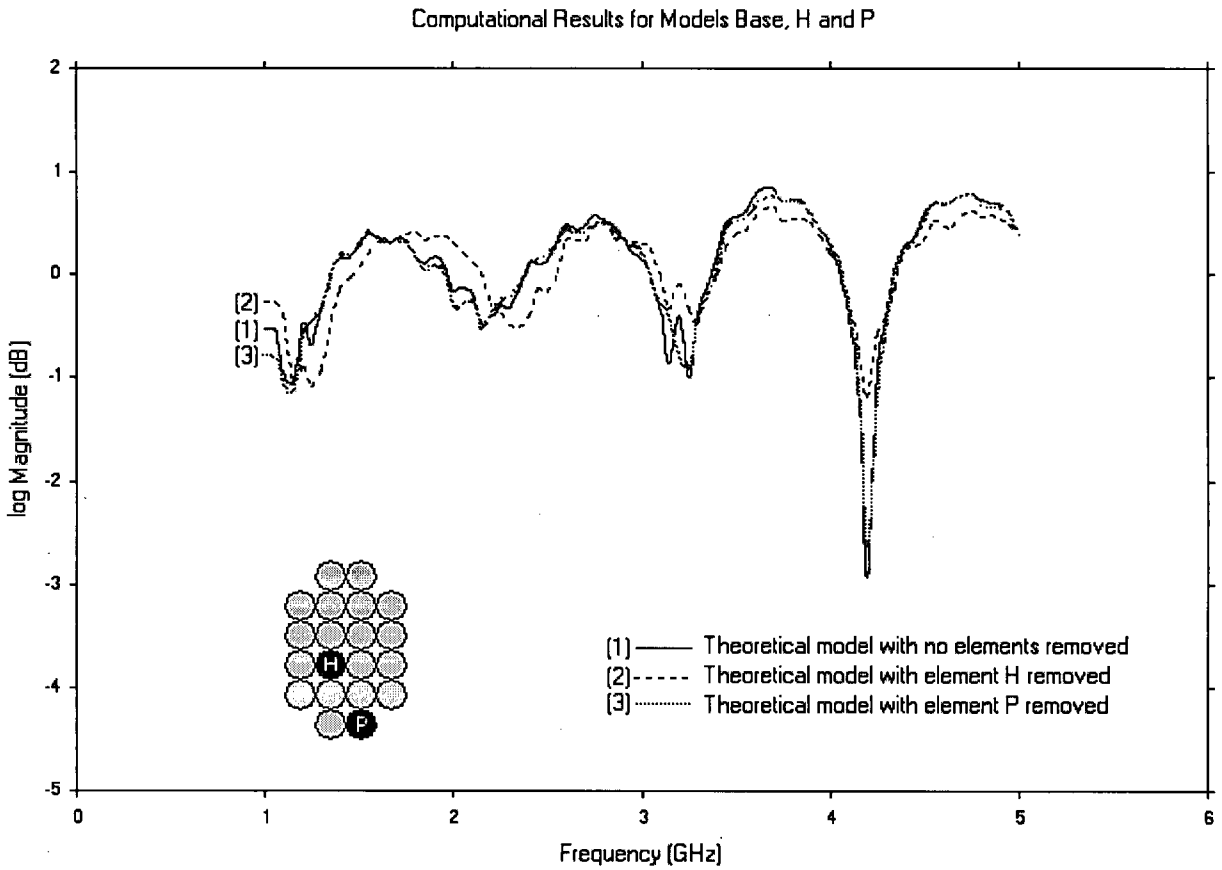

Figure 1.1: Theoretical Spectral Curves

small differences between them that appear when a larger frequency range is examined. The information from a single frequency is not sufficient to differentiate between the signals generated by the removal of the different elements. To successfully differentiate between the removal of the different elements, the profiles must be recorded over an wider bandwidth. Even over a relatively large bandwidth of a GHz or two, there is not a sufficient difference in the spectral curves to uniquely determine which element was removed from the model. To differentiate between the curves generated by the removal of the different elements, it will be necessary to use an ultra-wide bandwidth of more than a few GHz.

1.5 Ultra-wideband RF Void Detection

The hypothesis for this project is that the dielectric properties of a wood sample will differ due to the contributions made by the different polarization components. These dielectric properties will also differ between clear wood and wood with defects or voids present in the sample due to the absence of the various polarization components. The differing net dielectric properties of the wood and the voids will produce differing responses to radio signals at different frequencies. Transmitting a number of microwave radio frequency signals over an ultra-wide bandwidth through a sample of varying composition should result in a set of spectral curves that are directly related to the composition of the sample. It should be possible, having previously identified these spectral curves for objects with voids in known locations, to identify the location of a void in an unknown sample by comparing newly obtained spectra to those previously collected for known voids. By use of a wide range of frequencies rather than a single frequency or a small range of frequencies, it should be possible to overcome the problems associated with current microwave methods and repeatably and uniquely identify the location of voids in wooden objects.

Chapter 2

2.0 Antenna Characteristics

Since one of the goals of this thesis is to measure the properties of wood over a wide range of microwave frequencies, it was necessary to use a wide bandwidth antenna to transmit the test signals. Most antennas radiate with varying efficiency at different frequencies, and this variation can lead to problems with signal degradation [27]. If the input impedance of an antenna varies with the frequency, the signal entering the antenna will be distorted by the varying impedance match [28, 29] and will result in poor measurement results or insufficient uniqueness in the data due to domination by a smaller number of frequencies. Since we expect to see small differences between the spectral curves produced by voids at different locations, this project requires an antenna that is capable of radiating over a multi-gigahertz bandwidth with a flat input impedance response so that the effects of varying power radiation and signal distortion can be minimized. For ultra-wideband antennas, a good impedance match must be designed from first principles, "not added as an afterthought" [30].

2.1 Antenna Measurements and Characterization

For this thesis a network analyser was used to measure the frequency response characteristics, and the antenna was treated as if it were a circuit element. As such, the antenna can be thought of as simply another component in the transmission line circuit. For this antenna, as well as for all other transmission line circuits involving antennas, the main purpose was to provide an impedance match between an electromagnetic wave propagating in a waveguide or cable and a wave propagating in free space [31]. As such, the characterization of an antenna involves measuring both those parameters. There were, however, additional important antenna characteristics that also needed to be considered when choosing the antenna for this project, such

as the antenna's radiation pattern and polarization [27]. This chapter will give a brief explanation of those parameters that are important for the antenna, as well as some relationships between them.

2.2 Impedance Matching, VSWR and S_{11}

There are many parameters characterizing the match or mismatch of one circuit element with another: impedance, reflection coefficient and voltage standing-wave ratio. The main measure of an antenna's input performance that is normally reported is its S_{11} impedance match over the antenna's bandwidth. For a transmission line circuit (as shown in Figure 2.1)

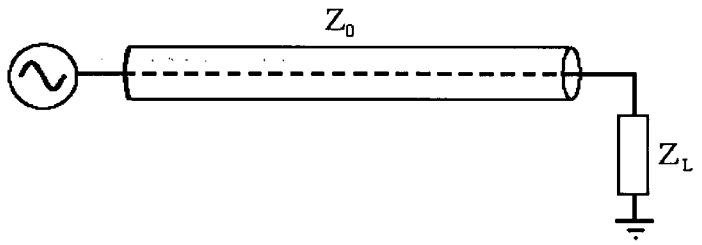

Figure 2.1: Transmission Line Circuit

when a signal is injected into the circuit, if there is a mismatch between the line impedance Z_0 and the load impedance Z_L, some of the energy of the injected signal is reflected back into the circuit. For an antenna this means that any mismatch between the antenna's impedance and that of free space will cause less energy to be radiated by the antenna on transmission, or less energy to be absorbed by the antenna on reception.

This reflection loss is expressed by means of the Voltage Standing-Wave Ratio (VSWR), which is defined as the ratio between the magnitude of E_{max} and the magnitude of E_{min}.

$$VSWR = \frac{|E_{max}|}{|E_{min}|} \tag{2.1}$$

where

E_{max} = the maximum voltage in the standing wave pattern

E_{min} = the minimum voltage in the standing wave pattern.

While low VSWR is not a design necessity as long as the antenna is an efficient radiator, if the VSWR is high, some form of matching network must be placed between the transmitter and antenna to minimize mismatch loss. If there are reflections in the circuit, then E_{max} is defined as the maximum voltage of the peak in the standing wave caused by the reflection and E_{min} is the minimum voltage of the trough of the standing wave. If there is a perfect match with no reflection, then there is no standing wave generated and E_{max} equals E_{min}. In this case the VSWR is equal to 1. As the mismatch between the circuit and load impedance increases, the standing wave grows and the size of the VSWR increases. The mismatch is also often characterized by a reflection coefficient known as Γ, where Γ is defined as

$$\Gamma = \frac{Z_L - Z_0}{Z_L + Z_0} \quad . \tag{2.2}$$

The reflection coefficient is related to the VSWR by equation (2.3):

$$VSWR = \frac{1 + |\Gamma|}{1 - |\Gamma|} \quad . \tag{2.3}$$

Chapter 2 - Antenna Characteristics

An antenna is a two-port device and as such can be analysed like any other network component. For a general two-port device under test (DUT) as is shown in Figure 2.2 all four S parameters are shown.

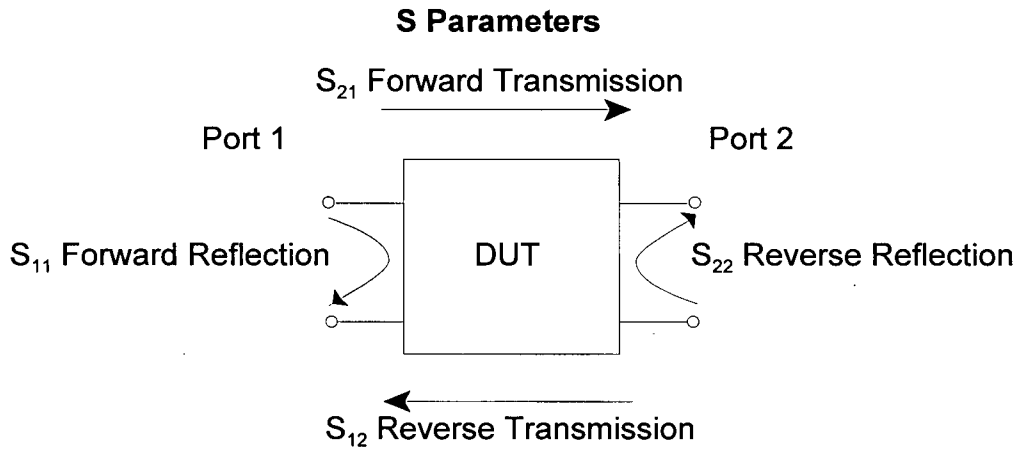

Figure 2.2: S Parameters for a two-port device

The S_{11} is the forward reflection coefficient and is identical to Γ. Hence,

$$S_{11} = \frac{Z_L - Z_0}{Z_L + Z_0} = \Gamma \qquad (2.4)$$

Although the reflection coefficient S_{11} is a vector, which has both magnitude and phase, it is commonly reported as a scalar value (as is the VSWR) which is the magnitude of S_{11}. All S_{11} and VSWR values presented in this thesis will be given in dB.

In addition to being a measurement of the mismatch between the circuit and load impedance, the reflection coefficient S_{11} is also a measure of the power that is transferred to the device under test. In our case, since the device under test is an antenna, S_{11} is a measure of the power that is radiated by the antenna versus the power that is supplied to the antenna. This

relationship is given by

$$Percent\ of\ Power\ Transferred = (1 - |S_{11}|^2) * 100 \qquad (2.5)$$

For an antenna the bandwidth is determined by the upper and lower frequencies where a VSWR = 2.0 corresponds to an S_{11}(dB) $\approx$ -10 dB [32]. Although this is a somewhat arbitrary value, for an S_{11} below -10 dB, 90% of the power supplied to the antenna is transmitted.

2.3 Polarization

For an electromagnetic wave sinusoidally varying in time, the wave is characterized at any observation point by its frequency, magnitude, phase and polarization. The polarization of an antenna is the polarization of the wave radiated by the antenna when transmitting. At some point in space, at a distance sufficiently far from the antenna, the phase front (surface of constant phase) of the radiated wave becomes nearly planar. At this point the wave is referred to as a plane wave, and its electric field (**E**-field) and its magnetic field (**H**-field) lie in the same plane. The polarization of a plane wave is defined as its electric field vector orientation as a function of time, at a fixed position in space. Specifying only the electric field is sufficient since the magnetic field is readily found from **E** using Maxwell's equations.

In general, an electric field traces out an elliptical path over time. If that ellipse is collapsed along the x or y axis, the resulting figure is a vertical or horizontal line. In these cases the antenna is said to have vertical or horizontal *linear* polarization, as shown in Figure 2.3 (a) and (b). In many cases the E-plane is shown to correspond to the x axis. The field can, however, be oriented in any fixed direction in the x-y plane.

If the two axes of the ellipse are identical the figure traced is a circle. For this to happen the magnitude of the E-field does not change with time; only its orientation in space changes. An antenna that produces a wave front with this property is said to have *circular* polarization, as shown in Figure 2.3 (c) and (d). For a circularly polarized antenna there are two further possibilities. While the E-field is rotating it can rotate to the right or to the left. If the wave front is travelling towards the observer (i.e., the observer is looking at the antenna) and the E-field rotates clockwise, the polarization is said to be *left-hand* polarized; if it rotates counter clockwise it is said to be *right-hand* polarized. If both the magnitude and direction of the E-field vector change in time, the figure produced is an ellipse and the antenna will have *elliptical* polarization. Elliptical polarization is also either right-handed or left-handed, as shown in Figure 2.3 (e) and (f).

The polarization of an antenna is important because it affects the strength of the signal that ultimately reaches the receiver. If the polarization of the transmitting antenna does not match the polarization of the receiving antenna, there is a resulting drop in the power that is transferred between the transmitter and the receiver. If the two antennas are oriented in such a way that their E-planes align, then the two antennas are said to be co-polarized. If the E-plane of one antenna is aligned with the H-field of the other antenna (in which case the two E-planes are rotated at 90 degrees to each other) then the two antennas are said to be cross-polarized.

2.4 Antenna / Radiation Pattern

A radiation pattern, also known as an antenna pattern, is a graphical representation of an antenna's far-field radiation properties. For any given antenna the radiation pattern will vary in terms of distance and observation angle in three-dimensional space. Typically, radiation pattern

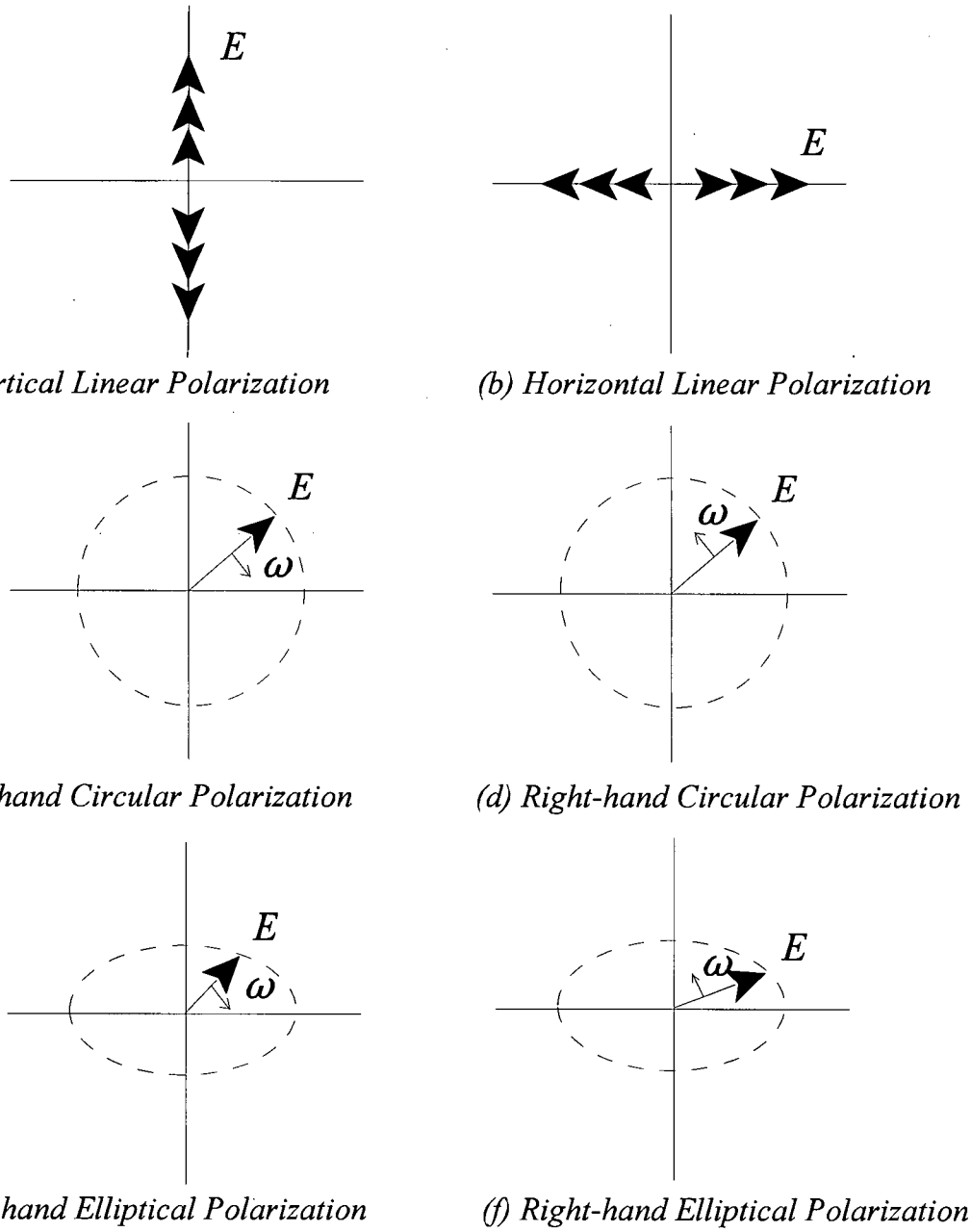

(a) Vertical Linear Polarization

(b) Horizontal Linear Polarization

(c) Left-hand Circular Polarization

(d) Right-hand Circular Polarization

(e) Left-hand Elliptical Polarization

(f) Right-hand Elliptical Polarization

Figure 2.3: Linear, Circular and Elliptical Polarizations

measurements are taken in the two principal planes of the antenna, the E-plane, which is the plane that contains the E-field vector, and the H-Plane, that contains the H-field Vector. These planes are perpendicular to each other and are also perpendicular to the wave front plane for a transverse electromagnetic wave. Since the magnitudes of the E and H-fields in free space are related by

$$E = \sqrt{\mu_0/\varepsilon_0}\,H \approx 120\pi\, H\Omega \qquad (2.6)$$

the resulting radiation patterns can be reported in terms of the E-field or the H-field intensity [11].

If the radiation pattern is plotted in terms of the field strength, such as volts per metre, or the power density in watts per square metre, then the pattern is called an absolute radiation pattern. In most cases, however, antenna patterns are plotted in relative terms. In other words, the field strength is plotted in terms of its ratio to some reference value that is generally the peak value of the field strength. This is called a normalized radiation pattern. For this thesis, E-field intensity measurements have been used, which will be shown as a normalized rectangular logarithmic plot of relative intensity versus angle.

2.5 Phase Measurements

The radiation pattern of an antenna is actually a vector field and is described by both the magnitude and the phase of the radiated field. Typically, only the magnitude of the radiation pattern is measured. However, for this thesis, the phase component of the field is also important. The variation in the far field of the magnitude and phase will provide information about the nature of the wave that is impinging on objects in the field. The knowledge of the shape of the

wave is important, since one often needs to know that the wave front is planar and in what direction the wave is propagating, in order to determine the orientation of the wave front. If the wave front is not planar or if the wave front is not oriented perpendicular to the central axis of the scanner, the result will differ from the case in which those two conditions are met. For example, if the radiation fields produced by either the transmitting or receiving antennas are not planar or the phase centre is off axis, then measurements of the fields will not show symmetry around the central axis of the antennas. As for most antenna designs, it is the far field and not the near field measurements that are commonly given [31].

2.6 Gain Measurement

In addition to the measurements discussed in previous sections, the gain of an antenna is also needed for complete antenna characterization. Gain is an absolute quantity and is much more difficult to measure. The gain of an antenna in a particular direction is the ratio of power radiated per steradian in that direction compared to the power that would be radiated per steradian by a lossless isotropic radiator with the same applied power.

Although it is possible to determine the absolute gain of an antenna from first principles, it is more often determined in relation to an antenna of known gain. This method is known as the *gain transfer* or *gain comparison* method [31]. It would be best to use an ideal lossless isotropic radiator for the comparison, but since this type of antenna does not exist in practice, the comparison antenna is usually a dipole or standard horn antenna whose gain has been calibrated in a previous measurement.

To perform a gain transfer measurement, a transmitter of fixed peak power P_t is connected to the source antenna that is one of a pair of standard gain antennas. The receiving standard gain

antenna is then positioned so that the peaks of the radiation patterns for both antennas are aligned. This will ensure the maximum power transfer P_S between the pair of standard gain antennas, which will give a measurement for the maximum gain G_S between these two antennas.

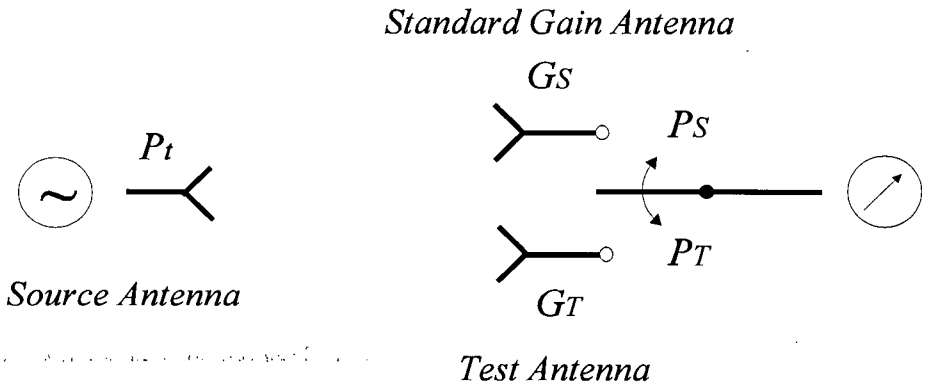

Figure 2.4: Test Arrangement for Gain Transfer Method

Once the power measurement has been taken for the standard gain pair, the receiving antenna is replaced with the test antenna. The power measurement P_T is then repeated for the test antenna. The gain of the test antenna G_T is then calculated from the known gain of the standard gain antenna from the ratio of the received powers.

$$G_T = \frac{P_T}{P_S} G_S \tag{2.7}$$

The relationship is often more conveniently expressed in terms of decibels as

$$G_T(dB) = P_T(dB) - P_S(dB) + G_S(dB) \tag{2.8}$$

2.7 Frequency Dependence

A typical antenna radiates at a number of different frequencies, and the frequency-wave number representation for an electromagnetic wave is given as

$$\vec{E} = E_0 \vec{p} \exp(j\omega t - j\vec{\beta} \cdot \vec{r}) \tag{2.9}$$

where E_0 is the amplitude of the electromagnetic wave, $\vec{p}$ is the polarization vector, ω is the angular frequency, $\vec{\beta}$ is the wave vector, and $\vec{r}$ is the position vector. Note that the wave vector can have both a real and negative imaginary part.

All antenna parameters are frequency dependent and values such as the gain of the antenna under test should be written as $G_T(\omega)$ rather than just G_T [33]. For many applications, the frequency dependence can be ignored since the range of frequencies being used is narrow and the frequency dependencies are small. However, for an application in which a wide range of frequencies is being used, frequency dependencies may vary greatly over the band and can introduce non-linear effects. For example, if an antenna's gain varies greatly over the range of interest, frequencies that have a high gain may overwhelm equipment and prevent the detection of signals where there is lower gain.

Chapter 3

3.0 Wideband Antennas

One of the requirements for designing an ultra-wideband system, such as the one that is proposed for this project, is for a suitable pair of antennas that can be used to transmit and receive the ultra-wideband signals. Most conventional antennas radiate efficiently at a single frequency or over a very small frequency range. There are, however, a number of antenna designs that will radiate over a wider range of frequencies, and these types of antennas are known as broadband, wideband and ultra-wideband antennas, depending on the range of frequencies they cover. Whereas there is no single definition for the terms broad or wideband, a broadband antenna will typically cover a frequency range of a few hundred megahertz (MHz). Wideband and ultra wideband antennas, on the other hand, may cover a frequency range of a few gigahertz (GHz) to 10 GHz or more [34-38].

3.1 Existing Ultra-Wideband Antenna

There are a number of different kinds of wideband antennas, each with its advantages and disadvantages [39]. The history of wideband antennas goes back many years. In 1898 Oliver Lodge patented a number of antenna designs, precursors to some of the modern day ultra-wideband antennas [40]. The patent showed early versions of bow-tie and biconical antennas, which were later shown to have significant wideband properties. Further types of wideband antennas were designed in the 1930s and 1940s. These included further biconical antenna designs as well as spherical dipole and coaxial, conical and rectangular horn antennas [40].

Since the 1960s other classes of wideband antennas have been introduced. These include wideband notch antennas [41], ellipsoid mono and dipole antennas [40], large current radiator antennas [42], magnetic UWB antennas [43], spiral and helical antennas [44-48], bow-tie antennas [49-53] , microstrip antennas [54-58] and tapered slot and Vivaldi type antennas [59, 60]. In addition, there are specialty antennas, which do not fall into the classes of antennas previously mentioned, such as printed and stepped fat-dipole [61, 62], fractal [63], dielectric wedge [64, 65], disk and half disk [66] and quasi-horn microstrip antennas [67] all of which have also been previously investigated.

The wideband properties of all of the above antennas depend on two key antenna characteristics: 1) their shape and 2) the type of dielectric material present (if any) in their design. The bandwidth of the antenna is affected by the impedance match between the feeding circuit and free space. This in turn is affected by the currents flowing in the antenna. Currents flowing in the antenna are changed by modifying the shape and dielectric properties of the antenna. These modifications will cause the antennas to radiate with varying degrees of efficiency by one of two main mechanisms: 1) a travelling wave mechanism or 2) a resonance mechanism [68].

The bandwidths of these antennas vary greatly within each class of antenna as well as between the different classes and types of antennas, and each have bandwidths from hundreds of MHz to tens of GHz depending on their designs. The one feature that they all share, however, is a greatly varying impedance match over their bandwidth.

3.2 Broadband Microstrip Patch Antennas

Since the early 1970s, a particular class of antennas, know as microstrip patch antennas, has been the subject of a large and on-going series of investigations [69]. Although not all of these types of antenna are broadband, it is instructive to look at this class of antenna in its

simplest form, as it demonstrates the effects that dielectric materials can have on antenna performance. Figure 3.1 shows the construction of a typical microstrip patch antenna.

For antennas of this design, the bandwidth is proportional to the thickness h of the substrate and inversely proportional to ε_r, the dielectric constant of the substrate material [68],

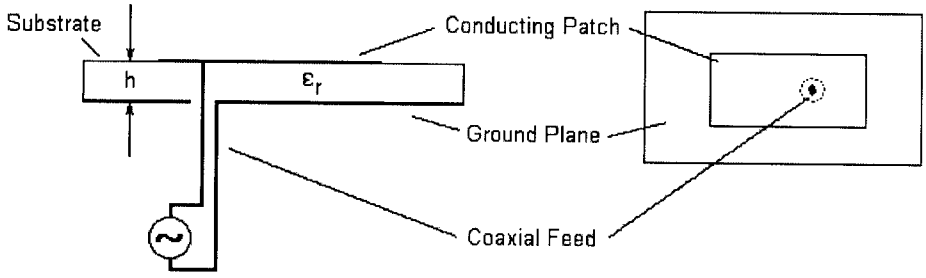

Figure 3.1: Microstrip Patch Antenna Construction

$$BW \propto \left[\left(\frac{16}{3}\right)\left(\frac{h}{\varepsilon_r}\right)\left(\frac{pc_1}{\lambda_0}\right)\left(\frac{W_e}{L_e}\right)\left(\frac{1}{e_r^{hed}}\right)\right] \qquad (3.1)$$

where

p is a power ratio dependent on the ratio of patch size to wavelength λ_0

c_1 is a constant dependent on the index of refraction of the material

λ_0 is the wavelength of the centre frequency

W_e is the effective width of the conducting patch

L_e is the effective length of the conducting patch

e_r^{hed} is the radiation efficiency of a horizontal electric dipole on a lossless substrate.

This means that, as the dielectric constant of the antenna's substrate increases, the bandwidth of the antenna decreases. Although these antennas offer the advantages of a low profile - compatibility with integrated circuit technology and the ability to conform to a shaped surface, which have led to their use in numerous applications such as aircraft, satellite, GPS, mobile communications and remote sensing - the principle disadvantage of these antennas is the limited bandwidth caused by the limited choice of dielectric materials from which a particular design can be fabricated.

3.2.1 Air Core Microstrip Antenna

As demonstrated in equation 3.1, one of the fundamental properties of a microstrip antenna is the bandwidth dependance upon the dielectric material [69]. It is not possible to obtain materials that possess a dielectric constant outside a narrow range [68]. Typical dielectrics have a dielectric constant value between 2.1 and 5, with some special materials as high as 10 or more, none of which would provide designs for antennas that would be useful for this application . To produce antennas with a wider bandwidth, specialized materials such as microcell foams and air gels have been produced with lower dielectric constants. There are, however, rigidity problems with using these materials. The microcell foams and air gels can be used only in limited thickness ranges and do not stand up well to bonding and manufacturing processes.

To further examine the effects of the dielectric constant on bandwidth, as part of the preliminary investigation for this thesis, a series of microstrip patch antennas with air between the conducting patch and the ground plane, rather than a dielectric material, were designed and constructed. These antennas did indeed show an improved bandwidth over those constructed from printed circuit board material. The standard patch antennas manufactured out of printed circuit board material with ε_r of between 2.2 and 3.2 typically have a bandwidth of around 4MHz [70]. The air core patch antennas that were designed demonstrated a bandwidth of approximately

107 MHz, as shown in Figure 3.2, which indicates a failure of equation 3.1 to predict bandwidth behaviour for patches with air rather than a dielectric substrate between the planes.

Although removing the dielectric material did provide a significant improvement for the bandwidth of the patch style antenna, the overall bandwidth for this type of antenna was still only about 100MHz.

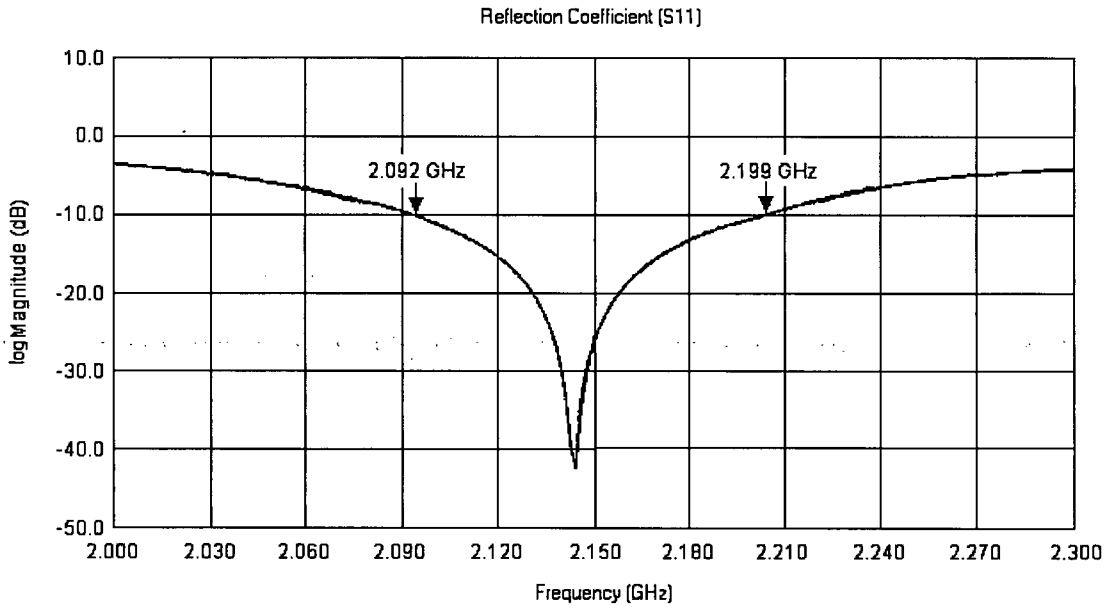

Figure 3.2: S_{11} Reflection Coefficient Showing 10dB Bandwidth for Air Core Patch Antenna

3.3 Tapered Slot Antennas

The second class of antennas that are useful to examine for this project are the tapered slot antennas (TSA), also known as notch antennas, that belong to a class known as endfire travelling wave antennas. Like patch antennas, they are manufactured on printed circuit board material, but unlike patch antennas, which radiate perpendicular to the conducting surface, they radiate from the edge of the conducting surface [68]. This class of antennas displays one of the widest

bandwidths of any type of antenna and exhibits an S_{11} curve that is typical of most ultra-wideband antennas - a large bandwidth with many significant dips in the impedance match.

Figure 3.3 shows a number of typical tapered slot antennas and feed arrangements. Those with straight edges on the flare are referred to as linear slot antennas. Those with exponentially curved edges on the flare are referred to as Vivaldi-style antennas due to the V-horn shape of the slot taper. Despite its superior performance, in the past, the TSA antenna was not able to generate broad interest in the research community. This has been due to the fact that the fundamental operation of tapered slot antennas is still not fully understood. As a result, these antennas have been based primarily on empirical designs [68, 71]. They do, however, demonstrate one of the largest bandwidths available and are currently being more vigorously investigated due to the availability of electromagnetic analysis software.

The original tapered slot antennas were manufactured on a single-sided printed circuit board with the antenna comprised of a single endfire microstrip. The flare in the microstrip channel was designed to provide an impedance match between the feed and free space. Although this did provide an improved impedance match, the bandwidth was still quite small, only a few GHz [68].

To improve the impedance match over a wider range of frequency, the antipodal tapered slot antenna shown in Figure 3.4 was introduced. This consisted of a double-sided circuit board with an active member (light grey) on the top side of the dielectric substrate (white) and a ground plane (dark grey) on the bottom side. This design did improve the impedance match somewhat and provided a larger bandwidth of 10 to 20 GHz, albeit showing the same significant dips in the impedance match. The main problem with this new design, however, was that the antenna showed high levels of cross polarization in the upper frequency ranges [72].

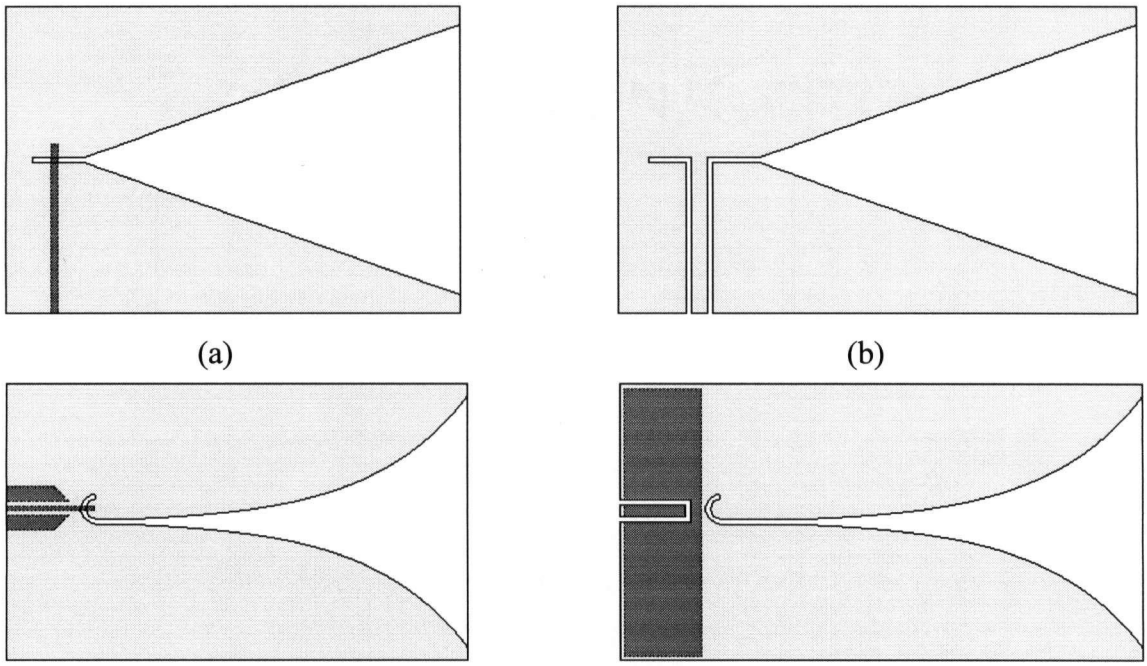

Figure 3.3: Examples of Tapered Slot Microstrip Antennas: (a) Linear Taper Microstrip Line Fed (b) Linear Taper Coplanar Waveguide Fed (c) Exponential Taper Ground Plane Coplanar Waveguide (d) Exponential Finite Ground Plane Coplanar Waveguide

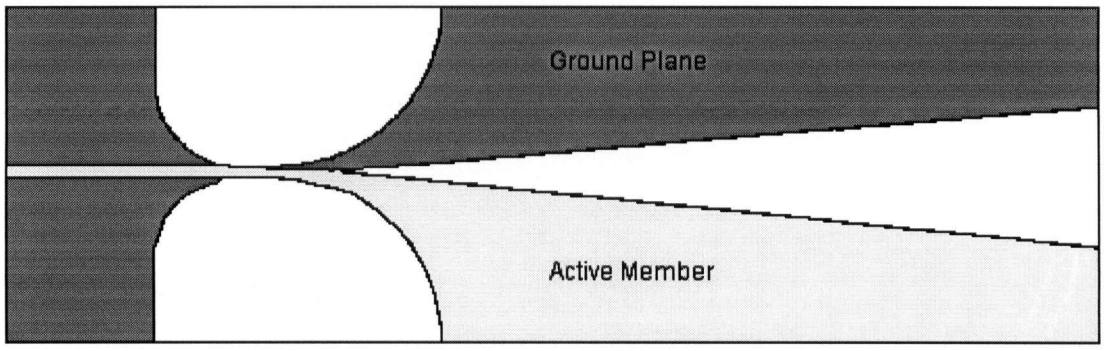

Figure 3.4: Antipodal Linear Tapered Slot Antenna Configuration

A new type of antipodal TSA was developed by E. Guillanton et. al. [72, 73] in order to address some of the problems with the basic antipodal antenna. This new antenna attempted to overcome the polarization problems by creating a "balanced" three-layered structure with an additional ground plane on the opposite side of the active member. Figure 3.5 shows the substrate

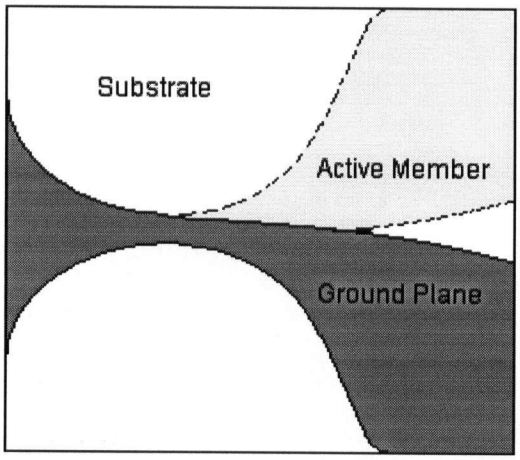

Figure 3.5: Side View of Guillanton Balanced Antipodal Vivaldi Antenna

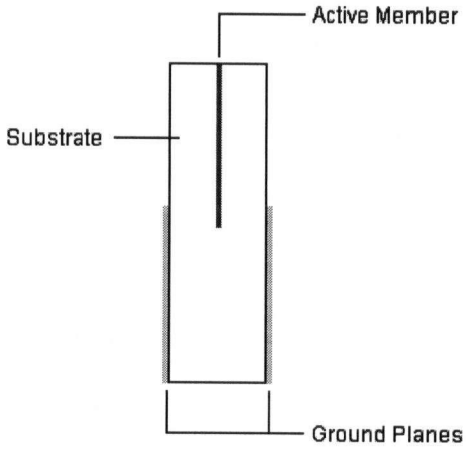

Figure 3.6: End View of Guillanton Balanced Antipodal Vivaldi Antenna

material (white) with metalization on the top for one of the two ground planes (dark grey) and the metalization for the active radiating member (light grey) sandwiched in the middle of the substrate. The second ground plane is located directly behind the visible dark grey ground plane shown in the diagram.

Figure 3.6 shows the second ground plane metalization, which is identical to the first, located on the other outer layer.

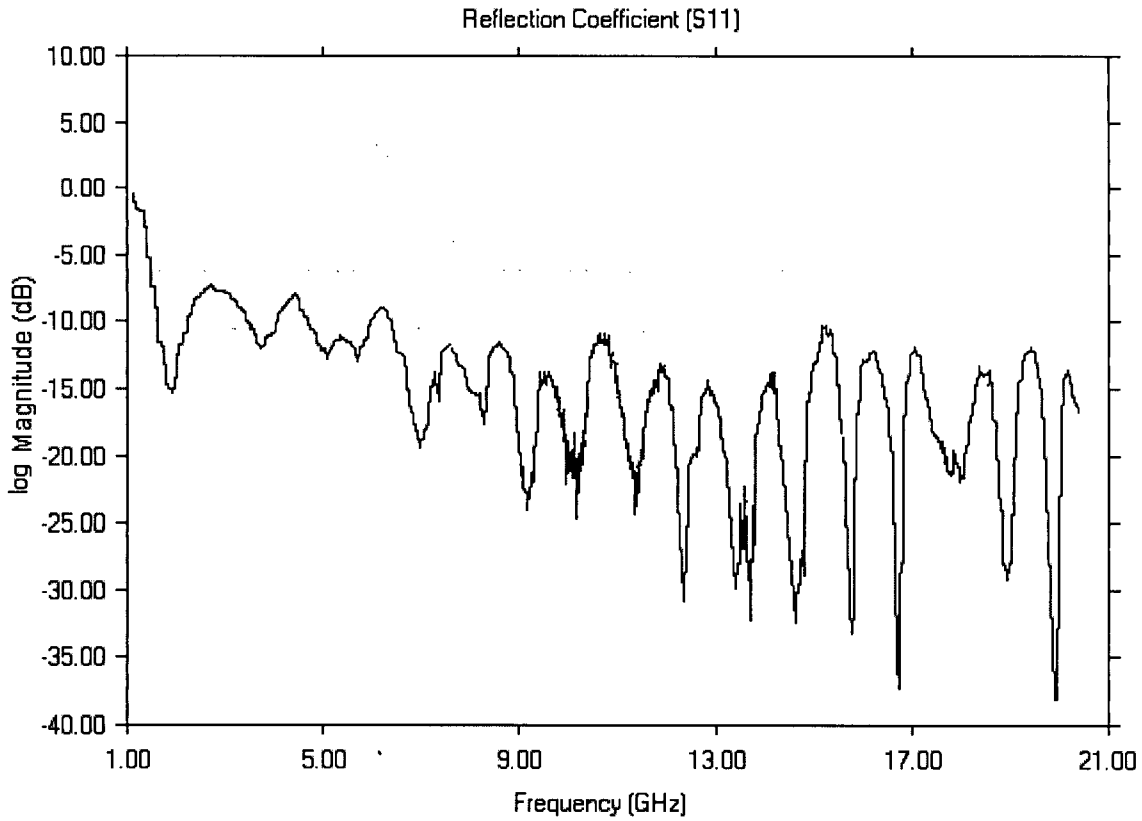

Figure 3.7: S_{11} Reflection Coefficient for Guillanton Balanced Antipodal TSA

The new design did help solve the polarization problem. Although the Guillanton Vivaldi antenna does have a large bandwidth, as can be seen from Figure 3.7 , the S_{11} curve does not

remain below the -10 dB point until after 6 GHz and does not radiate efficiently from 1 to 6 GHz [73]. In addition, the S_{11} curve still varies greatly over the bandwidth, with many peaks and valleys. As discussed before, this is not the optimal design for an ultra-wide bandwidth antenna.

Chapter 4

4.0 Fleur-de-Lis Antenna

As stated earlier, one of the main characteristics that needs to be considered for any ultra-wideband antenna used for this project is the S_{11} *vs.* frequency behaviour of the antenna [28]. Any short time duration signal, such as a pulse generated by the measurement equipment, will contain a number of frequency components with a specific amplitude and phase relationship. If the antenna's input impedance varied with frequency then the signal applied to the antenna would be modified, causing signal distortion [27].

Since the antennas used in this project acted like a bandpass filter [29], as for any other bandpass filter, the ideal antenna "filter" response should have a flat amplitude and phase response across the bandwidth, as shown in equations 4.1 and 4.2.

$$C(j\omega) = R(j\omega)\, G(j\omega) \tag{4.1}$$

$C(j\omega)$	response of the system after transmitted signal has been received
$R(j\omega)$	signal applied to system
$G(j\omega)$	transfer function of pair of receiving and transmitting antennas

For a matched pair of antennas the ideal transfer function would be

$$|G(j\omega)| = \begin{cases} 1 & \omega_0 - \omega_c < \omega < \omega_0 + \omega_c \\ 0 & elsewhere \end{cases} \tag{4.2}$$

where ω_c is the desired ½ bandwidth.

Chapter 4 - Fleur-de-Lis Antenna

For our application, the antennas used were required to provide a flat S_{11} response (or small variation) over a bandwidth of 13.5 GHz (the available bandwidth of the network analyser that was used for this project) or greater in order to minimize errors introduced by the antenna's frequency dependence.

Although some of the existing UWB antennas described earlier have shown an improved impedance match over their bandwidth, their reflection coefficients still show large variations in magnitude. To improve on this, a new antenna design is required.

As the Vivaldi class of antennas have the largest available bandwidth, the Vivaldi type of antenna was chosen as the basis for the development of a new antenna for this thesis. To provide a standard for comparison, the Vivaldi antenna created and characterized by Guillanton [74] was chosen as the starting point for the new design. It is hoped that, by modifying the Guillanton antenna, a smoother S_{11} return loss can be designed into the new antenna.

The first difference between the new antenna design and the existing Vivaldi antenna design was that, unlike the Vivaldi antenna, the new antenna has no dielectric material between the active and ground plane members. As for the microstrip patch antenna, the dielectric material between the active members and the ground planes has a large effect on the antenna's bandwidth [72]. The bandwidth of the new antenna should increase by removing the dielectric material from between these members and relacing it with air, as it did for the microstrip patch antenna.

The second design difference between the new antenna and the Guillanton antenna is the position and shape of the antenna's ground planes relative to the active member. There have been a number of studies on the effects of changing the shape of the active member and the ground planes on the S_{11} Return-Loss response [72-74], but none of these studies has attempted to change

the distance between the ground plane and the active member other than to change the thickness of the substrate. Since the Vivaldi antenna's active member and ground planes are bound to the dielectric substrate, typically a Printed Circuit Board (PCB), they must be maintained at a fixed distance apart over the entire length of the antenna. Because the new antenna is no longer manufactured on a dielectric substrate, the spacing between the ground plane and the active members no longer requires to be fixed.

When both of these design considerations were implemented, the general shape of the new antenna was similar to the design shown in Figure 4.1

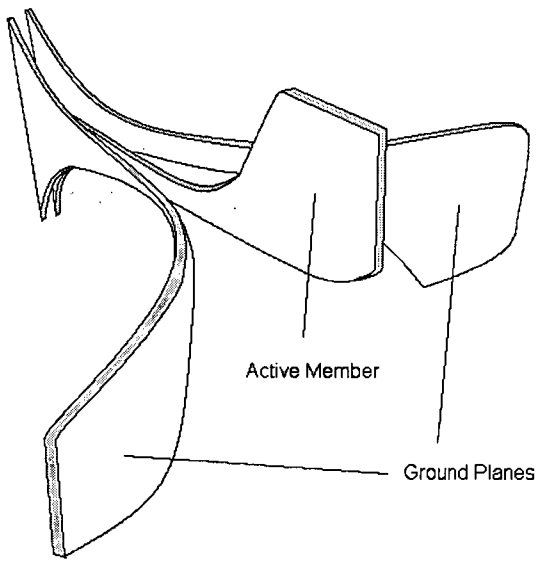

Figure 4.1: Fleur-de-Lis Antenna

The name Fleur-de-Lis (FDL) was chosen for the new antenna design due to the antenna's resemblance to the French fleur-de-lis when the antenna is viewed from above.

Chapter 4 - Fleur-de-Lis Antenna

4.1 FDL Antenna Design

All of the antennas designed for this thesis were manufactured from 20-oz. (~0.675 mm thickness) copper sheet. Although other metals should work equally well, the 20-oz. copper sheet was chosen because of its ease in machining and bending. To feed the antenna, the active member of the antenna was soldered directly to the coaxial pin of an SMA connector. The two ground planes were connected by bolts to the mounting bracket of the SMA connector, which was in turn connected to signal ground. Photos of the antenna are shown in Appendix H.

Figures 4.2 through 4.4 show the design parameters for the FDL antennas used in this thesis.

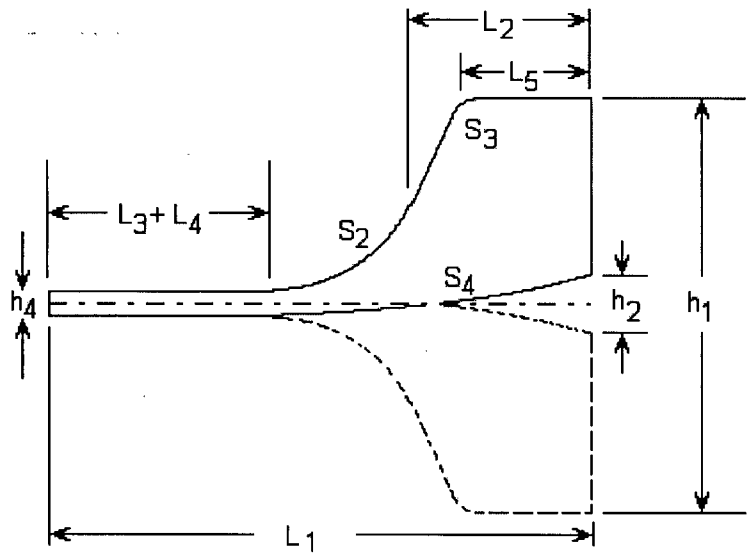

Figure 4.2: Design Parameters for FDL Active Member: L_1 - overall length, L_2 - distance from end of antenna to start of segment S_2, L_3+L_4 - distance from segment S_2 to connector end of antenna, L_5 - width of lobe of antenna, h_1 - height of antenna at flare end, h_2 - separation at end between ground and active member, h_4 - height of connector end of active member.

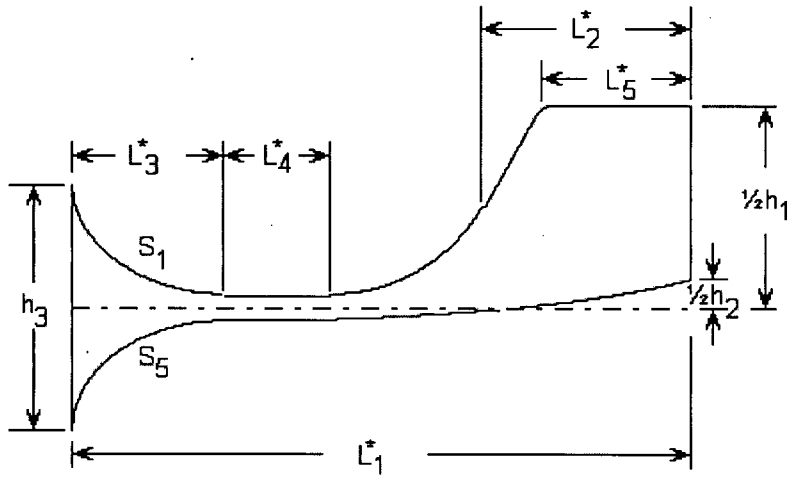

Figure 4.3: Design Parameters for FDL Ground Planes: L^*_1 through L^*_5 scaled lengths to allow for alignment of curved ground planes, h_3 - height of tail flare of ground planes.

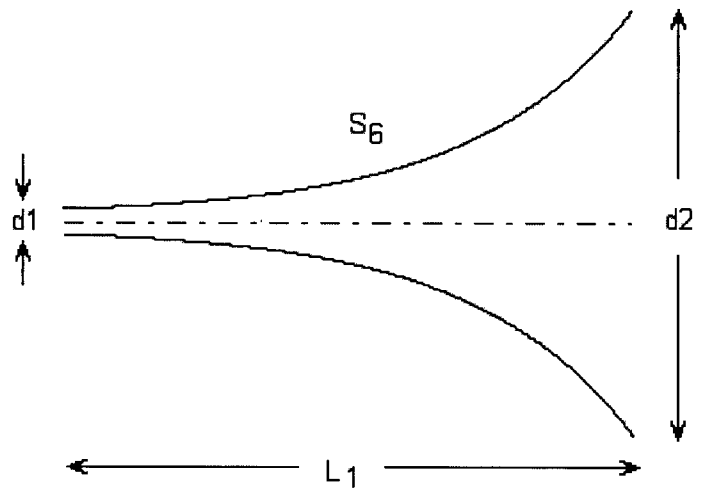

Figure 4.4: Design Parameters for FDL Ground Plane Flare: d_1 - separation of ground planes at connector end of antenna, d_2 - separation of ground planes at flared end of antenna.

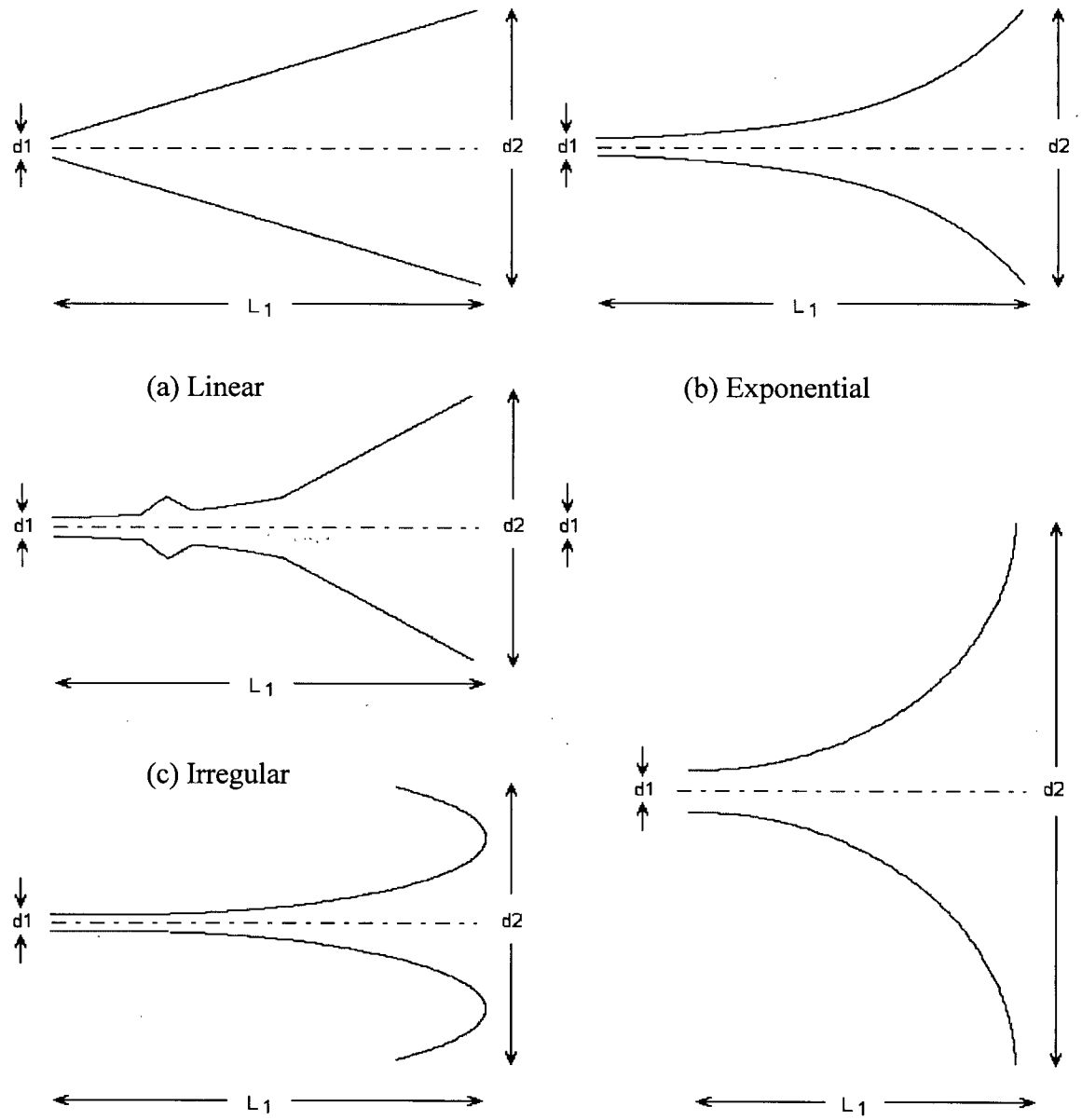

Figure 4.5: Possible Ground Plane Curvatures for the FDL Antenna Segment S_6.

Chapter 4 - Fleur-de-Lis Antenna

A number of individual line segments, each with its own geometry, controls the overall shape and size of the antenna by specifying its outline. The curved segments S_1 and S_5 are elliptical and symmetrical, segments S_2 and S_3 are circular and segment S_4 is exponential in profile. These segments and profiles were chosen as they best matched the original Guillanton design as well the segmentation used in other studies [72].

As can be seen from Figure 4.1 the ground planes of the antenna are curved while the central active member of the antenna is flat. Due to this curvature, the ground planes of the antenna must be manufactured longer in length than the active member. The ground planes are scaled in length by proportionally scaling each of the linear segments marked L_1* through L_5*. If this scaling is not performed, then the ends of the ground planes would not align with the ends of the active member, which would lead to a change in the direction of the field vectors at the radiating end of the antenna.

The curved segment S_6 shown in Figure 4.4, which lies in the antenna's H-Plane, can take on a variety of profiles. As shown in Figure 4.5(a) through 4.5(e), the S_6 segment can be linear (flat), exponential, irregular, elliptical or circular. It will be shown later in the analysis portion of this paper that the shape and extent of the S_6 curvature has a major impact on the performance of the FDL antenna.

4.2 FDL Antenna Characterization

Since the FDL-style antenna was of a type never before investigated, much of the antenna work in this thesis involved characterizing the basic properties of the antenna. These properties were then compared to those of a Vivaldi antenna of similar dimensions to give a measure of the improvement of the FDL antenna over the Vivaldi antenna, particularly for the S_{11} parameter.

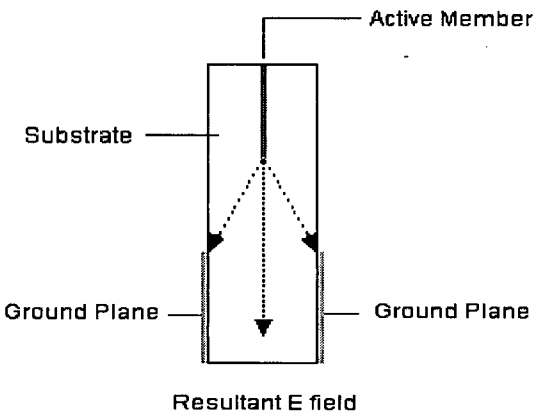

(a)

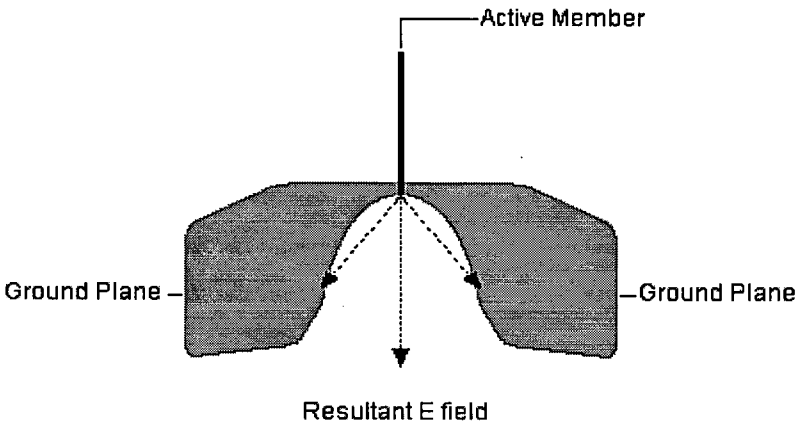

(b)

Figure 4.6: (a) Cancellation of the Horizontal Component of the E-field for Balanced Vivaldi Antenna. Looking end on to printed circuit board (b) Cancellation of the Horizontal Component of the E-field for FDL Antenna looking end on at flared ground planes (in the plane of the active member)

In addition, the behaviour of the FDL-style antenna was investigated to determine the effect that changes in parameters such as the separation angle between the ground plane and active members would have on the antenna's performance. This chapter will show the results of these investigations.

4.2.1 S_{11} Return Loss

As described earlier, one of the most important measures of antenna performance is the S_{11} return loss. Figures 3.5 and 3.6 show the design of a balanced antipodal-type Vivaldi antenna [73, 75] upon which the antennas developed for this thesis were based. For the initial FDL designs, the overall length L_1 and the heights of the ground plane and active members h_1, h_2 and h_3 were taken from the existing antenna developed by Guillanton [73]. This was done intentionally to enable a direct comparison between the FDL antenna and the Guillanton Vivaldi antenna.

The E-field for the Vivaldi antenna is between the active member and ground planes as shown in Figure 4.6 (a). The horizontal components for the E-field cancel each other out leaving only the vertical component of the E-field. The resultant E-field for the FDL antenna will also be determined by the configuration shown in Figure 4.6 (b). In both cases the horizontal components of the E-field from the active member to the individual ground planes cancel each other out, leaving the E-field in the vertical direction. This cancellation of the horizontal components of the E-field is what accounts for the improved cross polarization characteristics of the balanced antipodal antennas versus the non-balanced antennas [75]. Since the FDL antenna also shares the balanced horizontal E-fields one would expect that the cross polarization performance of the FDL antenna, for a moderate flare (small S_6 curvature), should be similar to that of the Guillanton Vivaldi antenna.

4.2.1.1 S_{11} Reflection Coefficient Results

For most of the experiments performed in this thesis, a Wiltron 37225A Vector Network Analyser, with a bandwidth limited to a range of 1 GHz to 13.5 GHz, was used to obtain the S_{11}, S_{21} , cross and co-polarization and gain information. As a result, most of the information presented in this paper is limited to this bandwidth. However, to make a more accurate comparison with the existing Guillanton Vivaldi antenna [73] an Agilent 8510C Vector network analyser, which was not available for most of the void detection measurements, was also used to provide an S_{11} curve over a wider bandwidth range of 1 GHz to 21 GHz.

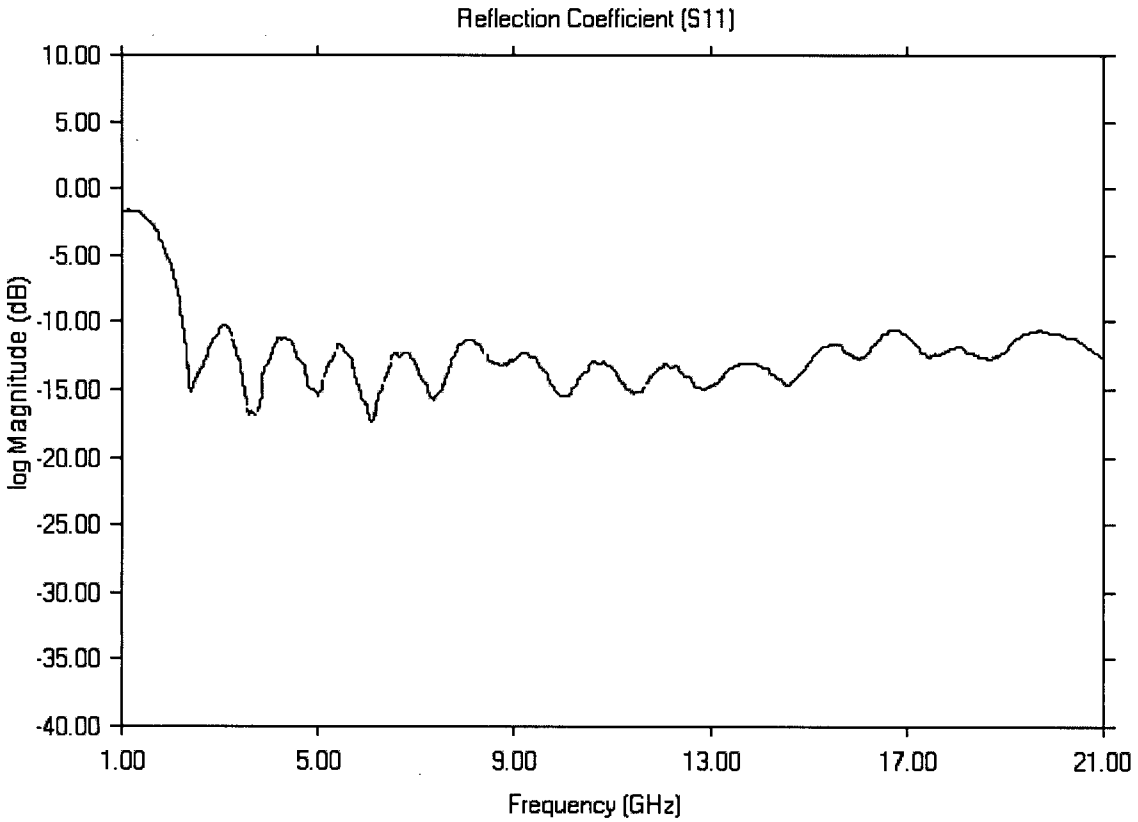

Figure 4.7: FDL S_{11} Reflection Coefficient from Agilent 8510C Network Analyser

Figure 4.7 shows the S_{11} curve for the FDL antenna configuration that produced the smallest deviation across the largest bandwidth. When this is compared with the S_{11} curve shown for the Vivaldi-type antenna in Figure 3.7, it can be seen that the FDL antenna clearly has a flatter profile with no sharp spikes in the S_{11} curve. The FDL antenna also shows an S_{11} below -10 dB across the bandwidth from 2.1GHz to beyond the limits of the Analyser at 21 GHz, which is larger than the bandwidth of approximately 6 GHz to 21 GHz, where the curve remains below the -10 dB line. Both the FDL and Vivaldi antennas show poor impedance matching characteristics below the 2 GHz limit.

4.2.1.2 Change in S_{11} with Angle of Flare

The design of the best FDL antenna used for this project was produced by experimentation. One of the parameters that determines the behaviour of the antenna is the angle between the ground planes and the active member of the FDL antenna called the Flare angle (shown in Figure 4.8).

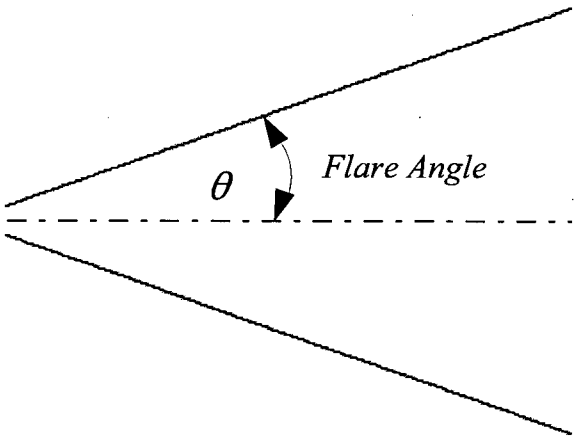

Figure 4.8: FDL Flare Angle

Chapter 4 - Fleur-de-Lis Antenna

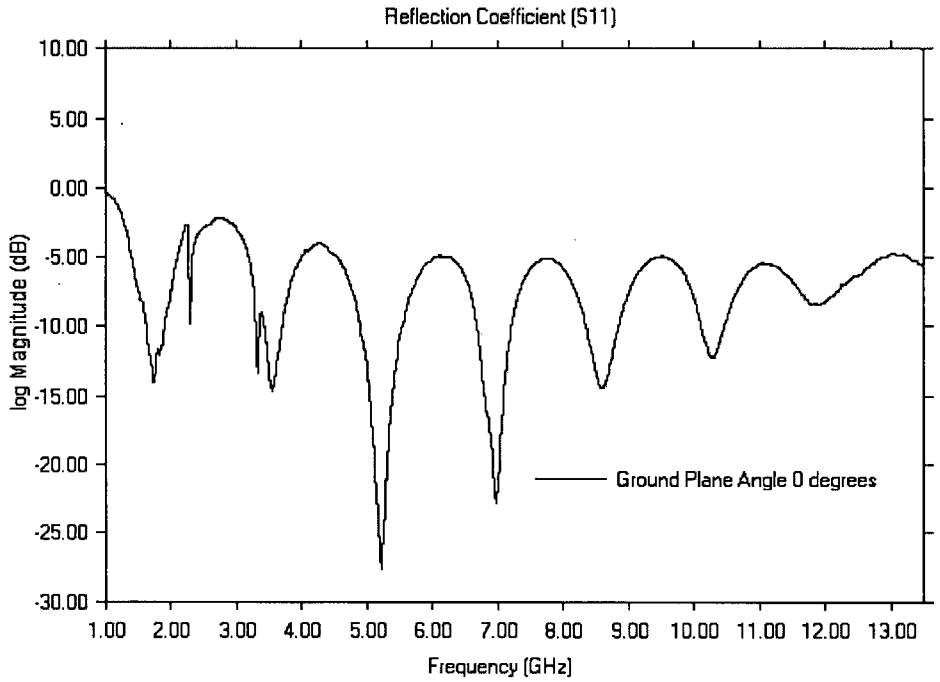

Figure 4.9: S_{11} Reflection Coefficient for FDL Antenna with Flare Angle of 0 degrees

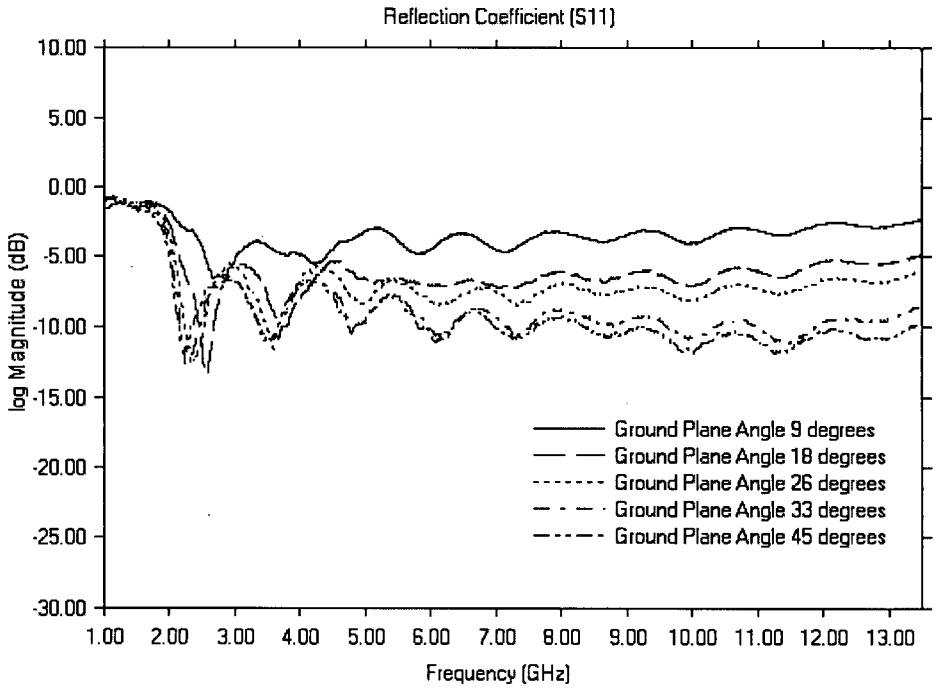

Figure 4.10: S_{11} Reflection Coefficient for FDL Antenna for Flare Angles of 9 to 45 degrees

Chapter 4 - Fleur-de-Lis Antenna

Figure 4.9 shows the S_{11} curve for an FDL antenna with a flare angle of zero degrees. This is, in effect, a Vivaldi-style antenna with no dielectric material between the ground planes and the active member. Although the S_{11} curve for the FDL antenna with a zero flare angle looks similar to that for the Guillanton Vivaldi, the FDL antenna only radiates efficiently at the resonant peaks and not across the bandwidth like the Guillanton Vivaldi.

Figure 4.10 shows the S_{11} returns loss of the FDL antenna as the flare angle is changed between 9 degrees and 45 degrees (the individual spectral curves are shown in Appendix A). The deep resonances in the spectral curve disappear between 0 degrees and 9 degrees. Between 9 degrees and 45 degrees, the shape of the S_{11} curve remains relatively constant but the average value of the S_{11} reflection coefficient over the bandwidth decreases as the flare angle increases. This decrease in the S_{11} reflection coefficient means an increase in the impedance match for the antenna as the flare angle is increased, resulting in an increase in the radiated power.

Figure 4.11 shows the S_{11} curve as the angle is increased from 45 degrees to 53 degrees. Between 45 degrees and 49 degrees the S_{11} curve remains relatively constant. The curves for the angles 45 and 49 degrees overlap in the figure shown. Between 49 and 53 degrees the average value of the S_{11} reflection coefficient starts to increase, showing a decrease in antenna performance. This decrease in performance continues as the ground planes are angled further and further away.

The graphs in Figures 4.10 and 4.11 for S_{11} versus flare angle show that for an FDL antenna with flat (no S_6 curvature) ground planes, the performance of the antenna can clearly be shown to be dependent on the angle of the ground planes with respect to the active member, something that cannot be changed for a Vivaldi-style antenna due to its construction

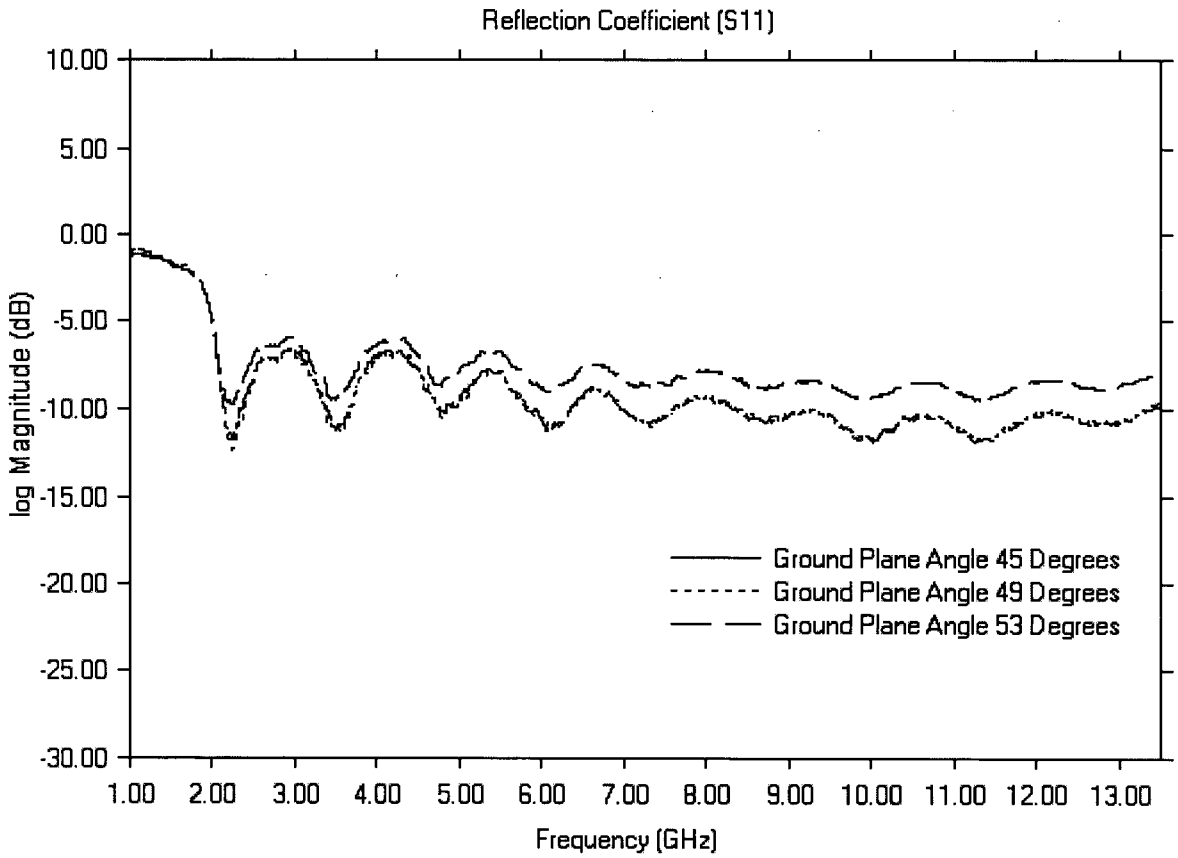

Figure 4.11: S_{11} Reflection Coefficient for FDL Antenna for Flare Angles of 45 to 53 degrees

on substrates of fixed thicknesses. The graphs also show that there is an optimal angle for which the FDL has its best S_{11} performance, and that angle is approximately 45 to 49 degrees. The fact that the S_{11} performance changes with flare angle is due to the change in configuration. As shown in the previous studies mentioned earlier, the shape of the horn of the Vivaldi antenna affects the impedance match much in the same way as the shape of a horn antenna affects its impedance match. The impedance match of the FDL antenna is improved by creating a "horn-like" structure by producing a flare in the 3rd dimension,.

4.2.1.3 Change in S_{11} with Curvature of Flare

Although the performance of an FDL antenna improves as a function of flare angle, simply changing the angle between the ground planes and the active member does not produce the optimal design for an FDL antenna. The performance of the FDL antenna can also be improved by changing the shape of the ground planes. The S_{11} response for the FDL antenna can be improved by bending the ground planes to give them a curved profile (S_6) as shown in Figure 4.4.

Figures 4.13 through 4.17 show the effects of changing the flare curvature from 3 to 13 cm for an exponential S_6 profile. Figure 4.18 shows all five flare curvatures on a single graph to make a comparison of the S_{11} curve versus flare curvature easier.

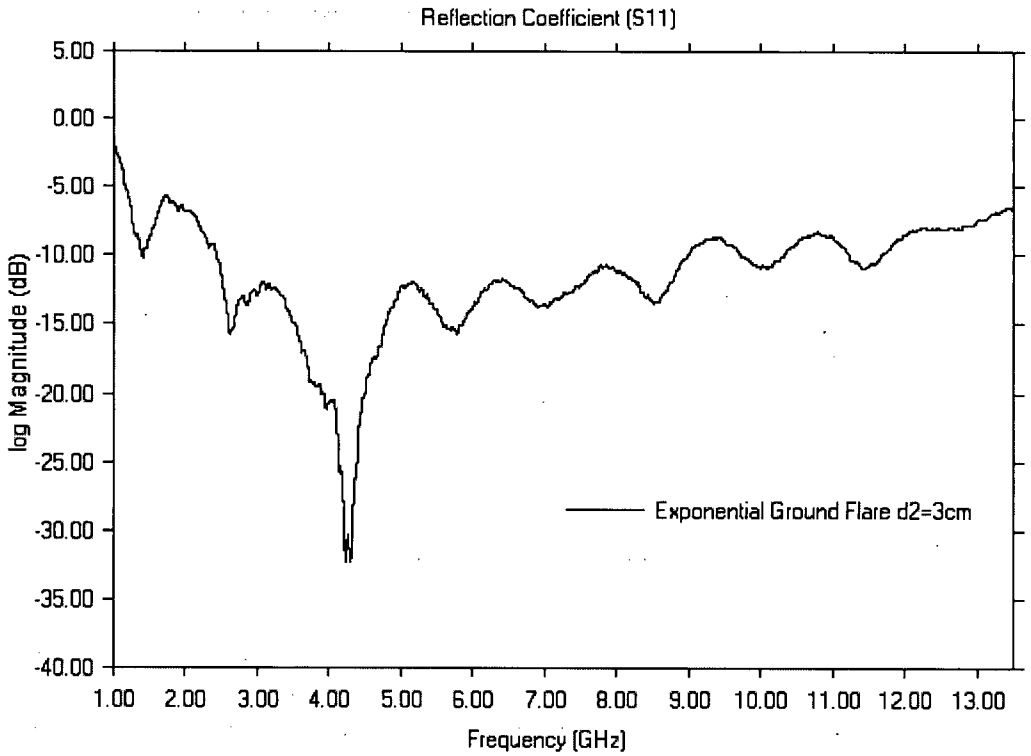

Figure 4.13: S_{11} Reflection Coefficient for FDL Antenna with Exponential Curve d_2=3cm

Chapter 4 - Fleur-de-Lis Antenna

Figure 4.13 shows the S_{11} curve for an exponential curve where the separation of the ends of the ground planes , dimension d_2 from Figure 4.4, was set at 3cm. It can be seen that, while there is a change from the S_{11} curve for the Vivaldi antenna, the curve still shows at least one deep resonance similar to those found in the Guillanton Vivaldi S_{11} curve shown in Figure 3.7.

For a flare with d_2 equal to 6 cm, shown in Figure 4.14, the resonances are gone, but the S_{11} curve is above the 10 dB point for most of the bandwidth. Although the S_{11} profile now appears to be more regular, approaching the idealized flat filter profile, in fact, the antenna is not radiating efficiently at this point. This appears to be the transition point between Vivaldi type behaviour and FDL behaviour.

As the flare curvature increases the performance of the antenna improves. Figure 4.15 to Figure 4.17 show the S_{11} curve for flare curvatures of 9 cm, 12 cm and 13 cm respectively. As the flare curvature increases, the S_{11} curve returns to below the -10 dB level. All three flare curvatures between 9 cm and 13 cm show improved S_{11} curves. Although the average value of the S_{11} reflection coefficient is lower for the flare curvature of 9cm, the S_{11} reflection coefficient curves for the 12cm and 13cm flares show a smoother profile. Again, as for change in the flare angle, changing the curve of the ground planes produces a better impedance match by providing a smoother electrical transition between the metal of the antenna and free space. For this thesis the optimal flare for the FDL antenna is between 9 cm to 13 cm for dimension d_2.

4.3 Cross and Co-Polarization

As stated earlier, due to the similar configuration of the E-fields between the FDL and the Guillanton Vivaldi, it was hoped that the FDL antenna would show a similarly good cross-polarization performance. There appeared to be one area, however, where the FDL antenna

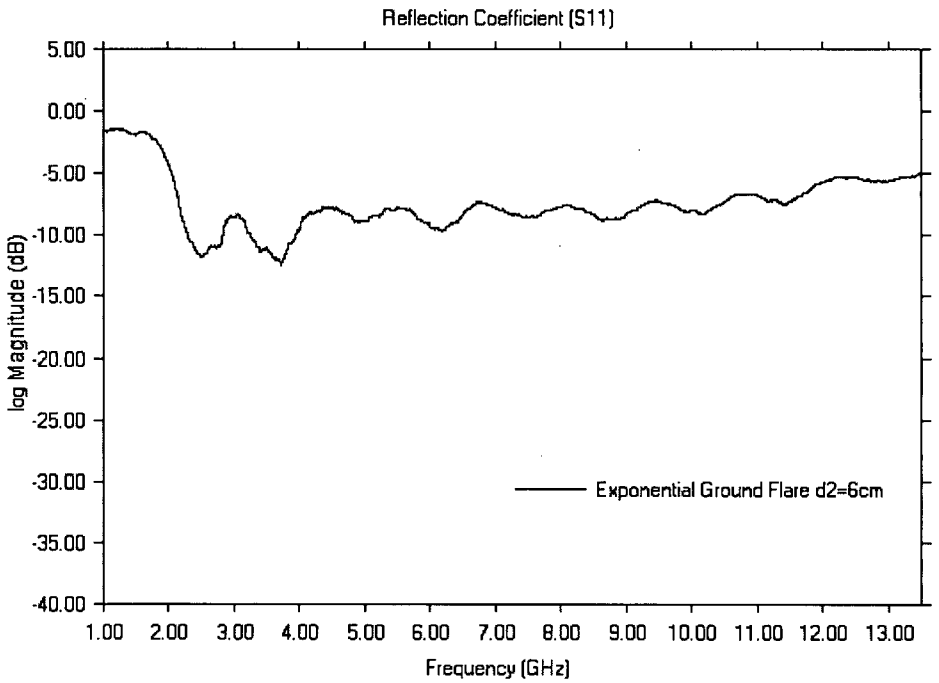

Figure 4.14: S_{11} Reflection Coefficient for FDL Antenna with Exponential Curve d_2=6cm

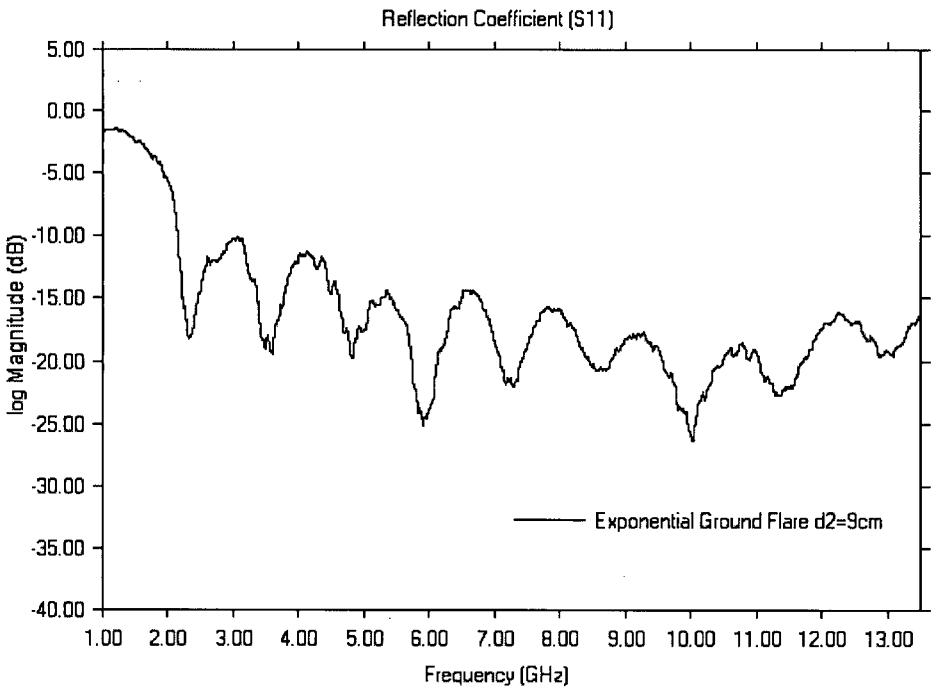

Figure 4.15: S_{11} Reflection Coefficient for FDL Antenna with Exponential Curve d_2=9cm

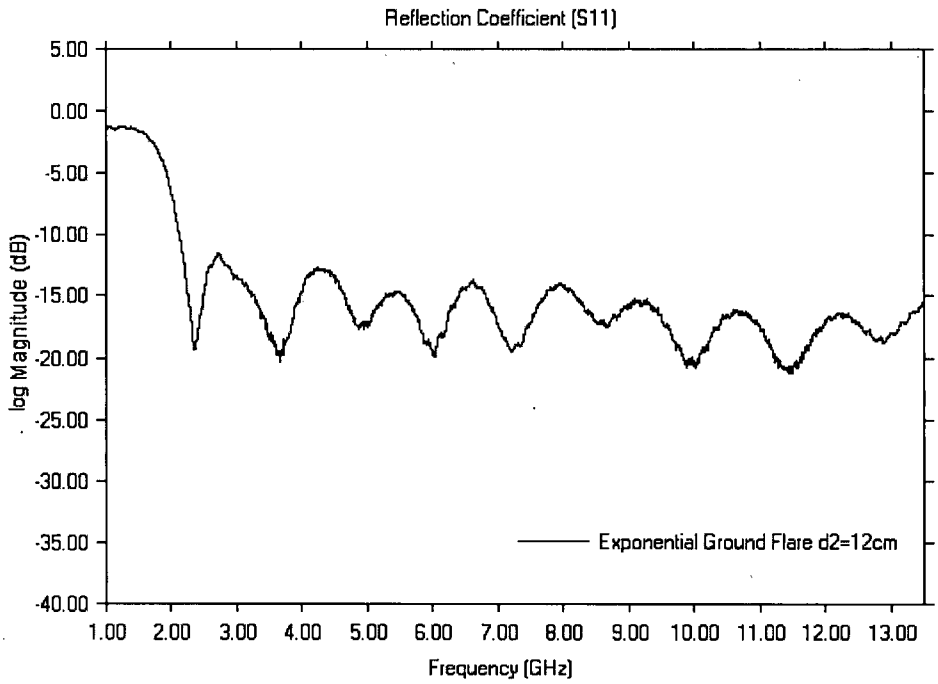

Figure 4.16: S_{11} Reflection Coefficient for FDL Antenna with Exponential Curve d_2=12cm

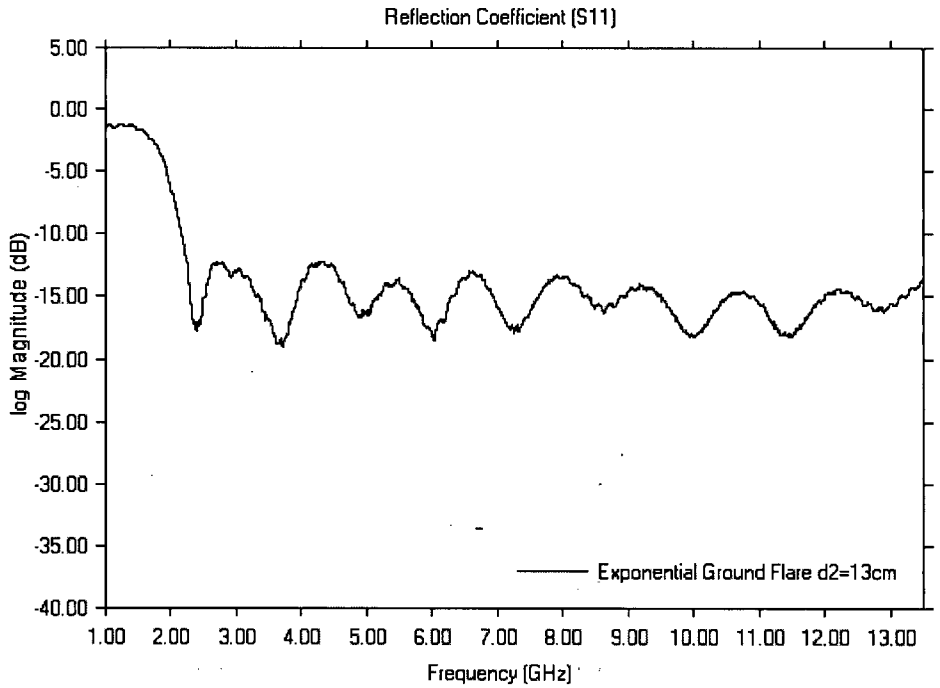

Figure 4.17: S_{11} Reflection Coefficient for FDL Antenna with Exponential Curve d_2=13cm

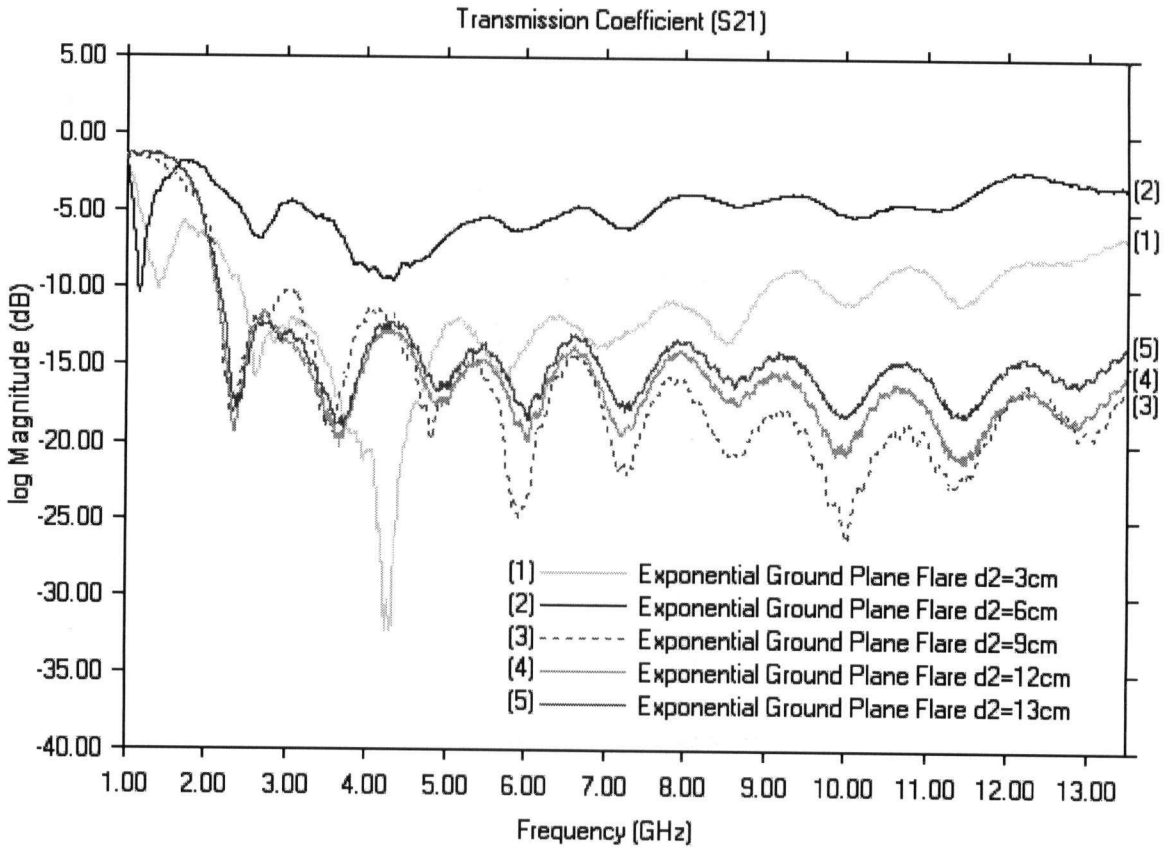

Figure 4.18: S_{11} Reflection Coefficient for FDL antenna with curvatures of 3cm to 13cm

did not outperform the Vivaldi antenna at larger flare curvatures. This did not create a problem for this application as the measurements that were taken were performed along the axis of the antenna where the cross-polarization is low at all frequencies and flares.

Figure 4.19 shows the E-Plane cross and co-polarization pattern for the Vivaldi antenna from the Guillanton paper at 9 GHz. Figure 4.20 shows the H-Plane cross and co-polarization pattern for the same antenna. The Vivaldi shows good results for both the E and H-planes, with the cross-polarization down approximately 18 dB along the bore sight for the E-plane and 16 dB

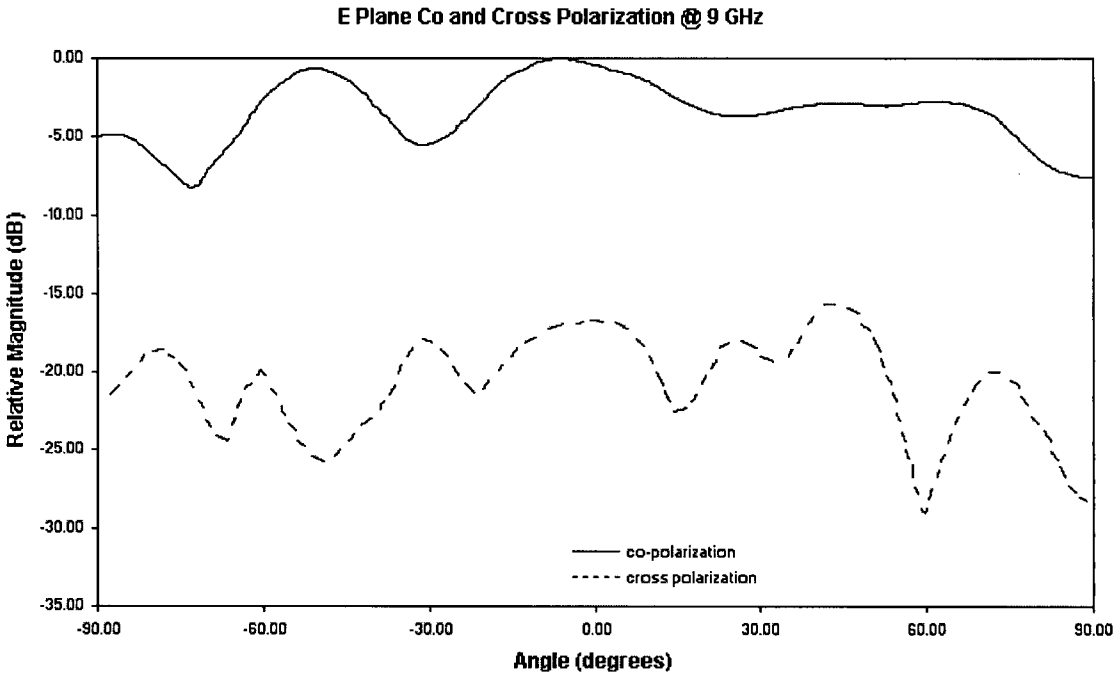

Figure 4.19: E-Plane Cross and Co-Polarization for Guillanton Vivaldi

for the H-plane. The E-plane cross-polarization remains lower than the co-polarization amplitude for the entire range between -90 degrees and 90 degrees. The H-plane cross-polarization becomes comparable to the co-polarization at angles around +/- 45 degrees.

Figures 4.21 and 4.22 show the E and H-plane cross and co-polarization readings for the FDL antenna with no flare (flat ground planes) at 9 GHz as well. As would be expected, the E-Plane cross-polarization level is approximately 14 dB lower than the co-polarization level for FDL antenna, versus 16 dB for the Vivaldi antenna. For the E-plane, however, the FDL antenna showed a drop in the co-polarization curve towards the outer edges (corresponding to higher angles) which the Vivaldi antenna does not show. The H-plane performance of the FDL antenna

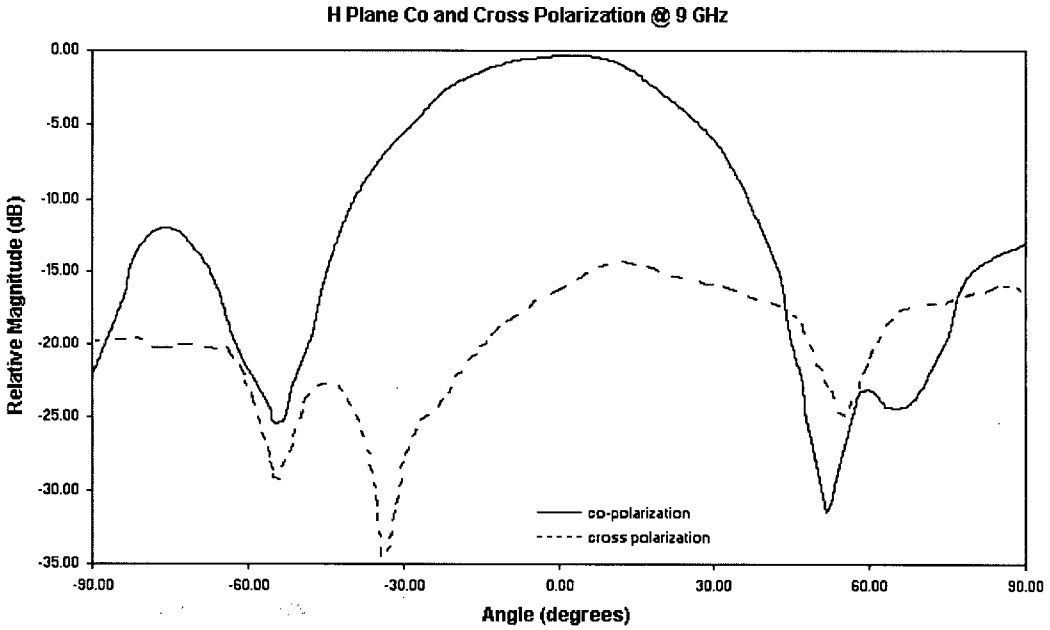

Figure 4.20: H-Plane Cross and Co-Polarization for Guillanton Vivaldi

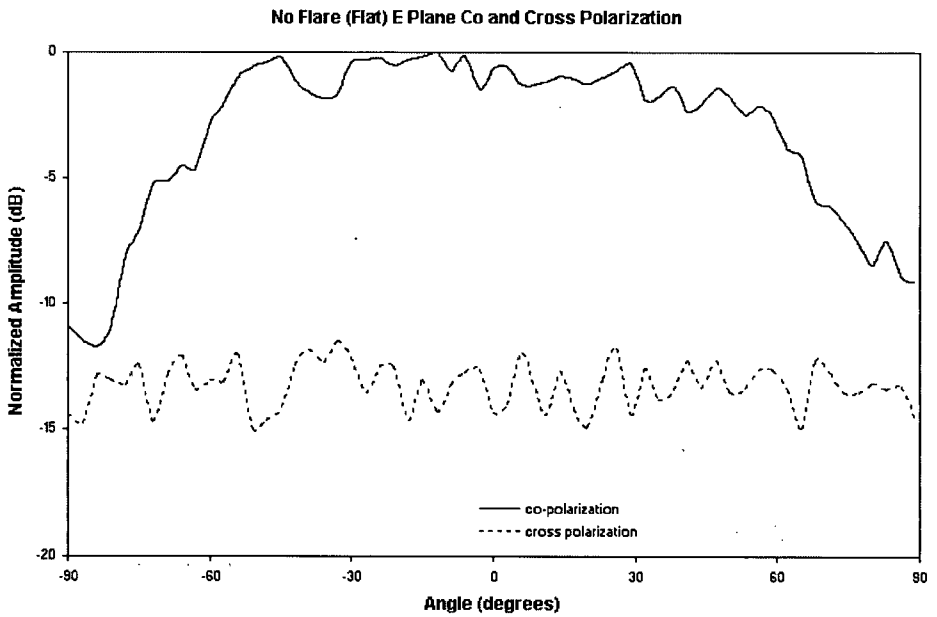

Figure 4.21: E-Plane Cross and Co-Polarization for FDL Antenna with No Flare

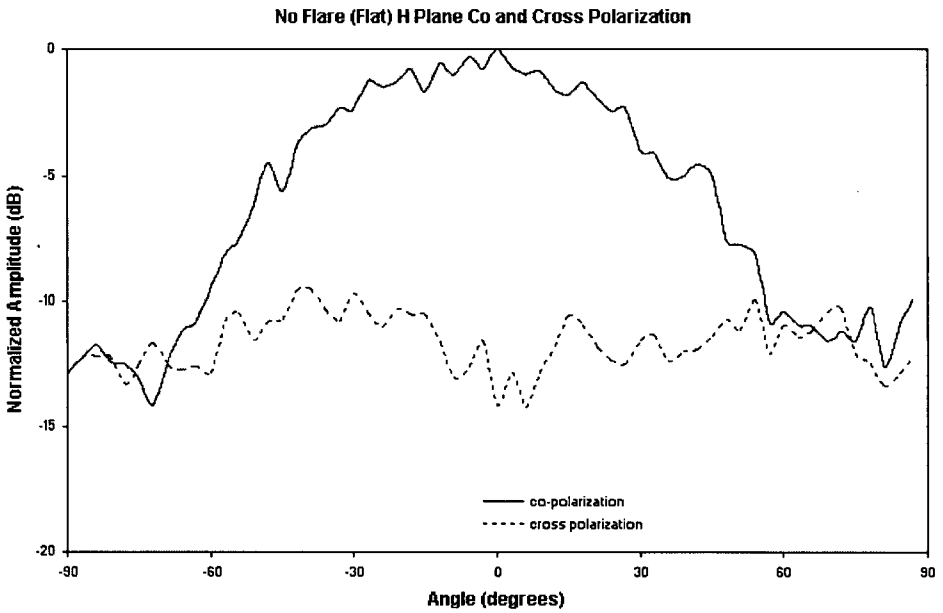

Figure 4.22: H-Plane Cross and Co-Polarization for FDL Antenna with No Flare

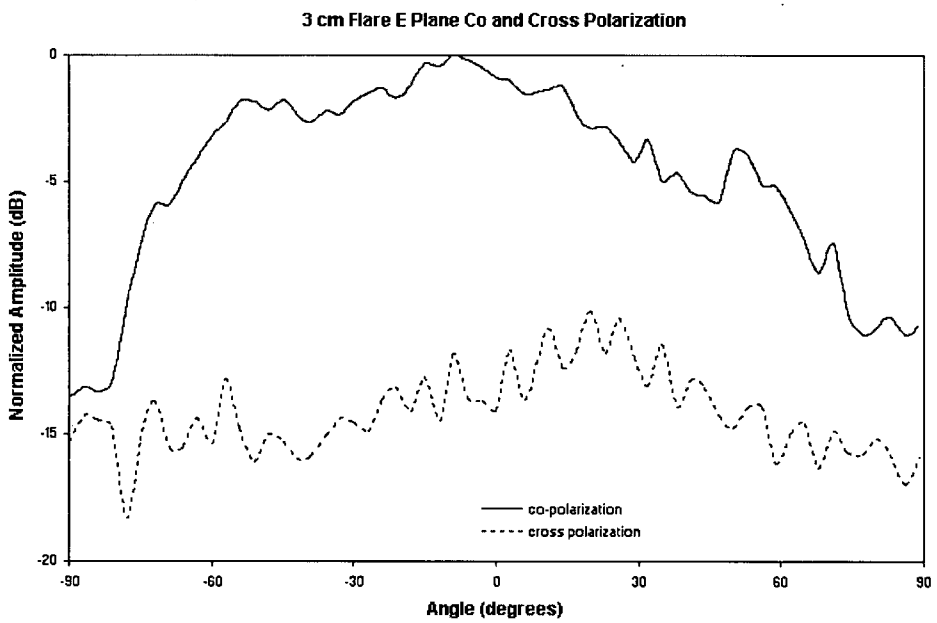

Figure 4.23: E-Plane Cross and Co-Polarization for FDL Antenna with 3cm Flare

Chapter 4 - Fleur-de-Lis Antenna

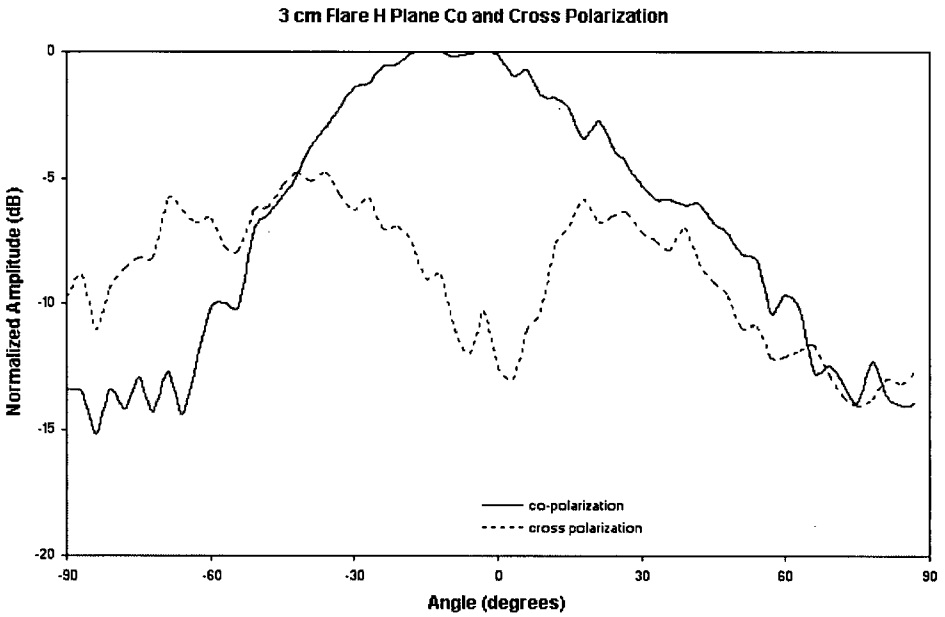

Figure 4.24: H-Plane Cross and Co-Polarization for FDL Antenna with 3cm Flare

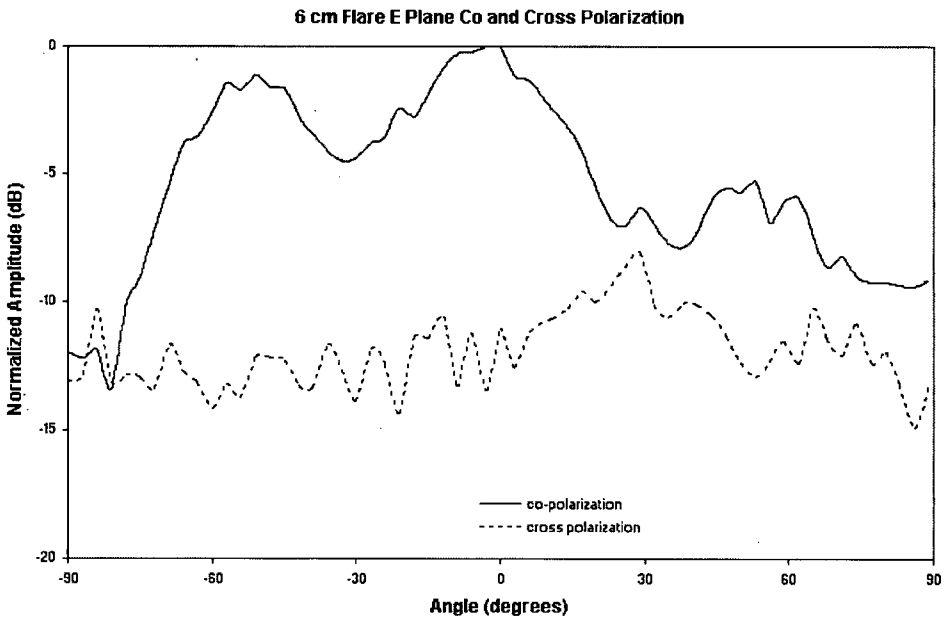

Figure 4.25: E-Plane Cross and Co-Polarization for FDL Antenna with 6cm Flare

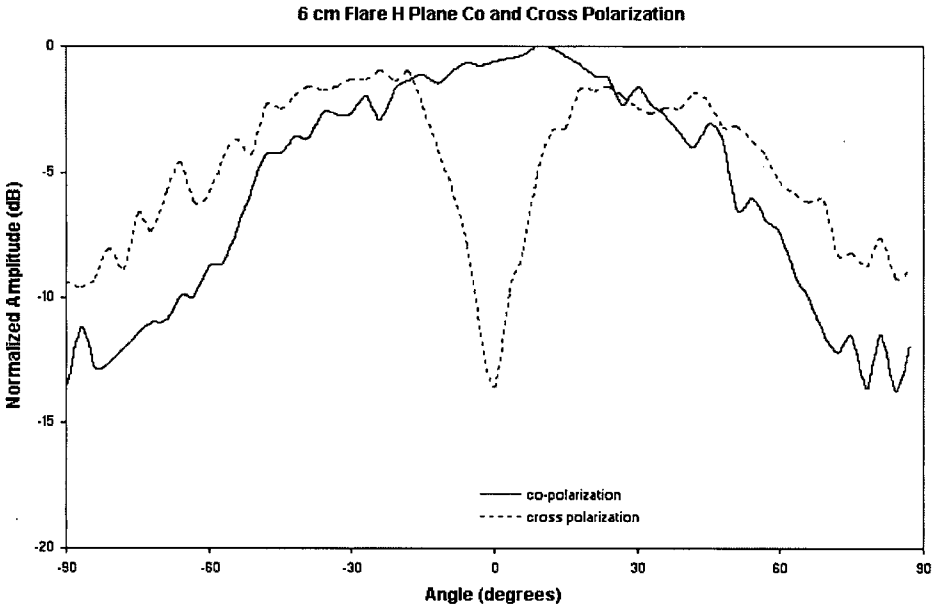

Figure 4.26: H-Plane Cross and Co-Polarization for FDL Antenna with 6cm Flare

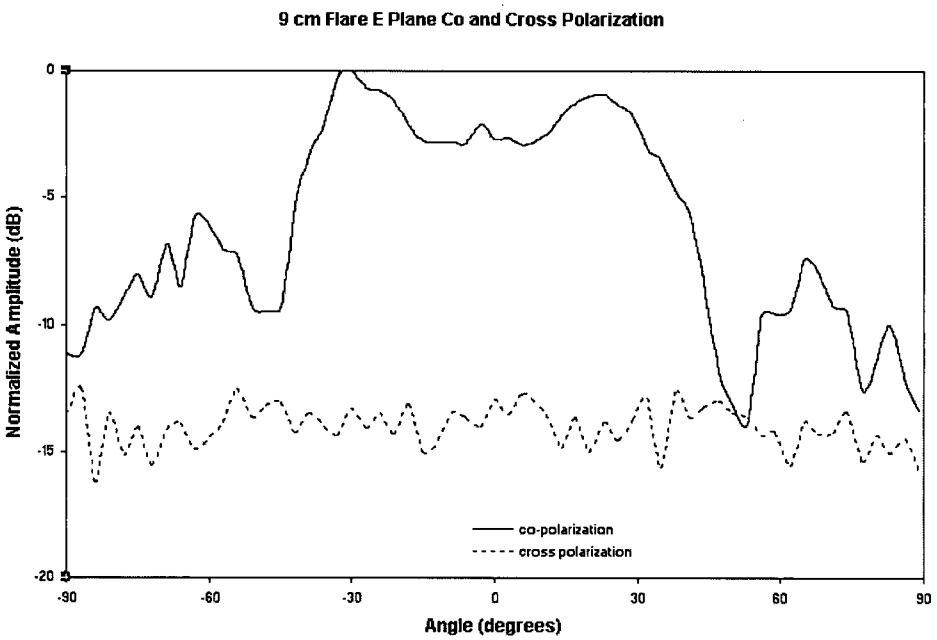

Figure 4.27: E-Plane Cross and Co-Polarization for FDL Antenna with 9cm Flare

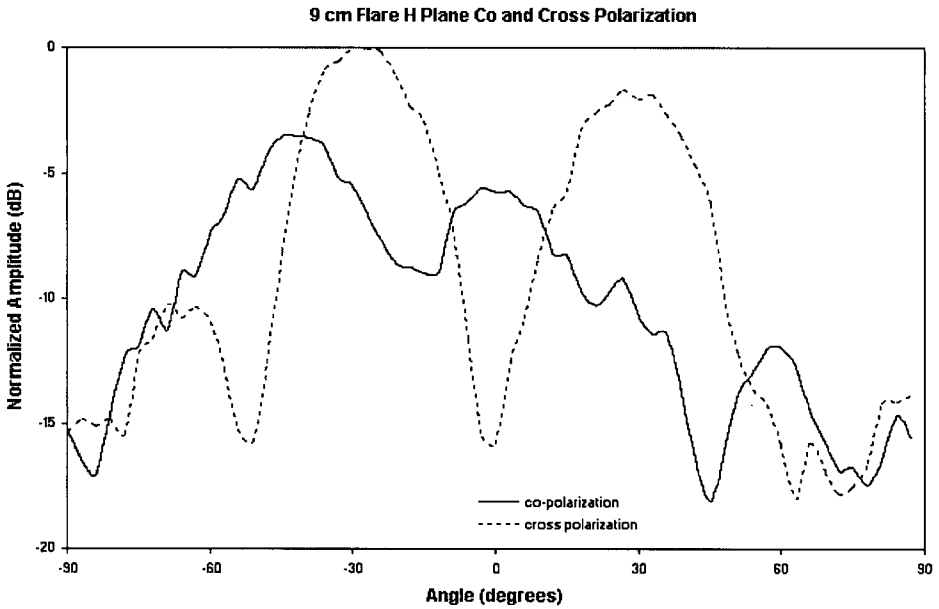

Figure 4.28: H-Plane Cross and Co-Polarization for FDL Antenna with 9cm Flare

was slightly improved over that of the Vivaldi antenna. While the polarization curves for the Vivaldi antenna meet at an angle of approximately 45 degrees, the curves for the FDL antenna do not meet until past 60 degrees.

The fact that there are differences between the cross- and co-polarization of the two antennas is due to the mechanical differences between them. Since the Vivaldi antenna's ground and active members are closely spaced, there is only a small current induced in the antenna by a wave polarized perpendicular to the surface of the antenna. This current is less affected by the angle at which the antenna is oriented in this plane due to the endfire nature of the Vivaldi antenna. For the FDL, however, the wide separation between the active and the ground members allows a stronger current to be induced and shows a stronger angle dependency since, unlike the

Vivaldi antenna, the profile of the FDL antenna that is exposed to the incoming wave changes greatly with the angle.

Figures 4.21 through 4.28 show the change in shape of the cross- and co-polarization curves as the flare is increased from flat through 9 cm. As the flare increases, the E-plane cross-polarization levels remain relatively constant when compared to the co-polarization level along the main axis. The cross-polarization remains around 12 dB to 14 dB lower than the co-polarization level at zero degrees and the cross-polarization curve remains relatively flat. The E-plane co-polarization curve, however, changes in shape as the flare is increased, changing from a relatively flat shape to one with multiple valleys. Once the flare reaches d_2 = 9cm, the cross and co-polarization curves meet briefly at around 50 degrees, at which point, due to geometry, the exposed profiles of the antennas in the E and H-planes lead to similarly induced currents in both planes.

The co-polarization curve for the H-plane changes like that of the E-plane co-polarization curve, with multiple peaks and valleys occurring as the flare curvature increases. The H-plane co-polarization level does not appear to change as fast as that of the E-plane, with the multiple peaks showing up at a flare curvature with d_2 = 9cm for the H-plane co-polarization curve versus d_2 = 6cm for the E-plane. The H-plane cross-polarization curve shows the most dramatic change as the flare curvature increases. For the E-plane the cross-polarization level is always below that of the co-polarization level. As the flare curvature increases the cross-polarization curve loses its "flat" profile and starts to develop symmetrical peaks at around the +/- 30 degree angle, again due to the antenna's geometry. These peaks increase in height until the cross-polarization is at the same level as the co-polarization, at an angle of 30 degrees for a flare curvature with d_2 = 6cm. At d_2 = 9 cm the cross-polarization levels at 30 degrees are significantly above those of the co-

polarization. The cross-polarization curve always shows a minimum value at 0 degrees (along the main axis).

As stated earlier, the minimum at zero degrees and the maximum at around 30 degrees can be explained by the geometry of the FDL antenna. In cross-polarization measurements the E-field from the transmitting antenna is oriented in the H-plane of the receiving antenna. At zero degrees the antenna is symmetric to the incoming E-field around the E-plane of the antenna. Therefore, any electric fields induced between the active member and the grounds are cancelled out due to symmetry. As the receiving antenna is rotated in the H-plane, the symmetry is lost, with one of the ground planes being more exposed to the incoming electric field than the other. The electric fields no longer cancel each other, resulting in an increase in power transmitted to the receiving antenna. As the antenna is further rotated, the active member of the antenna becomes shielded by the ground plane and the gap between the active member and the ground planes is no longer in the correct orientation to induce currents in the antenna.

4.4 Gain Measurements

To perform relative gain measurements, an antenna with a known gain calibration must be used for the calculation. Since there are no standard antennas that will cover the entire 1 - 13.5 GHz bandwidth of the FDL antenna, multiple standard gain antennas would have been needed to cover the entire frequency range. The results for gain versus frequency for this thesis are limited to the range of 8 GHz to 12 GHz because only one standard gain antenna was available for use. Gain measurements were performed using a Narda model 640 Standard Gain horn, which has a range of 8 GHz to 12.25 GHz.

Chapter 4 - Fleur-de-Lis Antenna

Table 4.1 shows the gain results for the FDL Antenna, with exponential S_6 profile d_2 = 9cm, compared to those for the Guillanton Vivaldi antenna. Upon first examination it appears that the gain for the FDL antenna is significantly lower than that for the Vivaldi antenna. However, an examination of the S_{11} curve in Figure 3.7 for the Guillanton antenna shows that the reported

Frequency (GHz)	2	4	6	8	9	10	11	12
FDL Gain (dB)	N/A	N/A	N/A	3.7	3.6	4.4	4.8	4.7
Vivaldi Gain (dB)	3.2	5.8	4.2	N/A	7.8	8.2	N/A	8

Table 4.1: Gain versus Frequency For Optimal FDL and Guillanton Vivaldi Antennas

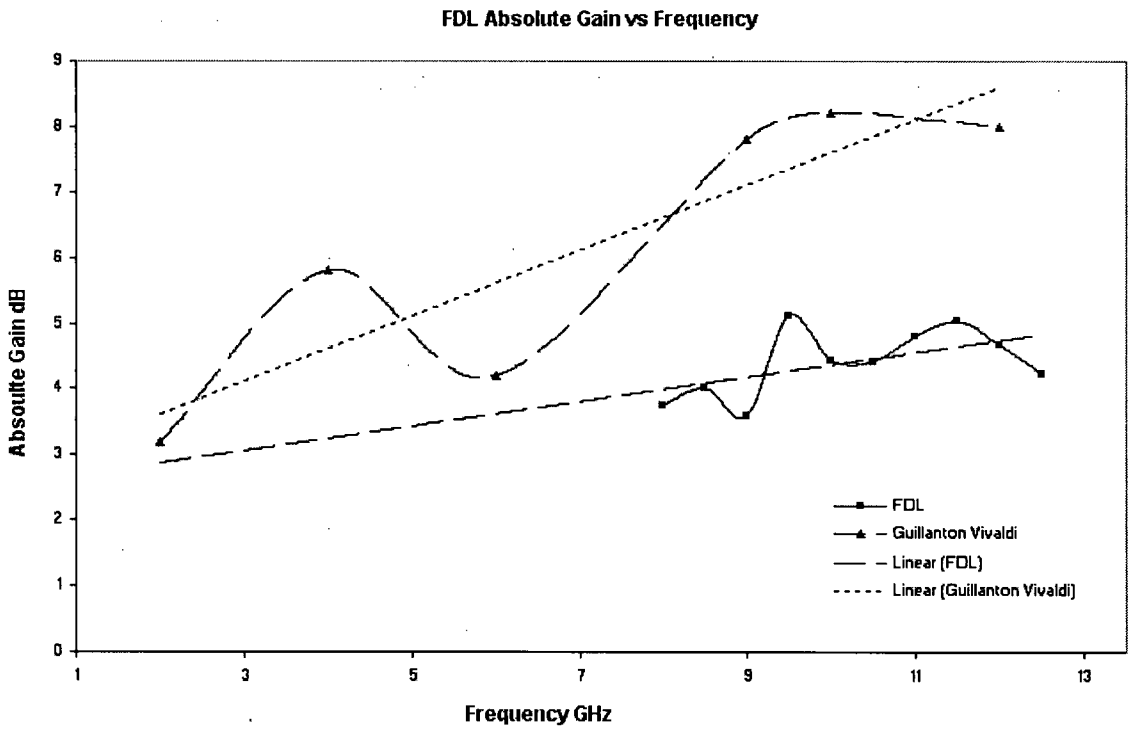

Figure 4.29: Absolute Gain versus Frequency for the FDL and Guillanton Vivaldi Antennas

gain measurements for the Vivaldi antenna in the range between 8 GHz and 12 GHz were taken from the peak resonance frequencies shown at 9 GHz, 10 GHz and 12 GHz. These measurements give a false impression of the overall gain of the antenna.

Table 4.1 shows that the gain of the Guillanton antenna at 2 GHz and 6 GHz as listed at 3.2 dB and 4.2 dB. These values correspond to points on the S_{11} curve in Figure 3.7 where there is no sharp peak. At these points the gain of the Vivaldi antenna is similar to the gain of the FDL antenna and is in the range of 3 to 4 dB.

Figure 4.29 shows a graph of the FDL and Guillanton antennas' gain versus frequency. The dotted trend lines, calculated by least squares fit, as shown in Figure 4.29, also show that the FDL and Vivaldi's antenna's gain generally increases as the frequency increases. This is normal for most wideband antennas such as the Vivaldi and the horn antennas [73, 76].

Chapter 5

5.0 Antenna Modelling

Since the FDL antenna is a new design that produced results significantly different from any other antenna, it was not possible to check the experimental results against an existing FDL antenna. To determine a design for an FDL antenna that gave the flattest S_{11} response, a series of computer simulations were run using the FEKO electromagnetic field analysis software.

The name FEKO is an abbreviation derived from the German phrase ***FE****ldberechnung bei* ***K****örpern mit beliebiger* ***O****berfläche* (field computations involving bodies of arbitrary surface) [77]. Among its other uses, such as the analysis of electric fields around objects in space, FEKO can be used to calculate the various parameters of a model antenna. FEKO is based on the Method of Moments (MoM) and calculates the electric surface currents on conducting surfaces and equivalent electric and magnetic surface currents for dielectric materials. Once the current distributions are calculated for the model antenna, the near field, the far-field, the input impedance and the S parameters of the antenna can be determined.

For this thesis, the FEKO simulations for the FDL antenna were created by varying each of the L_1, L_2, L_3, L_4, L_5, h_1, h_2, h_3, h_4, d_1 and d_2 parameters independently to see how these would affect the performance of the FDL antenna's S_{11} Return-Loss response. Due to limitations in time and available computing power, it was not possible to create models and produce results for the complete model space, nor was it possible to run cross and co-polarization and radiation patterns for models for all values of L_1 through d_2. Cross and co-polarization and radiation patterns for a single representative model were also run, corresponding to one of the physical antennas created during this project.

Chapter 5 - Antenna Modelling

To calculate the S_{11} graphs and far field plots, FEKO was run using a single instance of this FDL antenna model. To calculate the cross and co-polarization values, two instances of the FDL model were used. The second instance of the FDL model was rotated 180 degrees around the z axis and then translated in the model's space so that the two instances of the FDL model were facing each other at a distance.

5.1 FEKO Model FDL Antenna

Figure 5.1 shows the model antenna divided into 2700 triangular sections. The surfaces are divided up automatically by the FEKO program. The number of sections is dependent upon the target analysis frequencies and is calculated to guarantee a valid solution. An example of an original FEKO design file is shown in Appendix B.

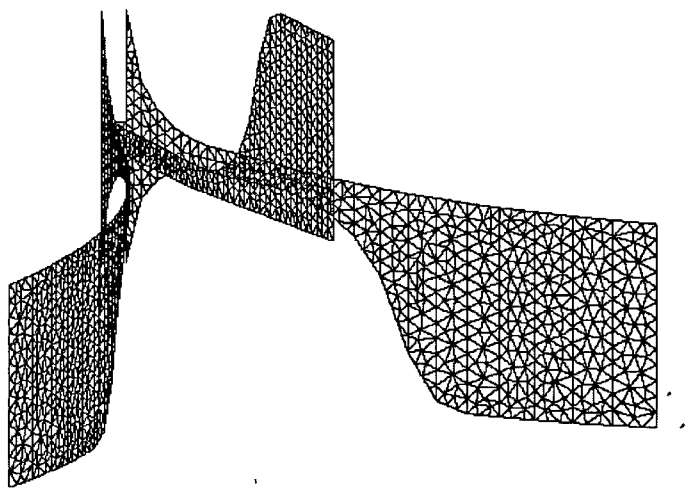

Figure 5.1: FEKO Model FDL Antenna

5.2 FEKO Model S_{11} Return Loss Coefficient Results

Figures 5.2 to 5.37 show the results of the FEKO calculations for the FDL model antenna's S_{11} parameter. In addition to comparing the FEKO results to measurements for one of the FDL antennas constructed for this project, a sensitivity study was performed using FEKO to determine which of the design parameters were most important in determining S_{11} behaviour and to determine the values that give the best S_{11} performance.

5.2.1 FEKO Design Parameter Sensitivity Study

As shown earlier in Figures 4.3 and 4.4, the FDL antenna design is based on constructing the antenna from a number of segments. The critical parameters for determining the shape of the antenna were the length parameters L_1 through L_5, the height parameters h_1 through h_4 and the separation parameters d_1, d_2, which control the spacing and the curvature of the ground planes with respect to the active member.

As can be seen from figures 5.2 through 5.36, varying each of the parameters has an effect on the S_{11} parameters for the model antenna. There are, however, four parameters that have a greater effect on flattening the S_{11} curve below the -10 dB level than the others. These four parameters are L_1, h_4, d_1 and d_2. For shorter overall lengths, L_1 produces an S_{11} curve that has deep valleys, with one significant one at around 6 GHz. The frequency of the centre point of this valley decreases proportionally with the increase in the over all length, L_1, of the antenna. This feature is similar to other antennas where a single radiation mode dominates and produces a resonance at which most of the antennas energy is radiated.

As the height, h_4, of the throat of the active member of the antenna is changed, the S_{11} curve tends to remain reasonably flat, or at least does not develop any deep resonances. The curve's position does, however, drop below the -10 dB level, to a minimum value at around h_4=0.7 cm. For h_4 values above or below this value, the curve tends to rise above the -10 dB level which would indicate that the match is not as good. The throat of the active member is where the antenna signal is fed into the antenna via the connection to the SMA connector. The FDL and Vivaldi antennas are based on tapered slot antennas, which are often fed with varying stripline arrangements. For the FDL antenna, it is most likely that the poor impedance match with the varying h_4 values is due to similar slotline impedance mismatches between the coaxial feed and the throat.

The d_1 parameter that controls the spacing between the ground planes and the active member of the antenna near the throat at the SMA connector shows a similar behaviour to that of the h_4 parameter. This is also most likely due to the stripline feed behaviour, which like tapered slot antennas, also depends upon the distance between the ground plane and the active member. For tapered slot antennas the stripline behaviour also depends upon the dielectric material as well as the distance between the planes. For the FDL, however, as stated earlier, there is no dielectric material present between the ground planes and the active member.

The parameter that makes the biggest difference in the flatness of the S_{11} curve is the d_2 parameter, which controls the size and curvature of the flare of the ground planes. This dependence on d_2 is what was found experimentally and is confirmed by the FEKO models. As seen in Figures 5.33 through 5.36, changing the distance d_2 does not affect the frequency of the resonances, only the depth. As the size of d_2 approaches its optimal value at about 11 cm, the valleys in the S_{11} curve reach a minimum as the energy radiated by the antenna is more evenly

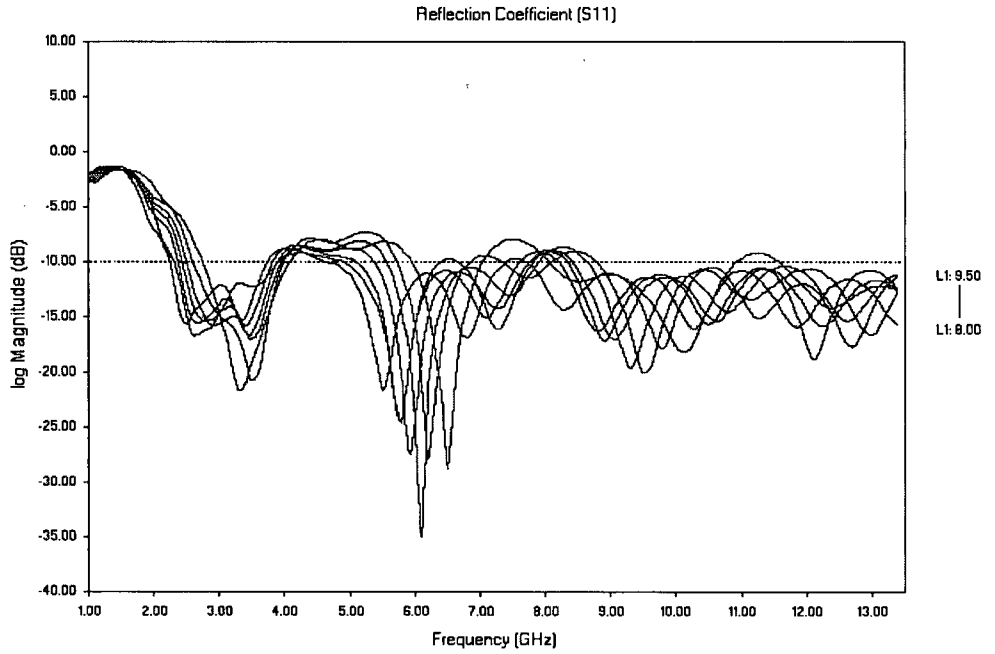

Figure 5.2: FEKO Model FDL S_{11} for L_1=8.00 cm to 9.50 cm (0.25 cm increments)

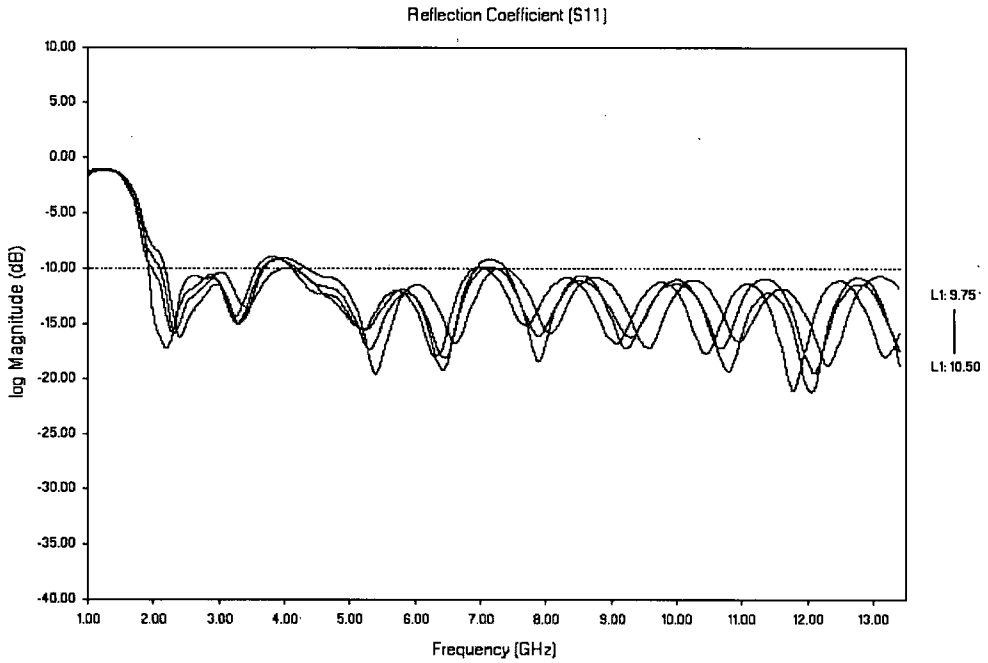

Figure 5.3: FEKO Model FDL S_{11} for L_1=9.75 cm to 10.50 cm (0.25 cm increments)

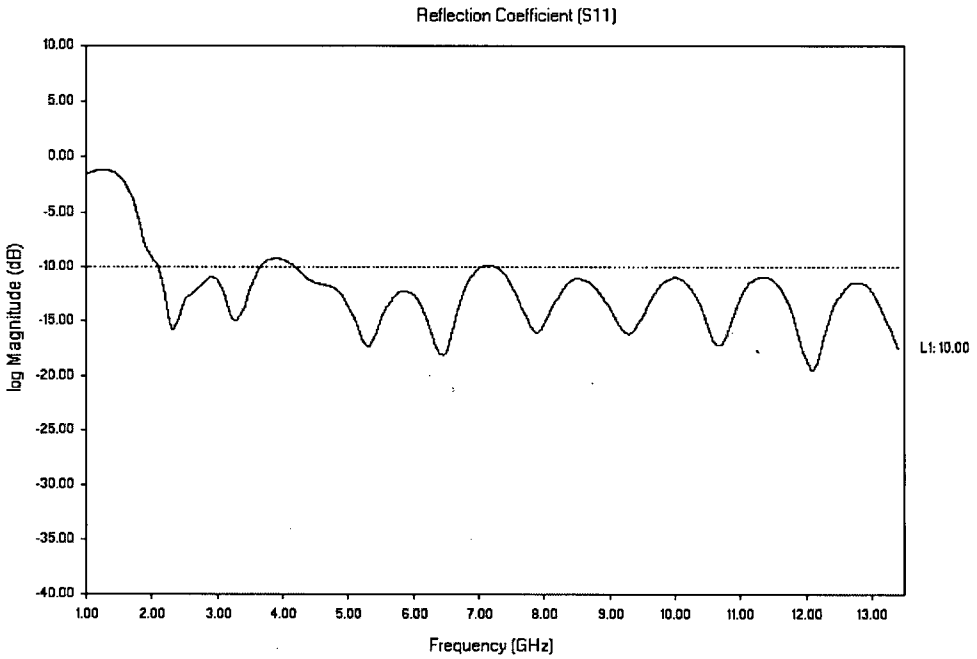

Figure 5.4: FEKO Model FDL S_{11} for L_1=10.00 cm

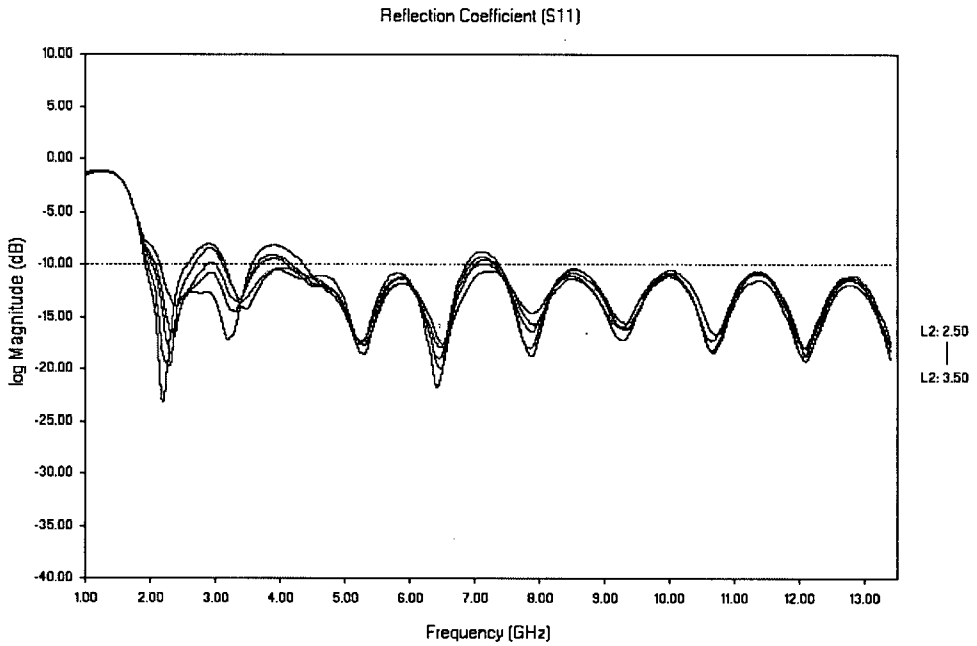

Figure 5.5: FEKO Model FDL S_{11} for L_2=2.50 cm to 3.50 cm (0.25 cm increments)

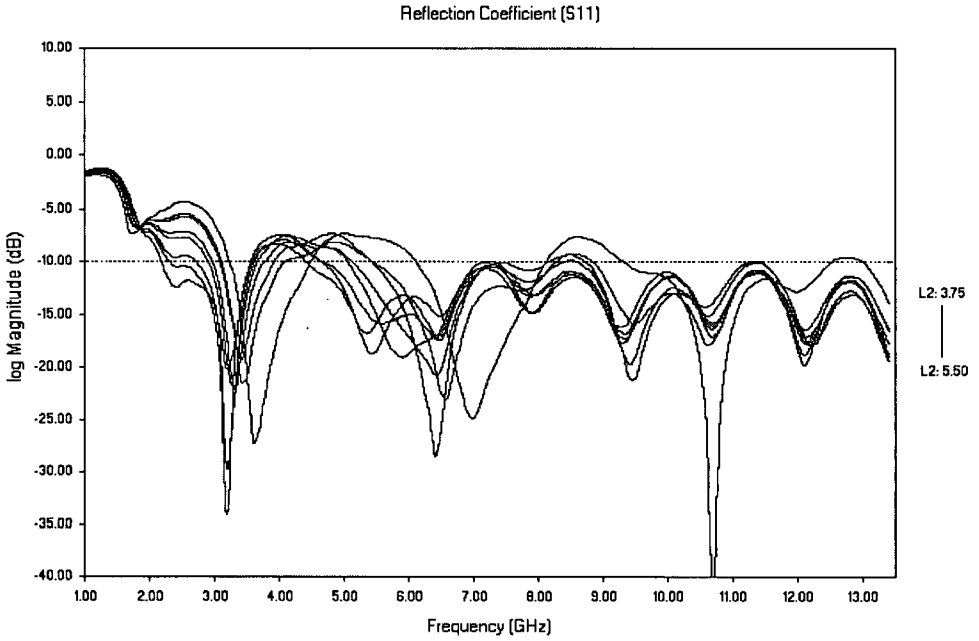

Figure 5.6: FEKO Model FDL S_{11} for L_2=3.75 cm to 5.50 cm (0.25 cm increments)

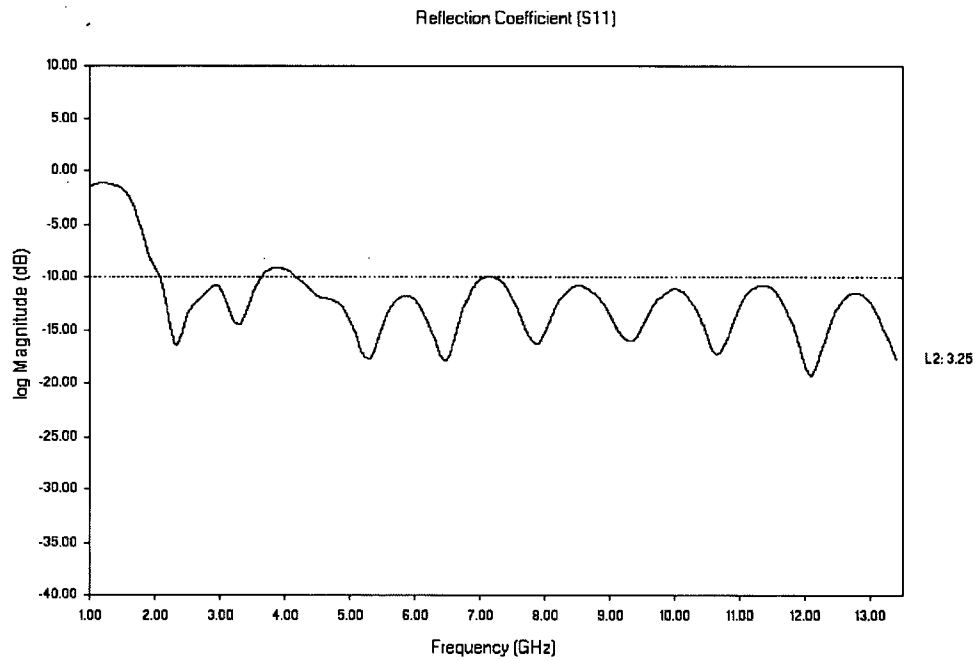

Figure 5.7: FEKO Model FDL S_{11} for L_2=3.25 cm

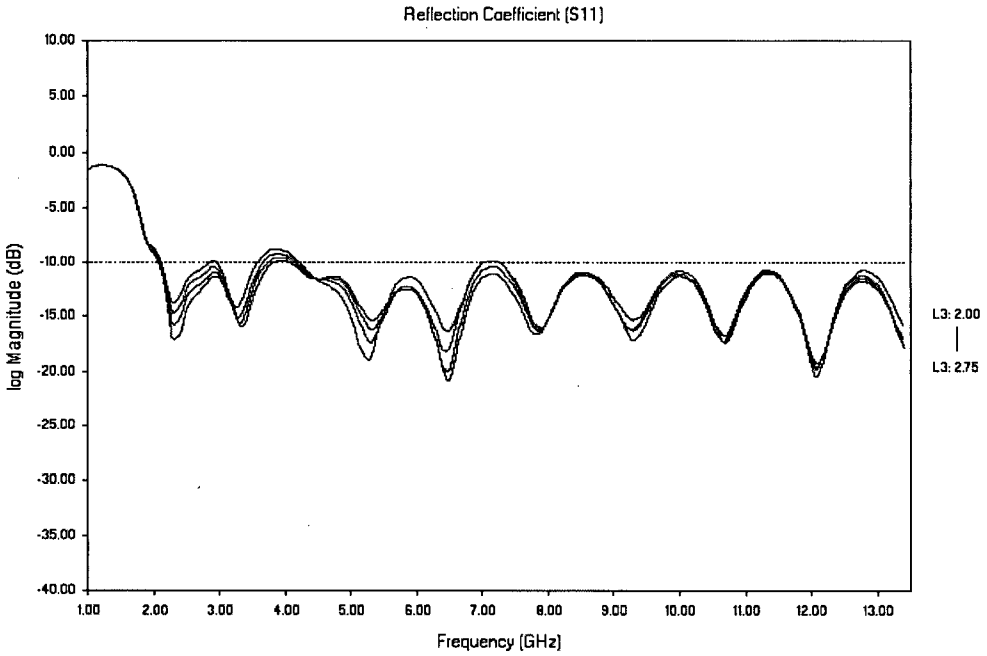

Figure 5.8: FEKO Model FDL S_{11} for L_3=2.00 cm to 2.75 cm (0.25 cm increments)

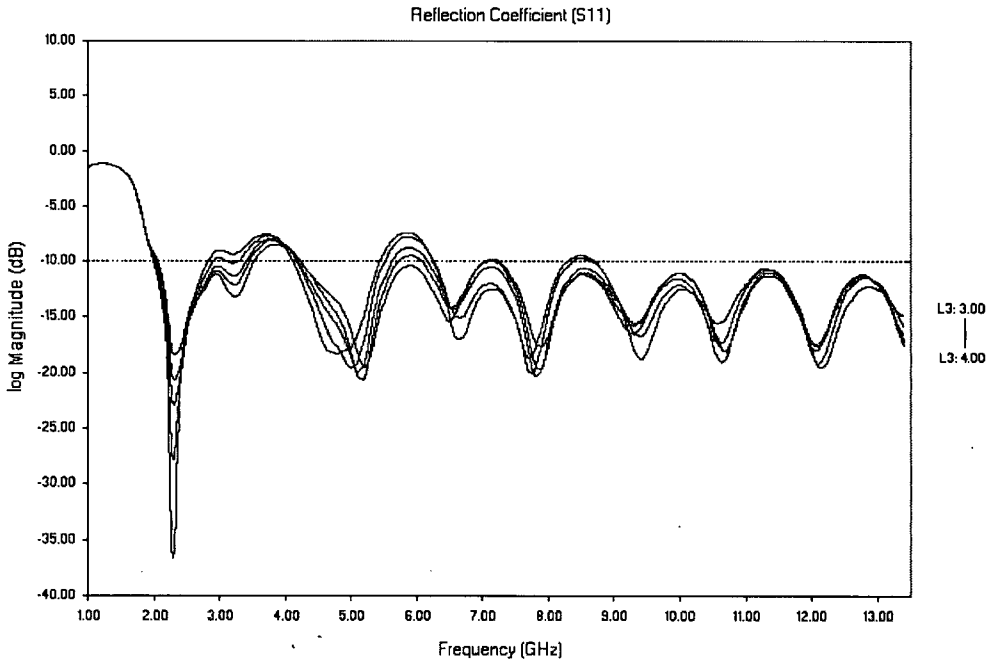

Figure 5.9: FEKO Model FDL S_{11} for L_3=3.00 cm to 4.00 cm (0.25 cm increments)

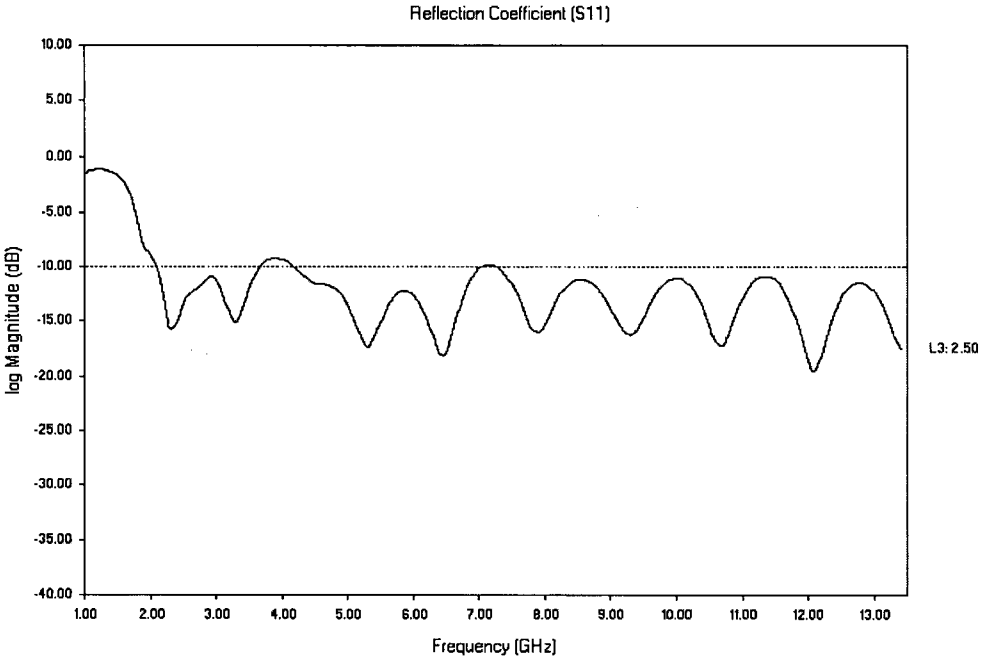

Figure 5.10: FEKO Model FDL S_{11} for L_3= 2.5 cm

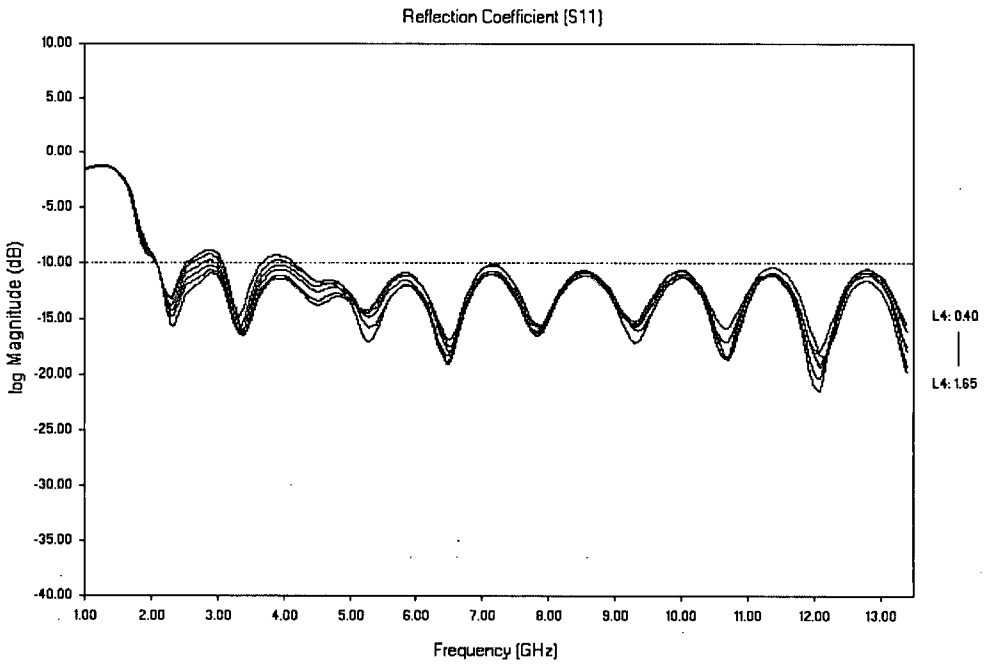

Figure 5.11: FEKO Model FDL S_{11} for L_4=0.40 cm to 1.65 cm (0.25 cm increments)

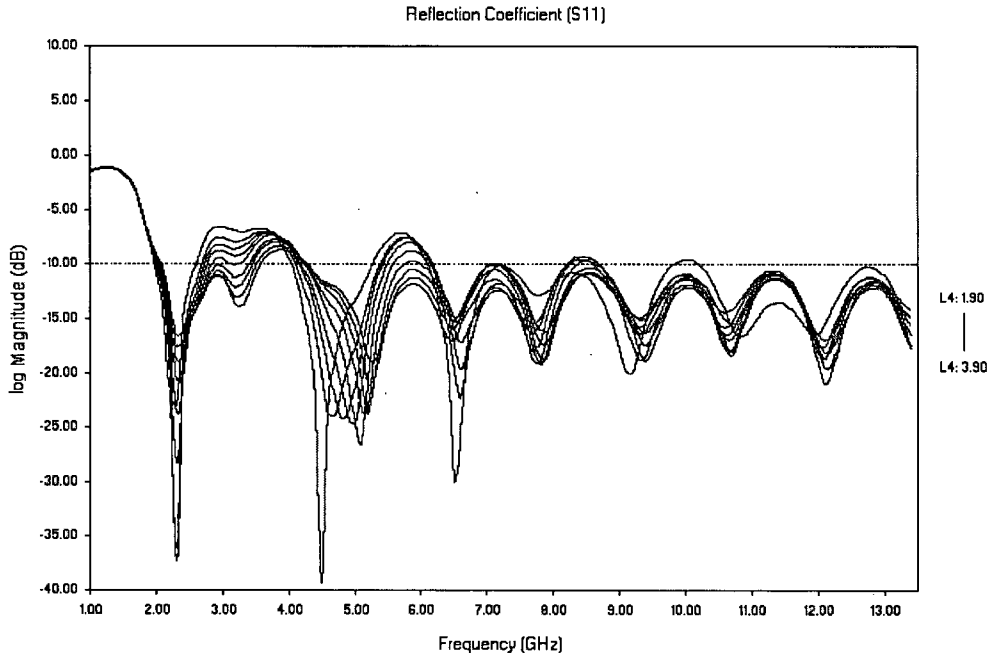

Figure 5.12: FEKO Model FDL S_{11} for L_4=1.90 cm to 3.90 cm (0.25 cm increments)

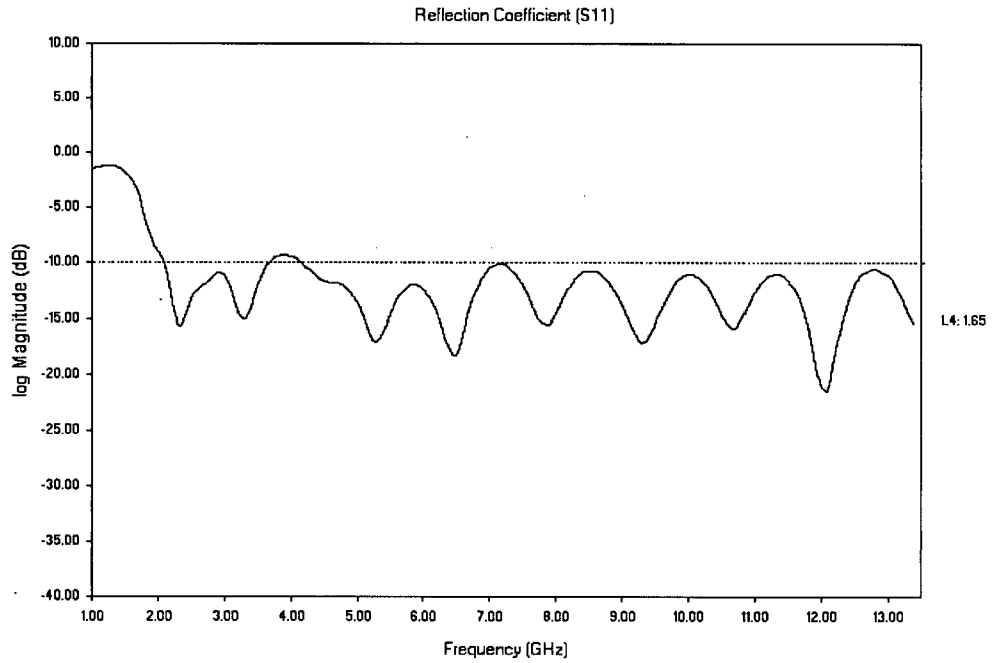

Figure 5.13: FEKO Model FDL S_{11} for L_4=1.65 cm

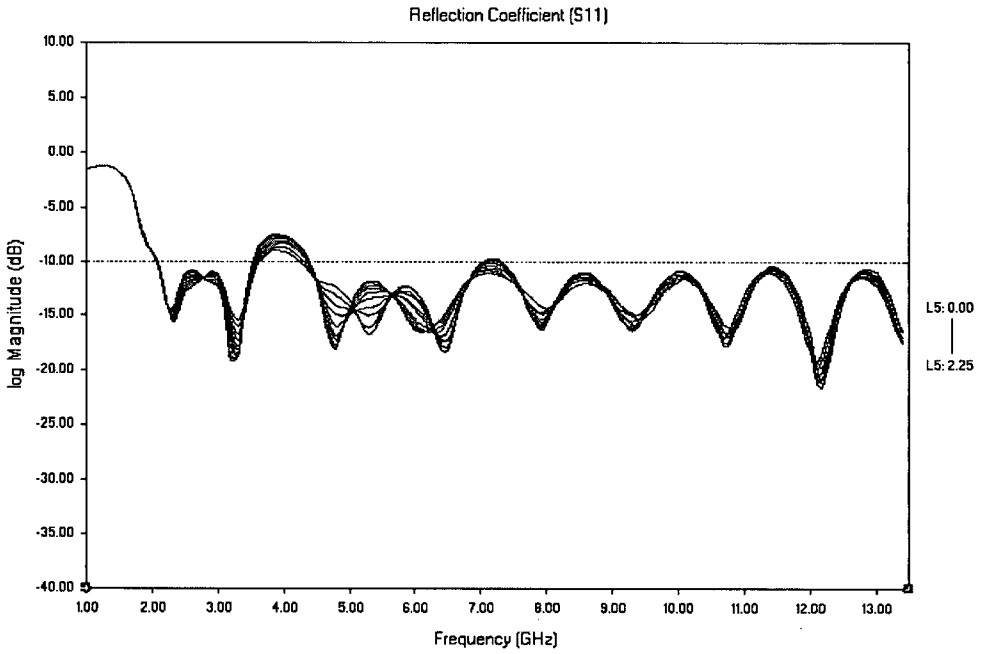

Figure 5.14: FEKO Model FDL S_{11} for L_5=0.00 cm to 2.25 cm (0.25 cm increments)

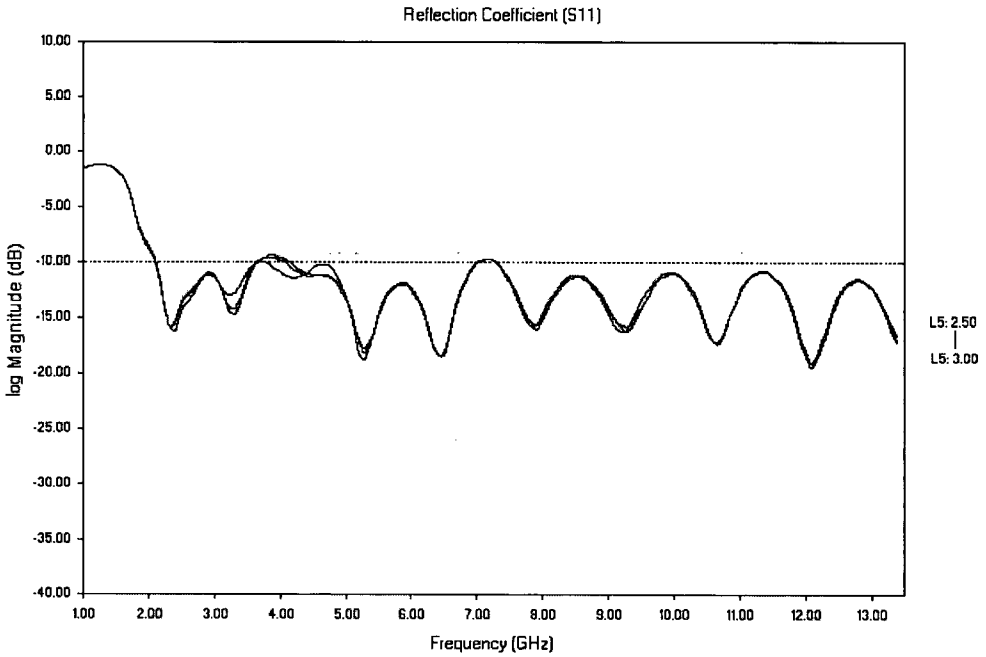

Figure 5.15: FEKO Model FDL S_{11} for L_5=2.55 cm to 3.00 cm (0.25 cm increments)

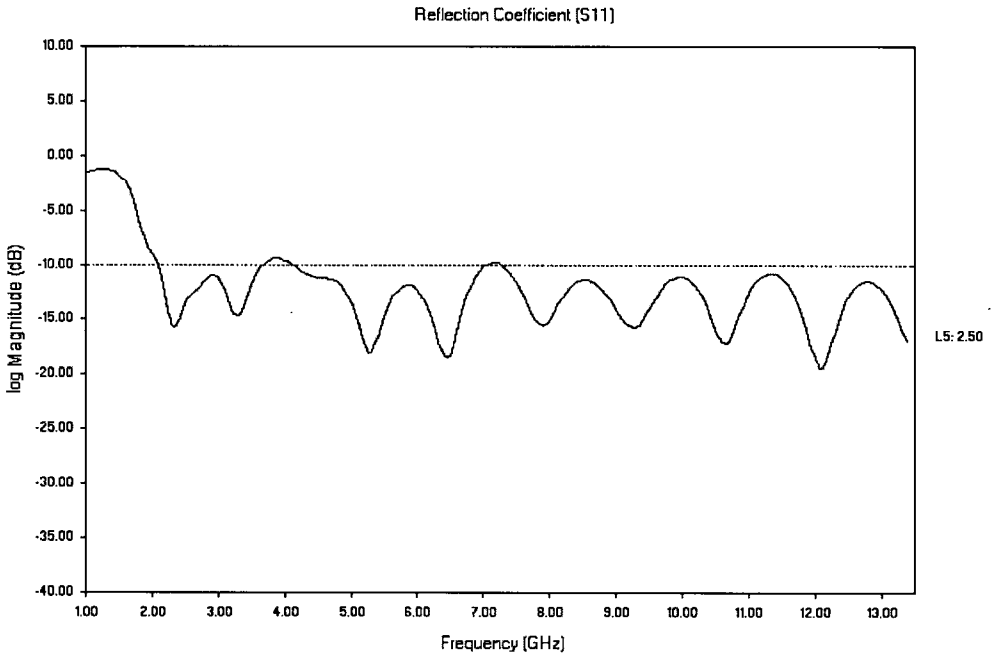

Figure 5.16: FEKO Model FDL S_{11} for L_5=2.50 cm

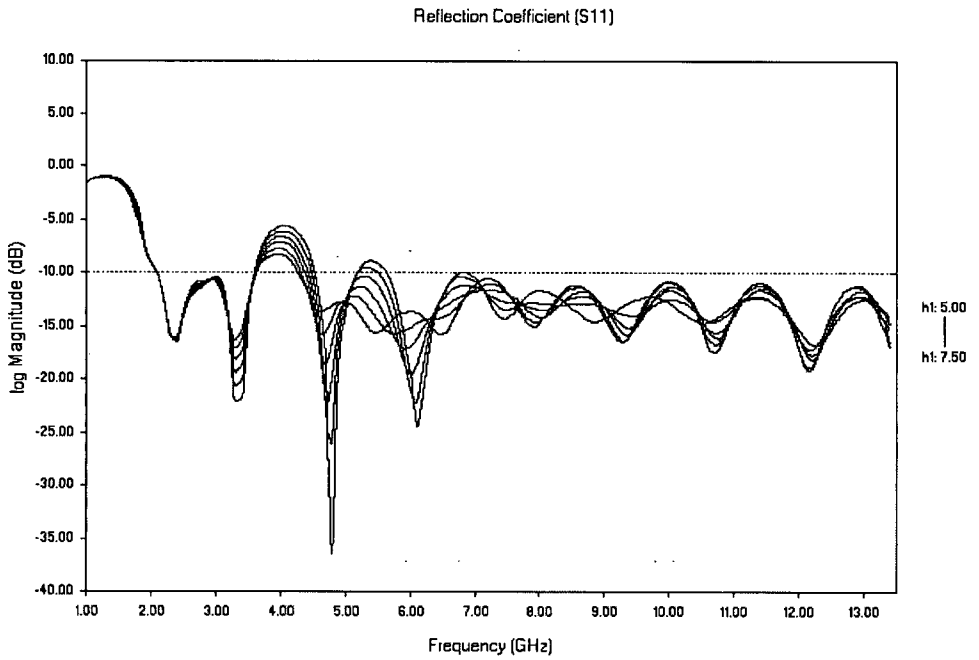

Figure 5.17: FEKO Model FDL S_{11} for h_1=5.00 cm to 7.50 cm (0.50 cm increments)

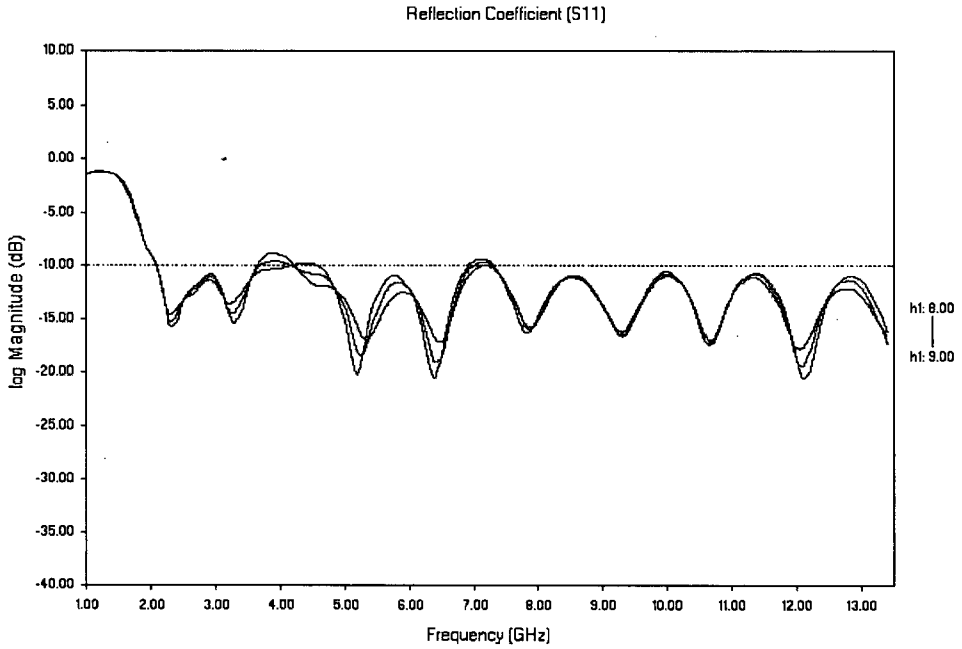

Figure 5.18: FEKO Model FDL S_{11} for h_1=8.0 cm to 9.0 cm (0.50 cm increments)

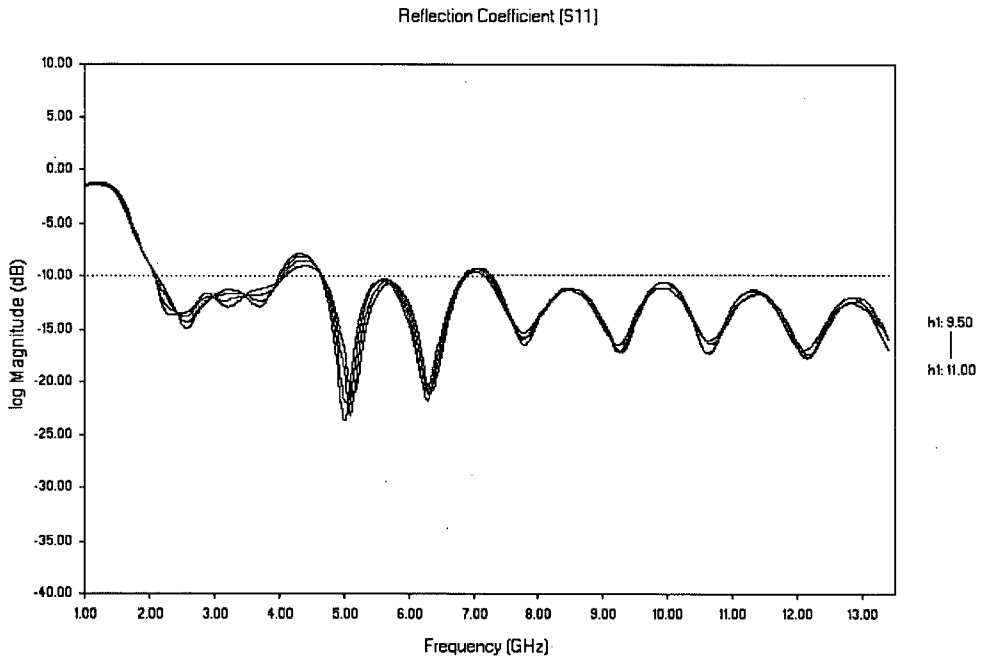

Figure 5.19: FEKO Model FDL S_{11} for h_1=9.50 cm to 11.00 cm (0.50 cm increments)

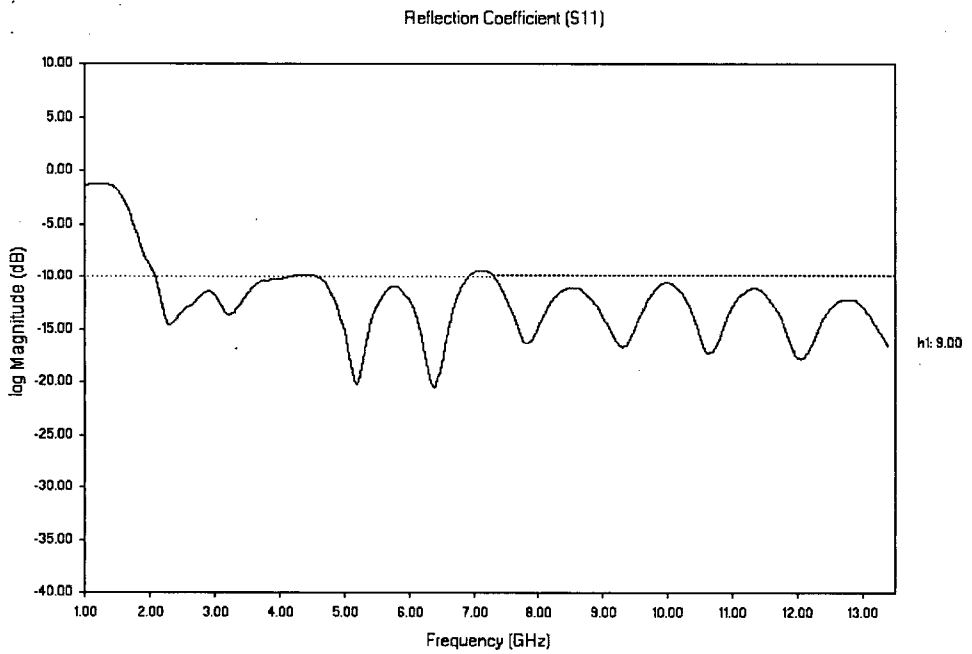

Figure 5.20: FEKO Model FDL S_{11} for h_1=9.00 cm

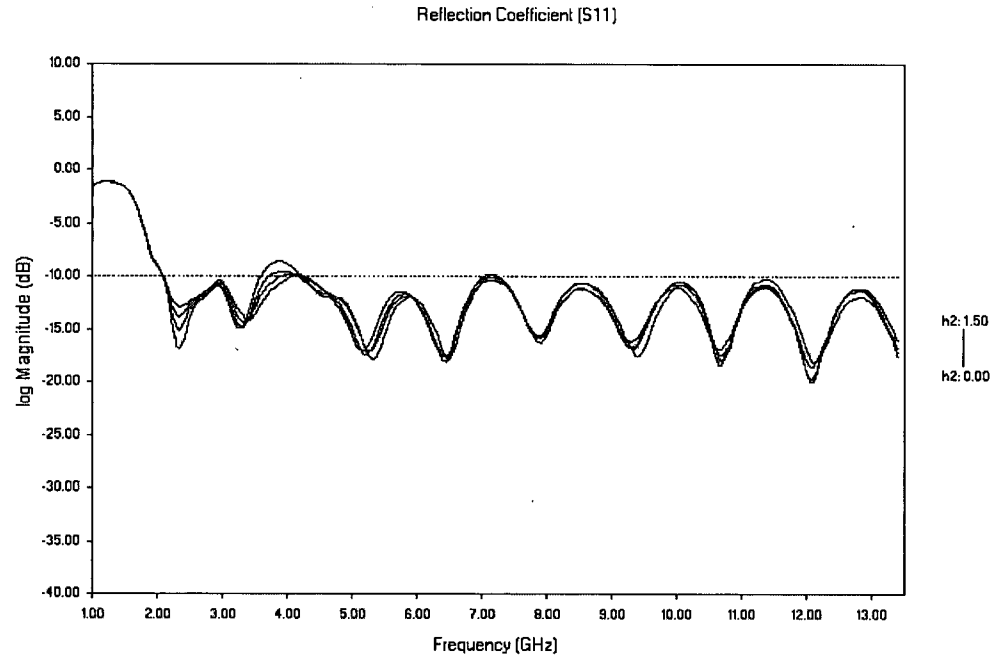

Figure 5.21: FEKO Model FDL S_{11} for h_2=0.00 cm to 1.50 cm (0.50 cm increments)

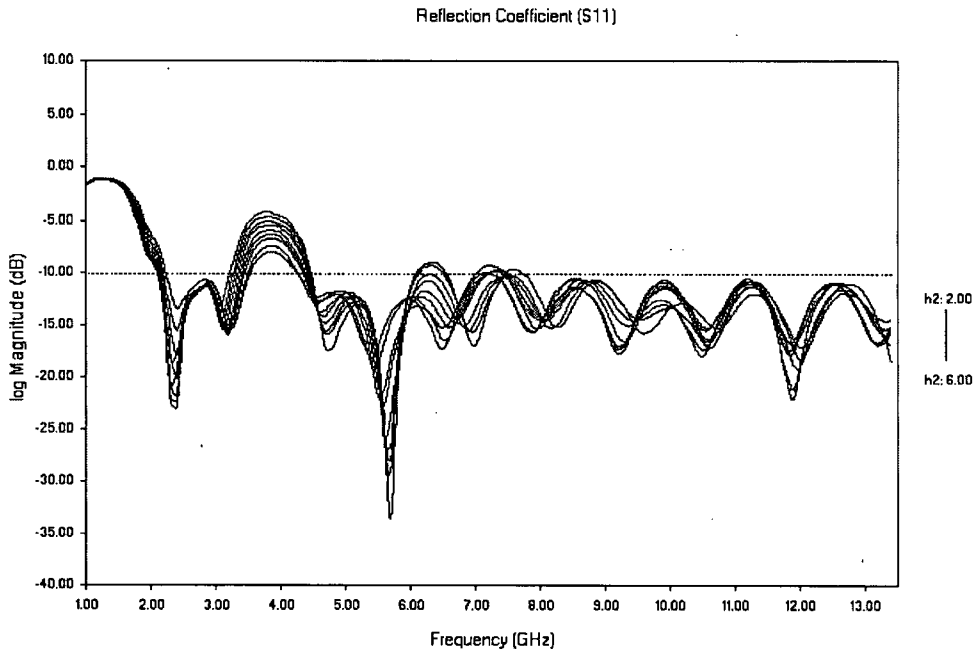

Figure 5.22: FEKO Model FDL S_{11} for h_2=2.00 cm to 6.00 cm (0.50 cm increments)

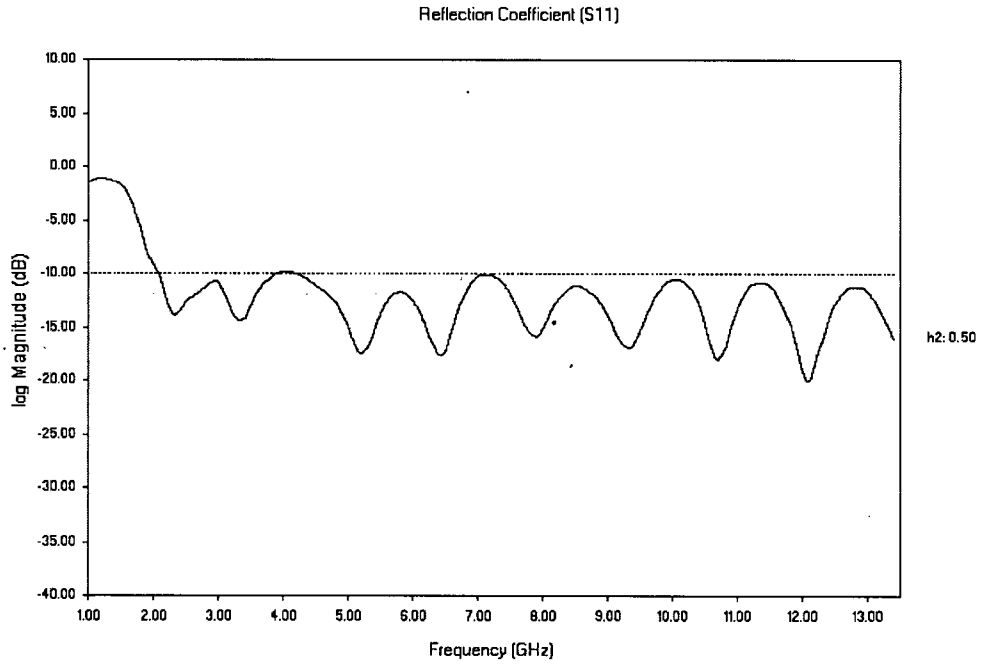

Figure 5.23: FEKO Model FDL S_{11} for h_2=0.50 cm

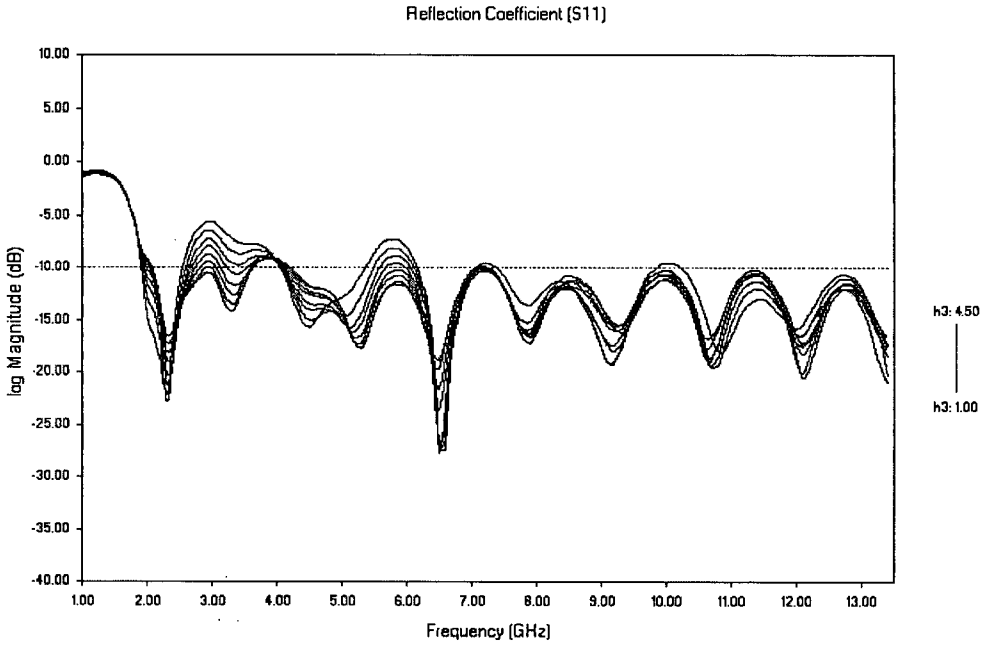

Figure 5.24: FEKO Model FDL S_{11} for h_3=1.00 cm to 4.50 cm (0.50 cm increments)

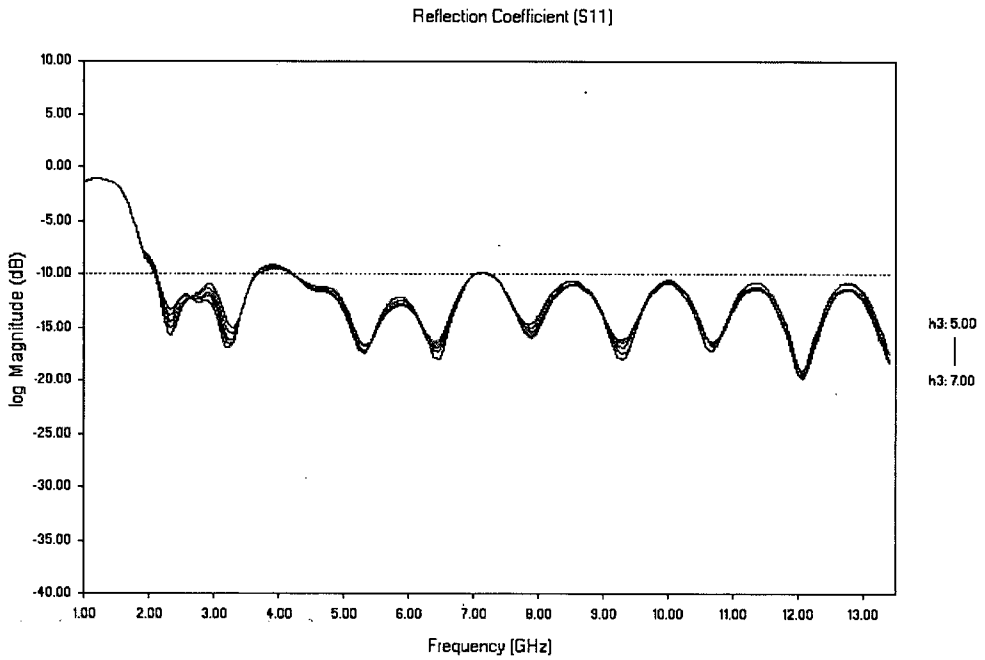

Figure 5.25: FEKO Model FDL S_{11} for h_3=5.00 cm to 7.00 cm (0.50 cm increments)

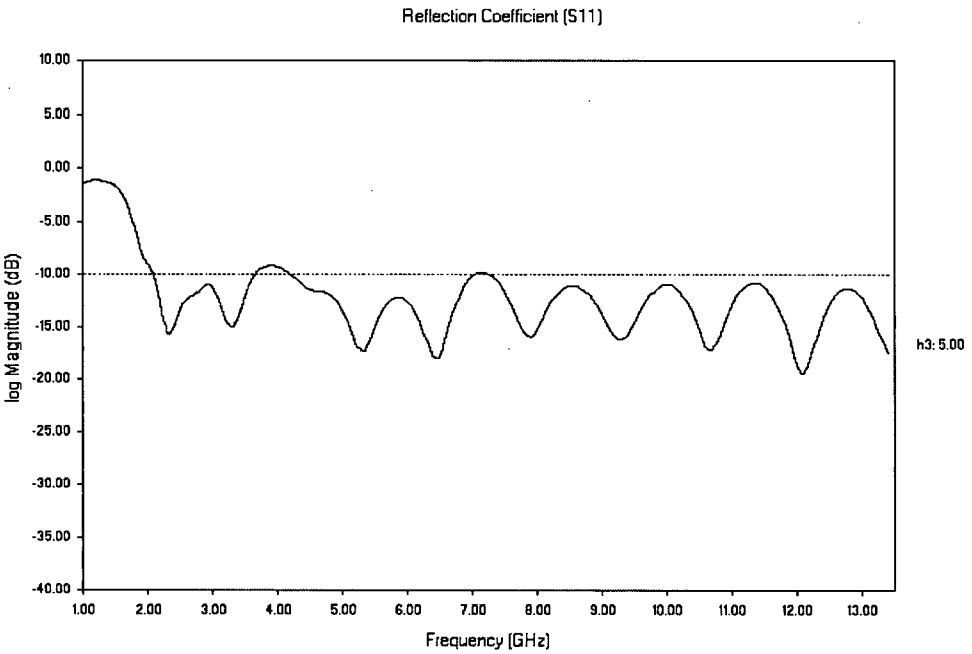

Figure 5.26: FEKO Model FDL S_{11} for h_3=5.00 cm

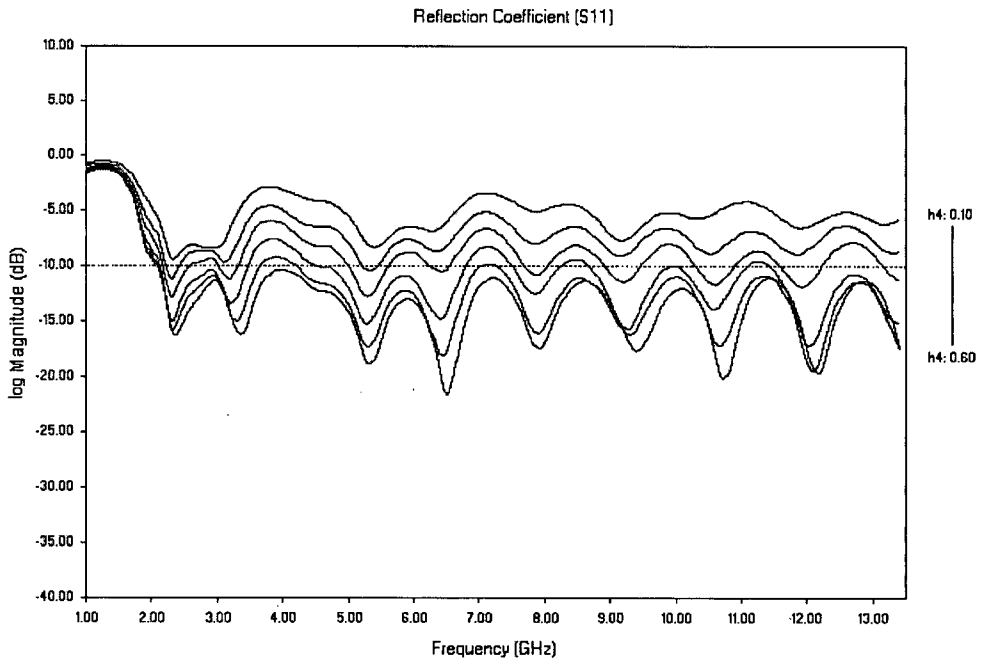

Figure 5.27: FEKO Model FDL S_{11} for h_4=0.10 cm to 0.60 cm (0.10 cm increments)

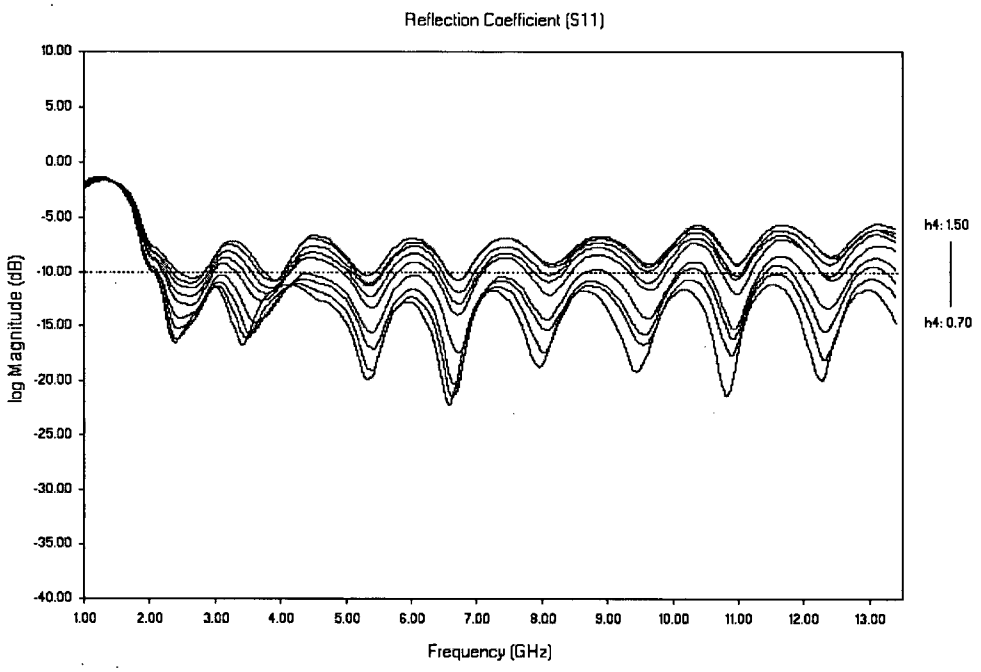

Figure 5.28: FEKO Model FDL S_{11} for h_4=0.70 cm to 1.50 cm (0.10 cm increments)

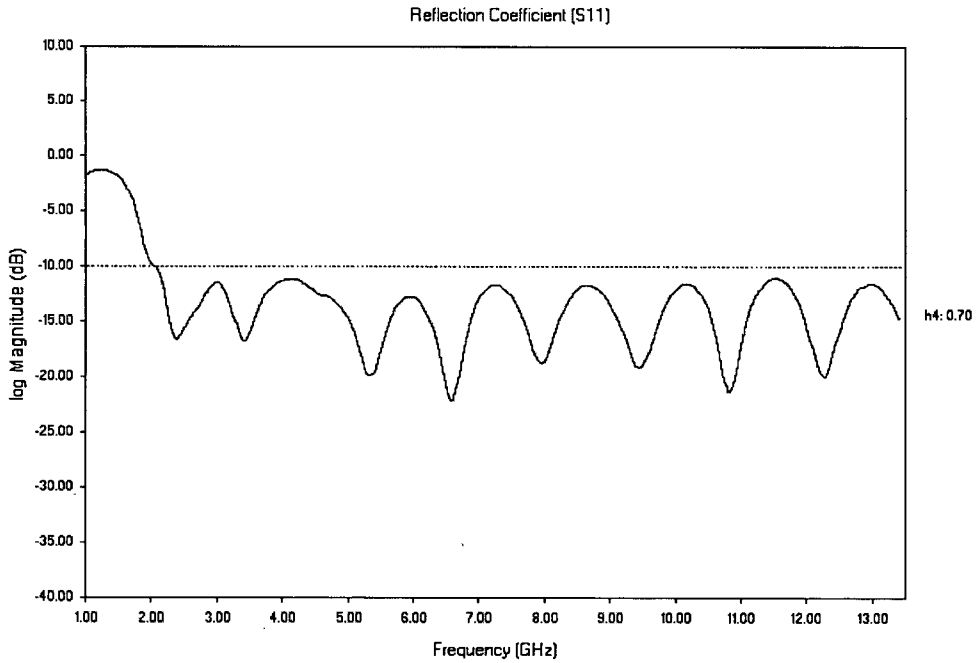

Figure 5.29: FEKO Model FDL S_{11} for h_4=0.70 cm

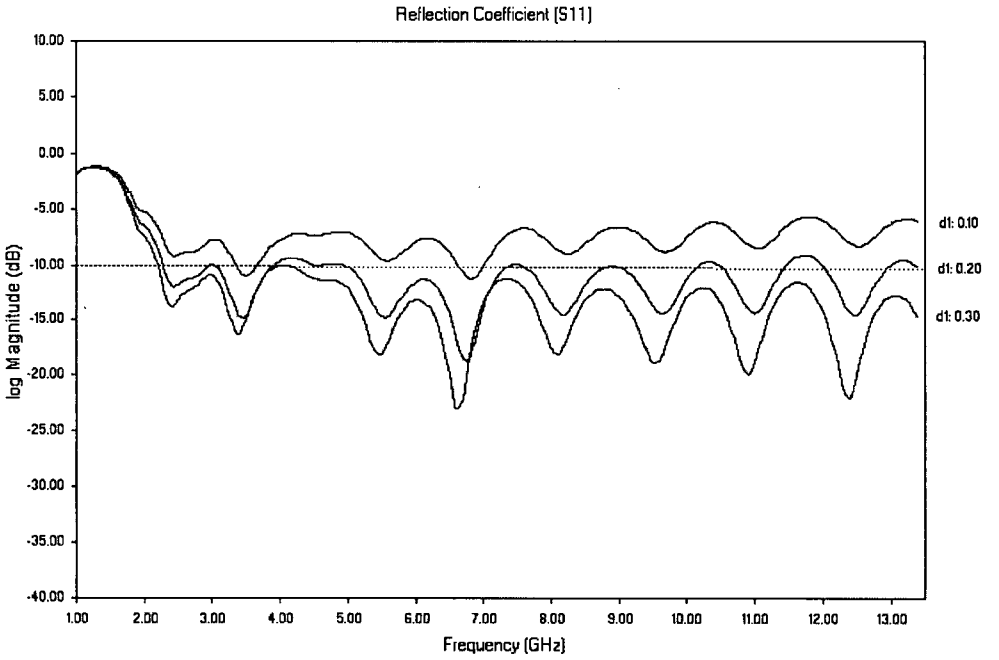

Figure 5.30: FEKO Model FDL S_{11} for d_1=0.10 cm to 0.30 cm (0.10 cm increments)

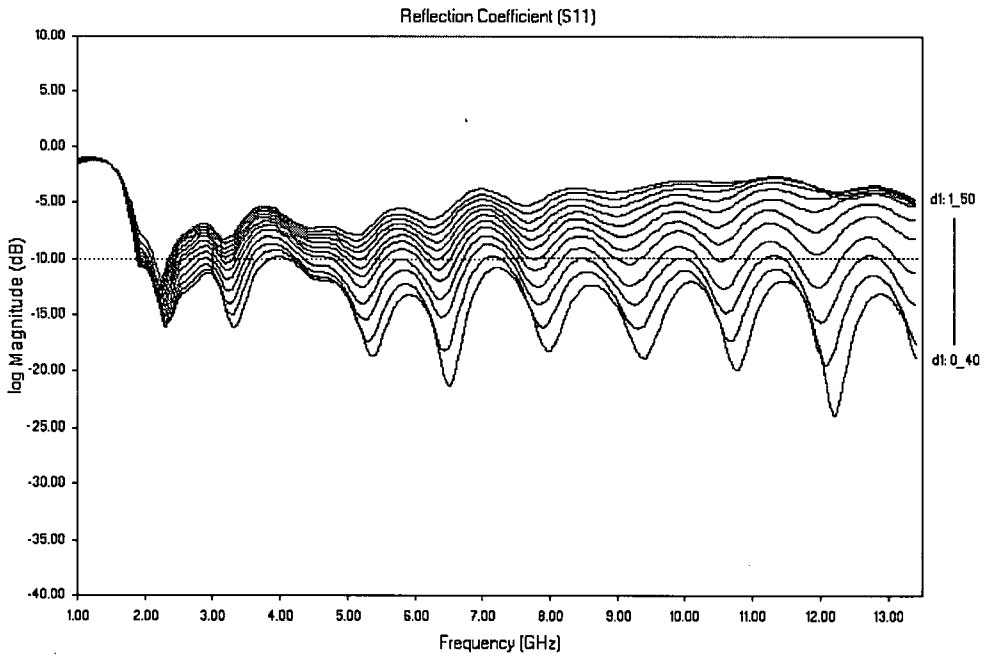

Figure 5.31: FEKO Model FDL S_{11} for d_1=0.40 cm to 1.50 cm (0.10 cm increments)

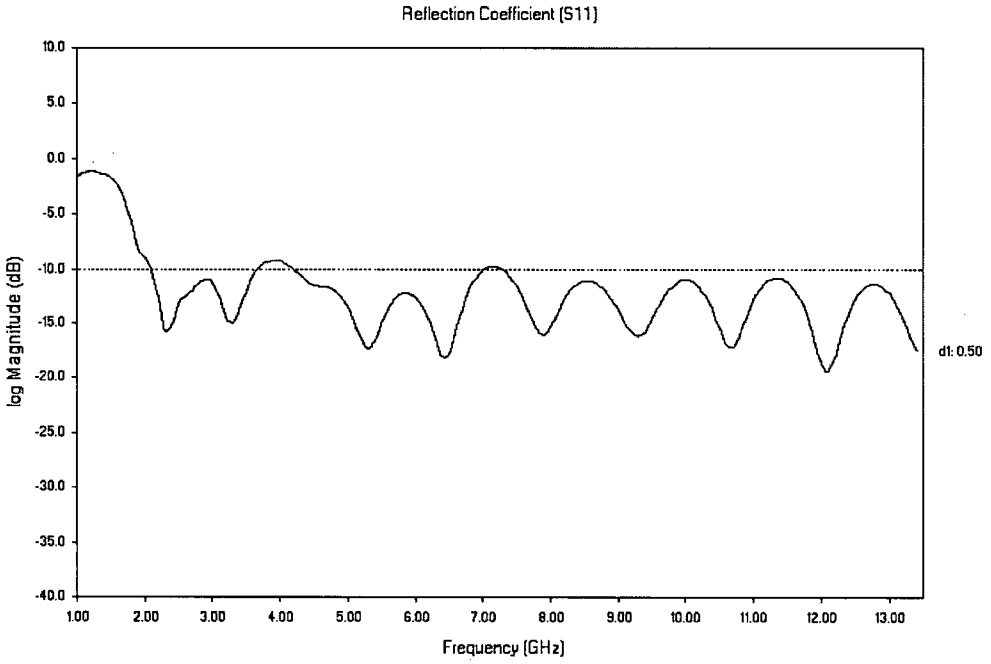

Figure 5.32: FEKO Model FDL S_{11} for d_1=0.50 cm

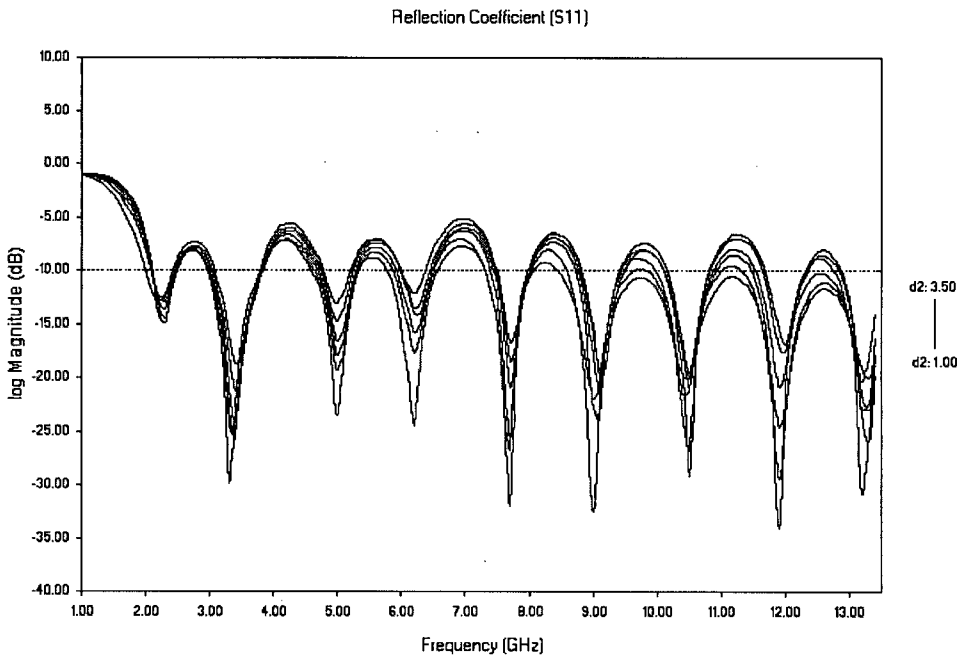

Figure 5.33: FEKO Model FDL S_{11} for d_2=1.00 cm to 3.50 cm (0.50 cm increments)

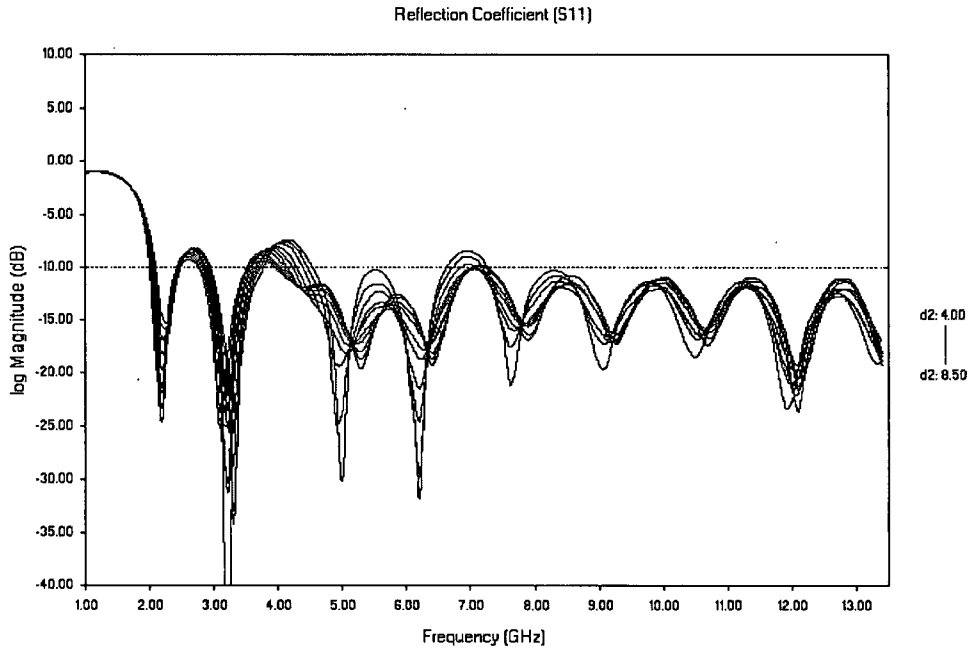

Figure 5.34: FEKO Model FDL S_{11} for d_2=4.00 cm to 8.50 cm (0.50 cm increments)

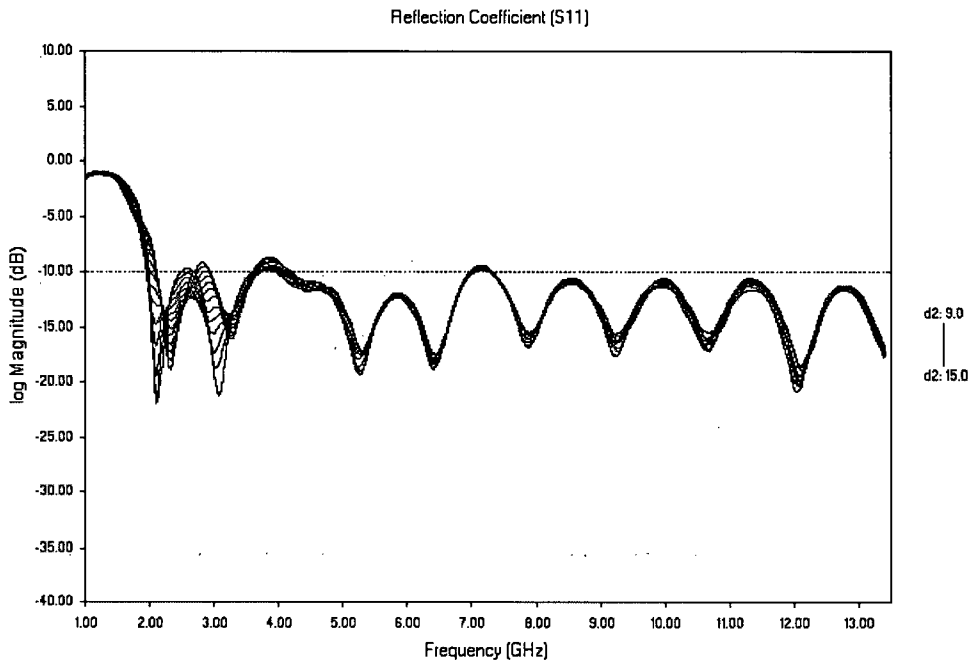

Figure 5.35: FEKO Model FDL S_{11} for d_2=9.00 cm to 15.00 cm (0.50 cm increments)

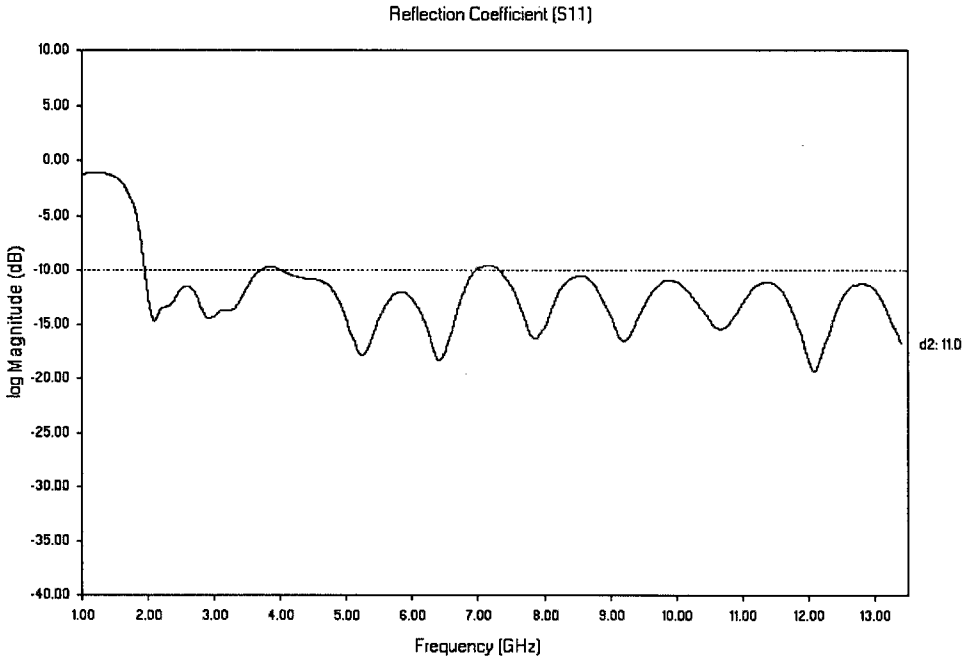

Figure 5.36: FEKO Model FDL S_{11} for d_2=11.00 cm

distributed across the bandwidth. This is the behaviour that the FDL antenna design was intended to produce.

The other parameters do not play as large of overall role in flattening the S_{11} curve. In some cases, L_2, L_3, L_4, h_1 and h_2, there is a single large drop in the S_{11} at one or two frequencies, which would indicate a single resonant mode. In other cases, such as h_3 and L_5, there appears to be little dependence on the parameter, with no resonances appearing. The sensitivity study did show, however, that the overall shape of the antenna is important and that each of the parameters that control the shape of the antenna has a role in flattening the S_{11} return loss curve.

The design for the FDL antenna, which was determined by the FEKO sensitivity study, was: L_1=10 cm, L_2=3.25 cm, L_3=2.50 cm, L_4=1.65 cm, L_5=2.5 cm, h_1=9.0 cm, h_2=0.5 cm, h_3=5.0

cm, h_4=0.7 cm, d_1=0.5 cm, d_2=11.0 cm, with the corresponding S_{11} curve shown in Figure 5.37. This FEKO design corresponds very well to the best FDL design that was constructed and tested in the lab. The design for the best antenna was: L_1=10 cm, L_2=3.3 cm, L_3=2.50 cm, L_4=1.7 cm, L_5=2.4 cm, h_1=8.2 cm, h_2=1.2 cm, h_3=5.0 cm, h_4=0.5 cm, d_1=0.5 cm, d_2=11.0 cm. For the antennas tested in the lab, there was little difference in the measured S_{11} curve for values between d_2=9 cm and d_2=13 cm.

5.2.2 Comparison of FEKO Model Results and S_{11} Measurements

Figure 5.37 shows the S_{11} curve for the FEKO model FDL antenna configuration that corresponds to the actual antenna that produced the maximum bandwidth with the flattest

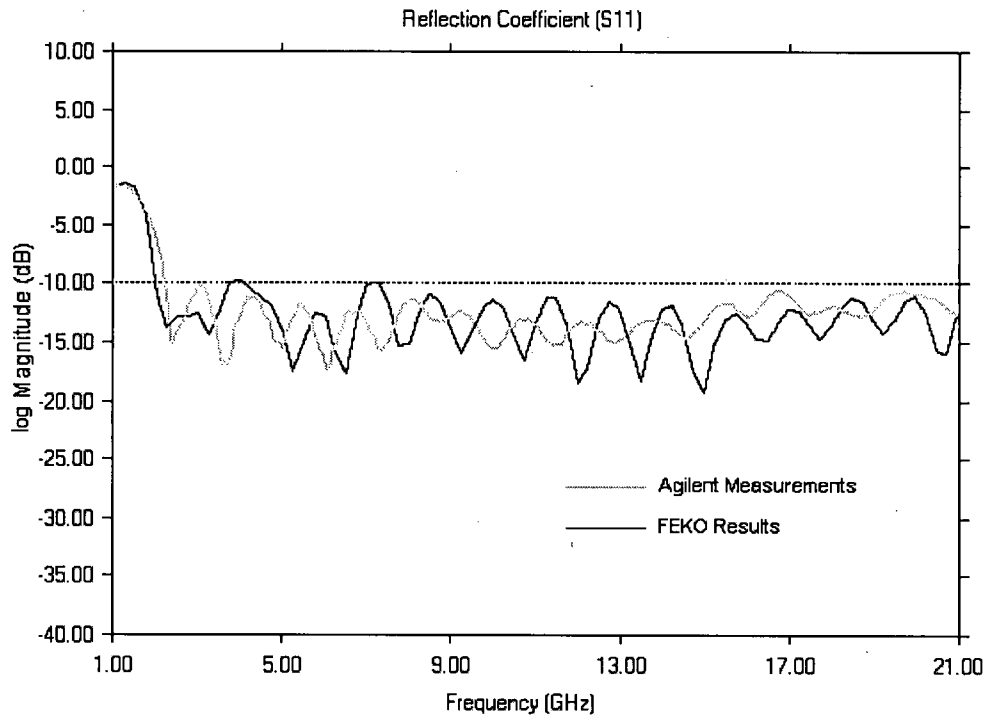

Figure 5.37: Optimal FEKO Model FDL S_{11} Reflection Coefficient

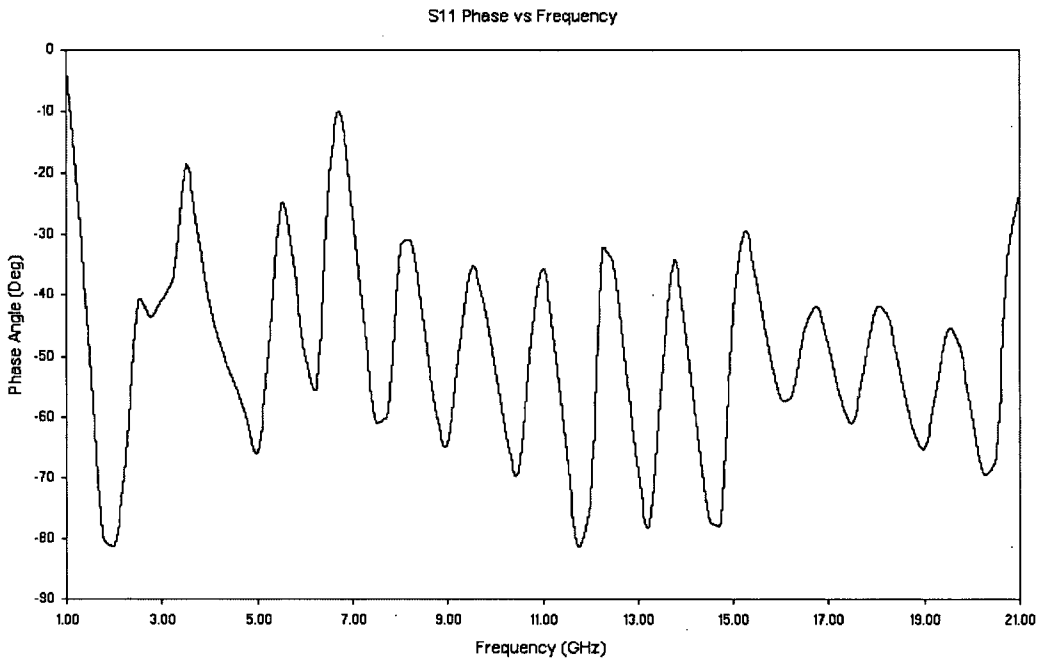

Figure 5.38: FEKO Model FDL S_{11} Reflection Coefficient Phase

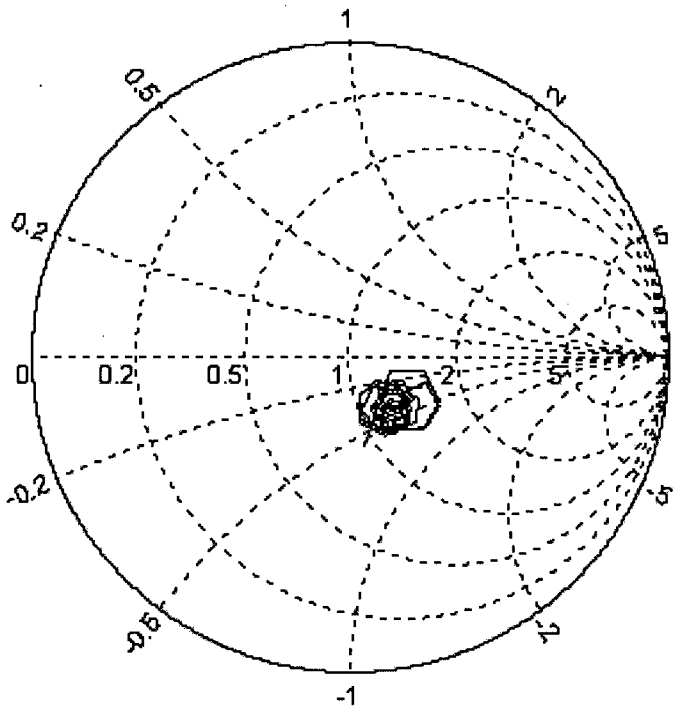

Figure 5.39: FEKO Model FDL S_{11} Smith Chart

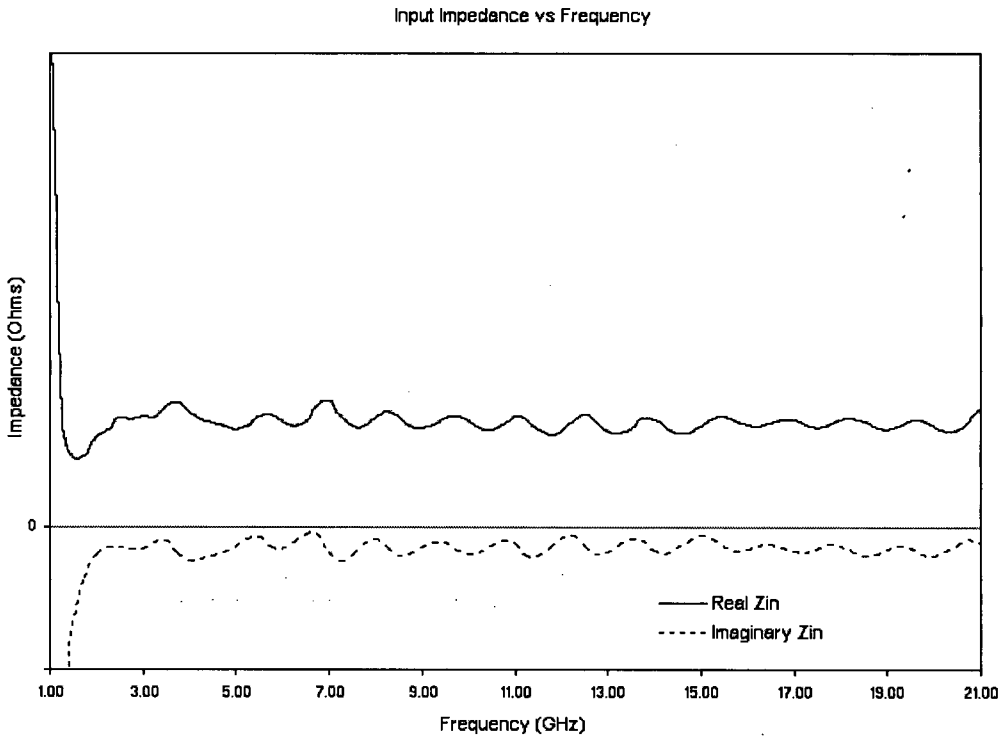

Figure 5.40: FEKO Model FDL Antenna Input Impedance

S_{11} profile. When the S_{11} curve from the FEKO model is compared with the S_{11} curve shown for the actual antenna in Figure 4.7, and also shown in grey on Figure 5.37, it can be seen that FEKO model FDL antenna and the actual antenna both have a flat profile with no sharp spikes in the S_{11} curve. Although the FEKO model FDL antenna also shows an S_{11} below 10 dB across the entire bandwidth from 2.1GHz to 21 GHz, the measured S_{11} profile from the actual antenna is flatter than the FEKO model and slightly further below the - 10 dB level.

Figure 5.38 shows the phase of the S_{11} parameter that oscillates in a narrow range between -10 and -80 degrees. This is also demonstrated in Figure 5.39, which shows the Smith Chart for the antenna and Figure 5.40, which shows the real and imaginary parts of the antenna's

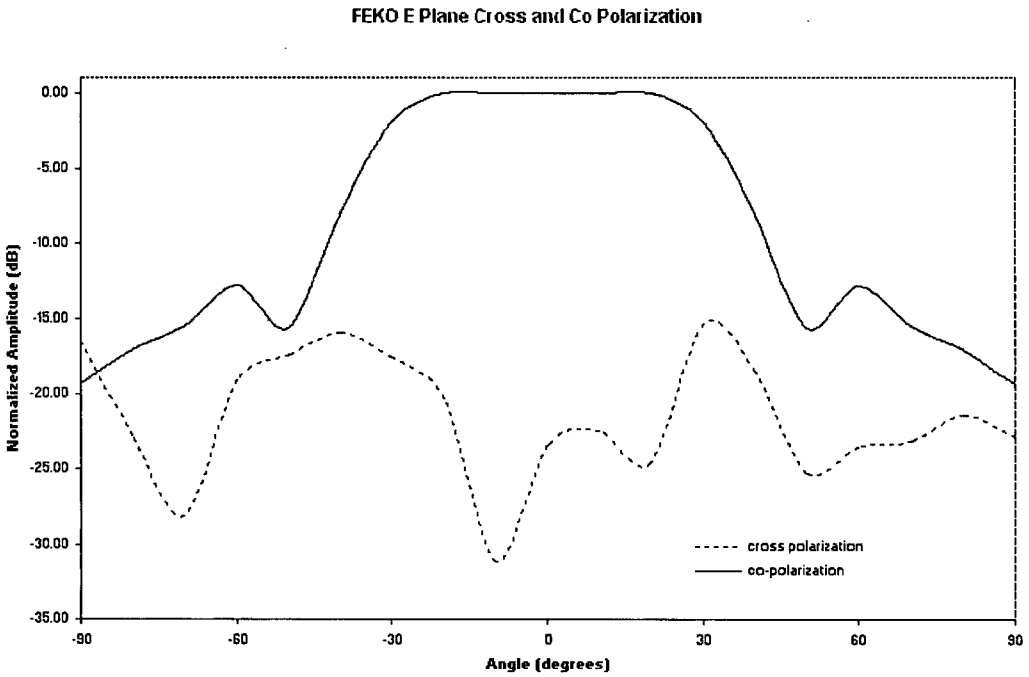

Figure 5.41: E-Plane Cross and Co-Polarization for FEKO Model FDL Antenna

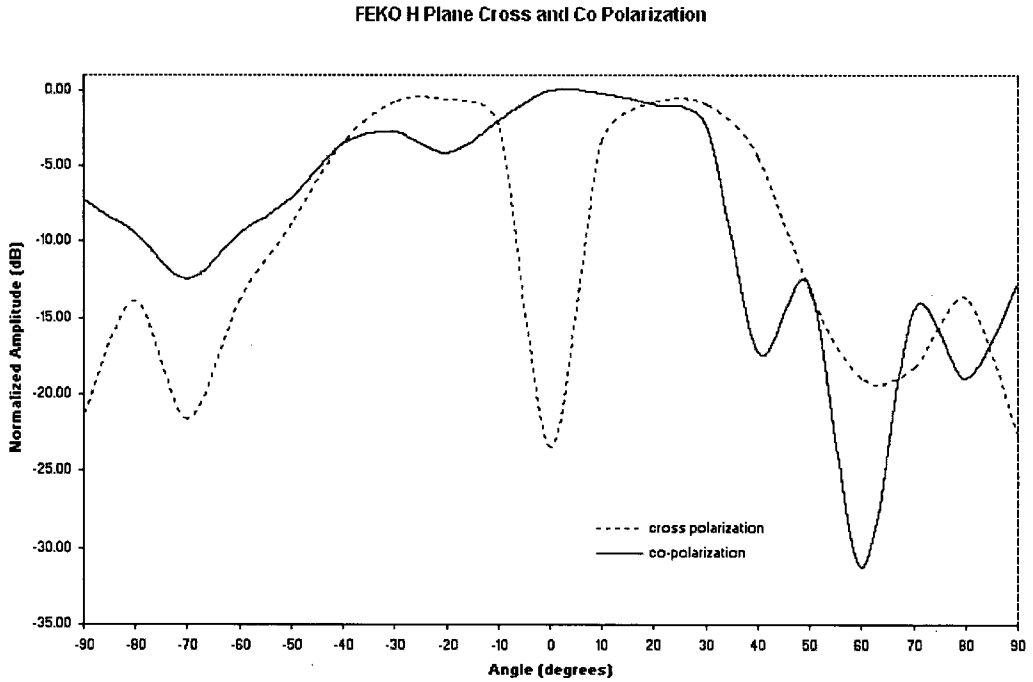

Figure 5.42: H-Plane Cross and Co-Polarization for FEKO Model FDL Antenna

input impedance over the bandwidth. These graphs show that the antenna does perform with constant impedance over the ultra-wide bandwidth from about 2 to 21 GHz.

5.3 FEKO Model Cross and Co-Polarization

Figures 5.41 and 5.42 show the cross- and co-polarization for the E and H-planes for the FEKO model FDL antenna with 9 cm flare. A comparison of these graphs with those shown in Figures 4.27 and 4.28 show that the relative magnitudes between cross- and co-polarizations for the model are very similar to those for the actual antennas. The model cross- and co-polarization graphs also show the same relative shapes as the actual antenna cross- and co-polarization graphs.

To calculate the cross- and co-polarization values, FEKO uses one model to describe both the transmitting and receiving antennas. As described earlier, the second antenna is created by rotating and repositioning a copy of the first antenna in FEKO's model space. In contrast, the experimental measurements for the actual antennas were performed using two different physical antennas. Although the two physical antennas were fabricated at the same time, differences in their flare profiles, due to the fact that the flares were bent by hand, means that, unlike the model antennas, the physical antennas are not identical to each other. An attempt was made to have the flares machine bent, but there was no equipment available that could perform the required task. In future, for mass production, the antennas could be machined using a tool and die process, but the cost for this was too prohibitive for prototyping.

In addition, as the values for the FEKO antennas are calculated in infinite space, conditions similar to those surrounding the physical test site are not replicated for the FEKO models. The site for the physical antenna measurements was located on the roof of a building, where the antennas under test are located approximately 2 metres above the roofing surface. One

of the antennas is mounted directly on the side of the roof's penthouse; the other is mounted on a movable dolly with a fibreglass mast. Although this arrangement gives reasonable results, the environment is not identical to the infinite space model that is used by FEKO. Also, in addition to the difference in physical surroundings, the FEKO models are not affected by gravity, whereas the spacing between the active member and the ground planes varies somewhat for the actual antennas as they are rotated in the E- and H-planes while performing the measurements.

Some of the resulting differences in the graphs between the models and the actual antenna are likely due to these differences between the model's configuration and the antenna's construction.

5.4 FEKO Model Far Field

Figures 5.43 through 5.47 show the far field lines of constant magnitude for the E- and H-planes as well as the total field for 3, 6, 9, 12 and 15 GHz. The FEKO software was limited to a maximum of 15GHz (above this frequency the model and analysis data would not fit into the existing program memory and a program error was generated). The graphs show that as the frequency increases the antenna remains roughly endfire with 2 frontal lobes. The number of side lobes tends to increase as the frequency increases, but the overall shape of the field does not change that greatly from 3 to 15 GHz, which suggests that the performance of systems using this type of antenna should remain consistent over this range. These radiation patterns are also similar to those for Vivaldi-type antennas [78].

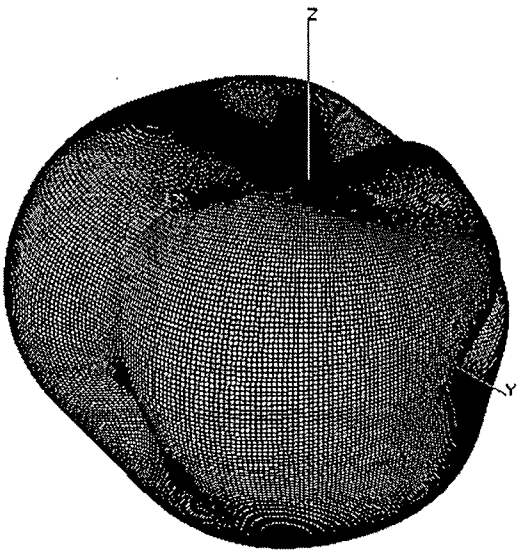

(a)

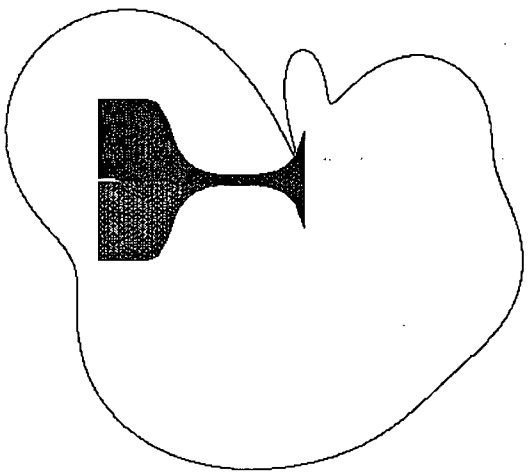

(b)

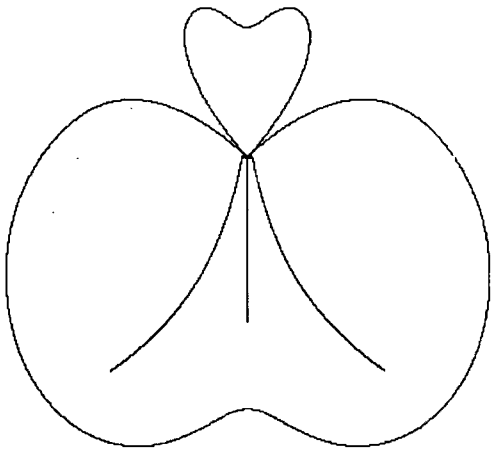

(c)

Figure 5.43: Radiation Pattern at 3 GHz (a) Total (b) E-plane (c) H-plane

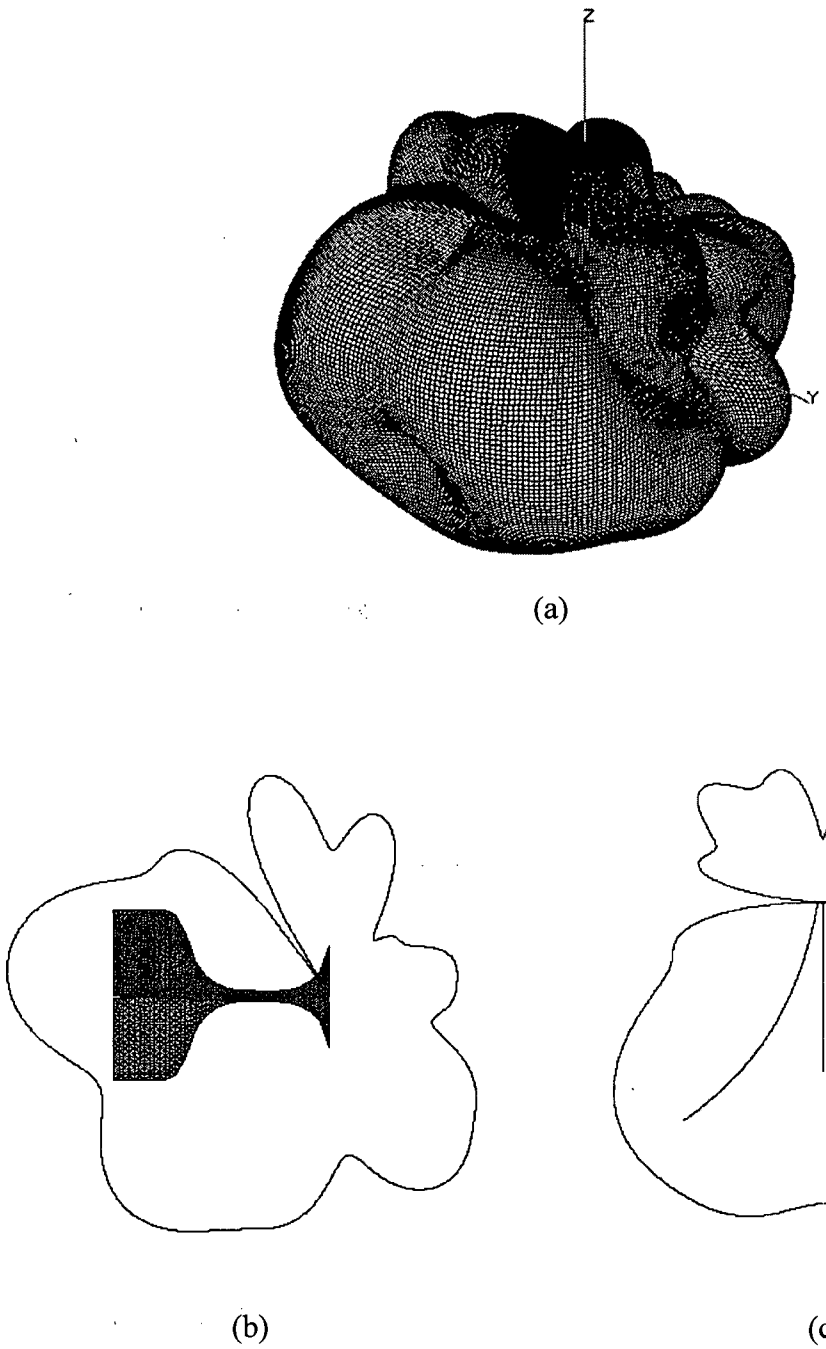

(a)

(b)

(c)

Figure 5.44: Radiation Pattern at 6 GHz (a) Total (b) E-plane (c) H-plane

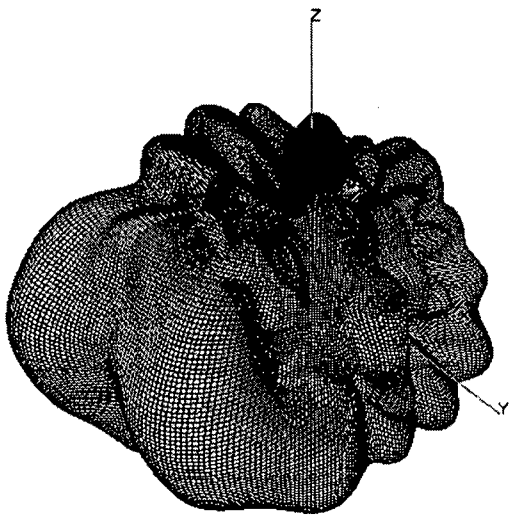

(a)

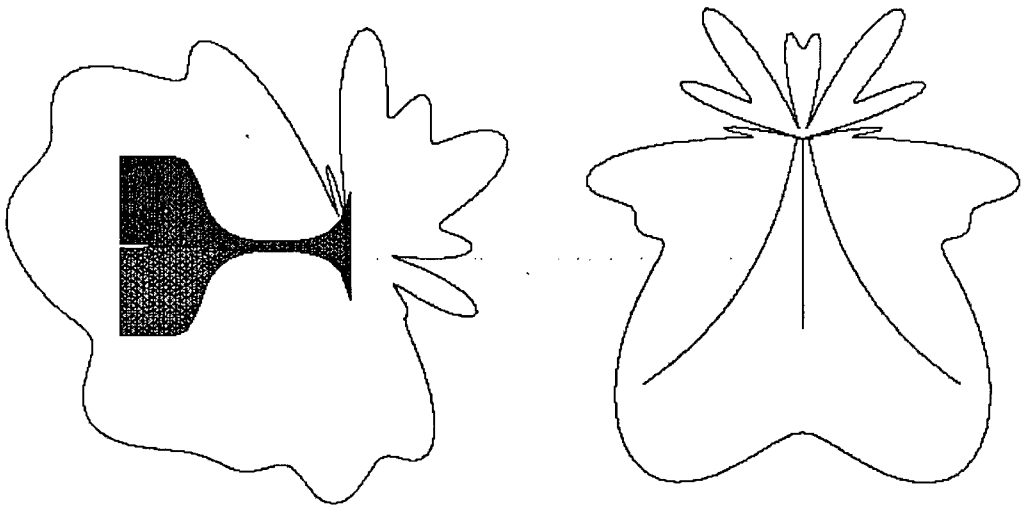

(b) (c)

Figure 5.45: Radiation Pattern at 9 GHz (a) Total (b) E-plane (c) H-plane

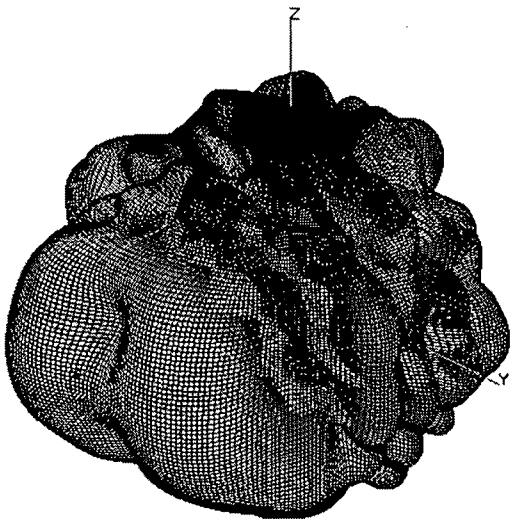

(a)

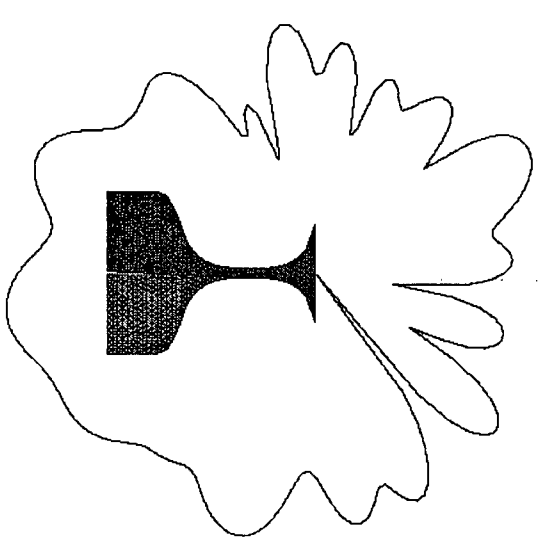

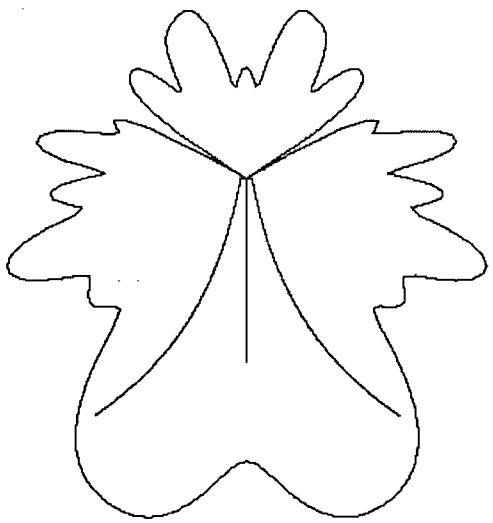

(b) (c)

Figure 5.46: Radiation Pattern at 12 GHz (a) Total (b) E-plane (c) H-plane

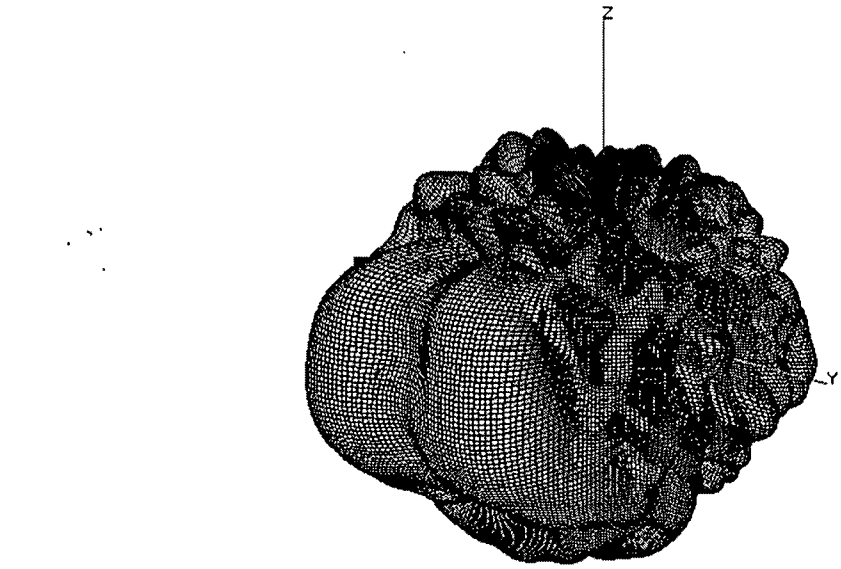

(a)

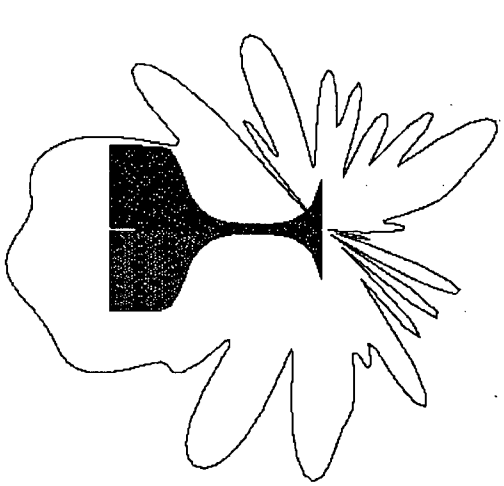

(b)

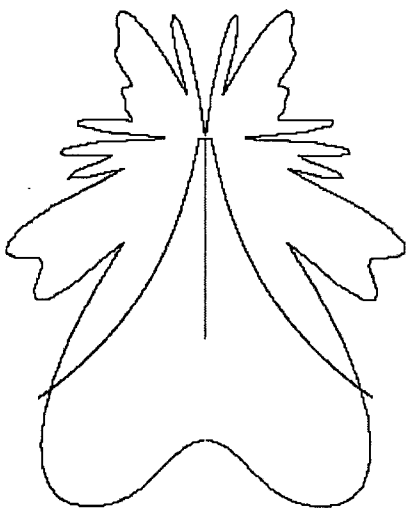

(c)

Figure 5.47: Radiation Pattern at 15 GHz (a) Total (b) E-plane (c) H-plane

Chapter 6

6.0 FDL Ultra-Wideband Scanner

6.1 Scanner Design

The proposal for this thesis, is to detect voids in wooden objects, such as trees or telephone poles, by transmitting rf signals through an object and measuring the received signals. These signals are then used to determine if enough information is present in the received signals to determine the location of the voids.

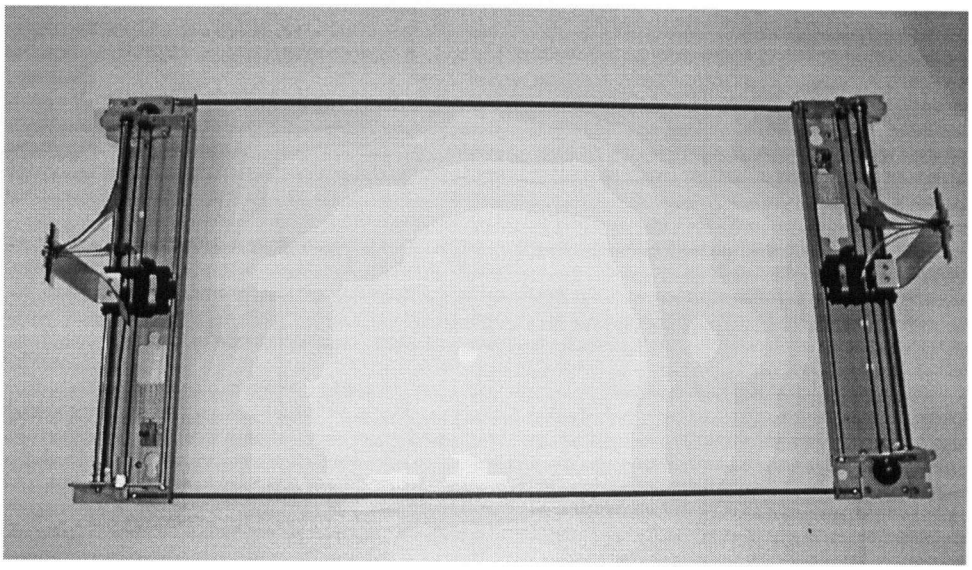

Figure 6.1: Prototype FDL Scanner System

To accomplish this, a prototype scanner, shown in Figure 6.1, was constructed. The scanner consisted of two FDL antennas mounted upon brackets, one for transmitting, the other for receiving at either end of the scanner. The two ends of the scanner were held together by a pair of solid rods that were used to maintain a fixed distance between the antennas and to ensure

that the antennas remain properly aligned. The distance between the antennas can be adjusted by replacing the separating rods with rods of varying length. At each end of the scanner the mounting brackets were affixed to a dot matrix printer carriage. The carriages were removed from a pair of Roland PR-1215 dot matrix printers, which gave the scanner a span of 14.75 inches (which corresponds to 1775 steps for the stepper motor drivers). This arrangement works out to approximately 120 steps/inch or a horizontal resolution of 0.00833 inches. Although the resolution is far greater than needed for scanning, the positioning of the antennas between test runs was critical, and the use of the printer mechanisms allowed for the accurate repositioning required.

The driving circuit for the stepper motors was constructed from components taken from the original printer drivers with the addition of a PIC 16C73B microcontroller. The scanner was controlled via the serial port of a standard MS Windows-based laptop. The magnitude and phase readings for the received S_{21} signal were recorded using a Wiltron 37225A Vector Network Analyser, which was controlled from the same laptop via a GPIB interface. Once the scanner and the analyser were connected to the laptop, the scanner operation and data recording were completely controlled and fully automated by the laptop.

6.2 Scanner Characterization

Since the scanner employed a pair of FDL antennas, rather than a single FDL antenna, some additional work was required to characterize the antennas within the scanner configuration. The following sections describe the results of this characterization.

6.2.1 Phase versus Distance Measurements

Although, as stated earlier, every attempt was made to manufacture two identical antennas, due to the exponential curvature of the FDL ground planes it was necessary to bend the ground planes by hand. Even for a single FDL antenna, the right side ground plane curve and the angle between the ground plane and the active member were not identical to those of the left side ground plane. Part of the characterization process for the scanner involved determining the shape of the wave front at the receiver and the zero phase alignment in the horizontal direction for the wave [80]. To accomplish this, four sets of measurements were taken. The first set of readings was taken between two known antenna horns to determine if the alignment of the scanner was correct. The second and third sets of readings were taken to determine if there was any phase offset between the alignment for the horn antennas and the alignment of a single horn antenna and a single FDL antenna. The fourth set of readings was used to check the alignment of the two FDL antennas when used as a transmitter/receiver pair.

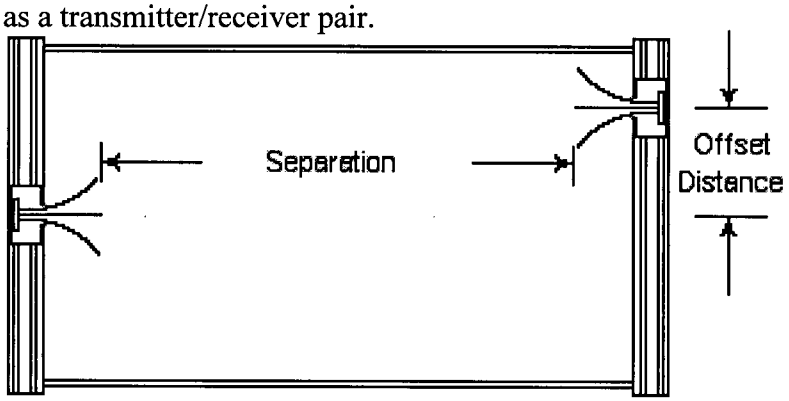

Figure 6.2: Alignment of Antennas in Prototype FDL Scanner

For each set of measurements, the antennas were first centred in the middle of their

horizontal range. The relative phase measurement between the two antennas was adjusted so that the angle was 0 degrees. The receiving antenna was then stepped horizontally along its range, and the phase was measured at a number of positions relative to the zero phase angle alignment. For planar wavefronts, in the far field of the antennas, if the transmitting and receiving antennas were perfectly aligned for the zero phase angle measurement, moving either one of the antennas from this position should have caused the phase angle measurement between the antennas to decrease. If the antennas were not aligned when the zero phase angle measurement was taken, then moving the antennas away from this position in one direction or the other would have resulted in an increase in the phase angle until the antennas were aligned. Once the alignment point had been reached, any further movement would have again resulted in a decrease of the measured phase angle.

The results for the four sets of measurements are shown in Figures 6.3 to 6.6. Figure 6.3 shows the phase versus horizontal offset for the two horn antennas. It shows that the alignment for the two horn antennas was correct. The minimum phase angle between the two antennas occurs at an offset distance of zero. This means that the transmitting and receiving horn antennas at either end of the scanner were correctly aligned for zero offset. This could only have occurred if the overall geometry of the scanner was correct.

Figure 6.4 shows the results of the Phase Angle versus Offset Distance measurements for transmission from a standard Horn to the first of two FDL antennas designated VH2A. The peak of the phase curve was at an offset of 5 mm from the zero phase alignment for the horn to horn transmission. With the 1288 mm separation between the antennas, this offset distance corresponded to an offset angle of approximately 0.22 degrees.

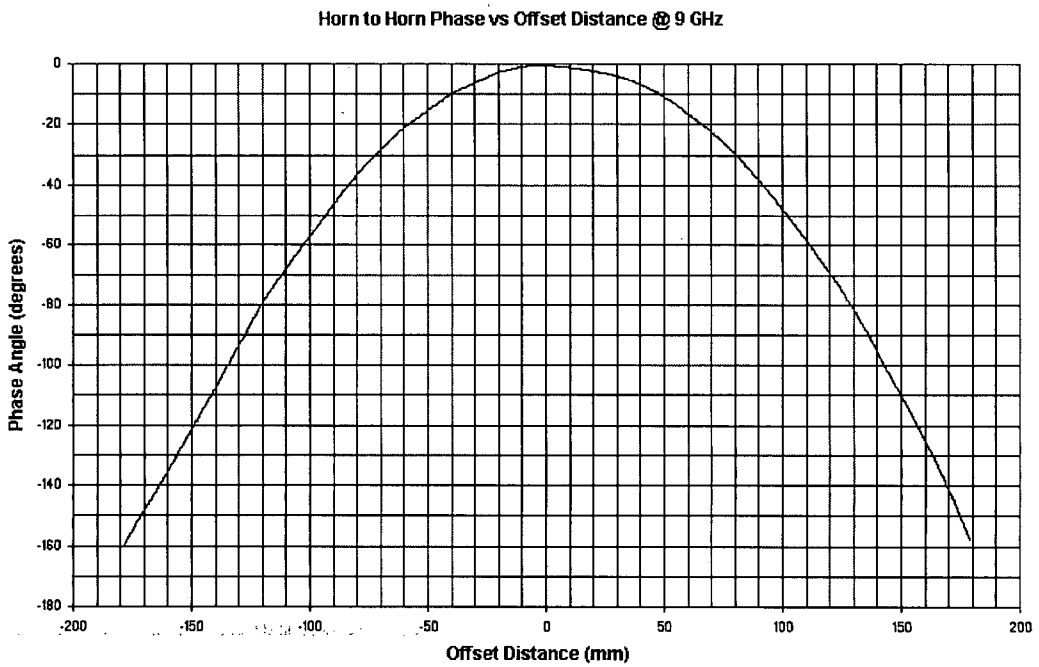

Figure 6.3: Phase Angle vs. Offset Distance For Horn to Horn

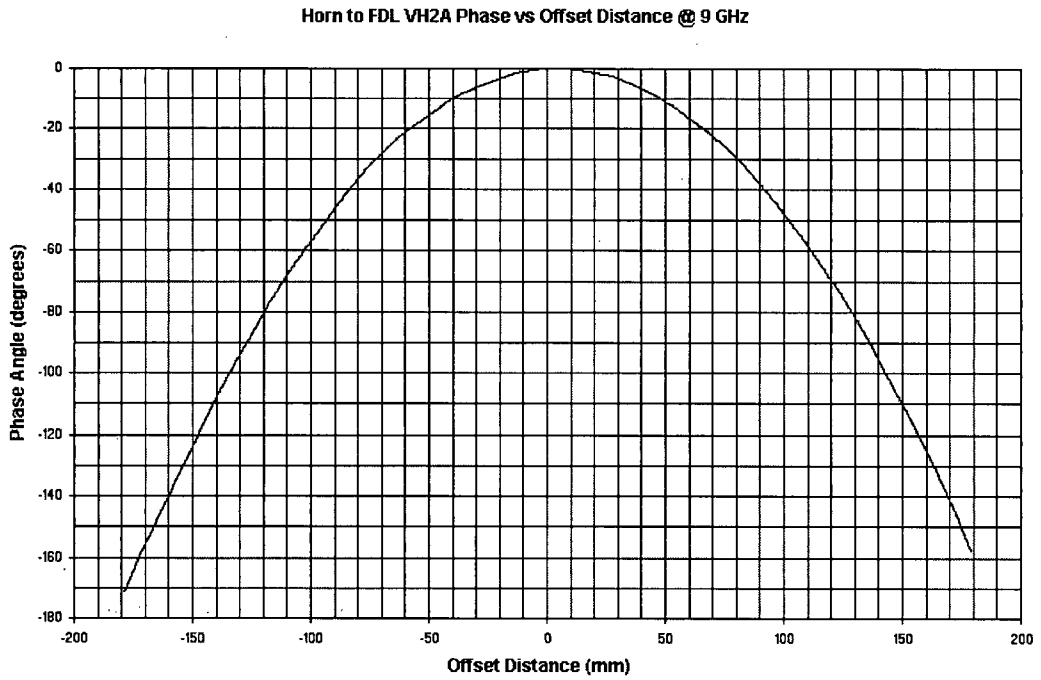

Figure 6.4: Phase Angle vs. Offset Distance For Horn to FDL VH2A

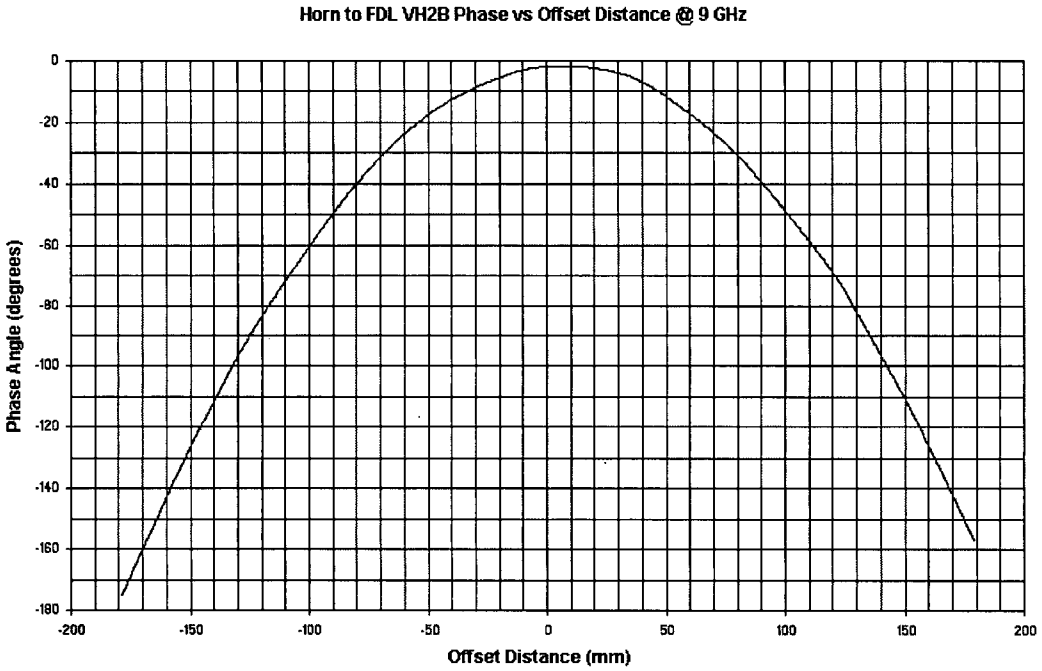

Figure 6.5: Phase Angle vs. Offset Distance For Horn to FDL VH2B

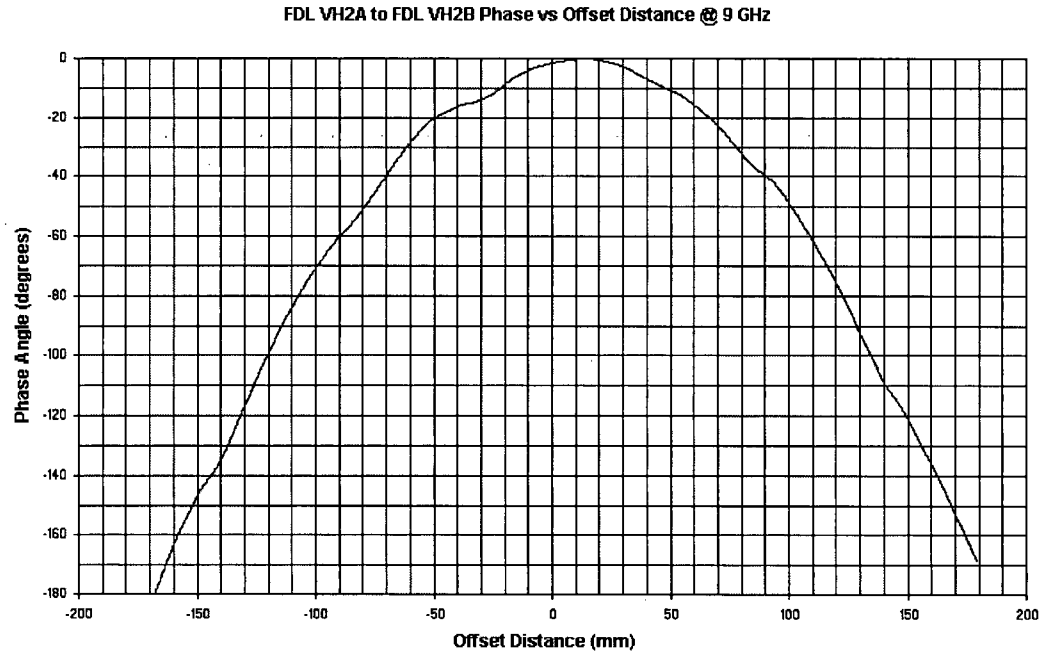

Figure 6.6: Phase Angle vs. Offset Distance For FDL VH2A to FDL VH2B

Figure 6.5 shows the results of the Phase Angle vs. Offset Distance measurements for transmission from a standard horn to the second of the two FDL antennas designated VH2B. This antenna showed the peak in the phase curve to be at an 8 mm offset from the horn to horn transmission, with a resulting offset angle of approximately 0.36 degrees.

Figure 6.6 shows the results of the Phase Angle vs. Offset Distance measurements for transmission from FDL antenna VH2A to FDL antenna VH2B. The phase peak for this pair occurred at an offset of 13 mm, which corresponds to an offset angle of 0.58 degrees. Since the measured offsets were very small, the total offset distance and angles for the FDL to FDL transmission are, as expected, equal to the sum of the offsets for the individual horn to FDL transmissions. The size of the relative offsets were very small, corresponding to 61 steps for the driving motor and belt, and could be corrected if required. For this project, an offset of the two antennas was actually desirable. If the antennas were perfectly aligned, if the fields between the two antennas were perfectly symmetrical and if the wooden model under test was completely homogeneous in its make up, then by reason of symmetry, the received spectra created by two different voids located symmetrically on opposite sides of the wooden model's central axis would be identical. If this were true we would lose the ability to uniquely determine the presence of the void. Ensuring that the antennas were not aligned means that the symmetry was eliminated.

6.2.2 Far Field Considerations

To ensure that the scanner would be free from any near field effects, it was necessary to determine the antenna's separation. In the far field the angular distribution of power is independent of the distance (i.e., the wavefront is planar) [32]. Typically, this distance is determined by the formula [80]

$$r = \frac{2D^2}{\lambda} \tag{6.1}$$

where

D is the maximum linear dimension of the antenna

λ is the operating wavelength.

Although the FDL antennas that were used with the scanner were capable of transmitting beyond 13.5 GHz, this was the maximum frequency of interest since this was the maximum frequency of the Wiltron Vector Analyser used for taking measurements. While we did not use all of the bandwidth of the antenna, the performance of the FDL antenna over this smaller range was still an improvement over existing antennas in terms of the flatter S_{11} curve and signal distortion. A frequency of 13.5 GHz corresponds to a λ of approximately 2.22 cm. The maximum dimension of the antenna is 10.2 cm, which gives the far field distance as

$$r = \frac{2 \cdot (10.2\,cm)^2}{2.22\,cm} \approx 94\,cm \qquad (6.2)$$

Therefore, to avoid possible near field effects, the transmit and receive antennas for the scanners needed to be located 2 metres apart so that the wooden models were placed in the far fields of both antennas.

6.2.3 Diffraction Effects

As well as determining the alignment and separation of the antennas, the scanner characterization had to take into account the effect of multiple signal paths due to diffraction over the top and bottom ends of a test model and reflection from surrounding objects.

Chapter 6 - Ultra-Wideband Scanner

To test for diffraction effects, a series of test models ranging in height from 1 inch (2.54 cm) to 36 inches (91 cm) were placed between the scanner antennas. The received spectrum between 1 GHZ and 13.5 GHz was recorded for each model. Figure 6.7 shows the results for models with heights of 69 cm, 76 cm and 84 cm. As the model height increases, the curves get closer and closer in profile. For model heights greater than 69 cm, there is almost no discernable difference between the curves, as is shown in the figure by the overlapping curves. This means that the minimum height of a model must be at least 69 cm to ensure that the height of the model was sufficient to avoid the effects of diffraction around the ends of the model.

To minimize reflections from surrounding objects, the testing and calibration of the scanner and the recording of model data were performed in appropriate locations. The scanner was positioned in an area where the nearest objects were located at a distance of at least 3 or more times the largest dimension of the scanner. The only object close enough to cause reflections was the table upon which the scanner was mounted. To test for a problem with reflections from the table, the scanner was placed on top of a large sheet of aluminum that extended past the outer dimensions of the scanner to provide a reflective surface beneath the scanner. The test with models of varying heights was repeated with the metal sheet in place.

Figure 6.8 shows the results for models with heights of 69 cm, 76 cm and 84 cm with the metal sheet in place. As for the measurements taken without the metal sheet, the measurements taken with the metal sheet showed the same height dependency. The spectral curves merged for model heights greater than 69 cm, again indicating that the minimum height of a model needed to be 69 cm or more to avoid diffraction effects.

The complete results for all models between 0 cm and 91 cm, as well as the calibration spectrum with no model between the antennas, appear in Appendix C.

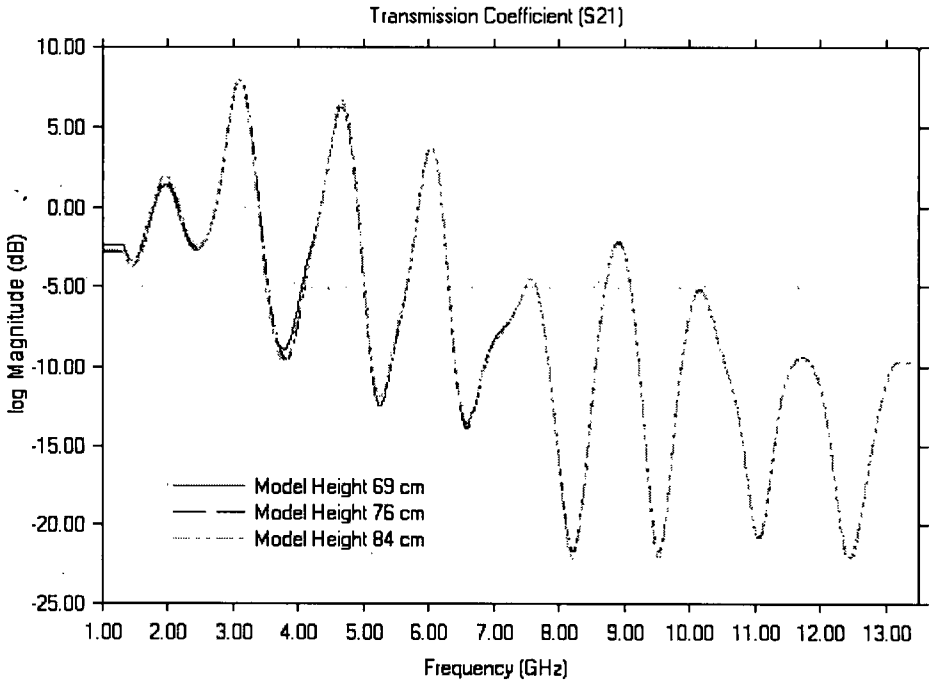

Figure 6.7: Transmission Coefficient S_{21} versus Model Height

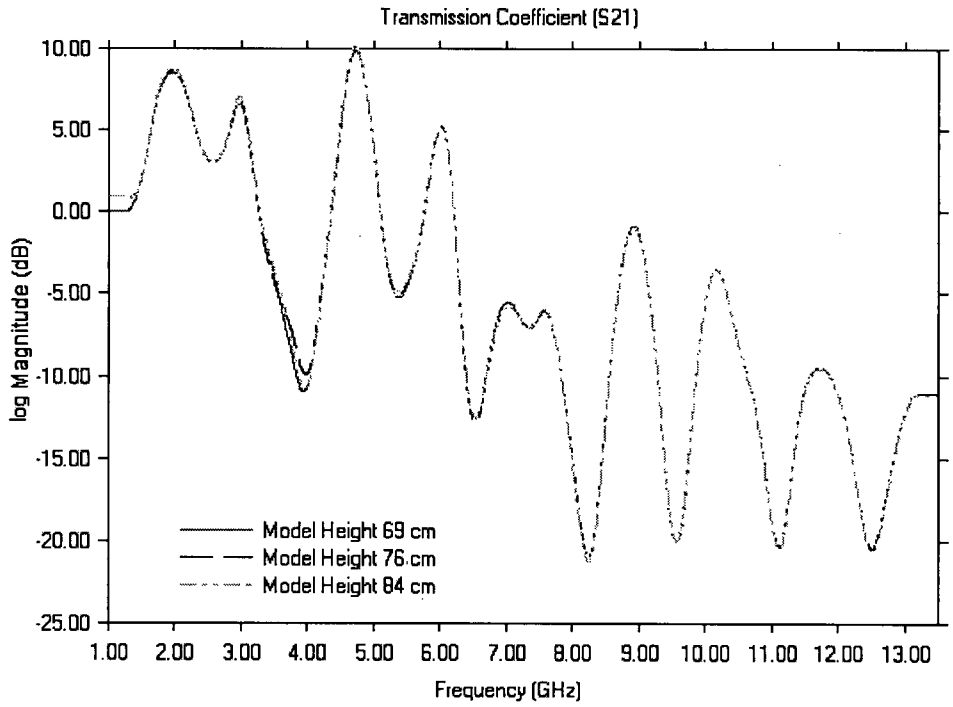

Figure 6.8: Transmission Coefficient S_{21} versus Model Height (reflective metal sheet)

Chapter 7

7.0 Void Detection

As stated at the beginning of Chapter 6, the objective of building the scanner was to determine the location of voids in wooden objects using ultra-wideband rf signals. Rather than using a standard tomographic approach, which requires too much time and precision for a cost effective industrial process [14, 17, 24], a pattern-matching algorithm was used to match the spectral curves from unknown samples to those from a set of previously recorded baseline spectra.

7.1 Detection of Voids

To determine if it is possible to detect voids inside a wooden cylinder using the FDL scanner, a simplified model was constructed from standard commercial 2x4 graded lumber. The model shown in Figure 7.1 consists of 20 lengths of kiln-dried fir 2x4 (SPF 1 grade) measuring 80 cm in length. This length was chosen to eliminate any diffraction effects, as previously discussed in section 6.2.3.

Each length of 2x4 was stood on end next to the others to form the roughly cylindrical shape shown. Each individual position in the models was labelled A to T to track which piece of the model was currently removed so that the model could be disassembled and reassembled. The figure shows the model in its normal position, but the model could also be rotated around its centre axis if needed. This model is referred to in this chapter as Model M_1 and element A from model M_1 is referred to as M_{1A}, element B M_{1B} and so on. A second model, called M_2, was also constructed from similar lengths of kiln-dried fir 2x4 to be used as our unknown sample model.

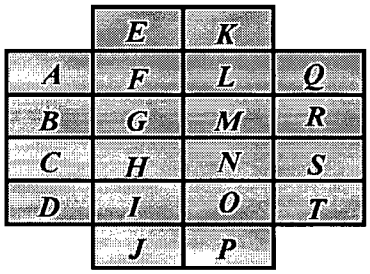

Figure 7.1: Diagram of Wooden Model showing Element Designation and Location

7.1.1 Model Analysis

An analysis of the wooden model using the FDL scanner was performed by placing the model between the two FDL scanner antennas, as shown in Figure 7.2 .

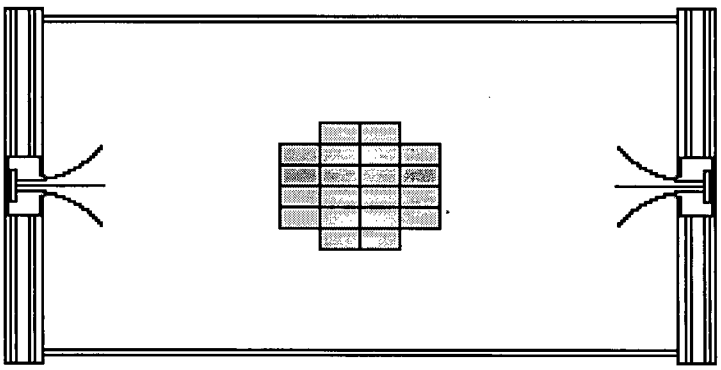

Figure 7.2: FDL Scanner with Model

Chapter 7 - Void Detection

Port 1 of the Wiltron Vector Analyser was then connected to the FDL antenna VH2B to be used as the signal transmitter. The FDL antenna V2HA was then connected to Port 2 of the Wiltron Analyser via a Cougar A2CP12029 wideband amplifier (see specifications in Appendix D) as shown in Figure 7.3. The wooden test model was placed at the midpoint between the scanner antennas, and the resulting S_{21} transmission spectrum was recorded using the Wiltron Analyser in a range from 1 GHz to 13.5 GHz. The S_{21}spectrum was first recorded for the basic model with all elements in place and then for the model with each one of its elements individually removed to determine the baseline spectral curves. The model was then rotated by 90 degrees and the measurements were repeated. This allowed the FDL Scanner system to record a large number of spectra, which could be used later for comparisons. In all, a combined total of 389 different spectra from models M_1 and M_2 were recorded for analysis. The scanning was automated via a Pentium III laptop running Win2K connected to the Analyser via the GPIB input.

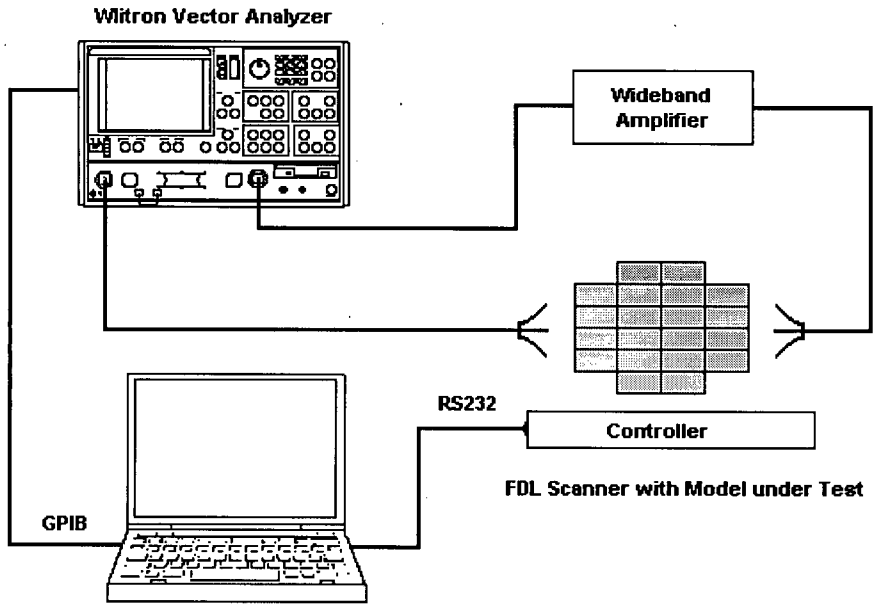

Figure 7.3: FDL Scanner with Wiltron Vector Analyser and Wideband Amplifier

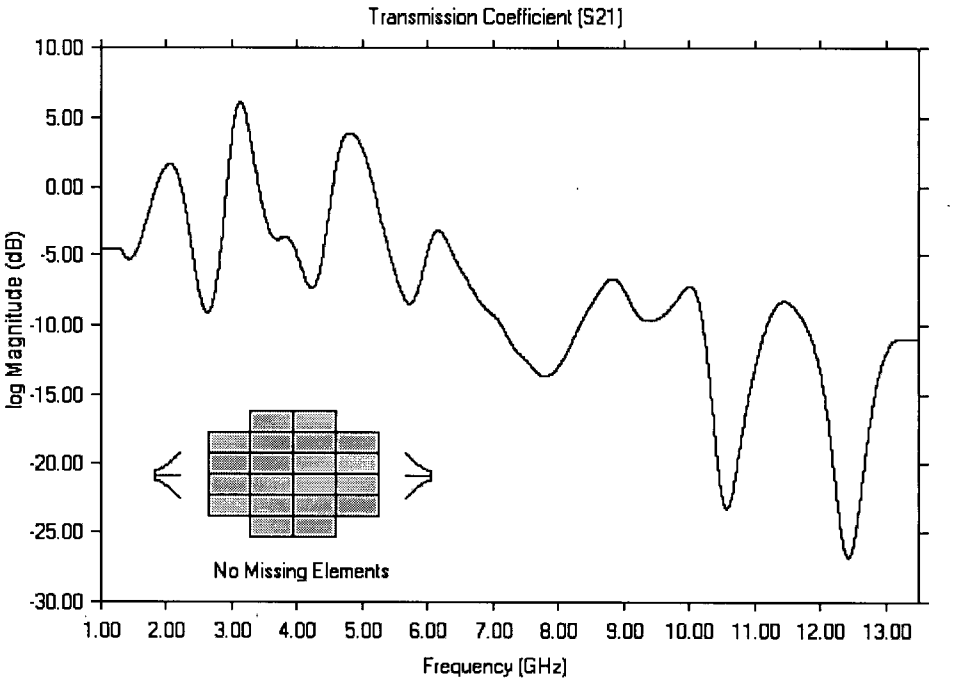

Figure 7.4: Spectral Curve from Intact Model M_1

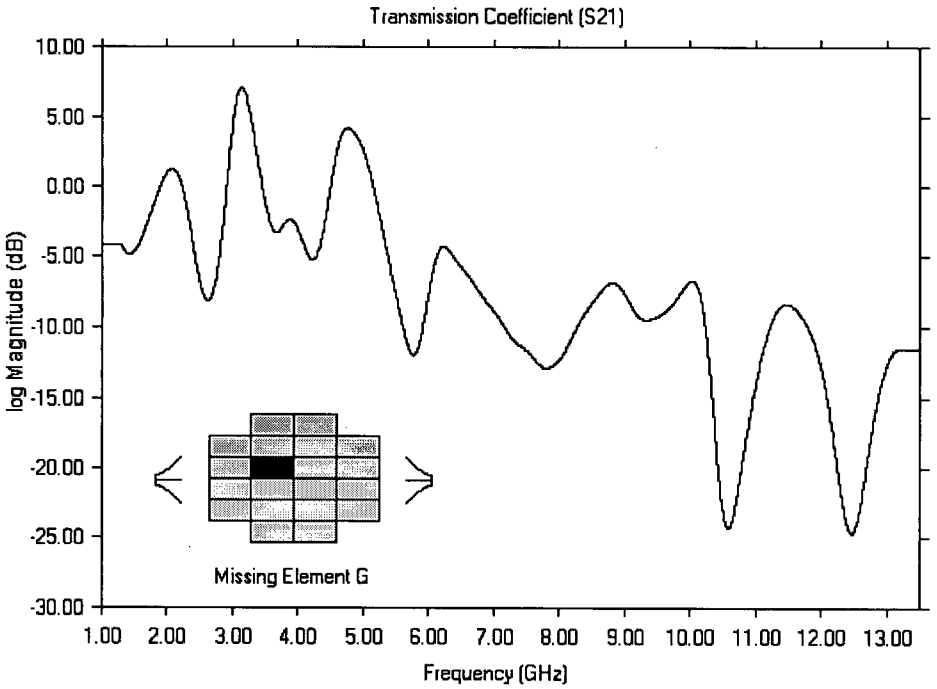

Figure 7.5: Spectral Curve from M_{1G}

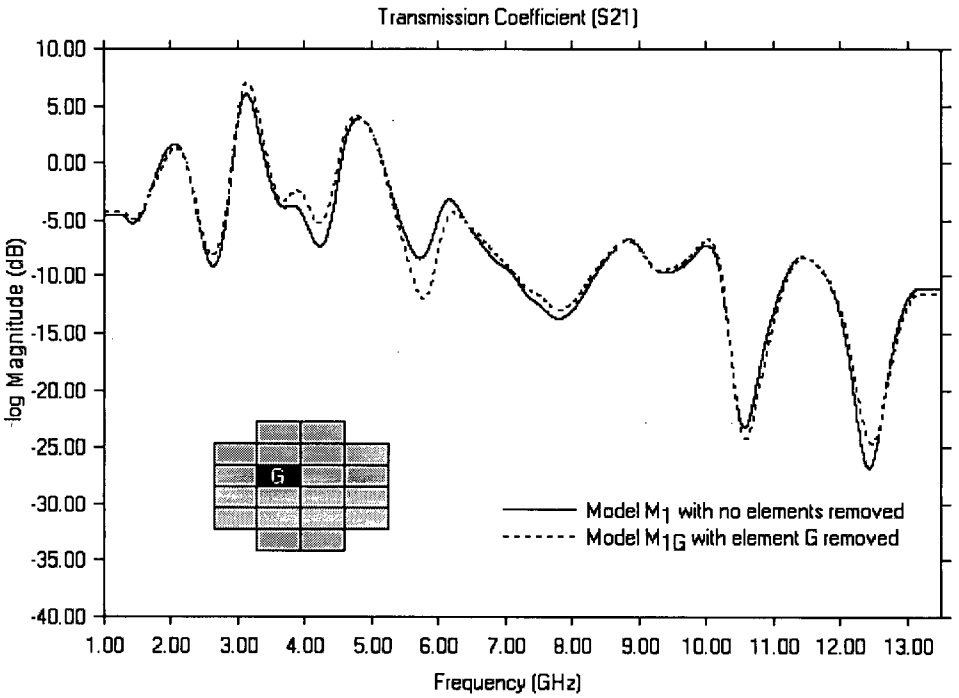

Figure 7.6: Spectral Curve Difference between M_1 and M_{1G}.

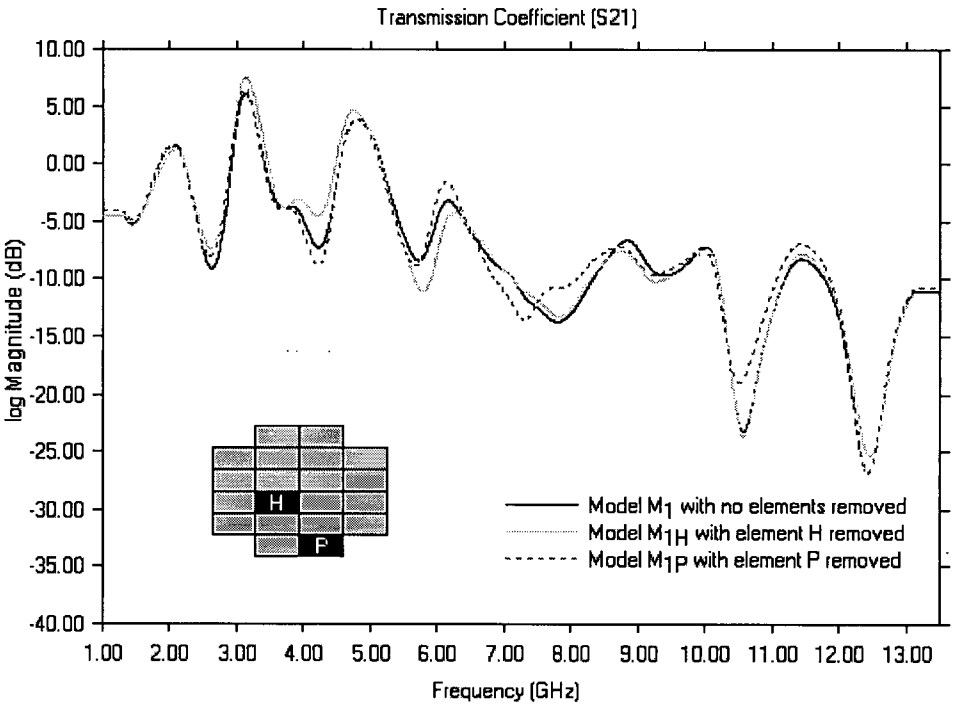

Figure 7.7: Spectral Curves for M_1, M_{1H} and M_{1P}

7.1.1.1 Position of Removed Elements versus S_{21} Spectral Curve

The first thing that can be seen from the initial scans of model M_1 with no elements removed versus scans of model M_1 with one or more elements removed is that the spectrum that is produced varies depending upon which element is removed from model M_1. Figure 7.4 shows the spectrum produced by irradiating the intact model M_1, and figure 7.5 shows the spectrum produced by removing a single element (M_{1G}) from the model. Although the two graphs look identical, if they are overlaid on the same graph, as is shown in Figure 7.6, there are small but measurable differences between the two curves, which is what was expected from the theoretical model.

Figure 7.7 shows three curves, one curve for the model M_1, one curve for the model M_{1H} and one curve for model M_{1P}, each overlapped on the same graph. Again, it can be seen from an examination of these three curves that there are differences between the spectra produced by the intact model and models that have a single void in them caused by the removal of a single element from the model. This difference shows that the shape of the spectral curves are due, at least in part, to the position of the element removed from the model. The same holds true for the curves produced by the removal of each of the other elements from the model. The graphs for the rest of the elements appear in Appendix F.

7.1.1.2 Spectral Comparison Between Models M_1 and M_2

As stated earlier, a second model was constructed from similar 2x4 material from a different set of 2x4s, and in addition to measuring the S_{21} responses for model M_1, with and without the elements removed, the S_{21} responses were measured for model M_2. It was hoped that

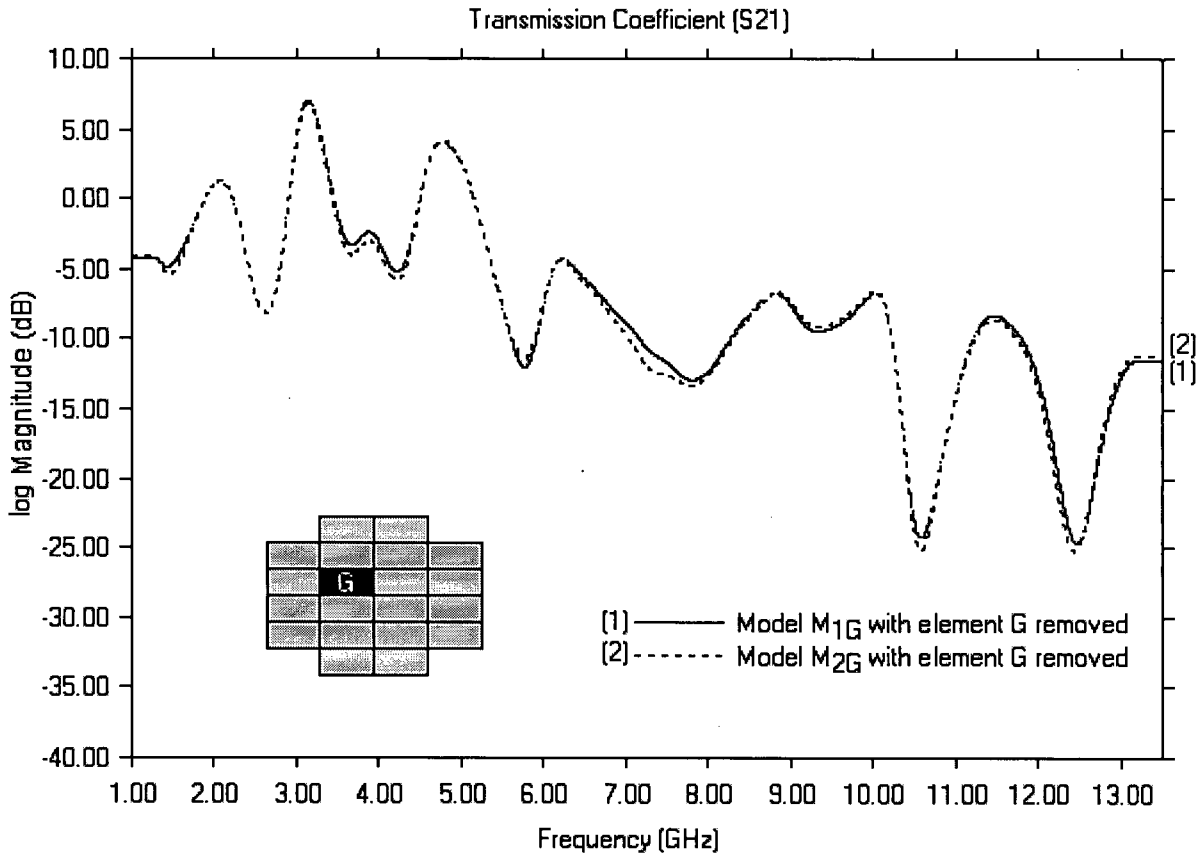

Figure 7.9: Spectral Results for models M_{1G} and M_{2G}

by comparing the sets of spectral curves from both models the differences in the curves could be attributed to the voids and not simply small differences in the wood that made up the models.

Figure 7.9 shows the results for the removal of element G from models M_1 (M_{1G}) and M_2 (M_{2G}) . Note that the two curves are similar but not identical. The question is, are these two curves similar enough to each other and different enough from all the other spectral curves produced by removing different elements that a unique match can be made? If a match between these two

curves can be determined then the location of an "unknown" void in model M_2 can be found by comparing the spectral curves from model M_2 with a baseline set of curves from model M_1.

7.1.1.3 Curve Matching and the Figure of Merit

A number of approaches can be used to determine the similarity between curves. Assume that there are two curves on a graph, a reference curve C_R and a sample curve C_S. The simplest matching algorithm is to compare the value of the C_R to the value of C_S at each point along the curve and count the number of matching points. The best match would then be assigned between the two curves with the highest number of matches.

The second method for matching two curves is to find the difference, δM, between these curves at each point along the curve . If this difference is then taken as the error in the match, a cumulative error can be calculated by summing the individual errors. Alternately, the absolute value of the individual errors can be summed to give a total error for the entire match. The larger the cumulative or absolute error, the worse the match. The best match between two curves would then be the two curves whose differences show the lowest cumulative error.

$$Cumulative\ Error = \sum_{i=1}^{N} \left| C_{Ri} - C_{Si} \right| \tag{7.1}$$

These approaches would work well for curves that are identical in magnitude along their entire length. For curves that possess the same relative shape, but are offset by a fixed difference in magnitude, as shown in Figure 7.10, these approaches will produce a large cumulative error (shown in grey) and poor matches by either algorithm. These methods would give a poor matching result even though the curves are very similar in shape.

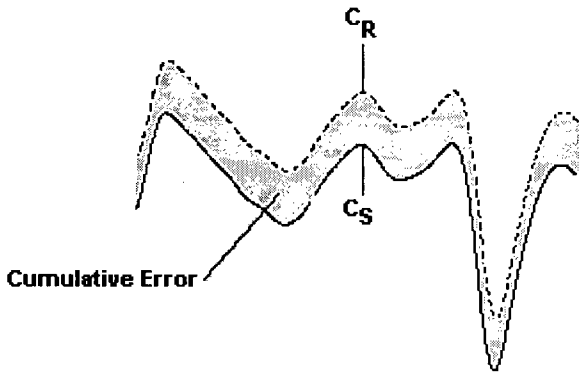

Figure 7.10: Two curves with similar shape with constant offset between them

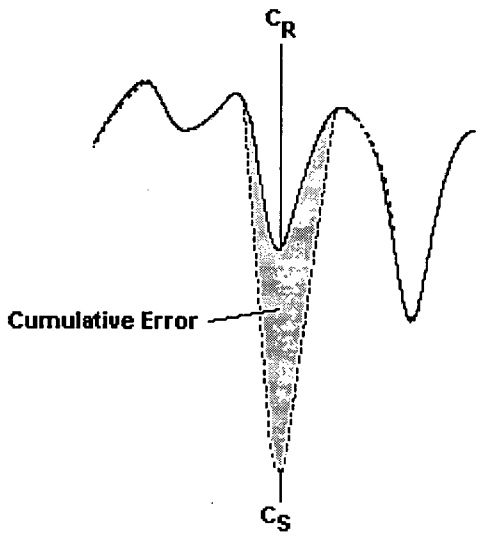

Figure 7.11: Two curves with similar shape with short span error

Similarly, curves that are very similar in shape over most of their length but have a short span where there is a major difference between the curves, as shown in figure 7.11, will also have a large cumulative error (shown in grey) and a poor match between the curves.

In practice, these two types of problems are likely to occur on a regular basis in the kinds of environments where an instrument based on the scanner would be used. In the field, or in an industrial environment such as a sawmill, electrical noise from motors and compressors is likely to affect the recording of the spectral data. Differences in relative magnitude are likely to occur due to calibration and power factors, and small "glitches" or spikes in the spectral curves are likely to occur from spurious electromagnetic radiation.

To overcome these problems, a new algorithm was developed for determining a match between two curves. Rather than examining the curves as a whole, the curves are examined in smaller sections to see if these sections match. The total number of matching sections between the two curves is summed to calculate a "figure of merit" for the match. If a large number of reference curves are compared with the sample curve at the same time, then the reference curve that has the highest number of matching sections (highest figure of merit) is deemed to be the match to the sample curve for the analysis.

The algorithm matches sections of curves by determining over what range of frequencies two curves share a similar shape. To accomplish this, a frequency is chosen as a starting frequency f_{Start}. The difference in magnitude between the sample curve and each of the reference curves at the starting frequency is calculated.

$$\delta M_{fstart} = C_{Rfstart} - C_{Sfstart} \qquad (7.2)$$

This is the same as the δM error as discussed earlier in this section. However, rather than summing this value to produce a cumulative error, δM is used as an offset target between the two curves at this frequency.

For this algorithm, the sections of two curves are said to match over the range of frequencies where δM remains constant to within a fixed percentage of the original separation distance. This means that the sections of the two curves that remain separated by a fixed offset (as shown in Figure 7.10) would be considered matching sections. The length of the matching section is determined by

$$Section\ Length = f_{Upper} - f_{Lower} \qquad (7.3)$$

where f_{Upper} is the lowest frequency greater than f_{Start} where δM no longer matches and f_{Lower} is the highest frequency less than f_{Start} where δM no longer matches (Figure 7.12).

In practice, if the algorithm tries to match the target δM exactly or within too small a percentage of the original separation, the length of a section does not extend more than a few frequencies on either side of the starting frequency. This result leads to many reference curves matching the sample curve over very small ranges of frequencies. This, in turn, makes it harder to distinguish a better match from a poorer one. If, however, the condition for matching δM is relaxed so that δM need only be constant within a 10% deviation, then the lengths of the sections grow to a reasonable size.

Once the length of the matching section for each of the reference curves has been calculated at a particular starting frequency, the best match to the sample curve (for that frequency) is chosen to be the reference curve that has the longest section length. A "win" is then

assigned to that reference curve. If there is a tie with two or more reference curves having the same longest section length for a particular starting frequency, then a win is awarded to each of those reference curves. This means that the total number of wins across all reference curves may not be the same in all instances.

This matching process is then repeated for each frequency across the entire spectral range. The cumulative number of wins is recorded for each of the reference curves and the reference curve that has the highest number of wins is considered the curve that best matches the sample curve. The code for the matching algorithm can be found in Appendix E.

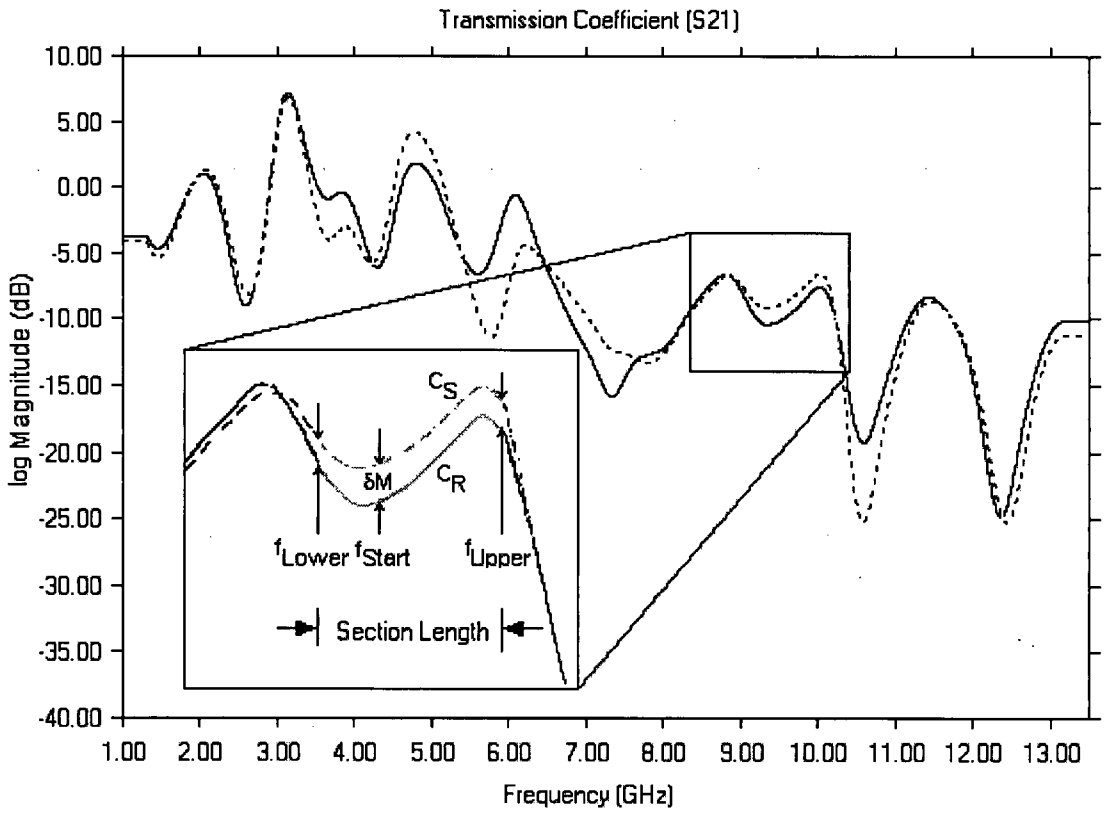

Figure 7.12: Section Length for f_{Start} showing f_{Lower} and f_{Upper}

7.1.1.4 Comparison of Magnitude, Cumulative Error and Pattern Matching Algorithms

Table 7.1 shows the results for the comparison of the M_{2G} spectral curves to the set of model curves M_1 through M_{1T} using the 4 different algorithms: point by point magnitude, cumulative error, cumulative absolute error and the new matching algorithm.

For the point by point magnitude comparison, the highest number in the column corresponds to the Model 1 curve that best matches the curve from model M_{2G}. For the cumulative error and the cumulative absolute error, the lowest number in each respective column corresponds to the best match between curves. For the new matching algorithm, it is again the highest number that corresponds to the best match between the reference and sample models. In each column, the number corresponding to the best match is indicated in bold.

For the point by point magnitude comparison method, the reference model that was selected by the algorithm was model M_{1M}. The correct curve M_{1G} was tied with two other reference models as the second best match. However, out of 1601 possible points to match, none of the matches scored greater than 17 points, which does not provide enough differentiation to make a good selection.

For the cumulative error comparison, the reference curve that was selected was model M_{1J}. The correct curve M_{1G} was chosen as the fourth best match. For the cumulative absolute error comparison, the reference curve that was selected as the best match was again M_{1M}. For this algorithm the correct model M_{1G} was chosen as the second best match.

Model	Point by Point	Cumulative Error	Absolute Error	Match
M_1	13	192	1181.5	53
M_{1A}	2	-305.3	2306.8	42
M_{1B}	3	405.88	2103.2	34
M_{1C}	4	398.5	1578.6	33
M_{1D}	5	-107.4	1606.2	53
M_{1E}	1	64.2	2111.9	86
M_{1F}	3	670.1	3023.3	6
M_{1G}	15	-38.6	576.3	**390**
M_{1H}	15	-66.9	859.5	137
M_{1I}	3	-356	2530.8	9
M_{1J}	3	**-6.5**	2045.1	27
M_{1K}	2	-25.5	2110.9	48
M_{1L}	15	-137.8	2352.2	60
M_{1M}	**17**	-70.8	**499.9**	269
M_{1N}	6	-168.6	1021.7	146
M_{1O}	2	-101.6	2500	78
M_{1P}	11	-364.4	2081.9	22
M_{1Q}	6	25.5	2162.5	18
M_{1R}	6	84.9	1318.6	40
M_{1S}	9	-70.5	1374.3	70
M_{1T}	4	-434.7	2409.4	25
M_{2G}	1601	0	0	1601

Table 7.1: Comparison of Matching Algorithms for M_{2G} vs. reference models M_{1A} thru M_{1T}.

The new algorithm, however, clearly chose M_{1G} as the best match to model M_{2G}. It is interesting to note that the three next best matches for the curve M_{2G} using the new algorithm were M_{1H}, M_{1M} and M_{1N}, which are the three locations nearest the M_{1G} that share a similar environment within the model.

Although the results in Table 7.1 are presented only for the comparison between model M_{2G} and the reference models, the different curve-matching algorithms show a similar behaviour for the other curves as well, with the new algorithm outperforming the others in all cases.

7.1.1.5 Void Detection using Pattern-Matching Algorithm

Tables 7.2(a) and 7.2(b) show the results for the matching algorithm for comparing the spectral curves for sample models M_{2A} through M_{2T}, with each of the curves for models M_1 through M_{1T}. Each entry in the table is the number of wins that each of the reference curves was assigned when compared to each of the sample curves. The highest number of wins for each model is shown in bold.

If the shape of the S_{21} curves are determined by the location of the voids in the models, then the largest number of wins for the sample model M_{2A} should correspond to the reference model M_{1A}, as should M_{2B} to M_{1B} and so on. This should lead to all of the entries on the diagonal of the table being highlighted in bold. As can be seen from Tables 7.2(a) and 7.2(b) this is indeed the case. The curves from the sample model are correctly matched to the curves from the reference model. This shows that there is information about the location of the voids being transmitted in the S_{21} spectrum, and it is possible to determine the location of the voids within the interior of the wooden models.

Model	M_2	M_{2A}	M_{2B}	M_{2C}	M_{2D}	M_{2E}	M_{2F}	M_{2G}	M_{2H}	M_{2I}	M_{2J}
M_1	**322**	n/a	68	102	n/a	n/a	43	101	40	36	n/a
M_{1A}	24	n/a	53	106	n/a	n/a	49	43	100	75	n/a
M_{1B}	31	n/a	**416**	235	n/a	n/a	148	164	205	46	n/a
M_{1C}	162	n/a	122	**277**	n/a	n/a	35	66	43	8	n/a
M_{1D}	62	n/a	81	91	n/a	n/a	36	37	37	71	n/a
M_{1E}	28	n/a	38	36	n/a	n/a	40	35	34	102	n/a
M_{1F}	43	n/a	55	38	n/a	n/a	**359**	18	36	30	n/a
M_{1G}	70	n/a	102	47	n/a	n/a	42	**239**	60	9	n/a
M_{1H}	66	n/a	79	31	n/a	n/a	98	215	**278**	10	n/a
M_{1I}	35	n/a	27	35	n/a	n/a	82	30	38	**467**	n/a
M_{1J}	67	n/a	41	50	n/a	n/a	146	47	20	61	n/a
M_{1K}	63	n/a	12	19	n/a	n/a	53	31	75	32	n/a
M_{1L}	25	n/a	89	34	n/a	n/a	209	21	33	59	n/a
M_{1M}	51	n/a	61	75	n/a	n/a	4	187	109	9	n/a
M_{1N}	187	n/a	94	46	n/a	n/a	92	148	129	16	n/a
M_{1O}	67	n/a	21	48	n/a	n/a	40	38	27	234	n/a
M_{1P}	47	n/a	58	28	n/a	n/a	32	26	76	55	n/a
M_{1Q}	82	n/a	85	41	n/a	n/a	27	37	88	70	n/a
M_{1R}	126	n/a	104	92	n/a	n/a	29	71	99	97	n/a
M_{1S}	87	n/a	57	86	n/a	n/a	17	57	40	40	n/a
M_{1T}	48	n/a	11	140	n/a	n/a	19	16	74	27	n/a

Table 7.2: (a) Number of comparison wins for sample models M_2 thru M_{2J} vs. reference models M_1 thru M_{1T}. Note n/a indicates data unavailable.

Model	M_{2K}	M_{2L}	M_{2M}	M_{2N}	M_{2O}	M_{2P}	M_{2Q}	M_{2R}	M_{2S}	M_{2T}
M_1	n/a	33	121	99	30	n/a	n/a	99	139	n/a
M_{1A}	n/a	16	53	71	29	n/a	n/a	16	89	n/a
M_{1B}	n/a	76	35	99	77	n/a	n/a	53	59	n/a
M_{1C}	n/a	23	155	98	34	n/a	n/a	115	73	n/a
M_{1D}	n/a	55	42	27	44	n/a	n/a	93	95	n/a
M_{1E}	n/a	84	43	51	22	n/a	n/a	13	56	n/a
M_{1F}	n/a	161	7	18	43	n/a	n/a	26	43	n/a
M_{1G}	n/a	16	83	98	11	n/a	n/a	80	71	n/a
M_{1H}	n/a	55	60	200	26	n/a	n/a	159	54	n/a
M_{1I}	n/a	40	7	39	158	n/a	n/a	49	44	n/a
M_{1J}	n/a	37	42	66	29	n/a	n/a	34	58	n/a
M_{1K}	n/a	96	61	62	118	n/a	n/a	28	48	n/a
M_{1L}	n/a	**495**	26	74	27	n/a	n/a	86	58	n/a
M_{1M}	n/a	45	**390**	92	23	n/a	n/a	69	169	n/a
M_{1N}	n/a	49	109	**290**	23	n/a	n/a	194	58	n/a
M_{1O}	n/a	33	85	40	**574**	n/a	n/a	5	102	n/a
M_{1P}	n/a	139	29	30	109	n/a	n/a	13	91	n/a
M_{1Q}	n/a	32	60	19	55	n/a	n/a	27	83	n/a
M_{1R}	n/a	74	139	113	24	n/a	n/a	**441**	115	n/a
M_{1S}	n/a	23	139	43	106	n/a	n/a	36	**904**	n/a
M_{1T}	n/a	41	25	22	44	n/a	n/a	49	51	n/a

Table 7.2 (b) Number of comparison wins for sample models M_{2K} thru M_{2T} vs. reference models M_1 thru M_{1T}. Note n/a indicates data unavailable.

Chapter 7 - Void Detection

The graphs of the S_{21} response curves for the reference model M_1, with no elements removed, and M_{1A} through M_{1T}, with single model elements A through T removed, are shown in Appendix F. Appendix G shows the results for the model rotated 90 degrees.

Data for Models M_{2A}, M_{2D}, M_{2E}, M_{2J}, M_{2K}, M_{2P}, M_{2Q}, M_{2T} are unavailable due to incorrect data returned by the Wiltron Vector Analyser. For these sample models, the data were returned as zeros. It was not possible to repeat these measurements later as the original test setup was no longer available.

7.2 Determination of the Outer Dimensions of a Cylindrical Model

The void detection algorithms presented in the preceding sections of this thesis depend upon the ability to compare unknown samples with the results from pre-scanned models. In order for an instrument based on this device to be useful, it would be necessary to make some initial selection of which models could be used for the comparisons. In practice, a catalogue of the various voids that would be found in a tree or log would be made from scanning a number of representative samples from trees or poles of various diameters.

When the initial characterizations for the scanner were performed, it was noticed that one of the abilities of the scanner was to easily determine the diameter of a cylinder placed between the antennas. The ability to determine the external size of the object under test could be used to provide the information required to perform the initial model selection from the catalogue described above. If pre-scanned spectral information is stored according to the external dimensions of the models tested, a new sample can then be compared to prestored models using size as one of the initial determining criteria.

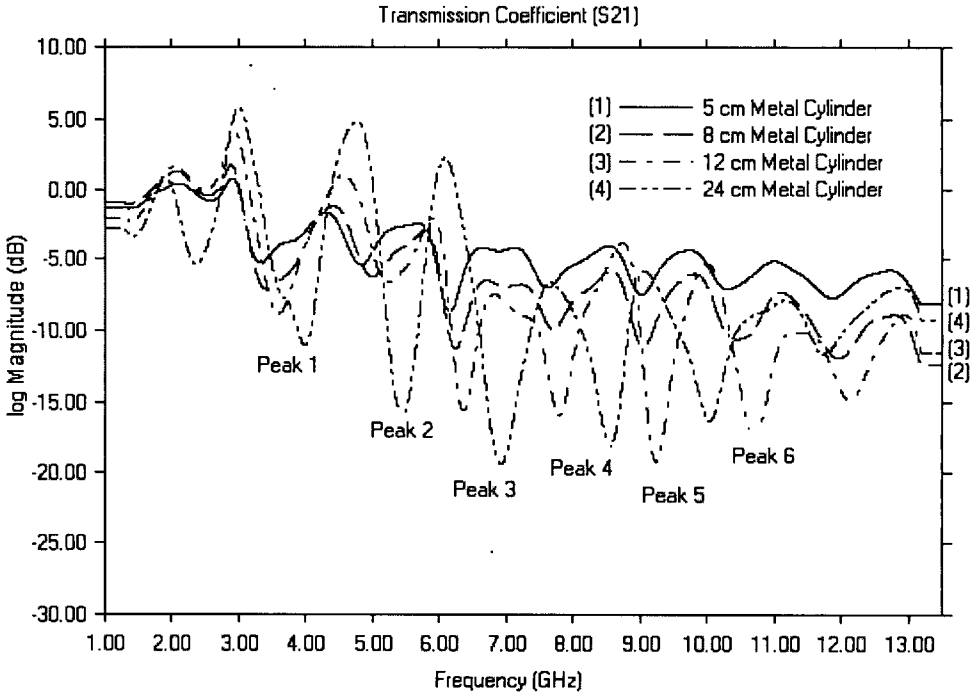

Figure 7.14: S_{21} log Magnitude versus Frequency for Metal Cylinders of varying size

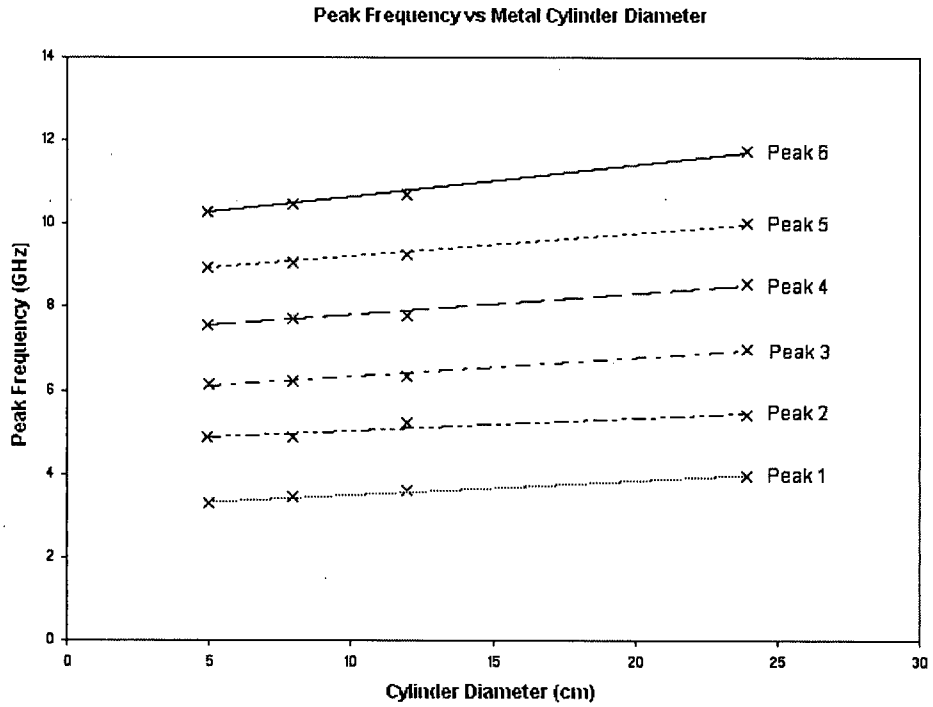

Figure 7.15: Plot of Peak Frequency versus Cylinder Size for Metal Cylinders

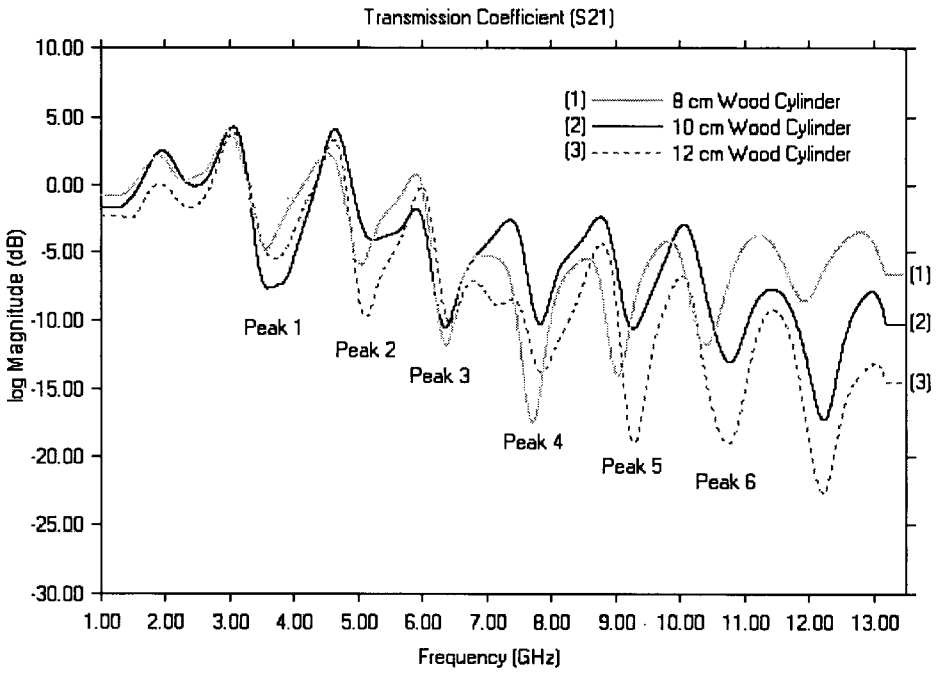

Figure 7.16: S_{21} log Magnitude versus Frequency for Wood Cylinders of varying size

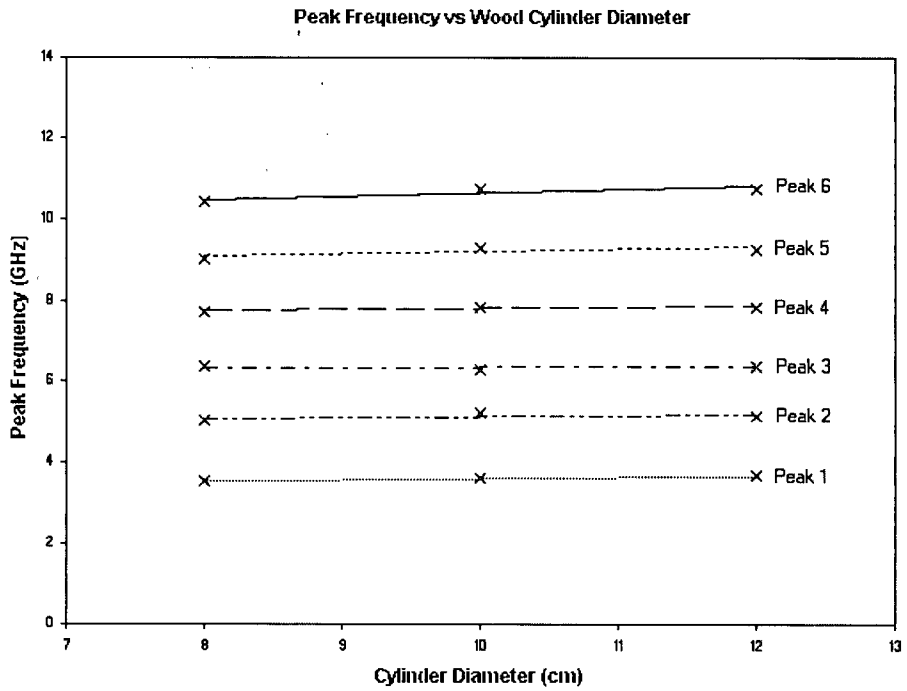

Figure 7.17: Plot of Peak Frequency versus Cylinder Size for Wood Cylinders

Chapter 7 - Experimental Results

The ability to detect the size of the cylinder between the antennas was characterized by the change in the frequency of six major valleys in the log Magnitude versus Frequency curves shown in Figure 7.14. If the frequency of each of these peaks is plotted versus the size of the cylinder and fitted with a linear interpolation, the result is a family of graphs. Figure 7.15 shows the family for the series of metal cylinders whose spectral curves are shown in Figure 7.14.

From the graph shown in Figure 7.15, it is quite easy to determine the diameter of an unknown cylinder by interpolating the results. Although the family of curves shown in Figure 7.15 is for metal cylinders, Figures 7.16 and 7.17 show the results for a set of wooden cylinders of differing diameters. The slopes of the curves differ from that for the metallic cylinders, but the shift in peak position changes in a similar fashion to that for the metallic cylinders.

Chapter 8

8.0 Conclusions and Future Work

The goal of this thesis is to determine if the detection of large scale voids in wooden objects was possible using a simple microwave rf device. The hypothesis for this thesis is that, due to the dielectric nature of the materials that make up wood, there should be a difference between the interaction of radio waves with an object composed of these dielectric materials when compared to the interaction of the radio waves with voids in these objects that contain no dielectric materials. It was also hypothesized that due to the complex nature of the materials and the construction of wood that these interactions would be frequency-dependent and that this frequency dependence could be used to locate voids within a solid wooden object.

This thesis has clearly shown that the transmission of electromagnetic waves through an object are affected by the difference in dielectric properties (presence or absence of a dielectric material) inside the object. It has also been demonstrated that the differences in the dielectric properties inside the object can be detected outside the object via the transmitted S_{21}spectrum. It has also been demonstrated that the effects on the transmitted EM waves are position-dependent and not simply a property of the bulk material, and that the effects are also frequency-dependent over an ultra-wide range of frequencies. It has also been shown that the frequency-dependent effects can be used to locate the position of voids within a dielectric object. It was also shown that the object's outer dimensions could be determined by examining the transmitted spectrum.

The construction of a prototype ultra-wideband scanner has demonstrated that, in addition to meeting the theoretical goals of this project, a practical instrument design is also possible. This prototype design provides the groundwork for an instrument capable of detecting large-scale voids in solid wood objects such as trees or telephone poles that is simple in construction, low in cost and requires only a simple comparison routine rather than a complete tomographic reconstruction.

Chapter 8 - Conclusions and Future Work

In addition to meeting the goals of large-scale void detection, this project also developed a new type of ultra-wideband antenna. The FDL antenna has an S_{11} reflection coefficient with a flatter response over an ultra-wide bandwidth than that of all existing antenna designs. The development of this novel antenna, and the corroboration of the physical design by computer modelling, should allow for further improvements in other areas where an ultra-wideband antenna is required such as impulse and ground penetrating radar and ultra-wideband communications. The FDL antenna is now covered under the World International Property Organization Patent Cooperation Treaty (PCT) Publication Number WO 02/089253 A1 [81], US Patent 20040150579, with further patent filings underway with individual applications filed in the US, Canada and Europe.

This thesis also presents a new algorithm for matching curves in 2D space. This algorithm performs better than standard comparison methods by allowing for offset errors and errors caused by short duration noise.

8.1 Future Work

While this thesis has answered a number of fundamental questions about the FDL antenna, it has also raised new areas for further investigation. The work on the FDL antenna and the scanner, while substantial, has just begun.

8.1.1 FDL Antenna

The optimal FDL antenna design described in this thesis is just one of many possible configurations covered in the FDL patent application, as shown in Figure 4.5. The profile for the

ground planes for the FDL antenna for this thesis is that of an ellipse. The other profiles, such as circular, parabolic and irregular that were mentioned, still need to be investigated to determine the complete characteristics for those styles of FDL antenna. The effects of these different profiles on the S_{11} reflection coefficient and the cross- and co-polarization are currently unknown. In addition, the effects of changing the overall size of the antenna as well as the shape of the antenna's active member and ground planes will need to be examined now that a basic model for computer analysis has been created.

8.1.2 Ultra-wideband Scanner

In addition to the FDL antenna itself, there are a number of avenues of further work to be done in the area of the ultra-wideband scanner. The work for this thesis involved the detection of singular regularly shaped voids in solid models of regular composition. In the field, there exists the need to detect multiple irregularly shaped voids in objects under examination and voids in objects of irregular composition. Work also needs to be done to determine the smallest size voids that can be detected for an antenna/scanner system within a given frequency range and the positional resolution of the scanner system.

The sliding window method used for a comparison of the spectral curves worked well for this thesis. This method of analysis, however, depends on having pre-determined models for comparison in order to perform its void detection. This approach works well in the lab and would work well in a controlled environment where a database of previously scanned samples could be used for comparison. Thus this scanner system may be well suited to a lumber mill or pole manufacturing/testing facility where large numbers of objects of similar size and shape are processed.

8.1.3 Full Tomographic Inversion

An alternate solution to the detection problem would be a full tomographic imaging solution in which no predetermined models are required. This approach is currently being investigated by Kim Lam, one of the other students in Dr. Matt Yedlin's research group working on the dielectric scattering approach [26].

8.1.4 Other Fields

While the work in this thesis focusses on the detection of voids in wooden models, the applications for an ultra-wideband antenna are numerous. Currently, there is much research taking place on the development of ultra-wideband systems for Ground Penetrating Radar (GPR), for Radar Imaging and for highspeed/high bandwidth communications. Because of its bandwidth, size and scalability, the FDL antenna could be used in all of these areas. In fact, the FDL antenna will be used as the transmitting and receiving antenna for a prototype ultra-wide bandwidth spread spectrum communications system currently being developed by Linn, Yedlin and Dotto [82].

Bibliography

[1] BC Hydro Climate Change Progress Report, September 2000, BC Hydro Corporate Environment Division, www.bchydro.com/environment/reports/greenhouse.html.

[2] R.J. Nevill, R.J. Whitehead, "Potential Loss Due To Decay and Insect Attack Following Selective Harvest in Coastal Montane Forests," Canadian Forest Service, November 1996.

[3] M. Fioravanti, R.Ricci, "Computerized tomography for wood density measurement: experimental research and methodology," Annali- Accademia Italiana di Scienze Forestali. 1991. 40: pp. 57 - 91.

[4] A. Habermehl, H.W. Ridder, "Application of mobile computer tomography for nondestructive investigations of the wood of standing trees. Investigations on avenue and park trees," Holz Als Roh-und Werkstoff. 1993. 51: 2, pp. 101 - 106.

[5] A. Habermehl, H.W. Ridder, "Computerised tomographic investigations of street and park trees," Arboricultural Journal. 1995. 19: 4, pp. 419 - 437.

[6] P. Niemz, L.J. Kucera, A. Flisch, E. Blaser, "Application of computer tomography to wood," Holz Als Roh-und Werkstoff. 1997. 55: 4, pp. 279 - 280.

[7] A. Habermehl , "A new non-destructive method for determining internal wood condition and decay in living trees. II: Results and further developments," Arboricultural Journal. 1982. 6: 2, pp. 121 - 130. 15 ref..

[8] M.T. Afzal, B. Colpitts, K. Galik, "Dielectric Properties of Softwood Species Measured with an Open-ended Coaxial Probe," Proceedings of the 8th International IUFRO Wood Drying Conference, Brasov, Romania, Aug. 2003, pp. 110 - 115.

[9] W.L. James, "Electric Moisture Meters for Wood," General Technical Report FPL-GTR-6, USDA Forest Service, June 1988, pp. 1 - 17.

[10] G.I. Torgovnikov, "Dielectric Properties of Wood and Wood-Based Materials," Springer-Verlag, 1993, TA 419 T67 1993, ISBN 3-540-55394-0, pp 1 - 14.

[11] U.S. Inan, A.S. Inan, " Engineering Electromagnetics," Addison Wesley, 1998, ISBN 0-8053-4423-3, pp. 615 - 645.

[12] J. Goldman, G.W. Swenson, "Radio Wave Propagation Through Woods," Antennas and Propagation Magazine, IEEE , Volume: 41 , Issue: 5 , Oct. 1999, pp. 34 - 36.

[13] J. Bodig , "The Process of NDE Reseach for Wood and Wood Composites," Keynote Address, Proceedings of the 12th International Symposium of Nondestructive Testing of Wood. University of Western Hungary, Sopron, Hungary. September 14-16, 2000. pp. 1 - 22.

[14] K.C. Schad, D.L. Schmoldt, R.J. Ross, "Nondestructive methods for detecting defects in softwood logs," Research Paper, Forest Products Laboratory, USDA Forest Service. USDA Forest Service, North Central Forest Experiment Station, Madison, USA: 1996. No. FPL-RP-546.

[15] J. Nystrom, O. Hagman, "Methods for Detection of Compression Wood in Green and Dry Conditions," EUROPTO Conference on Polarization and Color Techniques in Industrial Inspection, Munich Germany, June 1999, SPIE Volume: 3892 pp. 287 - 294.

[16] D.L. Schmoldt, " CT Imaging, Data Reduction and Visualization of Hardwood Logs," Proceedings of the 24th Annual Hardwood Symposium. May 8-11, 1996, pp. 69 - 80.

[17] D.L. Schmoldt, E. Scheinman, A. Rinnhofer, L.G. Occena, "Internal; Log Scanning: Research to Reality," Proceedings of the 28th Annual Hardwood Symposium. May 11-13, 2000, pp. 103 - 114.

[18] P.H. Steele, J.E. Cooper. 2000. "Estimating lumber strength with radio frequency scanning," Proceedings of the 12th International Symposium of Nondestructive Testing of Wood. University of Western Hungary, Sopron, Hungary. September 14 - 16, 2000. pp. 343 - 348.

[19] S. Rust, G. Landschaft, "A new Tomographic Device for the Non-destructive Testing of Trees," Proceedings of the 12th International Symposium of Nondestructive Testing of Wood. University of Western Hungary, Sopron, Hungary. September 14 -16, 2000. pp. 233 - 238.

[20] R. Guzenda, W. Olek, H.M. Baranowska, "Identification of Free and Bound Water Content in Wood by Means of NMR Relaxometry," Proceedings of the 12th International Symposium of Nondestructive Testing of Wood. University of Western Hungary, Sopron, Hungary. September 14 - 16, 2000. pp. 273 - 278.

[21] T. Tanaka, F. Divos , "Wood Inspection by Thermography," Proceedings of the 12th International Symposium of Nondestructive Testing of Wood. University of Western Hungary, Sopron, Hungary. September 14 - 16, 2000. pp. 439 - 449.

[22] O. Hagman, "Woodmetrics - Imaging Devices and processes in Wood Inspection at Lulea University of Technology," EUROPTO Conference on Polarization and Color Techniques in Industrial Inspection, Munich Germany, June 1999, SPIE Volume: 3892 pp. 148 - 159.

[23] A. Kaestner, "Microwave Polarimetry Based Wood Scanning," Proceedings of the 12th International Symposium of Nondestructive Testing of Wood. University of Western Hungary, Sopron, Hungary. September 14 - 16, 2000. pp. 249 - 256.

[24] D.L. Schmoldt, P. Li, A.L. Abbott, "CT Imaging of Hardwood Logs for Lumber Production," Proceedings of the 5th Industrial Engineering Research Conference. May 1996. pp. 387 - 392.

[25] J.H. Richmond, "Scattering by a Dielectric Cylinder of Arbitrary Cross Section Shape," IEEE Transactions on Antennas and Propagation, Volume: 13 , Issue: 3 , May 1965, pp. 334 - 341

[26] K. Lam, "Cylindrical RF Tomography," Master's Thesis, Department of Electrical & Computer Engineering, University of British Columbia, Nov. 2003.

[27] X.H. Wu, Z.N. Chen; M.Y.W. Chia,; "Note on antenna design in UWB wireless communication systems," Ultra Wideband Systems and Technologies, 2003 IEEE Conference on, Nov. 16 - 19, 2003, pp. 503 - 507.

[28] R. Harjani, J. Harvey, R. Sainati, "Analog/RF Physical Layer Issues for UWB Systems," VLSI Design, 2004. Proceedings. 17th International Conference on , 5 - 9 Jan. 2004 pp. 941 - 948.

[29] G. Lu, P. Spasojevic, L. Greenstein, "Antenna and Pulse Designs for Meeting UWB Spectrum Density Requirements," Ultra Wideband Systems and Technologies, 2003 IEEE Conference on, Nov. 16 - 19, 2003, pp. 162 - 166.

[30] H.G. Schantz, "A Brief History of UWB Antennas," Aerospace and Electronic Systems Magazine, IEEE , Volume: 19 , Issue: 4 , April 2004, pp. 22 - 26.

[31] J.S. Hollis, T.J. Lyon, L. Clayton Jr., "Microwave Antenna Measurements," Scientific Atlanta Inc., 1970, pp 2 - 1.

[32] W. L. Stutzman, G.A. Thiele, "Antenna Theory and Design," Second Edition, John Wiley and Sons, 1998, ISBN 0-471-02590-9, pp. 225.

[33] IEEE Standard Test Procedures for Antennas, ANSI/IEEE Std 149-1979, IEEE, Aug 1980, ISBN 0-471-08032-2.

[34] A. Kerkhoff, R. Rogers, H. Ling, "The use of the genetic algorithm approach in the design of ultra-wideband antennas," Radio and Wireless Conference 2001, RAWCON 2001, IEEE, 19-22, Aug. 2001, pp. 93 - 96.

[35] Y. Lin, S. Tsai, "Coplanar waveguide-fed uniplanar bow-tie antenna," Antennas and Propagation, IEEE Transactions on , Volume: 45 No. 2 , Feb. 1997 pp. 305 - 306.

[36] M. Kim, D. Oh, I. Park, J.T. Bernhard, "One-arm microstrip spiral antenna with a circular aperture on the ground plane," Antennas and Propagation Society International Symposium, 2002. IEEE , Volume: 3 , 16-21 June 2002, pp. 830 - 833.

[37] S.D. Targonski, R.B. Waterhouse, D.M. Pozar, "Design of wide-band aperture-stacked patch microstrip antennas," Antennas and Propagation, IEEE Transactions on , Volume: 46, No. 9, Sept. 1998, pp. 1245 - 1251.

[38] X. Liang, M. Chia, "Multiband characteristics of two fractal antennas," Microwave and Optical Technology Letters, Volume: 23, No. 4, November 1999, pp. 242-245.

[39] T.W. Barrett, "History of Ultra Wideband Communications and Radar: Part I, UWB Communications," Microwave Journal, January 2001Volume: 44, No. 1, pp. 22 - 56.

[40] H.G. Schantz, "Introduction to Ultra-Wideband Antennas," Ultra Wideband Systems and Technologies, 2003 IEEE Conference on , Nov. 16-19, 2003, pp. 1 - 9.

[41] G.R.P. Marie, "Wide Band Slot Antenna," US Patent 3,031,665, April 1962

[42] H.F. Harmuth, N.J. Mohamed, "Large-current radiators," Microwaves, Antennas and Propagation, IEE Proceedings H, Volume: 139 , Issue: 4 , Aug. 1992, pp. 358 - 362.

[43] H.G. Schantz, "UWB magnetic antennas," Antennas and Propagation Society International Symposium, 2003. IEEE , Volume: 3 , 22 - 27 June 2003, pp. 604 - 607.

[44] C. Kinezos, V. Ungvichian, "Ultra-wideband Circular Polarized Microstrip Archimedean Spiral Antenna Loaded with Chip-resistor," Antennas and Propagation Society International Symposium, 2003. IEEE , Volume: 3 , 22-27 June 2003, pp. 612 - 615.

[45] J.J. Van Tonder, J.K. Cloete, "A study of an Archimedes spiral antenna," Antennas and Propagation Society International Symposium, 1994. AP-S. Digest , Volume: 2 , 20 - 24 June 1994, pp. 1302 - 1305.

[46] P. van Genderen, L. Nicolaescu, J. Zijderveld, "Some experience with the use of Spiral Antennas for a GPR for Landmine Detection," Radar Conference, 2003. Proceedings of the International , 3 - 5 Sept. 2003 pp.219 - 223.

[47] M. Kim, D. Oh, I. Park; J.T. Bernhard, "One-arm Microstrip Spiral Antenna with a Circular Aperture on the Ground Plane," Antennas and Propagation Society International Symposium, 2002. IEEE , Volume: 3 , 16 - 21 June 2002, pp. 830 - 833.

[48] K. Nakayama, H. Nakano, " Radiation Characteristics of a Conformal Spiral Antenna," Electronic Communications in Japan, Part 1, Volume: 83, No. 5, 2000, pp. 107 - 114.

[49] D.F. Filipovic, "A Planar Wideband Circularly Polarized Antenna for Satellite Communications," Technologies for Wireless Applications, 1999. Digest. 1999 IEEE MTT-S Symposium on , 21 - 24 Feb. 1999, pp. 213 - 216.

[50] E.S. Eide, "Ultra-wideband Transmit/Receive Antenna Pair for Ground Penetrating Radar," Microwaves, Antennas and Propagation, IEE Proceedings , Volume: 147 , Issue: 3 , June 2000, pp. 231 - 235.

[51] Y.D. Lin, S.N. Tsai, "Coplanar Waveguide-Fed Uniplanar Bow-Tie Antenna," Antennas and Propagation, IEEE Transactions on , Volume: 45 , Issue: 2 , Feb. 1997, pp. 305 - 306.

[52] H. Wang, B. Gao, S. Yang, "A New Wide Band Planar Antenna," Proceedings of the XXVIIth General Assembly of URSI, URSI 2002, Maastricht, Netherlands, Aug. 2002, pp. p0082/1 - 4.

[53] E.A. Soliman, S. Brebels, P. Delmotte, G.A.E. Vandenbosch, E. Beyne, "Bow-tie Slot Antenna Fed by CPW," Electronics Letters , Volume: 35 , Issue: 7 , 1 April 1999 pp. 514 - 515.

[54] A.K.Y.. Lai, A.L,. Sinopoli, W.D. Burnside, "A Novel Antenna for Ultra-Wide-Band Applications," Antennas and Propagation, IEEE Transactions on , Volume: 40 , Issue: 7 , July 1992, pp. 755 - 760.

[55] N. Herscovici, "A Wide-Band Single-Layer Patch Antenna," Antennas and Propagation Society International Symposium, 1998. IEEE , Volume: 2 , 21 - 26 June 1998, pp. 1108 - 1111.

[56] S.D. Targonski, R.B. Waterhouse, D.M. Pozar, "Design of Wide-Band Aperture-Stacked Patch Microstrip Antennas," Antennas and Propagation, IEEE Transactions on, Volume: 46 , Issue: 9 , Sept. 1998, pp. 1245 - 1251.

[57] G.P. Gauthier, A. Courtay, G.M. Rebeiz, "Microstrip Antennas on Synthesized Low Dielectric-Constant Substrates," Antennas and Propagation, IEEE Transactions on , Volume: 45 , Issue: 8 , Aug. 1997, pp. 1310 - 1314.

[58] A. Hizal, C. Yardim, E. Halavut, " Wide Band Tapered Rolling Strip Antenna," Proceedings of the AP2000 Millennium Conference on Antennas and Propagation, Davos, Switzerland, April 2000, pp. p1553/1-4.

[59] M. Sato, F. Kong, Z. Zeng, G. Fang, "Antenna development and a stepped-frequency GPR system for landmine detection," Proceedings of the 2nd International Workshop on Advanced Ground Penetrating Radar, 2003, 14-16 May 2003, pp. 168 - 17.

[60] M.C. Greenberg, K.L. Virga, "Characterization of Bunny-Ear Antennas for Wireless Basestation Applications," Radio and Wireless Conference, 1998. RAWCON 98. 1998 IEEE , 9 - 12 Aug. 1998, pp. 87 - 90.

[61] T.G. Ma, S.K. Jeng, " A novel Compact Ultra-wideband Printed Dipole Antenna with Tapered Slot Feed," Antennas and Propagation Society International Symposium, 2003. IEEE, Volume: 3, 22 - 27 June 2003, pp. 608 - 611.

[62] K.H. Kim, S.B. Cho, Y.J. Park, H.G. Park, "Novel Planar Ultra Wideband Stepped-Fat Dipole Antenna," Ultra Wideband Systems and Technologies, 2003 IEEE Conference on , Nov. 16-19, 2003, pp. 508 - 512.

[63] X.Liang, M.Y.W. Chia, "Multiband Characteristics of Two Fractal Antennas," Microwave and Optical Technology Letters, Volume: 23, No. 4, Nov. 1999, pp. 242 -245.

[64] A.G. Yarovoy, A.D. Schukin, I.V. Kaploun, L.P. Ligthart, " The Dielectric Wedge Antenna," Antennas and Propagation, IEEE Transactions on , Volume: 50 , Issue: 10 , Oct. 2002, pp. 1460 - 1472.

[65] A.G. Yarovoy, A.D. Schukin, I.V. Kaploun, L.P. Ligthart, "Dielectric Wedge Antenna for Ground Penetrating Radars," Antennas and Propagation Society International Symposium, 2003. IEEE , Volume: 2 , 22-27 June 2003, pp. 247 - 250.

[66] T. Yang, S.Y. Suh, R. Nealy, W.A. Davis, W.L. Stutzinan, "Compact Antennas for UWB Applications," Aerospace and Electronic Systems Magazine, IEEE , Volume: 19 , Issue: 5 , May 2004, pp. 16 - 20.

[67] C.Nguyen, J.S. Lee, J.S. Park, "Ultra-Wideband Microstrip Quasi-Horn Antenna," Electronics Letters , Volume: 37 , Issue: 12 , 7 Jun 2001, pp. 731 - 732.

[68] K.F. Lee, W. Chen, "Advances in Microstrip and Printed Antennas," Wiley Interscience, 1997, ISBN 0-471-04421-0.

[69] R. Zentner, Z. Šipuš, J. Bartolic, "Synthesis of Broadband Microstrip Antennas," Proceedings of the AP2000 Millennium Conference on Antennas and Propagation, Davos, Switzerland, April 2000, pp. p0939/1 - 4.

[70] K.Dotto, "Air Core Microstrip Antenna Design," ECE 571 Practical RF Electronics Project, April 2000.

[71] C. Liu, J. Li, W. Gao, "Analysis of Vivaldi Antenna over a Heterogeneous Ground using 3-D TLM-CE Method," Proceedings. IGARSS 2000. IEEE 2000 International , Vol: 4 , 24 - 28 July 2000 pp. 1733 - 1735.

[72] E. Gazit, "Improved Design of the Vivaldi Antenna," Microwaves, Antennas and Propagation, IEE Proceedings H , Volume: 135 , Issue: 2 , April 1988, pp. 89 - 92.

[73] E. Guillanton, J.Y. Duavignac, C. Pichot, J. Cashman, "A New Design Tapered Slot Antenna for Ultra-Wideband Applications,"Microwave and Optical Technology Letters, Volume: 19 No.4 November 1998, pp. 286 - 289.

[74] R.Q. Lee, R.N. Simons, "Effect of Curvature on Tapered Slot Antennas,"Antennas and Propagation Society International Symposium, 1996, AP-S. Digest , Volume: 1, pp. 188 - 191.

[75] J.D.S. Langley, P.S. Hall, P. Newham, "Balanced Anitpodal Vivaldi Antenna for Wide Bandwidth Phased Arrays," IEE Proc. Microwave Antennas and Propagation, Volume: 143, No.2 April 1996, pp. 97 - 102.

[76] Absolute gain Calibration Chart, Narda Model 640 Standard Gan Horn, Loral Microwave.

[77] FEKO User's Manual, Suite 4.0, EM Software Systems, South Africa, 2002.

[78] H. Duncan, "The 2000 CAD Benchmark," Microwave Engineering Europe, October 2000 - January 2001, pp. 1 - 14.

[79] A. Prata, " Misaligned Antenna Phase-Center Determination Using Measured Phase Patterns," The Interplanetary Network Progress Report, IPN PR 42 - 150, April-June 2002, pp. 1 - 9.

[80] R. Bansal, "The Far Field: How Far is Far Enough?" Applied Microwave & Wireless, Nov 1999, Volume: 11, No. 11, pp 58 - 60.

[81] Ultra-Wideband Antennas, World International Property Organization Patent Cooperation Treaty (PCT) Publication Number WO 02/089253 A1, Nov. 2002.

[82] Y.Linn, M.Yedlin, K.Dotto, Ultra-Wideband Low Probability of Intercept, Jamming Resistant Communications System Project, UBC Department of Electrical and Computer Engineering, 2003-2004.

Appendix A - FDL S_{11} Reflection Coefficient versus Flair Angle for Flat Ground Planes

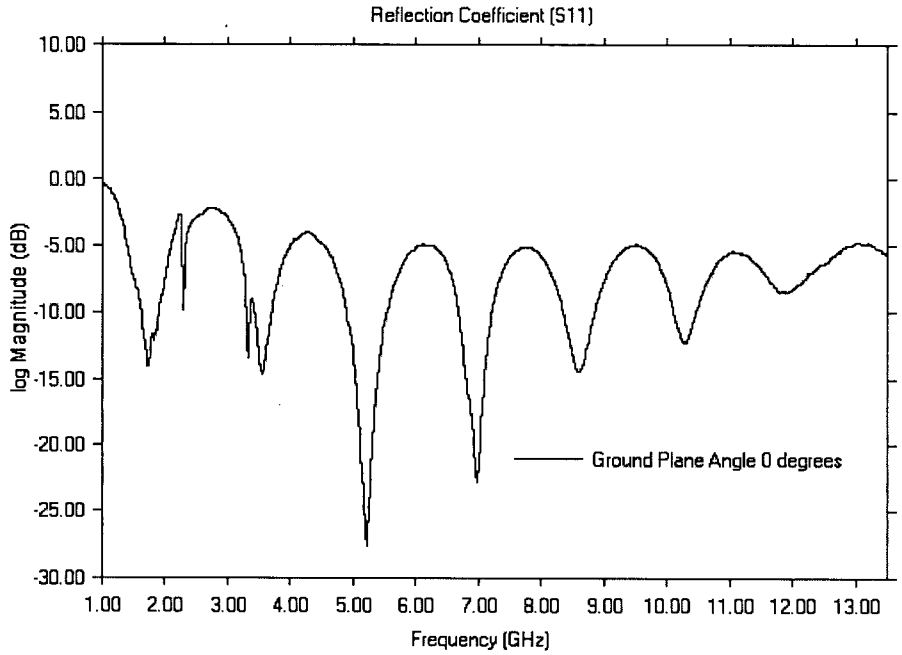

Figure A1: S_{11} Reflection Coefficient for FDL Antenna for Flare Angles of 0 degrees

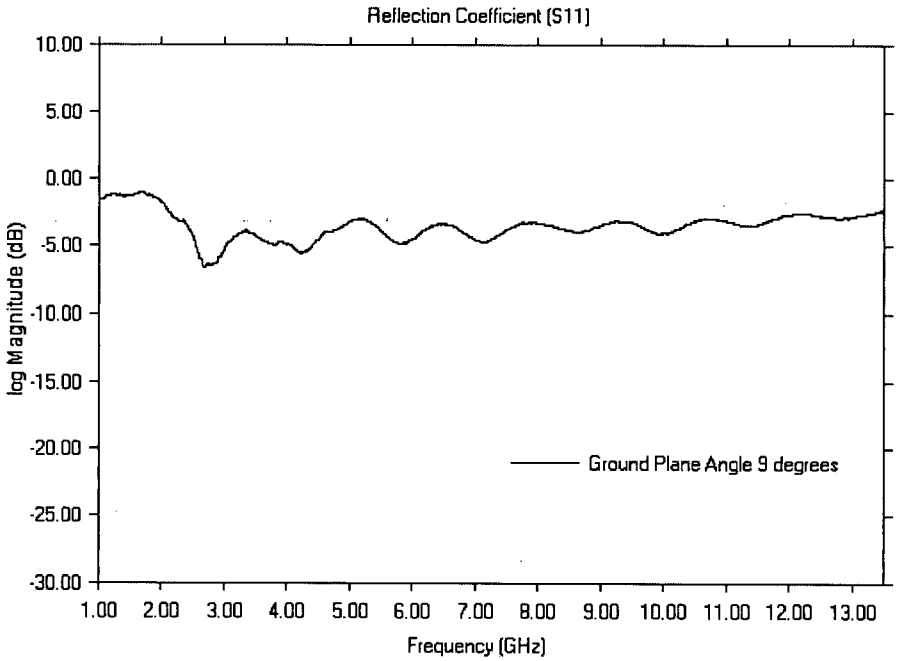

Figure A2: S_{11} Reflection Coefficient for FDL Antenna for Flare Angles of 9 degrees

Appendix A - FDL S_{11} Reflection Coefficient *vs.* Flair Angle for Flat Ground Planes

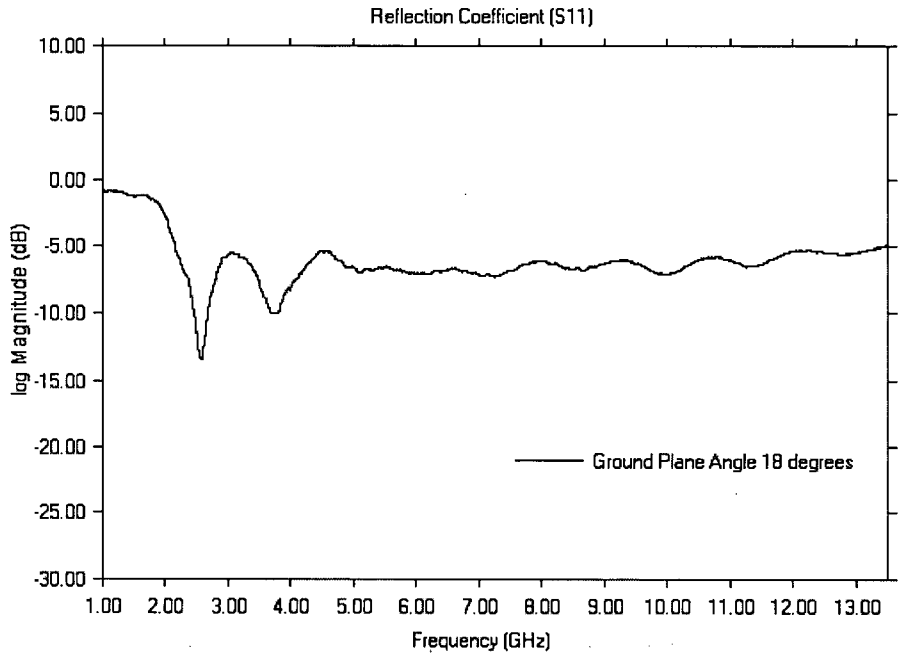

Figure A3: S_{11} Reflection Coefficient for FDL Antenna for Flare Angles of 18 degrees

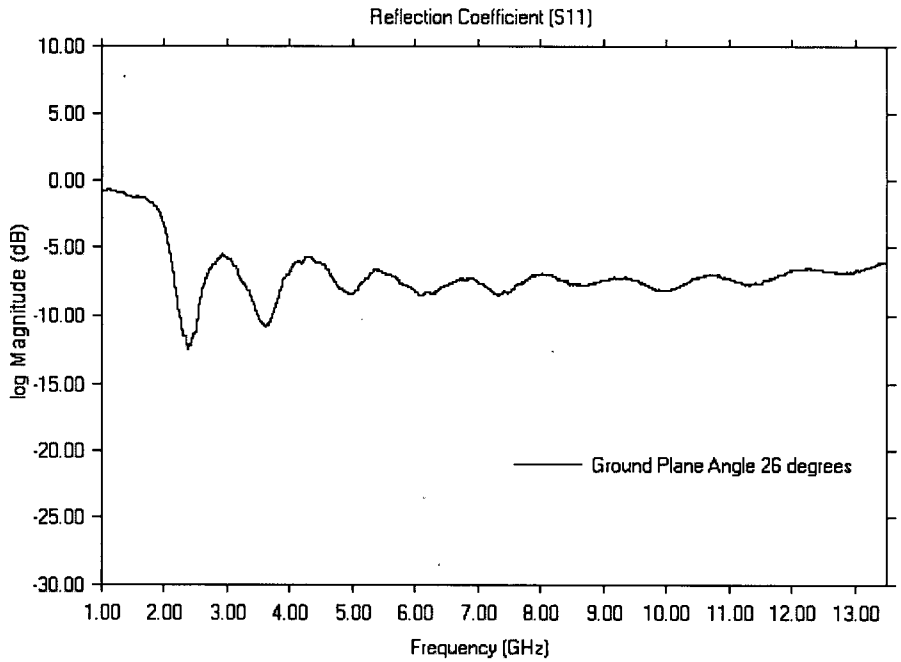

Figure A4: S_{11} Reflection Coefficient for FDL Antenna for Flare Angles of 26 degrees

Appendix A - FDL S_{11} Reflection Coefficient *vs.* Flair Angle for Flat Ground Planes

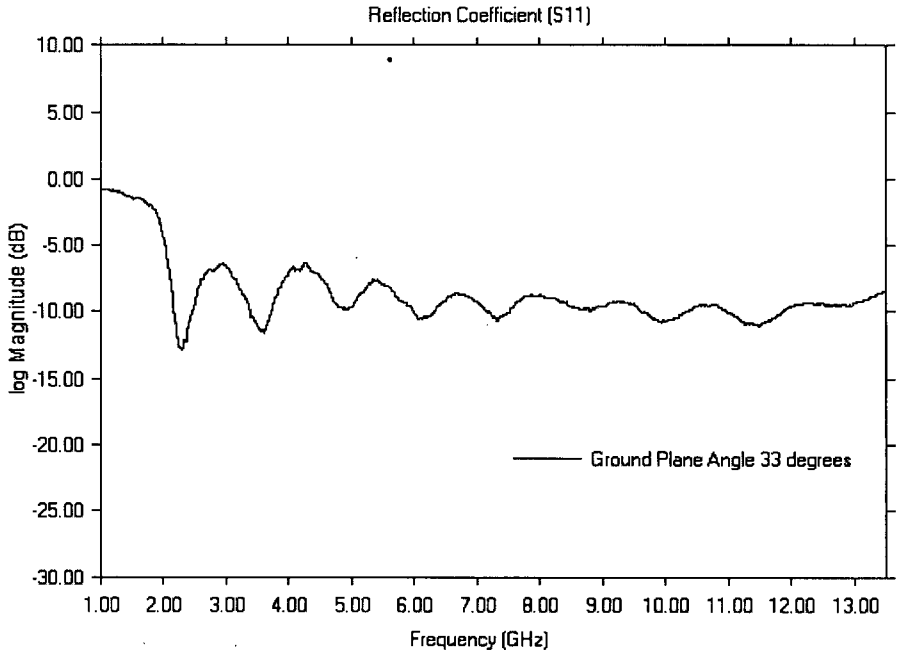

Figure A5: S_{11} Reflection Coefficient for FDL Antenna for Flare Angles of 33 degrees

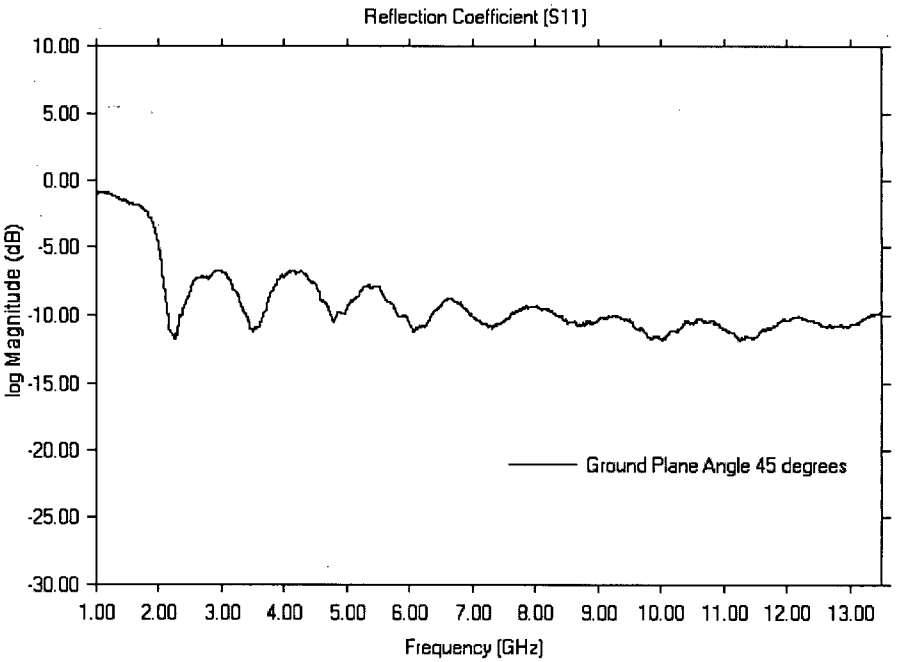

Figure A6: S_{11} Reflection Coefficient for FDL Antenna for Flare Angles of 45 degrees

Appendix A - FDL S_{11} Reflection Coefficient *vs.* Flair Angle for Flat Ground Planes

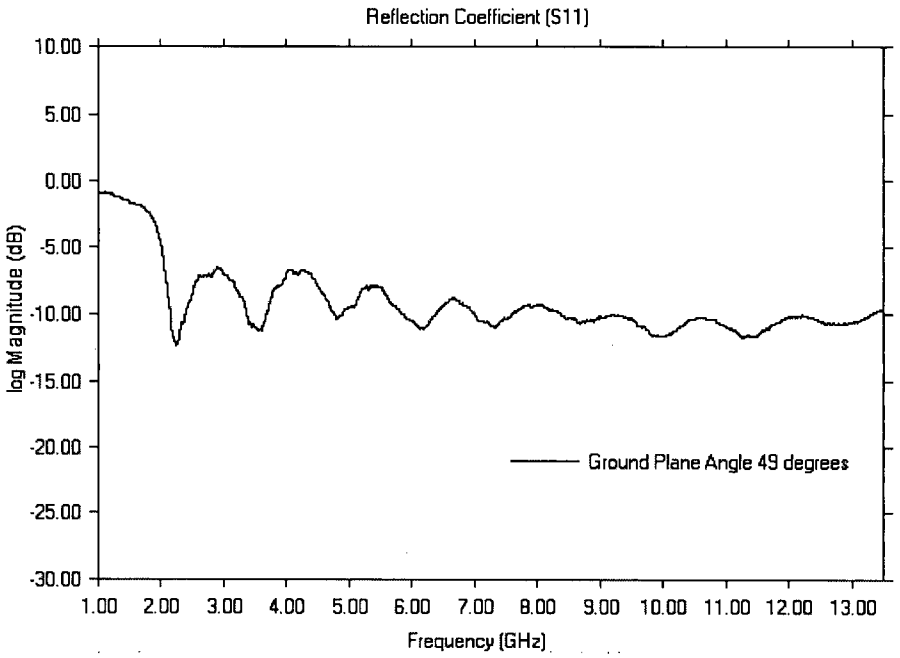

Figure A7: S_{11} Reflection Coefficient for FDL Antenna for Flare Angles of 49 degrees

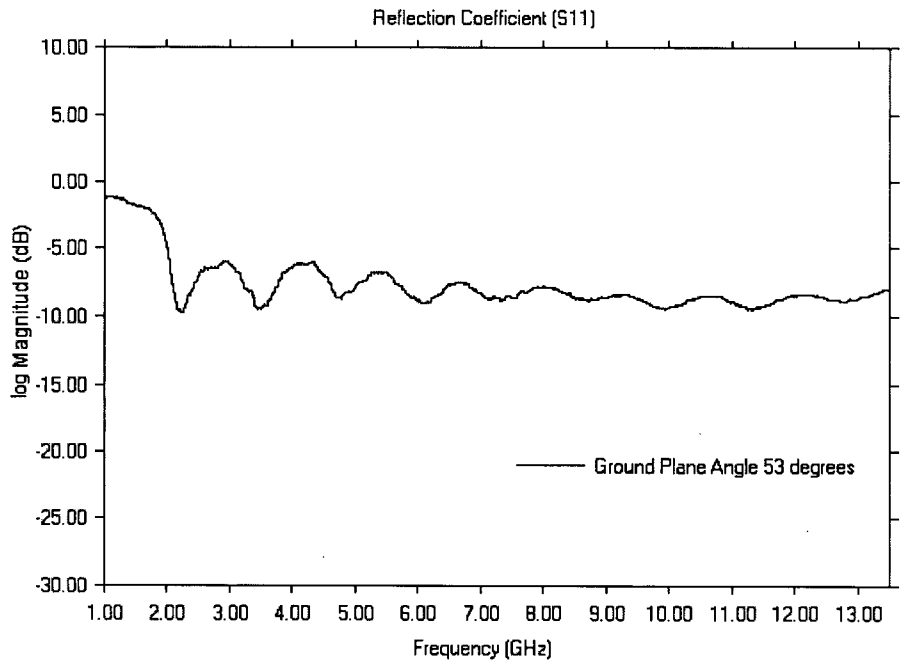

Figure A8: S_{11} Reflection Coefficient for FDL Antenna for Flare Angles of 53 degrees

Appendix B - Example FEKO Model Creation File For FDL Antenna

```
** Default PRE file for radiation problems
** Date created:    March 13 2003

** Variables
**   Optional scaling factor (e.g. set to 0.001 if all geometrical
**   coordinates etc. are to be defined in mm instead of metres)
#scaling = 1
**   Frequency and wavelength
#freq =1.5e10              ** frequency in Hertz
#lam = #c0/#freq       ** wavelength in metre,  #c0 = speed of light in vacuum
#lam = #lam/#scaling   ** scale the wavelength as desired (e.g. to mm)

** Parameters for segmentation
#seg_rad = #lam/1000   ** radius of the wire segments
#seg_len = #lam/10     ** maximum length of wire segments
#tri_len = #lam/12     ** maximum edge length for triangular patches
IP                              #seg_rad  #tri_len  #seg_len

** Geometry of radiating structure
** A FEMAP model may be included with the IN card
** IN   1  3  "filename.ext"

**  Add feed points
DP   GAM1                       0.0000    -0.0025   0.00250
DP   GAM2                       0.0000    -0.0025   -0.00250

DP   GBM1                       0.0000    0.0025    0.00250
DP   GBM2                       0.0000    0.0025    -0.00250

DP   GA1                        0.0000    -0.0025   0.0250
DP   GA2                        0.0000    -0.0025   -0.0250
DP   GA3                        0.0050    -0.0035   0.0115
DP   GA4                        0.0050    -0.0035   -0.0115
DP   GA5                        0.0100    -0.0046   0.0070
DP   GA6                        0.0100    -0.0046   -0.0070
DP   GA7                        0.0150    -0.0058   0.0044
DP   GA8                        0.0150    -0.0058   -0.0044
DP   GA9                        0.0200    -0.0072   0.0030
DP   GA10                       0.0200    -0.0072   -0.0030
DP   GA11                       0.0250    -0.0086   0.0025
DP   GA12                       0.0250    -0.0086   -0.0025
DP   GA13                       0.0300    -0.0102   0.0025
DP   GA14                       0.0300    -0.0102   -0.0025
DP   GA15                       0.0350    -0.0120   0.0025
DP   GA16                       0.0350    -0.0120   -0.0024
DP   GA17                       0.0400    -0.0140   0.0025
DP   GA18                       0.0400    -0.0140   -0.0022
DP   GA19                       0.0450    -0.0161   0.0027
DP   GA20                       0.0450    -0.0161   -0.0019
DP   GA21                       0.0500    -0.0185   0.0037
DP   GA22                       0.0500    -0.0185   -0.0017
DP   GA23                       0.0550    -0.0211   0.0058
DP   GA24                       0.0550    -0.0211   -0.0014
```

Appendix B - Example FEKO Model Creation File For FDL Antenna

```
DP   GA25                    0.0600    -0.0239   0.0094
DP   GA26                    0.0600    -0.0239   -0.0012
DP   GA27                    0.0650    -0.0271   0.0162
DP   GA28                    0.0650    -0.0271   -0.0009
DP   GA29                    0.0700    -0.0306   0.0303
DP   GA30                    0.0700    -0.0306   -0.0006
DP   GA31                    0.0750    -0.0344   0.0392
DP   GA32                    0.0750    -0.0344   -0.0004
DP   GA33                    0.0800    -0.0386   0.0410
DP   GA34                    0.0800    -0.0386   -0.0001
DP   GA35                    0.0850    -0.0432   0.0410
DP   GA36                    0.0850    -0.0432   0.0002
DP   GA37                    0.0900    -0.0483   0.0410
DP   GA38                    0.0900    -0.0483   0.0004
DP   GA39                    0.0950    -0.0539   0.0410
DP   GA40                    0.0950    -0.0539   0.0007
DP   GA41                    0.1000    -0.0600   0.0410
DP   GA42                    0.1000    -0.0600   0.0010
DP   GA43                    0.1050    -0.0668   0.0410
DP   GA44                    0.1050    -0.0668   0.0013

LA   1

PM   GA1  GA3  GA4  GA2      GAM2      GAM1
PM   GA3  GA5  GA6  GA4
PM   GA5  GA7  GA8  GA6
PM   GA7  GA9  GA10 GA8
PM   GA9  GA11 GA12 GA10
PM   GA11 GA13 GA14 GA12
PM   GA13 GA15 GA16 GA14
PM   GA15 GA17 GA18 GA16
PM   GA17 GA19 GA20 GA18
PM   GA19 GA21 GA22 GA20
PM   GA21 GA23 GA24 GA22
PM   GA23 GA25 GA26 GA24
PM   GA25 GA27 GA28 GA26
PM   GA27 GA29 GA30 GA28
PM   GA29 GA31 GA32 GA30
PM   GA31 GA33 GA34 GA32
PM   GA33 GA35 GA36 GA34
PM   GA35 GA37 GA38 GA36
PM   GA37 GA39 GA40 GA38
PM   GA39 GA41 GA42 GA40
PM   GA41 GA43 GA44 GA42

DP   GB1                     0.0000    0.0025    0.0250
DP   GB2                     0.0000    0.0025    -0.0250
DP   GB3                     0.0050    0.0035    0.0115
DP   GB4                     0.0050    0.0035    -0.0115
DP   GB5                     0.0100    0.0046    0.0070
DP   GB6                     0.0100    0.0046    -0.0070
DP   GB7                     0.0150    0.0058    0.0044
DP   GB8                     0.0150    0.0058    -0.0044
```

Appendix B - Example FEKO Model Creation File For FDL Antenna

```
DP   GB9                    0.0200    0.0072    0.0030
DP   GB10                   0.0200    0.0072    -0.0030
DP   GB11                   0.0250    0.0086    0.0025
DP   GB12                   0.0250    0.0086    -0.0025
DP   GB13                   0.0300    0.0102    0.0025
DP   GB14                   0.0300    0.0102    -0.0025
DP   GB15                   0.0350    0.0120    0.0025
DP   GB16                   0.0350    0.0120    -0.0024
DP   GB17                   0.0400    0.0140    0.0025
DP   GB18                   0.0400    0.0140    -0.0022
DP   GB19                   0.0450    0.0161    0.0027
DP   GB20                   0.0450    0.0161    -0.0019
DP   GB21                   0.0500    0.0185    0.0037
DP   GB22                   0.0500    0.0185    -0.0017
DP   GB23                   0.0550    0.0211    0.0058
DP   GB24                   0.0550    0.0211    -0.0014
DP   GB25                   0.0600    0.0239    0.0094
DP   GB26                   0.0600    0.0239    -0.0012
DP   GB27                   0.0650    0.0271    0.0162
DP   GB28                   0.0650    0.0271    -0.0009
DP   GB29                   0.0700    0.0306    0.0303
DP   GB30                   0.0700    0.0306    -0.0006
DP   GB31                   0.0750    0.0344    0.0392
DP   GB32                   0.0750    0.0344    -0.0004
DP   GB33                   0.0800    0.0386    0.0410
DP   GB34                   0.0800    0.0386    -0.0001
DP   GB35                   0.0850    0.0432    0.0410
DP   GB36                   0.0850    0.0432    0.0002
DP   GB37                   0.0900    0.0483    0.0410
DP   GB38                   0.0900    0.0483    0.0004
DP   GB39                   0.0950    0.0539    0.0410
DP   GB40                   0.0950    0.0539    0.0007
DP   GB41                   0.1000    0.0600    0.0410
DP   GB42                   0.1000    0.0600    0.0010
DP   GB43                   0.1050    0.0668    0.0410
DP   GB44                   0.1050    0.0668    0.0013

LA   3

PM   GB1  GB3  GB4  GB2        GBM2      GBM1
PM   GB3  GB5  GB6  GB4
PM   GB5  GB7  GB8  GB6
PM   GB7  GB9  GB10 GB8
PM   GB9  GB11 GB12 GB10
PM   GB11 GB13 GB14 GB12
PM   GB13 GB15 GB16 GB14
PM   GB15 GB17 GB18 GB16
PM   GB17 GB19 GB20 GB18
PM   GB19 GB21 GB22 GB20
PM   GB21 GB23 GB24 GB22
PM   GB23 GB25 GB26 GB24
PM   GB25 GB27 GB28 GB26
PM   GB27 GB29 GB30 GB28
```

Appendix B - Example FEKO Model Creation File For FDL Antenna

```
PM   GB29 GB31 GB32 GB30
PM   GB31 GB33 GB34 GB32
PM   GB33 GB35 GB36 GB34
PM   GB35 GB37 GB38 GB36
PM   GB37 GB39 GB40 GB38
PM   GB39 GB41 GB42 GB40
PM   GB41 GB43 GB44 GB42

DP   AM0                    0.0000    0.0000    0.0000
DP   AM1                    0.0000    0.0000    -0.0025
DP   AM2                    0.0000    0.0000    0.0025
DP   AM3                    0.0050    0.0000    -0.0025
DP   AM4                    0.0050    0.0000    0.0025
DP   AM5                    0.0100    0.0000    -0.0025
DP   AM6                    0.0100    0.0000    0.0025
DP   AM7                    0.0150    0.0000    -0.0025

DP   AM8                    0.0150    0.0000    0.0025
DP   AM9                    0.0200    0.0000    -0.0025
DP   AM10                   0.0200    0.0000    0.0025
DP   AM11                   0.0250    0.0000    -0.0025
DP   AM12                   0.0250    0.0000    0.0025
DP   AM13                   0.0300    0.0000    -0.0025
DP   AM14                   0.0300    0.0000    0.0025
DP   AM15                   0.0350    0.0000    -0.0025
DP   AM16                   0.0350    0.0000    0.0024
DP   AM17                   0.0400    0.0000    -0.0025
DP   AM18                   0.0400    0.0000    0.0022
DP   AM19                   0.0450    0.0000    -0.0027
DP   AM20                   0.0450    0.0000    0.0019
DP   AM21                   0.0500    0.0000    -0.0037
DP   AM22                   0.0500    0.0000    0.0017
DP   AM23                   0.0550    0.0000    -0.0058
DP   AM24                   0.0550    0.0000    0.0014
DP   AM25                   0.0600    0.0000    -0.0094
DP   AM26                   0.0600    0.0000    0.0012
DP   AM27                   0.0650    0.0000    -0.0162
DP   AM28                   0.0650    0.0000    0.0009
DP   AM29                   0.0700    0.0000    -0.0303
DP   AM30                   0.0700    0.0000    0.0006
DP   AM31                   0.0750    0.0000    -0.0392
DP   AM32                   0.0750    0.0000    0.0004
DP   AM33                   0.0800    0.0000    -0.0410
DP   AM34                   0.0800    0.0000    0.0001
DP   AM35                   0.0850    0.0000    -0.0410
DP   AM36                   0.0850    0.0000    -0.0002
DP   AM37                   0.0900    0.0000    -0.0410
DP   AM38                   0.0900    0.0000    -0.0004
DP   AM39                   0.0950    0.0000    -0.0410
DP   AM40                   0.0950    0.0000    -0.0007
DP   AM41                   0.1000    0.0000    -0.0410
DP   AM42                   0.1000    0.0000    -0.0010
DP   AM43                   0.1050    0.0000    -0.0410
```

Appendix B - Example FEKO Model Creation File For FDL Antenna

```
DP   AM44                      0.1050     0.0000     -0.0013

LA   2

BT   AM0  AM4  AM2
BT   AM0  AM3  AM4
BT   AM0  AM1  AM3
PM   AM3  AM5  AM6  AM4
PM   AM5  AM7  AM8  AM6
PM   AM7  AM9  AM10 AM8
PM   AM9  AM11 AM12 AM10
PM   AM11 AM13 AM14 AM12
PM   AM13 AM15 AM16 AM14
PM   AM15 AM17 AM18 AM16
PM   AM17 AM19 AM20 AM18
PM   AM19 AM21 AM22 AM20
PM   AM21 AM23 AM24 AM22
PM   AM23 AM25 AM26 AM24
PM   AM25 AM27 AM28 AM26
PM   AM27 AM29 AM30 AM28
PM   AM29 AM31 AM32 AM30
PM   AM31 AM33 AM34 AM32
PM   AM33 AM35 AM36 AM34
PM   AM35 AM37 AM38 AM36
PM   AM37 AM39 AM40 AM38
PM   AM39 AM41 AM42 AM40
PM   AM41 AM43 AM44 AM42

**  Add connecting strips
LA   0
PM   GBM1 GBM2 AM1  AM0        AM2
PM   GAM1 GAM2 AM1  AM0        AM2

** Apply the scaling factor
SF   1                         #scaling

** End of geometric input
EG   1    0    0    0    0
** Greens Functions for Homogenous space
GF   0
** Set the frequency
FR   1    0                   15e9       500e6
** Voltage gap excitation at end of active member
AE   0    0    2    0         1          0
** Radiation patterns calculated with the FF card
FF   1    360  360  0         0          0          1
** SParameters calculated with the SP card
SP                             50
EN
```

Appendix C - 1GHz to 13.5 GHz Results for Model Heights 0 to 91 cm

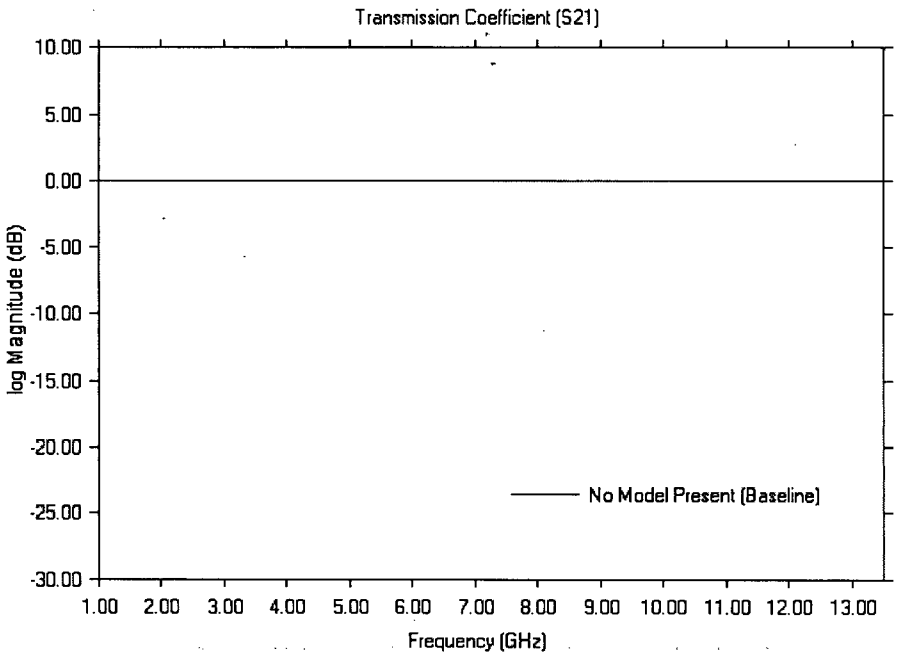

Figure C1: Transmission Coefficient S_{21} spectrum showing baseline with no model present

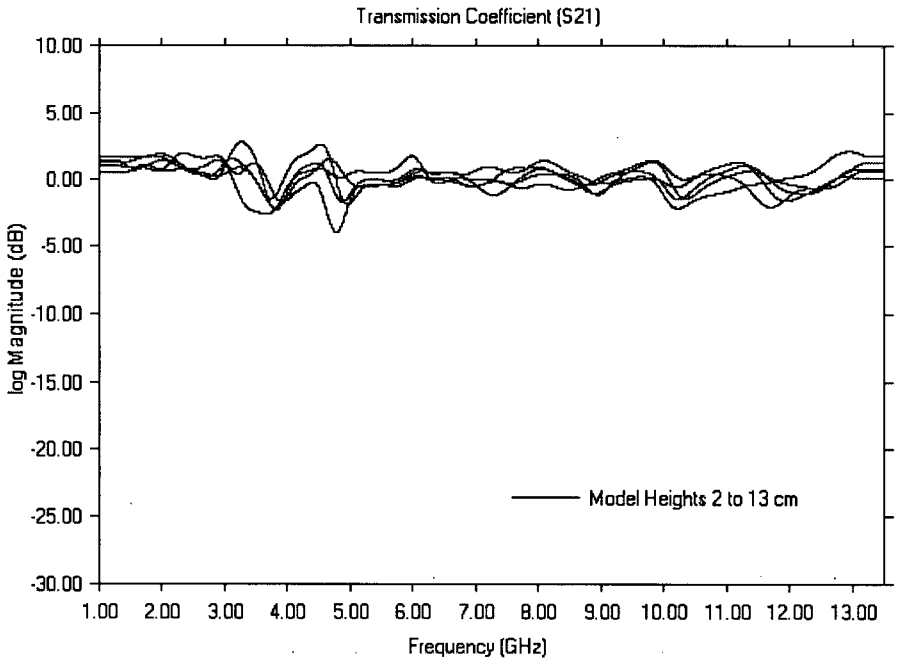

Figure C2: Transmission Coefficient S_{21} spectrum for Model Heights 2 to 13 cm

Appendix C - 1GHz to 13.5 GHz Results for Model Heights 0 to 91 cm

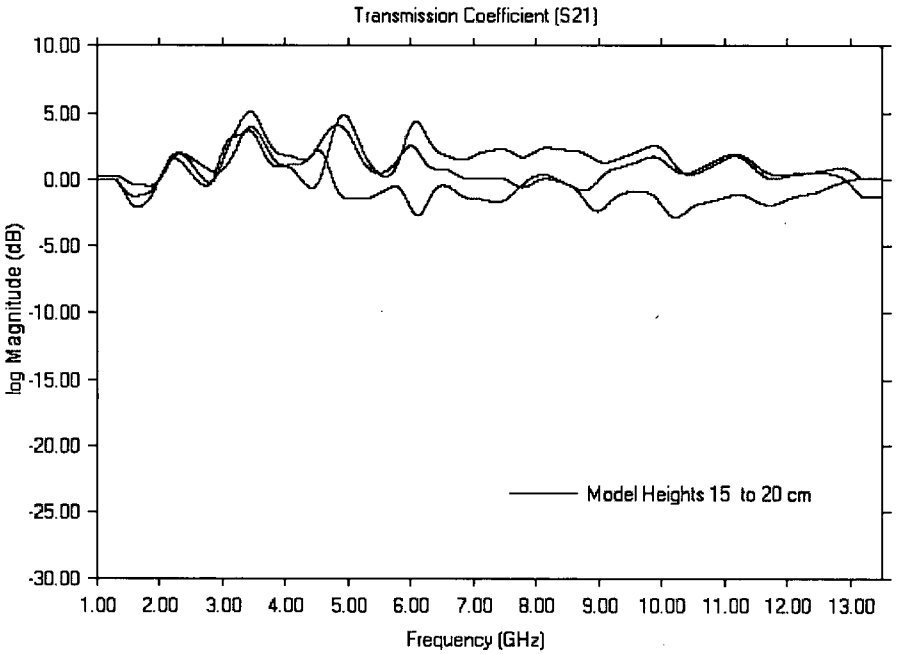

Figure C3: Transmission Coefficient S_{21} spectrum for Model Heights 15 to 20 cm

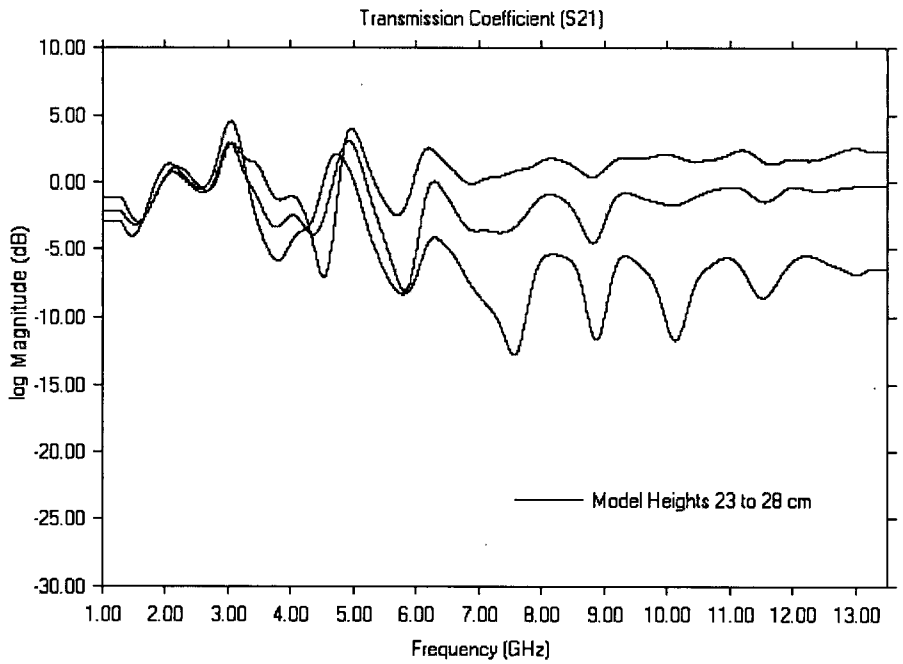

Figure C4: Transmission Coefficient S_{21} spectrum for Model Heights 23 to 28 cm

Appendix C - 1GHz to 13.5 GHz Results for Model Heights 0 to 91 cm

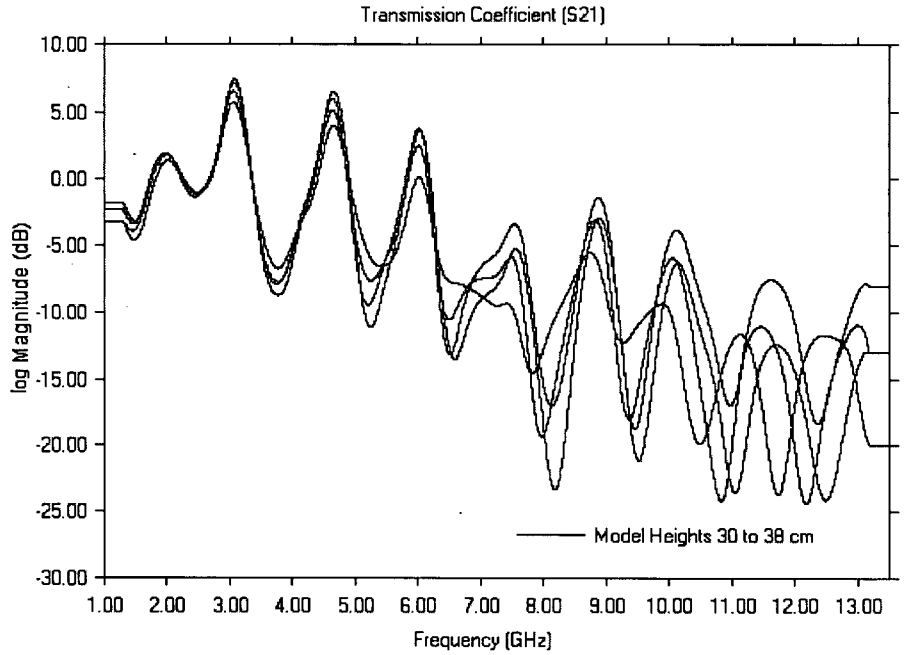

Figure C5: Transmission Coefficient S_{21} spectrum for Model Heights 30 to 38 cm

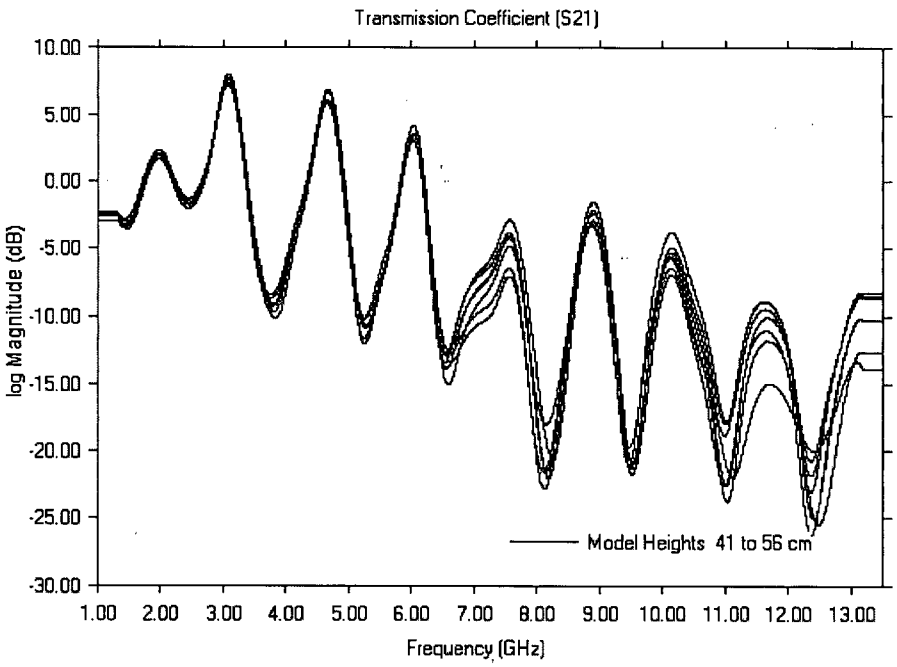

Figure C6: Transmission Coefficient S_{21} spectrum for Model Heights 41 to 56 cm

Appendix C - 1GHz to 13.5 GHz Results for Model Heights 0 to 91 cm

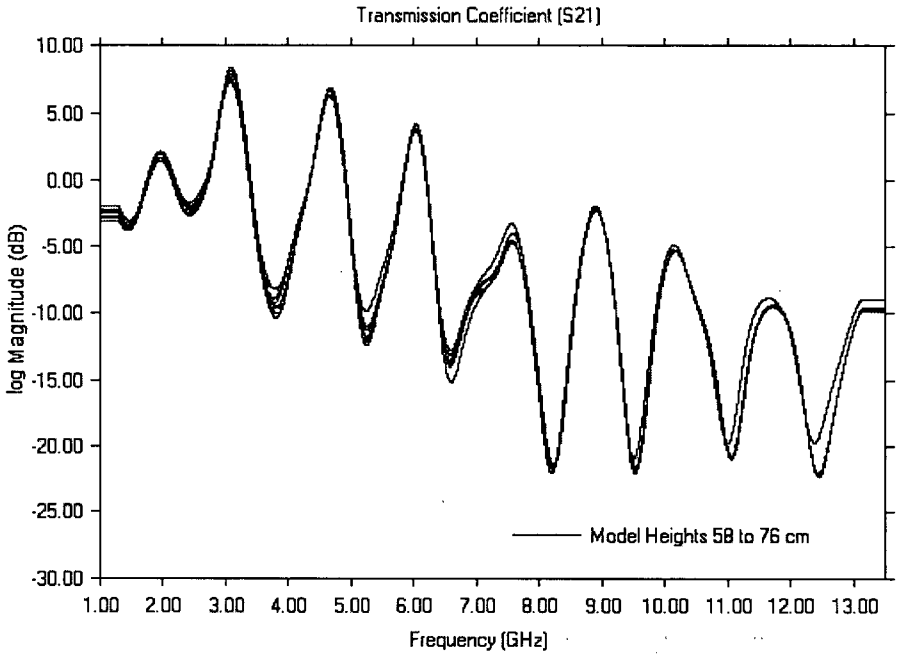

Figure C7: Transmission Coefficient S_{21} spectrum for Model Heights 58 to 76 cm

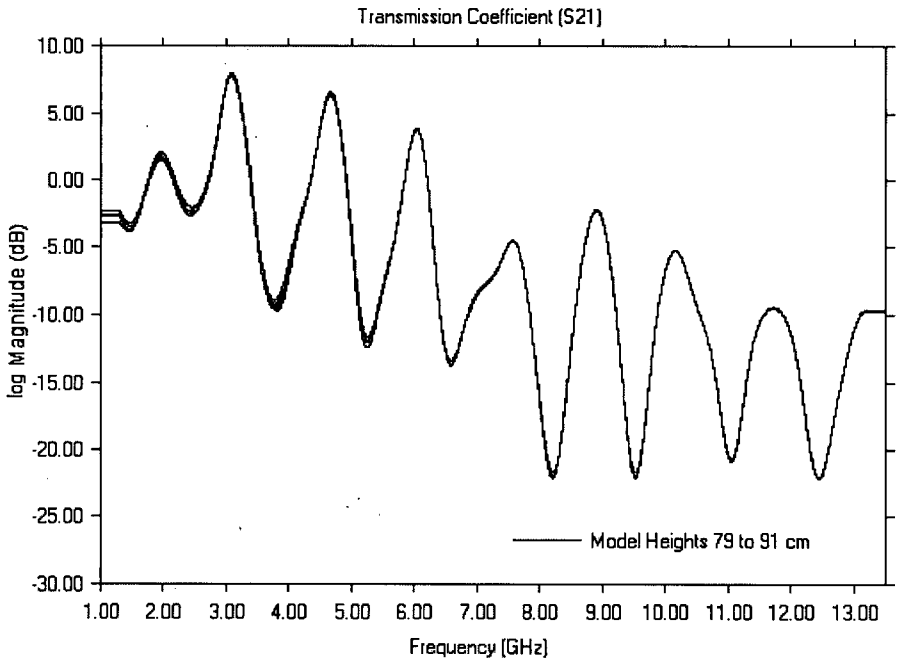

Figure C8: Transmission Coefficient S_{21} spectrum for Model Heights 79 to 91 cm

Appendix D - Cougar A2CP12029 Wideband Amplifier Specifications

COUGAR COMPONENTS

PRELIMINARY

A2CP12029 6.0 TO 12.0 GHz SMA CASCADED AMPLIFIER

Typical Values	A2CP12029
High Gain	23.0 dB
High Output Level	0.5 Watt
High Third Order I.P.	+37 dBm
High Second Order I.P.	+51 dBm
High Reverse Isolation	35 dB

High Performance Thin Film
CougarPak™ SMA Package

A2CP12029

CougarPak™ SMA Package
(two-stage)

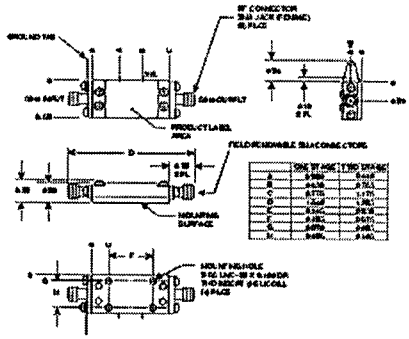

SPECIFICATIONS

Parameter	Typical	Guaranteed* 0 to 50° C	Guaranteed* -55 to +85° C
Frequency (Min.)	6.0-12.0 GHz	6.0-12.0 GHz	6.0-12.0 GHz
Small Signal Gain (Min.)	23.0 dB	20.5 dB	20.0 dB
Gain Flatness (Max.)	±0.8 dB	±1.0 dB	±1.2 dB
Noise Figure (Max.)	4.0 dB	4.5 dB	5.0 dB
SWR (Max.) Input/Output	1.8:1	2.0:1	2.0:1
Power Output (Min.) @ 1dB comp.	+27.5 dBm	+26.5 dBm	+26.0 dBm
Reverse Isolation	35 dB	—	—
DC Current (Max.)	335 mA	342 mA	350 mA

* Measured in a 50-ohm system at +10 Vdc unless otherwise specified.

INTERMODULATION PERFORMANCE

Typical @ 25° C	A2CP12029
Second Order Harmonic Intercept Point	+57 dBm
Second Order Two Tone Intercept Point	+51 dBm
Third Order Two Tone Intercept Point	+37 dBm

ABSOLUTE MAXIMUM RATINGS

Storage Temperature	-62 to 125° C
Maximum Case Temperature	+85° C
Maximum DC Voltage	+12 Volts
Maximum Continuous RF Input Power	+16 dBm
Maximum Short Term Input Power (1 Minute Max.)	100 Milliwatts
Maximum Peak Power (3 µsec Max.)	0.5 Watt
Q Series Burn-In Temperature	+85°C
Thermal Resistance[1] (θjc)	+18.2° C/Watt
Junction Temperature Rise Above Case (Tjc)	+62.1° C

[1] Thermal resistance is based on total power dissipation.

Figure D1: Cougar A2CP12029 Specifications

Appendix D - Cougar A2CP12029 Wideband Amplifier Specifications

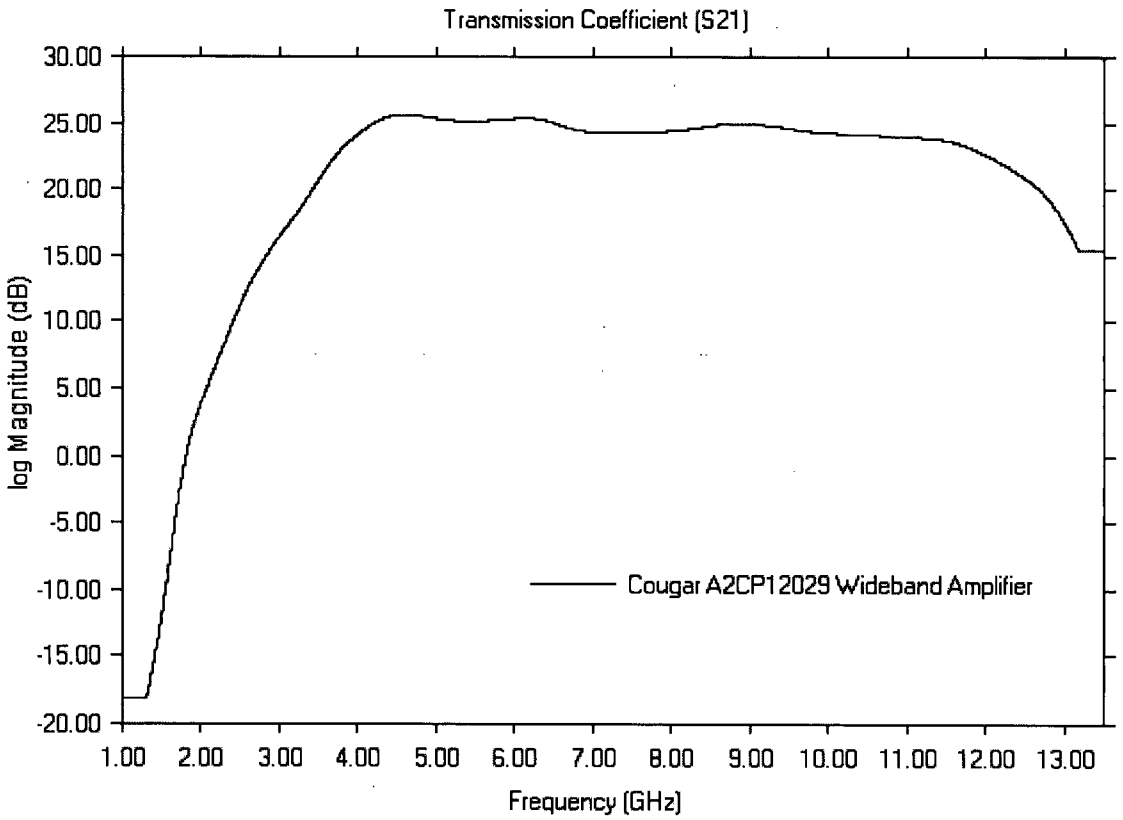

Figure D2: Transmission Coefficient S_{21} versus Frequency for Cougar A2CP12029

Appendix E - Spectral Curve Matching Algorithm Code

```
//Match: Two curves are compared for "similarity" in shape.  This algorithm is
//based on attempting to match two curves by matching similarity in the general
//shapes of the curves but allowing for offsets and minor inconsistencies.

procedure Match;
var
 i,j,k: integer;           //temporary loop variables
 model1,model2 : integer;  //temporary index for two models currently being compared
 pc : integer;             //PlusCount index counter for walk on curve in increasing
                           //direction
 mc : integer;             //MinusCount index counter for walk on curve in //decreasing
                           direction
 ts : string;              //temporary string conversion variable
 done : boolean;           //exit condition
 delta : real;             //offset between two curves at current +/- frequency
 longest: real             //longest length for match
 dp : real;                //dynamic plus/minus range for testing deltas
 cp : real;                //constant plus minus for testing deltas
 ModelWins : array [0..MaxModels] of integer; //storage array for number of wins
begin
 dp:=0.1;                                      //initialize dynamic range
 cp:=0.01;                                     //initialize constant error limit
 for i:=-5 to MaxModels do                     //for all models in memory
  for j:=0 to numfreq-1 do                     //for all frequencies in spectrum
   for k:=0 to 5 do                            //for all values (mag, log mag, phase)
    MatchData[i,j,k]:=0;                       //zero out all array entries

 for i:=0 to LoadedModels.Items.Count-1 do     //find original curve by looking for
  if LoadedModels.Checked[i] then              //the model checked in the listbox
    model1:=ExtractModelNumber(LoadedModels.Items[i]); //save model index

 for i:=0 to NumFreq-1 do                      //for each frequency across spectrum
  for j:=0 to LoadedModels.Items.Count-1 do    //for each standard model in memory
   begin
    model2:=ExtractModelNumber(LoadedModels.Items[j]); //get model index from list
    //MatchData[,,5] holds original difference between curves at centre frequency
    MatchData[model2,i,5]:=ScanData[model1,i,0]-ScanData[model2,i,0];
    mc:=i;                                     //set mc to point to centre frequency
    done:=false;                               //set loop condition to not done yet
```

Appendix E - Spectral Curve Matching Algorithm Code

```
    //This loop performs the walk along the curves towards the lower frequencies.
    //Start at the given frequency (fCenter) and decrease the index mc by 1 until
    //the magnitude difference between the two curves at frequency index mc is
    //larger or smaller than the magnitude difference between the two curves at the
    //original frequency fCentre.  The difference between the magnitude differences
    //is allowed a small error cp
    while not(done) do                          //while offset match is still valid
     begin
      dec(mc);                                  //move to the next lowest frequency
      delta:=ScanData[model1,mc,0]-ScanData[model2,mc,0];   //calculate delta mag
       if delta<MatchData[model2,i,5]-cp then done:=true;   //if current delta too
       if delta>MatchData[model2,i,5]+cp then done:=true;   //small or too big
       if mc<=0 then done:=true;                            //or out of data then
      end;                                                  //we are done walk

     //This loop performs the same walk as above but in the direction of increasing
     //frequency
     pc:=I;                                     //set pc to current centre frequency
     done:=false;                               //not done yet
     while not(done) do                         //while offset match is still valid
      begin
       inc(pc);                                 //move to next highest frequency
       delta:=ScanData[model1,pc,0]-ScanData[model2,pc,0];  //calculate delta mag
       if delta<MatchData[model2,i,5]-cp then done:=true;   //if current delta too
       if delta>MatchData[model2,i,5]+cp then done:=true;   //small or too big
       if pc>=NumFreq-1 then done:=true;                    //or out of data then
      end;                                                  //we are done walk

    //After we have performed the walk in both directions store the frequency
    //range over which the offset remained relatively constant
    MatchData[model2,i,0]:=pc-mc-2;     //store then length of the match by saving
                                        //high and low ends of the walk pc and mc
  end;

lbMatchData.Clear;                      //clear results window
//Now that all of the lengths of the matching curve sections have been recorded
//go through all of the results and check to see which curves are the best matches.
//The stored match lengths are then compared for all of the test curves at each
//frequency in the spectrum.  The curve which has the longest match length
//at that frequency is said to have "won" that comparison.  What this means is
```

Appendix E - Spectral Curve Matching Algorithm Code

```
//that the curve with the longest match is the curve that is most similar at that
//frequency. The curve which is the best match is the one which has the highest
//number of wins i.e. is the most similar to the sample curve at more points along
//the curve than any of the other curves.

for i:=-5 to MaxModels do ModelWins[i]:=0;    //set all win counts to zero

for j:=0 to NumFreq-1 do                      //at each frequency
 begin
  longest:=0;                                 //set longest length of match to zero
  for i:=0 to LoadedModels.Items.Count-1 do   //for each model in memory
   begin
     model2:=ExtractModelNumber(LoadedModels.Items[i]); //get model number
     if MatchData[model2,j,0]>delta then      //find length of longest match
      begin                                   //at the current frequency
       longest:=MatchData[model2,j,0];        //and save it
      end;
   end;
  for i:=0 to LoadedModels.Items.Count-1 do     //for each model in memory
   begin
    model2:=ExtractModelNumber(LoadedModels.Items[i]); //get model number
     //if this model's match length equals the longest match then it scores a win
     //if more than one model matches the longest length then they each score a win
    if (MatchData[model2,j,0]=longest) then inc(ModelWins[Model2]);
   end;
 end; //end of comparisons for each frequency

  for i:=0 to LoadedModels.Items.Count-1 do                //for model in memory
   begin
     model2:=ExtractModelNumber(LoadedModels.Items[i]);    //get model number
     ts:='Model'+inttostr(model2)+' Wins:'+inttostr(ModelWins[model2]);
     fmMatch.lbMatchData.Items.Add(ts);                    //add wins to output
    end;

fmMatch.Show;                                             //show 'wins' results

end;
```

Appendix F - Transmission Coefficient S_{21} versus Frequency for Standard Models

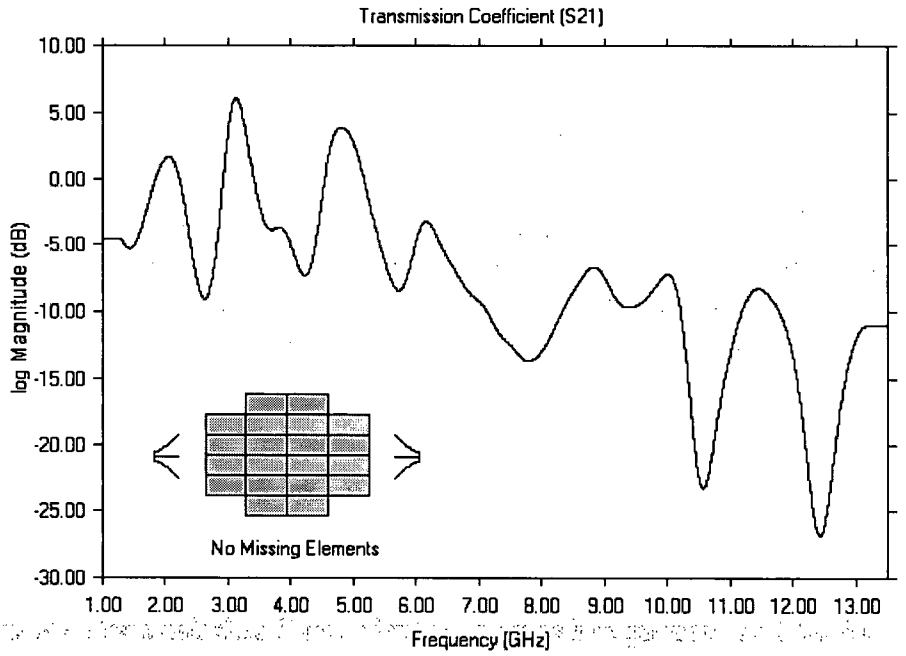

Figure F1: Transmission Coefficient S_{21} spectrum for model M_1

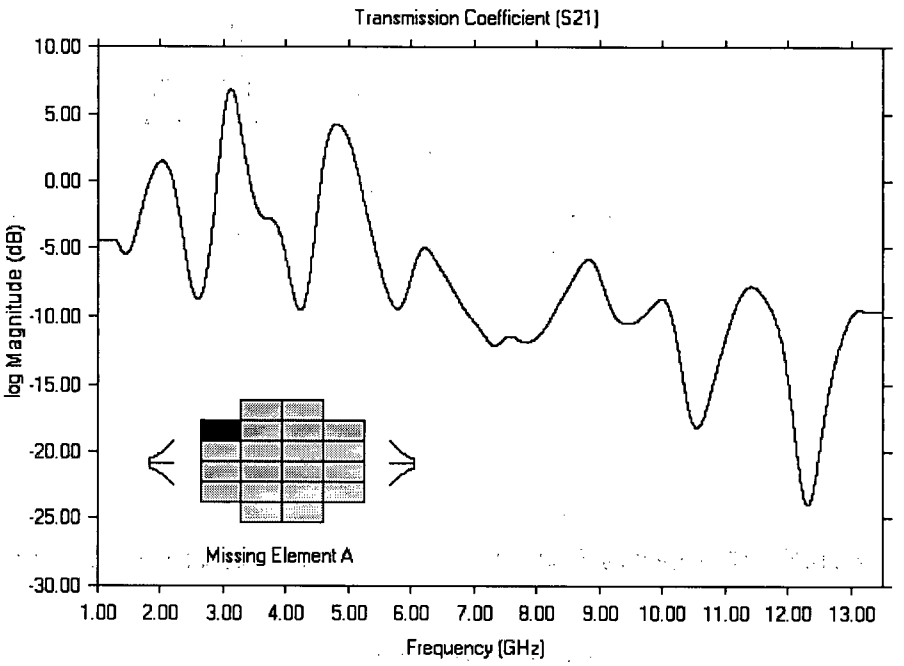

Figure F2: Transmission Coefficient S_{21} spectrum for model M_{1A}

Appendix F - Transmission Coefficient S_{21} versus Frequency for Standard Models

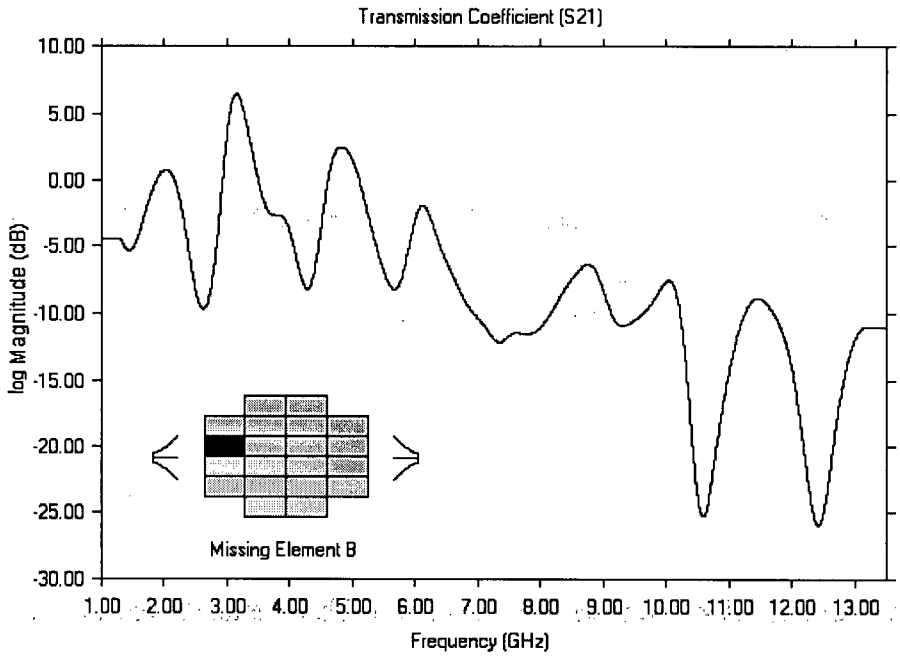

Figure F3: Transmission Coefficient S_{21} spectrum for model M_{1B}

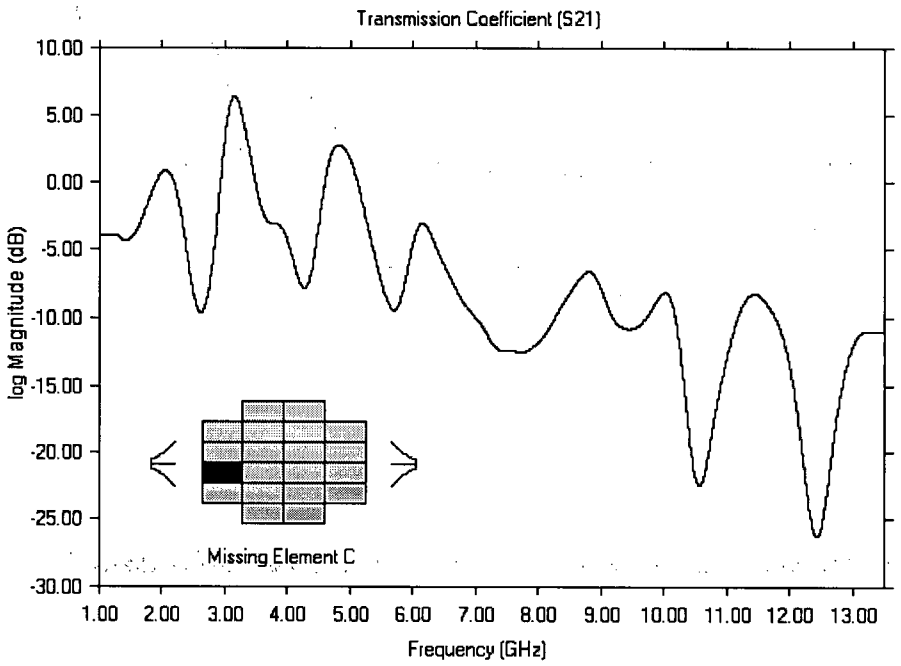

Figure F4: Transmission Coefficient S_{21} spectrum for model M_{1C}

Appendix F - Transmission Coefficient S_{21} versus Frequency for Standard Models

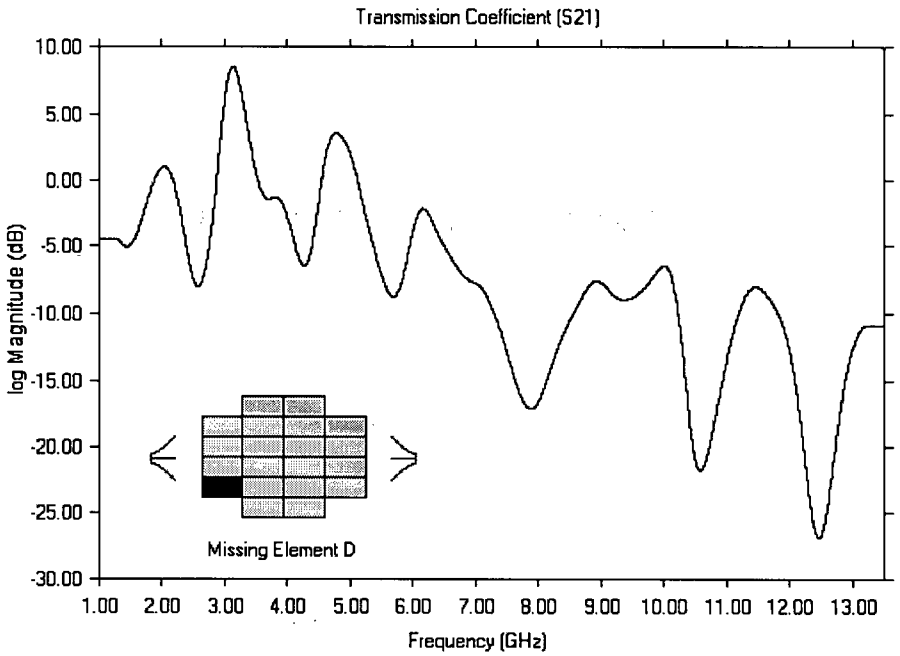

Figure F5: Transmission Coefficient S_{21} spectrum for model M_{1D}

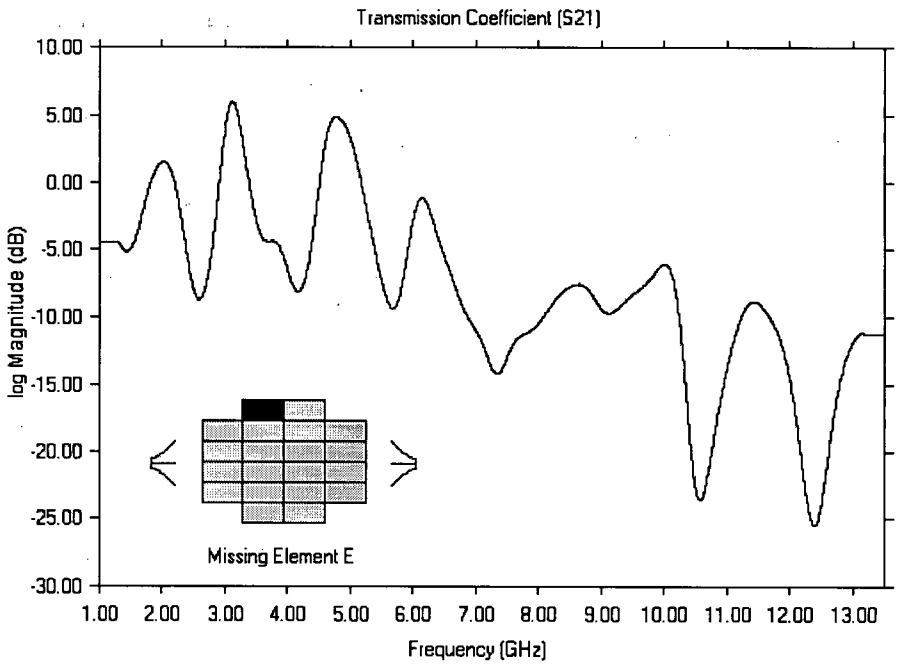

Figure F6: Transmission Coefficient S_{21} spectrum for model M_{1E}

Appendix F - Transmission Coefficient S_{21} versus Frequency for Standard Models

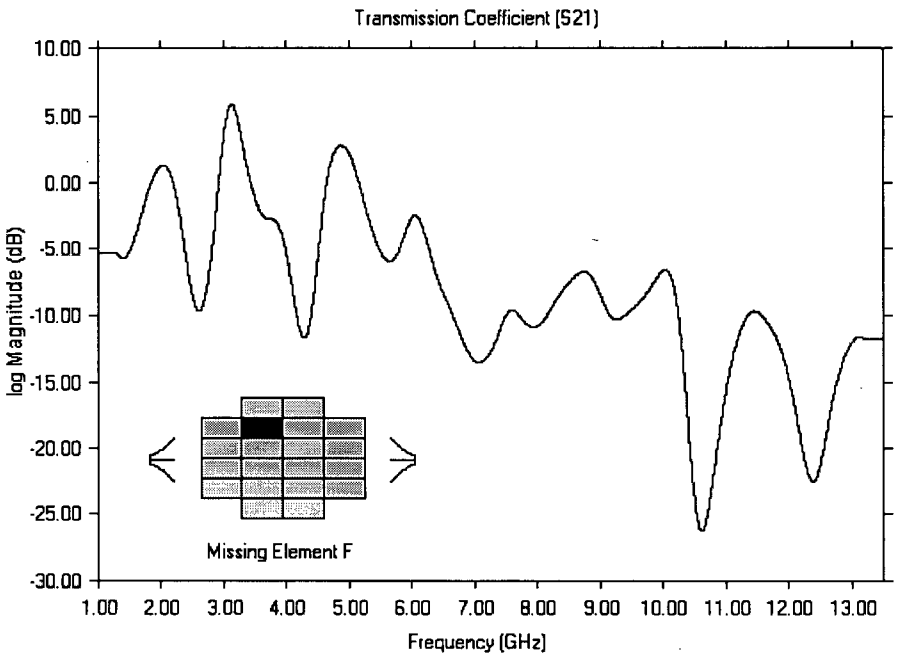

Figure F7: Transmission Coefficient S_{21} spectrum for model M_{1F}

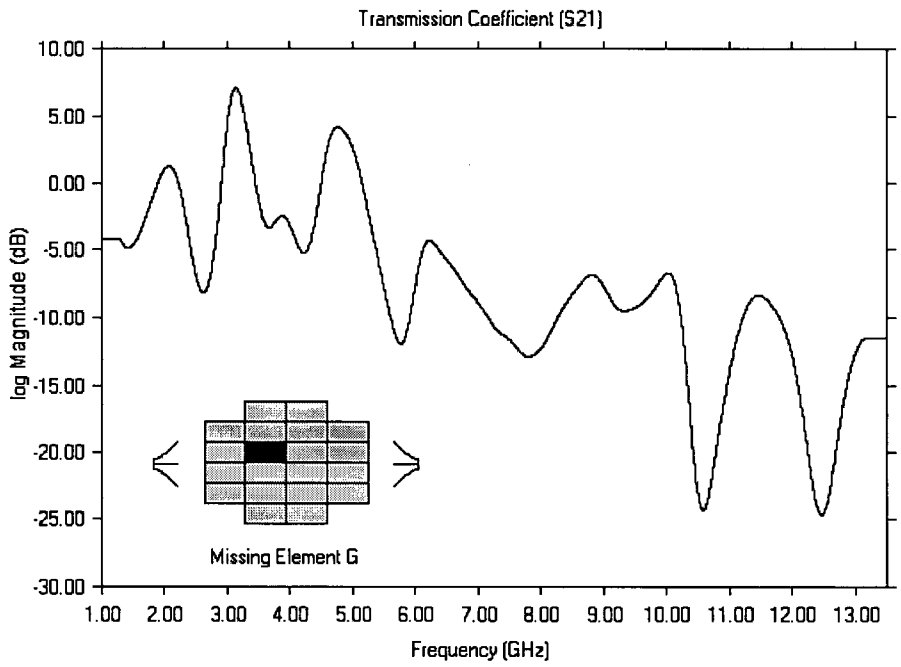

Figure F8: Transmission Coefficient S_{21} spectrum for model M_{1G}

Appendix F - Transmission Coefficient S_{21} versus Frequency for Standard Models

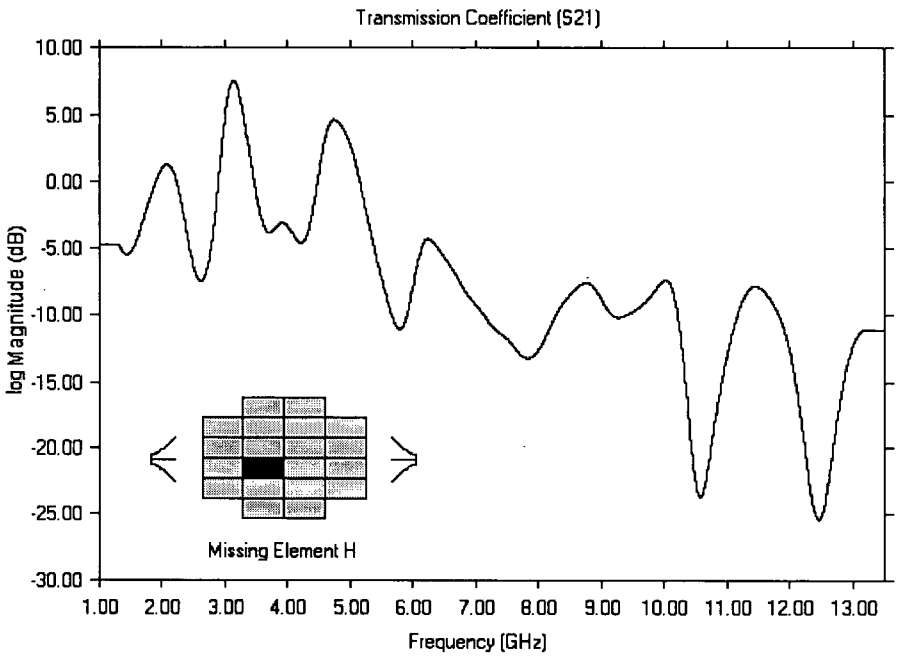

Figure F9: Transmission Coefficient S_{21} spectrum for model M_{1H}

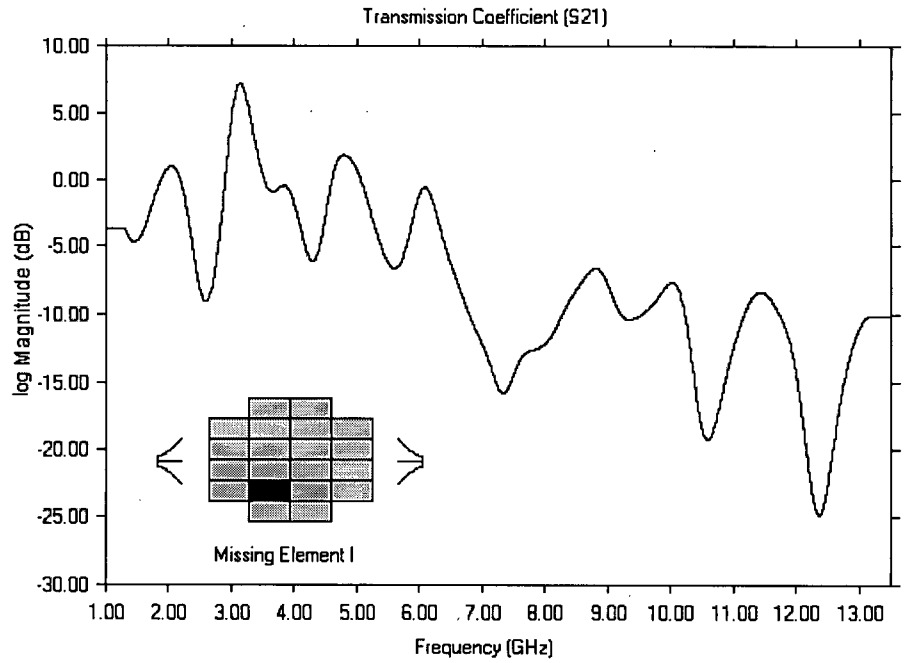

Figure F10: Transmission Coefficient S_{21} spectrum for model M_{1I}

Appendix F - Transmission Coefficient S_{21} versus Frequency for Standard Models

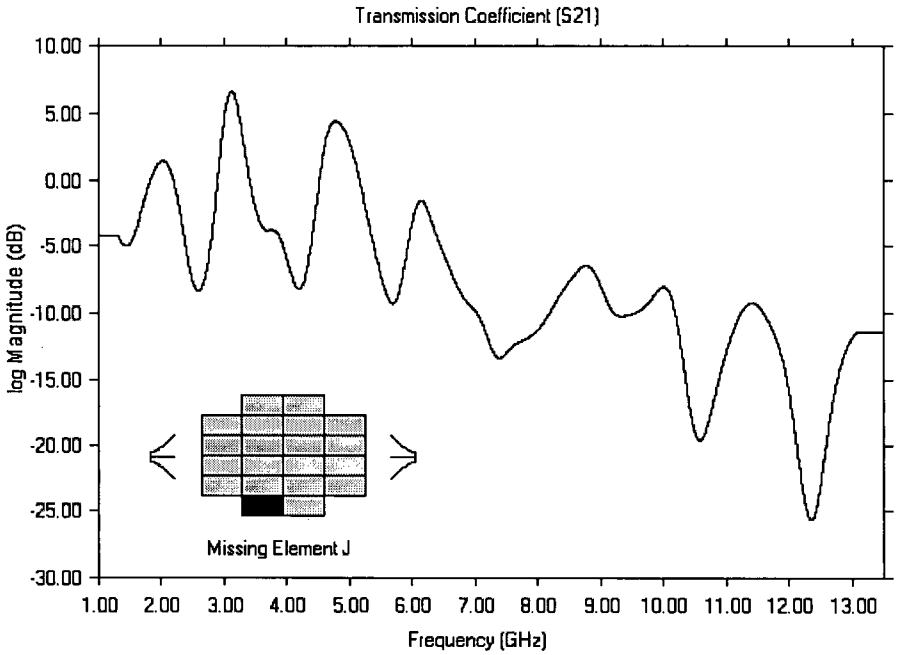

Figure F11: Transmission Coefficient S_{21} spectrum for model M_{1J}

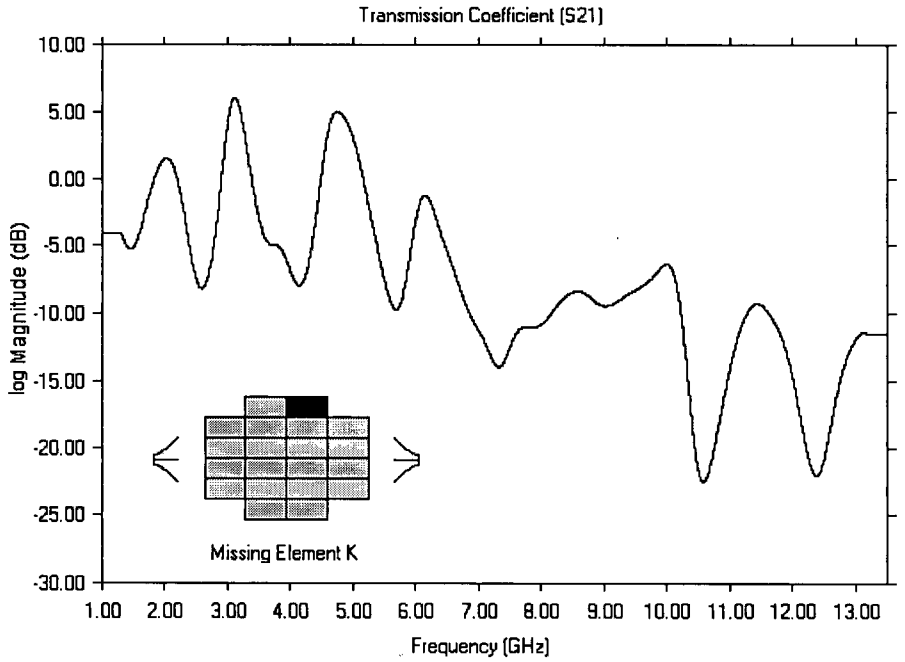

Figure F12: Transmission Coefficient S_{21} spectrum for model M_{1K}

Appendix F - Transmission Coefficient S_{21} versus Frequency for Standard Models

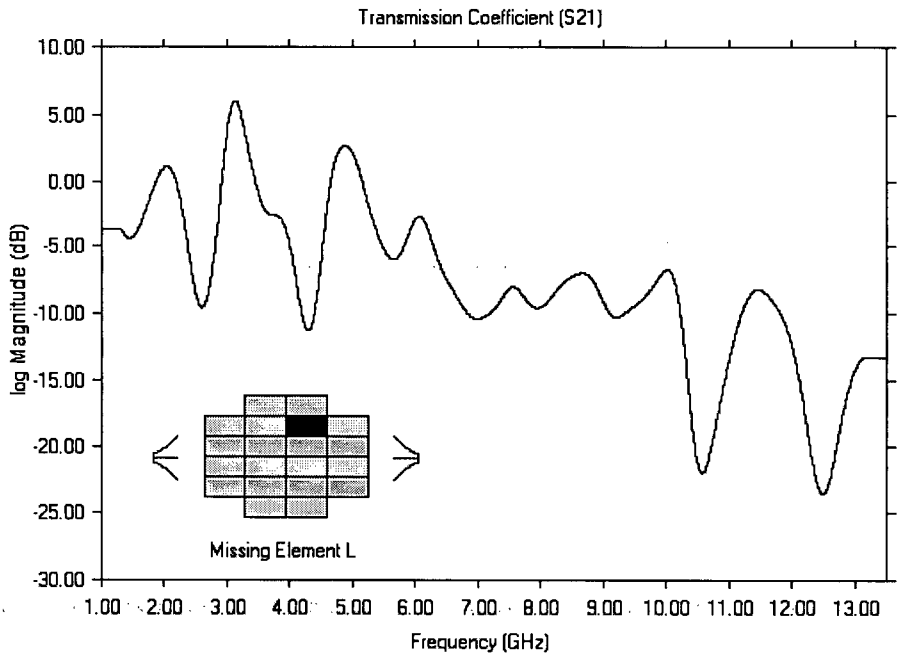

Figure F13: Transmission Coefficient S_{21} spectrum for model M_{1L}

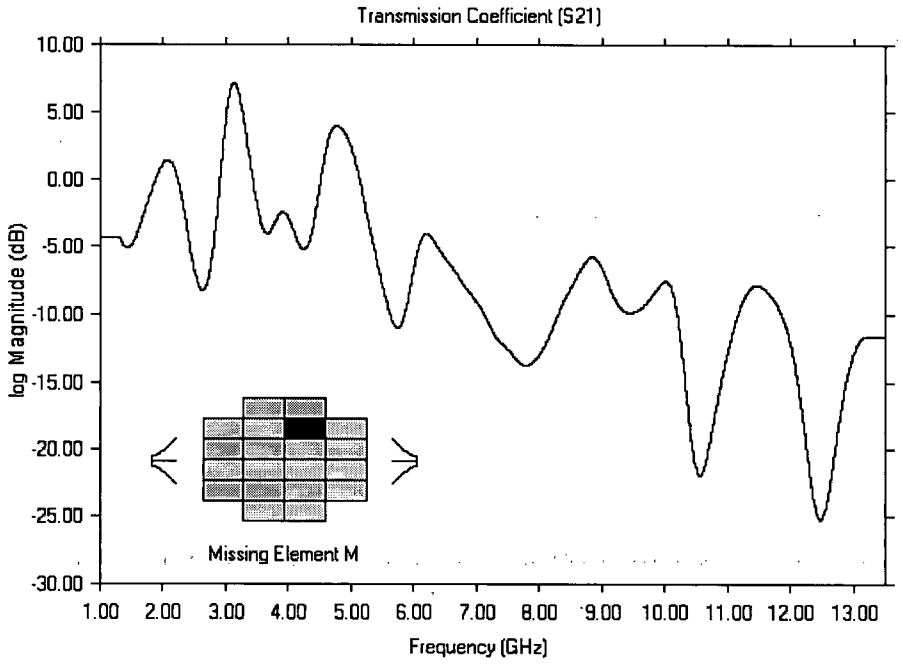

Figure F14: Transmission Coefficient S_{21} spectrum for model M_{1M}

Appendix F - Transmission Coefficient S_{21} versus Frequency for Standard Models

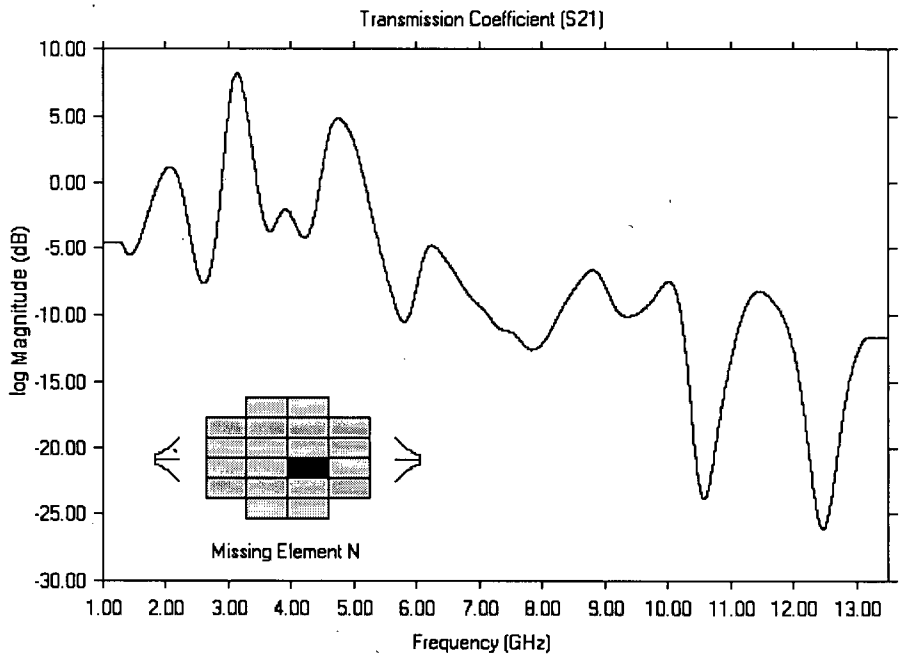

Figure F15: Transmission Coefficient S_{21} spectrum for model M_{1N}

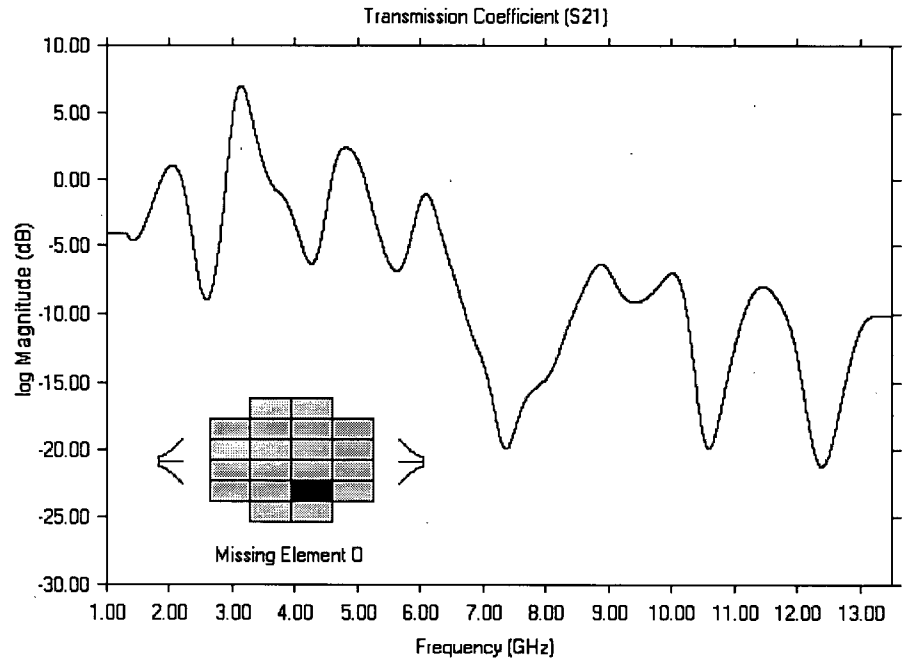

Figure F16: Transmission Coefficient S_{21} spectrum for model M_{1O}

Appendix F - Transmission Coefficient S_{21} versus Frequency for Standard Models

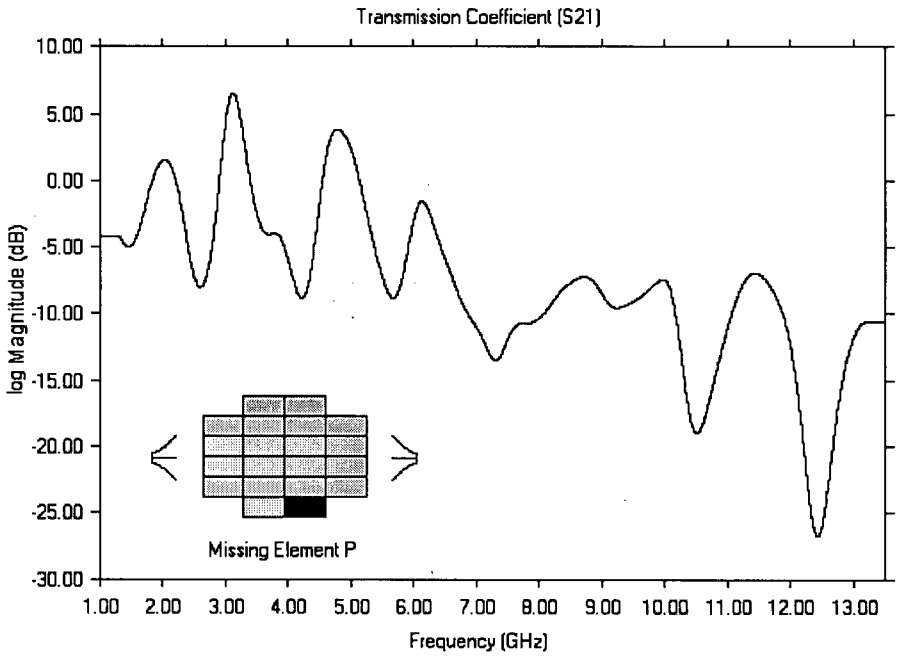

Figure F17: Transmission Coefficient S_{21} spectrum for model M_{1P}

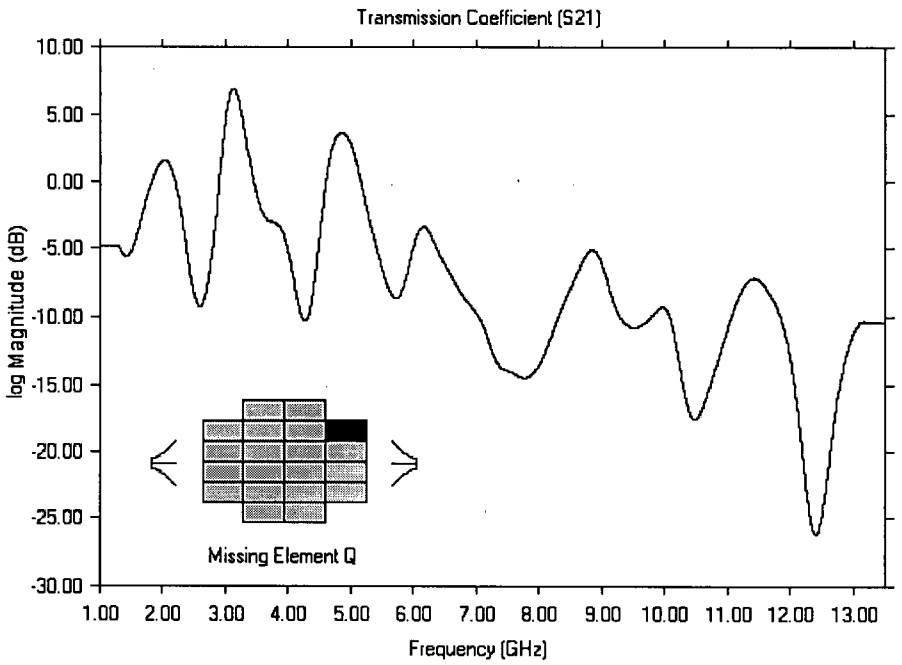

Figure F18: Transmission Coefficient S_{21} spectrum for model M_{1Q}

Appendix F - Transmission Coefficient S_{21} versus Frequency for Standard Models

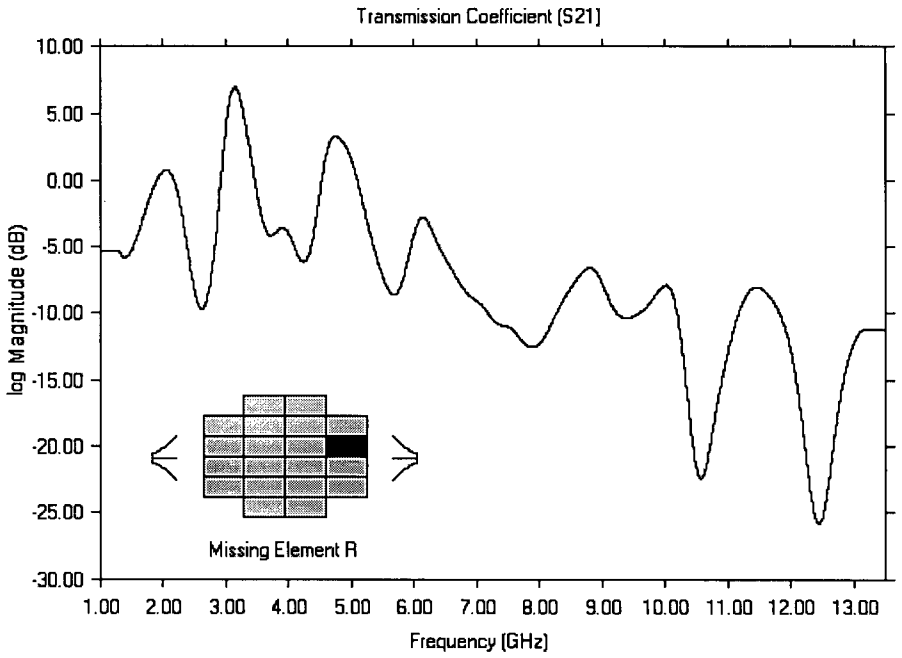

Figure F19: Transmission Coefficient S_{21} spectrum for model M_{1R}

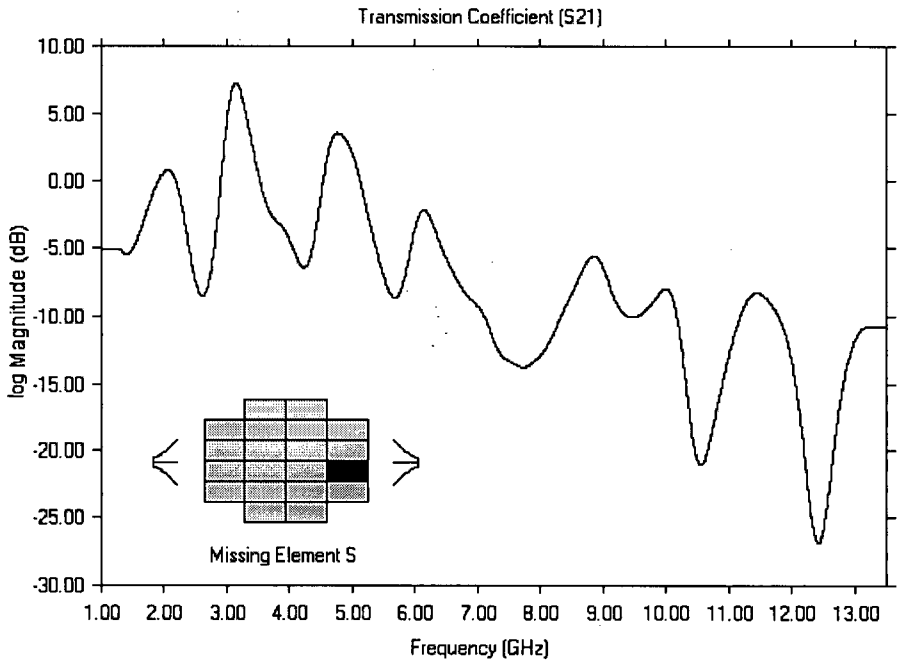

Figure F20: Transmission Coefficient S_{21} spectrum for model M_{1S}

Appendix F - Transmission Coefficient S_{21} versus Frequency for Standard Models

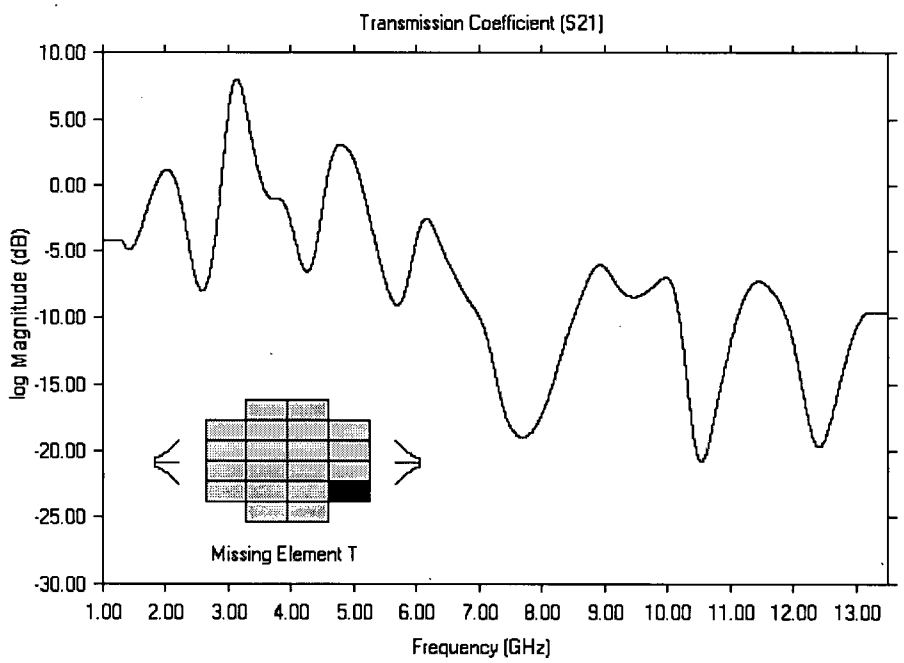

Figure F21: Transmission Coefficient S_{21} spectrum for model M_{1T}

Appendix G - Table of Model Wins vs. Element Removed for Model Rotated 90 degrees

Model	M_2	M_{2A}	M_{2B}	M_{2C}	M_{2D}	M_{2E}	M_{2F}	M_{2G}	M_{2H}	M_{2I}	M_{2J}
M_1	**914**	15	63	35	28	11	73	20	6	133	49
M_{1A}	27	**1026**	85	28	121	2	11	19	1	40	5
M_{1B}	30	7	**567**	215	35	11	13	18	18	91	11
M_{1C}	42	14	227	**776**	47	5	51	3	18	61	1
M_{1D}	9	104	82	335	**550**	0	6	5	7	44	11
M_{1E}	43	20	70	24	29	**1082**	206	31	53	158	219
M_{1F}	59	24	66	23	9	57	**318**	51	65	206	67
M_{1G}	49	5	61	24	7	38	134	**832**	130	135	23
M_{1H}	34	14	52	5	5	49	61	206	**1006**	125	46
M_{1I}	43	9	77	22	56	49	77	119	96	**495**	95
M_{1J}	24	30	53	78	70	113	142	43	18	120	**846**
M_{1K}	21	17	73	45	20	68	47	29	69	66	23
M_{1L}	57	13	56	40	14	24	247	69	15	167	76
M_{1M}	47	14	53	35	6	8	91	40	25	144	6
M_{1N}	30	4	52	23	13	6	50	70	75	114	26
M_{1O}	58	10	70	39	35	61	88	20	16	158	38
M_{1P}	102	30	54	29	12	55	29	81	19	42	92
M_{1Q}	30	21	124	13	32	4	32	8	50	51	3
M_{1R}	19	9	60	7	61	3	9	6	4	43	1
M_{1S}	73	13	77	20	112	9	2	1	8	44	1
M_{1T}	8	61	56	10	49	0	13	2	12	48	13

Table G1: (a) Number of comparison wins for sample models M_2 thru M_{2J} vs. reference models M_1 thru M_{1T} with both models rotated 90 degrees

Appendix G - Table of Model Wins vs. Element Removed for Model Rotated 90 degrees

Model	M_{2K}	M_{2L}	M_{2M}	M_{2N}	M_{2O}	M_{2P}	M_{2Q}	M_{2R}	M_{2S}	M_{2T}
M_1	48	33	26	41	26	98	56	63	20	52
M_{1A}	12	2	8	6	20	17	52	61	54	30
M_{1B}	32	19	7	17	59	14	115	72	39	13
M_{1C}	10	0	11	28	25	15	69	54	59	27
M_{1D}	3	0	2	0	0	6	70	68	61	40
M_{1E}	76	31	32	9	48	13	51	58	78	21
M_{1F}	44	137	84	40	31	55	45	63	6	10
M_{1G}	57	5	78	91	40	32	57	50	36	23
M_{1H}	29	55	157	62	41	12	50	49	17	22
M_{1I}	20	50	29	57	35	17	60	58	13	14
M_{1J}	107	78	44	39	38	13	53	70	77	27
M_{1K}	**886**	112	75	29	24	95	131	56	15	49
M_{1L}	51	**785**	77	147	140	17	58	59	5	16
M_{1M}	87	106	**730**	290	115	71	56	104	5	11
M_{1N}	9	122	104	**630**	101	90	98	61	12	23
M_{1O}	49	126	105	122	**774**	42	71	52	8	9
M_{1P}	114	40	51	32	113	**994**	128	59	16	82
M_{1Q}	9	18	3	6	43	13	**947**	100	88	105
M_{1R}	2	2	3	3	0	2	62	**475**	140	194
M_{1S}	13	0	0	1	0	2	62	214	**645**	29
M_{1T}	0	6	0	4	2	4	105	203	35	**394**

Table G1: (b) Number of comparison wins for sample models M_{2K} thru M_{2T} vs. reference models M_1 thru M_{1T} with both models rotated 90 degrees

Appendix H - Photos of FDL Antenna and Connector

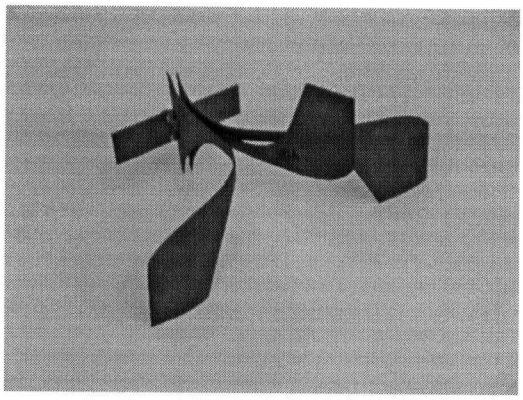

Figure H1: Three quarter View of FDL antenna

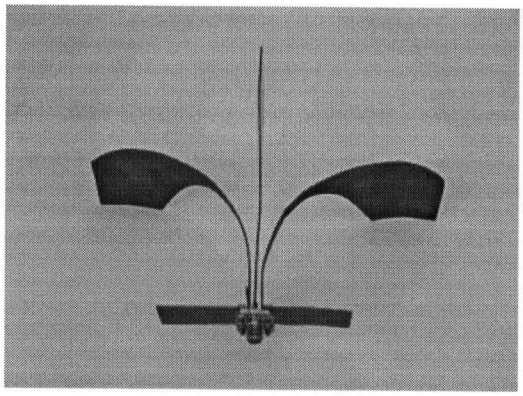

Figure H2: Top View of FDL Antenna Showing Fleur-de-Lis Profile

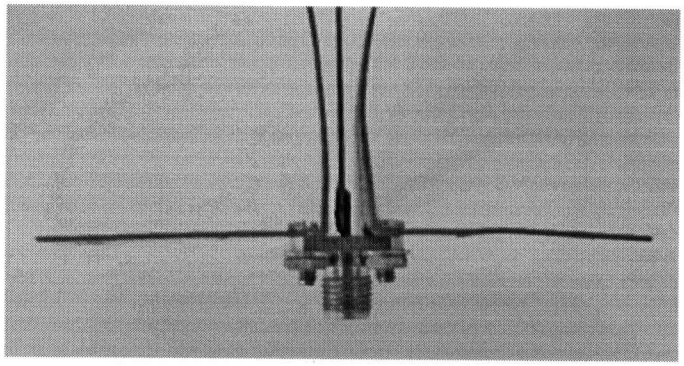

Figure H3: FDL Connector Showing Assembly Method. Note: Copper side strips are for mounting FDL to scanner and do not affect the antenna performance.